UNIVERSITY OF SOUTHAMPTON

FACULTY OF NATURAL AND ENVIRONMENTAL SCIENCES

School of Ocean and Earth Science

Temporal variations in continental weathering processes: Insights from Li and Mg isotopes

by

David Mike Fries

Thesis for the degree of Doctor of Philosophy

June 2018

À ma chère et tendre Maman,
Qui m'a appris à respirer la vie avec un beau sourire

Pou Manman mwen,
ki aprann mwen respiré la vi épi an bel souri

To my beloved Mummy,
Who taught me to breathe life with a beautiful smile

UNIVERSITY OF SOUTHAMPTON

ABSTRACT

FACULTY OF NATURAL AND ENVIRONMENTAL SCIENCES

Ocean and Earth Sciences

Thesis for the degree of Doctor of Philosophy

TEMPORAL VARIATIONS IN CONTINENTAL WEATHERING PROCESSES: INSIGHTS FROM LI AND MG ISOTOPES

By David Mike Fries

Continental weathering delivers elements to the oceans via rivers, is responsible for soil and landscape formation, and regulates the concentration of CO_2 in the atmosphere. There are multiple controls on rates of continental weathering that can vary in both space and time. This study utilises the lithium (Li) and magnesium (Mg) isotope composition (δ^7Li and δ^{26}Mg) of weathering products to better understand the hydrological controls on weathering processes in different environmental settings.

The effects of glacial weathering processes on the isotope signatures of Li and Mg delivered to the ocean are assessed by analysis of fjord waters in Greenland at times of high and low ice melt. These data demonstrate that glacial weathering is an insignificant source of both Li and Mg even when ice melt is high. The influence of melt water input on δ^7Li and δ^{26}Mg can only be detected at very high freshwater/seawater ratios (>5).

Although weathering rates in highly weathered tropical river catchments are typically considered to be very low, analyses of weathering products from the Quiock Creek catchment in Guadeloupe show that weathering processes can respond to short-lived rain events. The δ^7Li composition of the Creek decreases after a storm event because of increased input of Li from soil solutions input that have relatively low δ^7Li; however, there is little change in δ^{26}Mg after rain events because most of the Mg in the Creek is supplied by throughfall.

There are also significant differences in the δ^7Li value of the River Amazon between the high and low water stages. δ^7Li values are 0.7 to 8.7‰ higher in the wet season, which is attributed to increased input of Li stored in floodplains. However, input of Mg from floodplains has little effect on δ^{26}Mg.

Table of Contents

Table of Tables

Table of Figures

Academic Thesis: Declaration Of Authorship

I,David Mike Fries

declare that this thesis and the work presented in it are my own and has been generated by me as the result of my own original research.

Temporal variations in continental weathering processes: Insights from Li and Mg isotopes

I confirm that:

1. This work was done wholly or mainly while in candidature for a research degree at this University;
2. Where any part of this thesis has previously been submitted for a degree or any other qualification at this University or any other institution, this has been clearly stated;
3. Where I have consulted the published work of others, this is always clearly attributed;
4. Where I have quoted from the work of others, the source is always given. With the exception of such quotations, this thesis is entirely my own work;
5. I have acknowledged all main sources of help;
6. Where the thesis is based on work done by myself jointly with others, I have made clear exactly what was done by others and what I have contributed myself;
7. None of this work has been published before submission

Signed: .....

Date: .....

Acknowledgements

It is my great pleasure to show my appreciation to all the people who contributed in multiple ways to my 3 years and 8 months of my adventure in the United-Kingdom.

Firstly, I would like to express my sincere and extreme gratitude to my main supervisor, mentor and advisor, Rachael James, for all these years. I would like especially to thank you for the continuous support of my work with detailed and honest feedback, for your patience, all the motivation you gave me to go further, and for the trust and confidence that helped me to work to the best of my abilities in the laboratory and in my research in general. Thank you Rachael.

I am also grateful to my co-supervisors Damon Teagle and Doug Conelly who gave me this opportunity to work in Southampton. Together with my panel chair Gavin Foster they helped me to keep focused to develop my research to its full potential.

I would like to thank all of the IsoNose (Isotopic tools as Novel sensors of Earth surface resources) members and especially Friedhelm von Blanckenburg and Maja Tesmer who led this successful project where I have learnt an incredible amount of new skills.

Many thanks to Mark Hopwood for giving me my first water samples, freshly collected from Greenland. I am very grateful to Christopher Pearce for teaching me the essential skills of measuring Mg isotopes in the clean lab. I would like to thank Martin Voigt for his big help in doing the first Mg calibration. A huge thank you to Aurélien Beaumais, with whom I worked to resolve the “Mg mystery” and for being a fantastic lab colleague. I am deeply grateful to Matthew Cooper, Andy Milton and Kate Peel for their help to get the all the samples processed in this work, and for sharing their expert advice with me.

All the work done in Guadeloupe would not have been possible without the help and contributions of Julien Bouchez, Céline Dessert, Vincent Robert, Eric Lajeunesse, and Guillaume Roehm. They have all supported me in different ways but all in the best manner possible.

I am particularly indebted to the many colleagues at ETH in Zurich who gave me the opportunity to see the beauty of the Amazon River during wonderful fieldwork. I am especially grateful to Derek Vance and Brandi Revels for organising all the fieldwork, for performing major and minor element

analyses, and to have shared these samples with me. I am also grateful to Candido Moura, Chantal Freymond, Gabriela Santilli and Brandi Revels for being very pleasant co-workers on the boat and for their help to bring me back to UK after my passport was stolen.

One of the best thing that I have achieved during this 3 years was to create an awesome network of friends that constantly supported me, advised me, and encouraged me. It is a great pleasure to say thank you to my wonderful office friends: Elena, Katie, Clare, Abbie and Cobain, who have been with me since the beginning. Also to Charlotte, Claire and good luck to the newly arrived Maarten. Massive thanks to Adeline, Amaya, Anas, Aude, Barbara, Dan, Delphine (Dédé), Elwyn, Erik, Gavin, Giuseppe, Hachem, Hazel, James, Jens, Jérémy, Katerina, Lina, Luca, Maria, Marla, Matthias, Matthew, Melanie, Nathan, Sahoo, Séverine, Sophie and Xiaodong who have made this adventure in Southampton unforgettable with a lot of brilliant, enjoyable, incredible and fabulous moments.

I must say and address a huge thank you to my friends from Strasbourg (now all over the world) and mostly: Antoine, Laura, Hugo, Jeanne (V), Valentin, Jeanne (M), Mickaël, Marie-Eva, Yann, Sandrine, Vincent, Jérémy, Jérémie, Marc, Joseph, Patric, Alexandre, Camille, Carole, Rodolphe… you were and you are still magnificent.

Finally, I would like to thank and show my appreciation to all my family. I grew, learnt and developed myself with you and I hope and wish it will continue for a very long time. You are the best. Thank you in particular to my brother Allan, a future doctor in power (Qui vincit accipit), my sister Melissa, a brilliant and talented artist, and my dear father Hugo who always believed, and always supported me. However, I want and I need to dedicate this work to my beloved and missed mother, Maryse, who left this world too soon during the process of writing this PhD. I am sure she would have been proud to see her son submitting his PhD thesis. Je t'aime.

Chapter I. Introduction

I.1 Weathering

The Earth's surface has been in constant evolution since its formation about 4.566 billion years ago. A major driver of change at the Earth's surface is the operation of its hydrosphere. Based on evidence from the oxygen isotope composition of ancient zircons from Jack Hills in Western Australia, the Earth's hydrosphere formed around 160 million years after Earth accretion, when temperatures became low enough to allow liquid water to be present at the Earth's surface (Wilde et al., 2001; Valley et al., 2002). Water cycle is the principal operator of weathering processes.

I.1.1 Definition and generalities

Alteration of the Earth's surface by water and erosion is known as weathering. If the weathering process changes the chemical composition of the original mineral or rock, this is called chemical weathering, whereas breakdown of minerals or rocks without chemical modification is known as physical (or mechanical) weathering. Weathering processes drive soil and landscape formation (Figure I-1), and they transfer dissolved solutes and particulate material from the continents to the

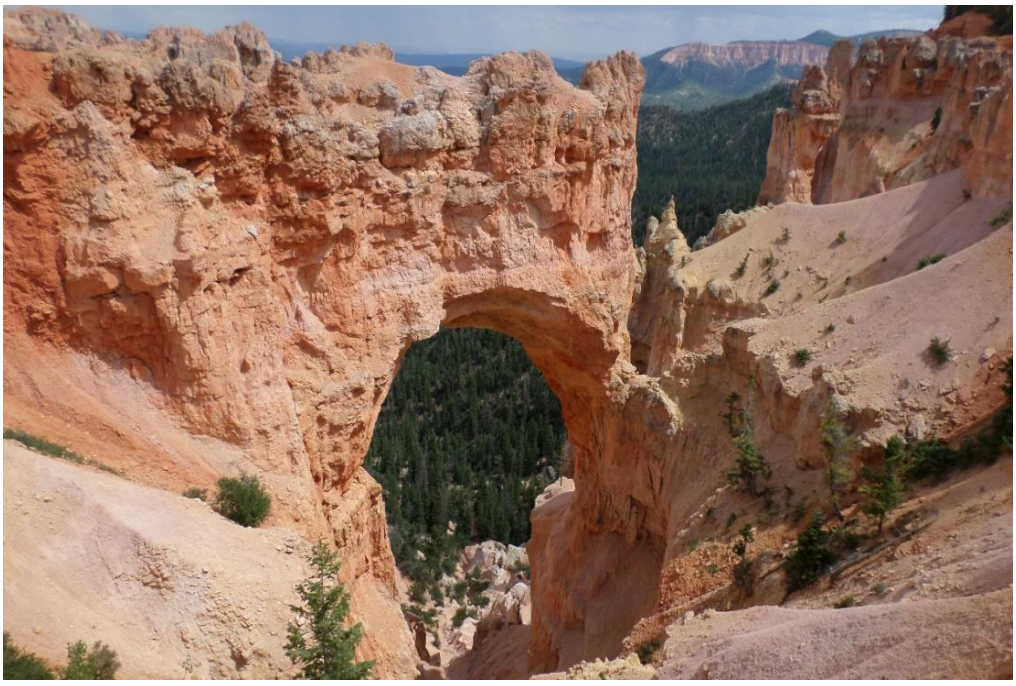

Figure I-1. Bryce Canyon (Utah, United States). Weathering processes have modified the landscape forming arches. Chemical weathering dissolves the limestone, and frost wedging shatters rocks apart. The rocks have a red /pink colour due to the presence of iron oxides.

ocean via rivers. Rates of weathering are determined by a combination of climate, tectonic, biological and geological factors:

- **Climate**: Temperature and rainfall are a key control on weathering rates and processes. For example in tropical areas, high temperatures and heavy rainfall promote faster chemical weathering (Gaillardet et al., 1999a). On the other hand, in polar regions, freezing of liquid water has the potential to widen cracks and push rocks apart because water expands in volume upon freezing.
- **Tectonics**: In tectonically active landscapes weathering fluxes can be low due to short soil residence time (Dixon et al., 2012). By contrast, due to low erosion rates, thick soils may develop in tectonically inactive regions (Heimsath et al., 1997).
- **Vegetation**: Soils host a variety of plants, bacteria, fungi and other organisms that increase chemical weathering by producing organic acids (Griffiths et al., 1994) as well as CO_2, which acts to increase the rate of chemical weathering (Eby, 2004). Additionally, tree roots have the capability to retain and protect soils from being eroded, increase the rate of physical weathering by fracturing and wedging the rock at different scales (rocks, minerals; Appendix A 1) and increase rate of chemical weathering via moisture flux along roots and root channels (Pawlik et al., 2016).
- **Lithology**: The structure and mineralogy of the rock affects weathering rates. Minerals like halite (NaCl) are readily soluble in water whereas quartz (SiO_2) is more resistant to dissolution. Similarly, igneous rocks like granite are less susceptible to cracking and fragmentation than sedimentary rocks like sandstone or limestone**.** Table I-1 lists common minerals in terms of their resistance to weathering (Berner and Berner, 1996; Eby, 2004). The length of time the rocks are exposed to the atmosphere/hydrosphere is also a major control of weathering rates. In old soils (~1 million years) weathering rates were found to be three to four orders of magnitude lower than in soils at an initial development stage (Egli et al., 2014). The longer rocks are exposed at the Earth's surface, the longer their interactions with water have the potential to modify the structure and mineralogy of the rock.

Table I-1 Resistance of various minerals to weathering from the less stable to the most stable.

Minerals	Composition	Resistance to weathering
Halite	NaCl	Less stable
Gypsum, Anhydrite	$CaSO_4.2H_2O$, $CaSO_4$	
Pyrite	FeS_2	
Calcite	$CaCO_3$	
Dolomite	$CaMg(CO_3)_2$	
Volcanic glass (not a mineral)	Ca,Mg,Na,K,Al,Fe-silicate	
Olivine	$(Mg, Fe)SiO_4$	
Ca-Plagioclase	$CaAl_2Si_2O_8$	
Pyroxenes	$(Mg,Fe)SiO_3$, $Ca(Mg,Fe)Si_2O_6$	Increasing stability
Ca-Na Plagioclase	$(Ca,Na)Al_3Si_3O_8$	
Amphiboles	$Ca_2(Mg,Fe)_3SiO_{22}(OH)_3$	
Na-Plagioclase	$NaAlSi_3O_8$	
Biotite	$K(Mg,Fe)_3(AlSi_3O_{10})(OH)_2$	
K-Feldspar	$KAlSi_3O_8$	
Muscovite	$KAlSi_3O_{10}(OH)_2$	
Vermiculite, Smectite	$(Mg,Ca)_{0.7}(Mg,Fe,Al)_6(Al,Si)_8O_{22}(OH)_4.8H_2O$ $(Na,Ca)_{0.3}(Al,Mg)_2Si_4O_{10}(OH)_2.nH_2O$	
Quartz	SiO_2	
Kaolinite	$Al_2Si_2O_5(OH)_4$	
Gibbsite, hematite, goethite	$Al(OH)_3$, Fe_2O_3, $FeO(OH)$	Most stable

I.1.2 Physical and chemical weathering

I.1.2.1 Physical weathering

Physical weathering is defined as the breakdown of rocks and decomposition of minerals without chemical changes. These mechanical processes increase the surface area to volume ratio by fragmenting of a rock/mineral (Figure I-2) so that subsequent chemical weathering is more

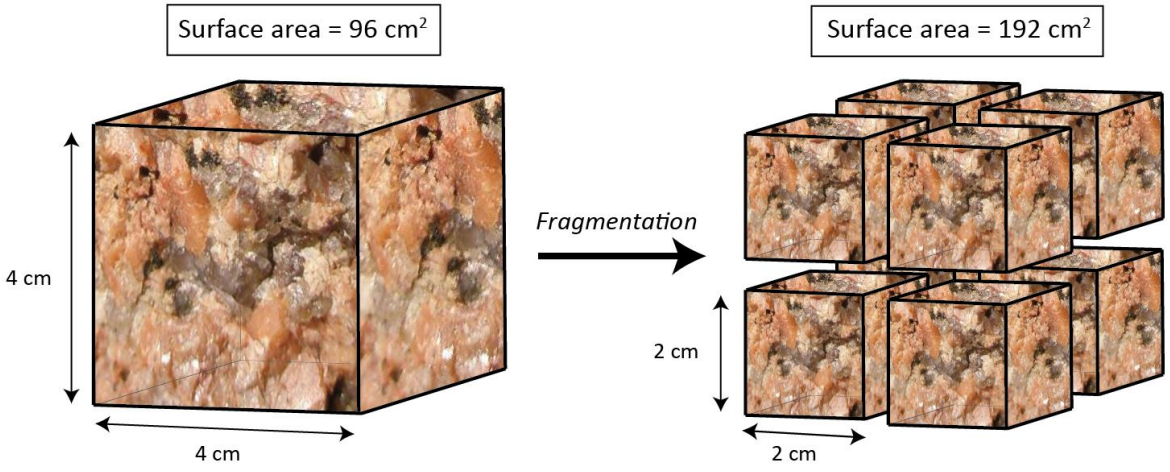

Figure I-2. Fragmentation increases the surface area of a rock, providing a greater surface area for chemical weathering.

effective. Tectonics affect erosion rates by elevating terrain so that erosive agents gain potential energy which tend to break fragments into smaller pieces, making them easier to transport by rivers and glaciers (Molnar et al., 2007). The action of plant roots has a strong impact on the physical properties of soils, depending of the size of the roots (Li et al., 2006). Crystallizing salts can also affect rates of physical weathering as crystal growth, hydration or thermal expansion can breakdown the soil matrix (Camuffo, 1995). In cold regions, rocks are subjected to freeze–thaw action. When the temperature of the rock drops below freezing, freeze-thaw cycles develop, and the pressure exerted by the growing ice crystals causes fracturing (Chen et al., 2004).

I.1.2.2 Chemical weathering

Chemical weathering is a surface process that takes place through interactions between water, air and a rock/mineral. On the continents, chemical weathering reactions include dissolution, precipitation, and oxidation-reduction mediated by an aqueous solution. These reactions alter the mineral composition of the weathered material and produce solid material with a new chemical composition (e.g. clay minerals, oxides and hydroxides) or transfer dissolved solutes into the fluid phase. Most weathering reactions involve the exchange of protons (H^+) or anions (OH^-), or the exchange of electrons (e^-) in the case of oxidation-reduction reactions (Bridge and Demicco, 2008). Oxidation-reduction reactions are especially important for the weathering of Fe-bearing minerals. Chemical weathering rates for specific minerals are mainly assessed by experimental studies in the laboratory (Lasaga et al., 1994; White, 2002). Field weathering rates can be orders of magnitude lower than those measured experimentally in the laboratory. This difference is mainly due to uncertainty in the duration of chemical weathering in field conditions and laboratory simulations that are too short to fully represent the natural system (White and Brantley, 2003). For instance, in natural conditions, weathering reactions can be close to thermodynamic equilibrium compared to highly unsaturated conditions during experimental reaction of a mineral, leading to variabilities of weathering rates. Figure I-3 is a chart summarizing the factors that influence weathering.

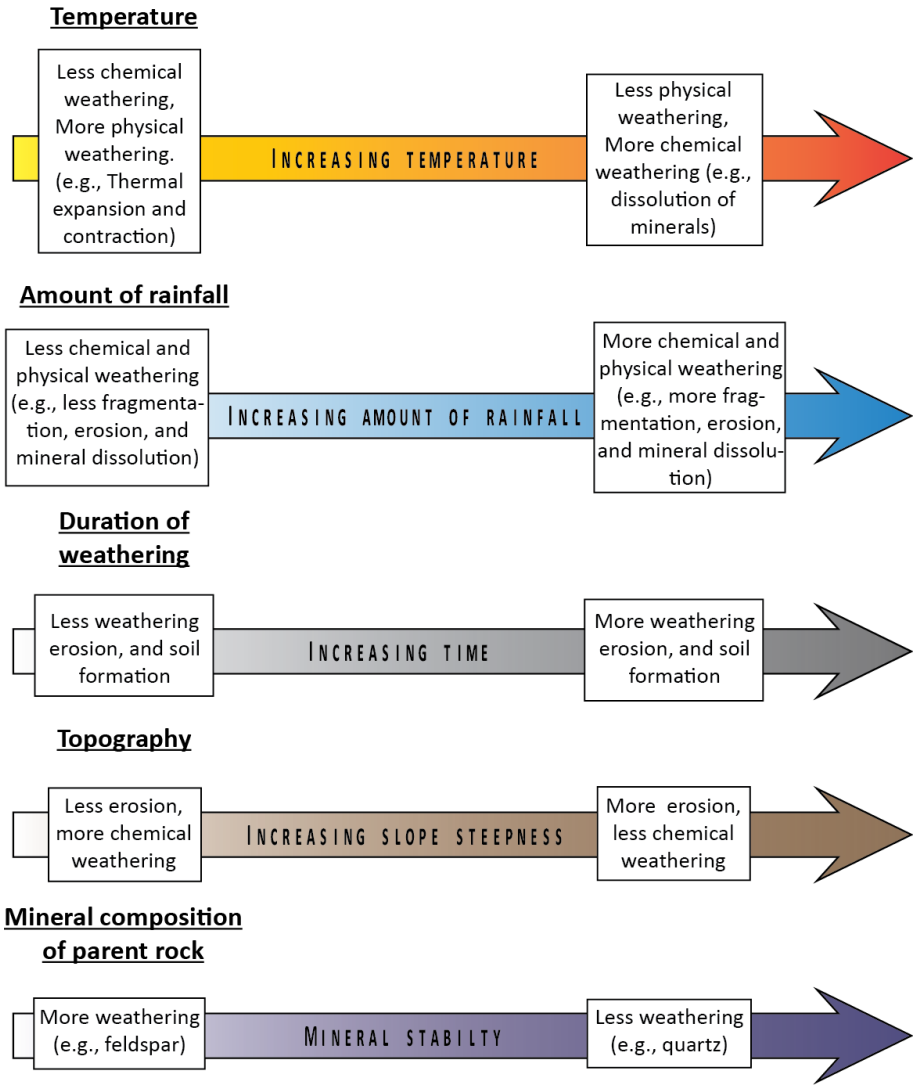

Figure I-3. Summary of different factors influencing weathering and erosion (modified from Grotzinger and Jordan, 2014).

I.1.3 Weathering regimes

Studies of large river systems (Gaillardet et al., 1999b), soil profiles (Riebe et al., 2001) and small, well characterised catchments (West et al., 2005) have shown correlations between mechanical erosion rates and chemical denudation. Two main weathering regimes have been characterized: Transport-limited weathering regimes and kinetically-limited weathering regimes (Stallard and Edmond, 1983; West et al., 2005). Transport-limited weathering regimes are characterized by low erosion rates, such that the supply of fresh minerals is the limiting factor for chemical weathering (Figure I-4). By contrast, kinetically-limited weathering regimes are characterized by higher erosion rates, such that chemical weathering is not limited by the supply of fresh minerals, but by water-

rock interaction time (or kinetics) that, in turn, is regulated mainly by temperature and runoff (Figure I-4 and Appendix A 2).

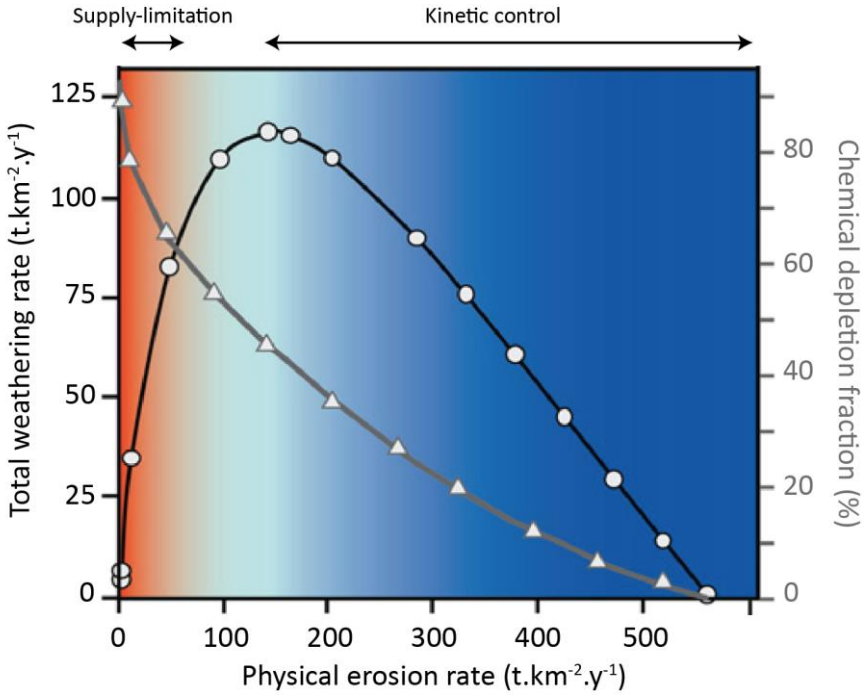

Figure I-4. Variation of weathering rate as a function of erosion rate (open circles) based on the model framework of Ferrier and Kirchner (2008). Supply-limitation refers to transport-limited weathering regimes (see I.3.1). Kinetic control occurs when physical erosion high. Chemical depletion fraction (or weathering intensity, see I.3.1; open triangles) decreases with increasing erosion rate reflecting the decreasing influence of the supply of fresh minerals from soil production (Dixon et al., 2012).

I.2 Weathering, climate and CO_2

The atmospheric concentration of CO_2 moderates the response of global mean temperature to Milankovich forcing (Petit et al., 1999). For instance, concentrations of CO_2 (and CH_4) in air bubbles trapped in the Vostok ice core over the last 300–400 kyr (thousand years) show a positive association with air temperature in Antarctica (Appendix A 4; Petit et al., 1999).

On geological time scales, amounts of CO_2 in the atmosphere, hydrosphere and soils are determined by processes such as carbon sedimentation (and burial), silicate weathering, and volcanic and/or metamorphic release of CO_2 (Figure I-5; Garrels et al., 1975). The silicate weathering time scale is thought to be between ~240 Kyr (range 170–380 Kyr; Colbourn et al., 2015) and >1 million year (Myr; Berner et al., 1983). Chemical weathering of silicates (Eq. I-1) consumes atmospheric CO_2 according to the reaction (Walker et al., 1981; Berner et al., 1983):

$$2CO_2 + 3H_2O + CaSiO_3 \rightarrow Ca^{2+} + 2HCO_3^- + H_4SiO_4 \qquad \textit{Eq. I-1}$$

In this reaction, CO_2 is converted to HCO_3^- (Eq. I-2) that is transported by rivers into the ocean, where it is eventually stored as carbonate in ocean sediments:

$$Ca^{2+} + 2HCO_3^- + H_4SiO_4 \rightarrow CaCO_3 + SiO_2 + CO_2 + 3H_2O \qquad \textit{Eq. I-2}$$

Thus, silicate weathering results in net consumption of 1 mole of CO_2 for every mole of Ca (or Mg) ions released (Eq. I-3). By contrast, weathering of carbonates results in no net consumption of CO_2:

$$CaCO_3 + CO_2 + H_2O \underset{\textit{Sedimentation in oceans}}{\overset{\textit{Weathering}}{\rightleftharpoons}} Ca^{2+} + 2HCO_3^- \qquad \textit{Eq. I-3}$$

To assess the linkages between weathering, CO_2 and climate, it is critical to better understand the parameters that regulate weathering processes. The study of elemental concentrations and isotope composition of lithium (Li) and magnesium (Mg) isotopes in the natural environment are promising tools to this end because the behaviour of their isotopes are sensitive to changes in weathering processes. Moreover, given that the compositions of both Mg and Li in seawater are principally

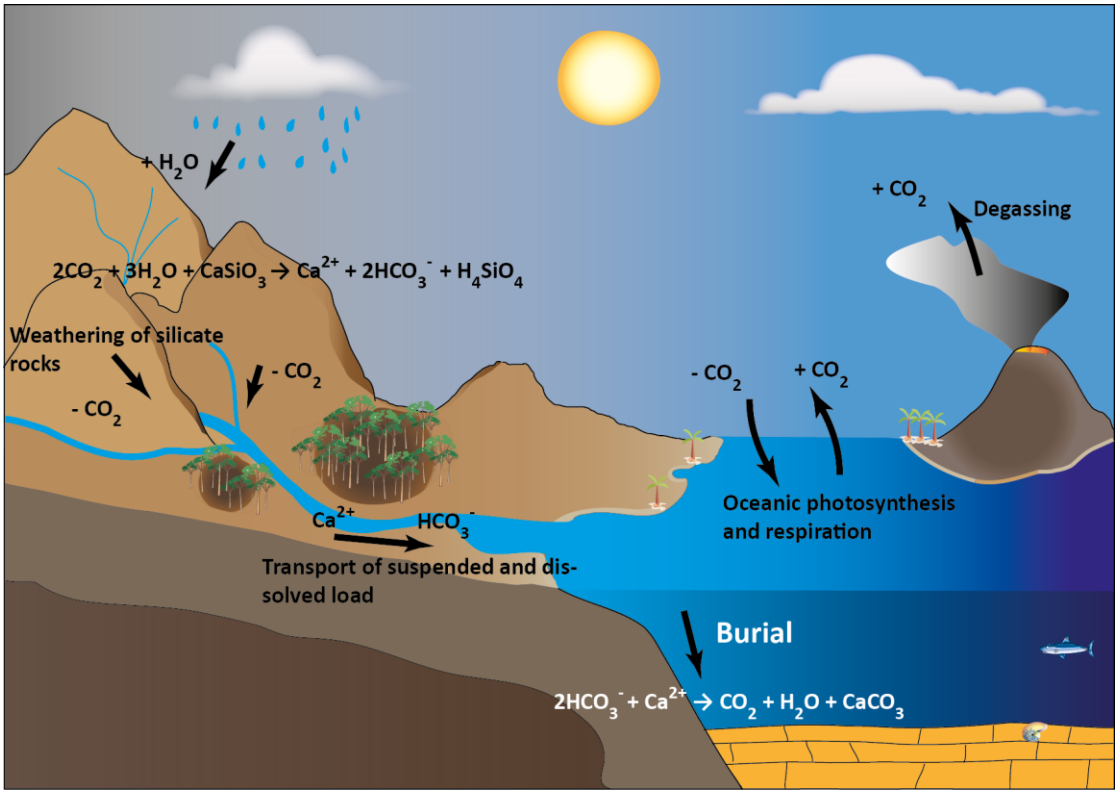

Figure I-5. Simplified scheme of the long-term carbon cycle. The weathering of silicates minerals leads to the consumption of CO_2 from the atmosphere which is stored in seawater as carbonate.

regulated by riverine inputs, information on weathering processes and rates of silicate weathering in the past can be determined from the marine sedimentary record.

I.3 Lithium isotopes

Lithium (Li) has two stable isotopes, ^{6}Li and ^{7}Li, with abundances, respectively, of 7.5% and 92.5%. The large relative mass difference between these isotopes (~16%) means that Li displays a wide variation in $^{7}Li/^{6}Li$ under Earth surface conditions (Figure I-6). Lithium isotopes are a powerful tracer of weathering processes, because:

- Lithium isotopes are fractionated during weathering processes (see section I.3.1).
- Lithium is not an essential plant nutrient and therefore it is unaffected by biological processes (Lemarchand et al., 2010; Clergue et al., 2015).
- The Li content of river water is principally (> 90%) derived from weathering of silicate rocks, even in catchments with predominantly carbonate bedrock (Kisakurek et al., 2005).
- Lithium is widely distributed in the Earth's crust, it is a fluid mobile element, and it is present only in the +1 valence state (Li^{+}), so its isotope composition is not influenced by redox reactions (Tang et al., 2007).

Lithium is a conservative element in the ocean and $[Li]_{SW}$ = 26 µmol/kg (Morozov, 1968). It has a residence time of ~1.2 million years (Misra and Froelich, 2012) which is long enough to allow a complete homogenisation of the Li isotope composition of seawater ($\delta^{7}Li_{SW=}$~31‰; James and Palmer, 2000a; Hall et al., 2005; Pogge von Strandmann et al., 2008b).

The Li isotope composition of natural samples is expressed as $\delta^{7}Li$ (Eq. I-4), which is given by:

$$\delta\ ^{7}Li = \left[\frac{\left(\frac{^{7}Li}{^{6}Li}\right)_{sample}}{\left(\frac{^{7}Li}{^{6}Li}\right)_{L-SVEC}} - 1\right] \times 10^{3} \qquad \textit{Eq. I-4}$$

The standard is conventionally the purified Li_2CO_3 reference material L-SVEC (Flesch et al., 1973).

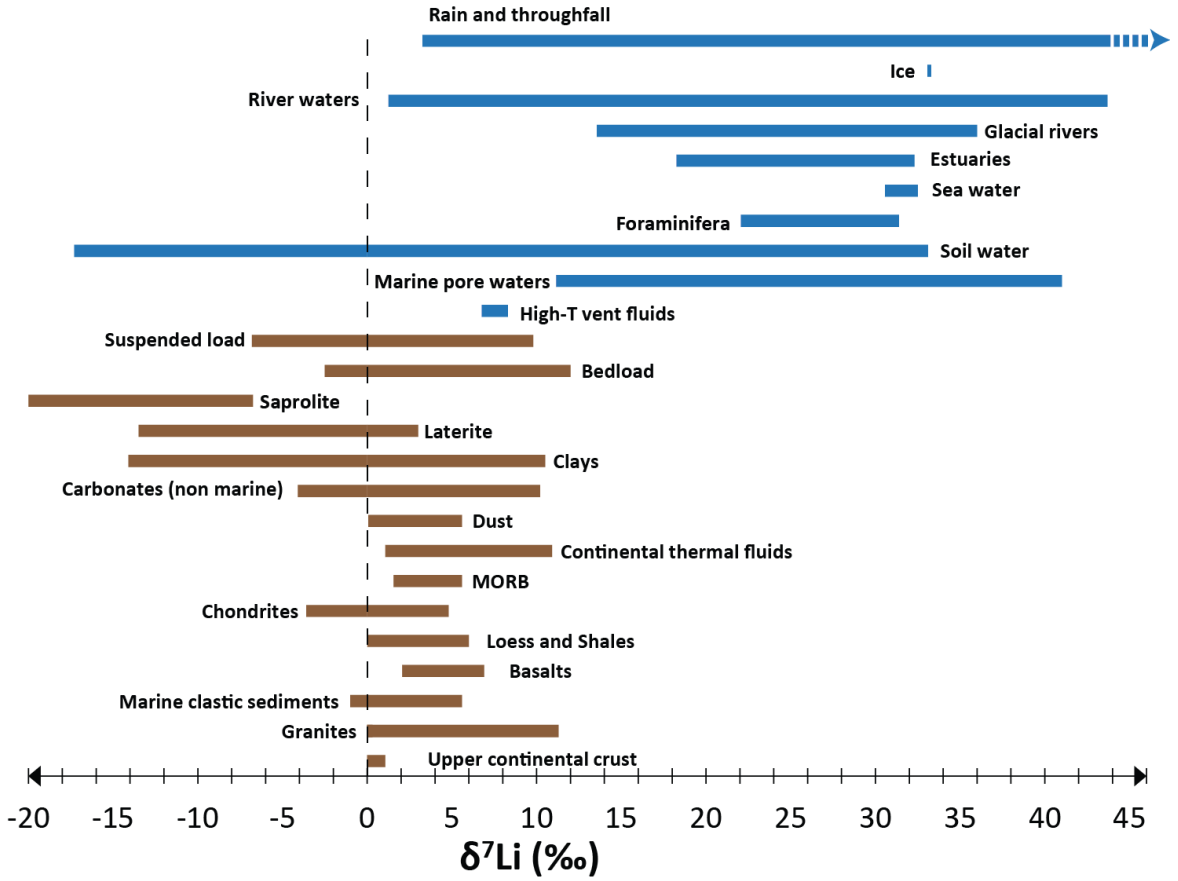

Figure I-6. Isotope composition of lithium in major Earth surface reservoirs.Data sources: Rain and throughfall (Millot et al., 2010a; Clergue et al., 2015) ice (Pogge von Strandmann et al., 2006) river waters (Huh et al., 2001; Bottomley et al., 2003; Kisakurek et al., 2005; Pogge von Strandmann et al., 2006; Lemarchand et al., 2010; Millot et al., 2010c; Pogge von Strandmann et al., 2010; Wimpenny et al., 2010b; Dellinger et al., 2015), glacial rivers (Wimpenny et al., 2010b), estuaries (Pogge von Strandmann et al., 2008b), seawater (James and Palmer, 2000a; Hall et al., 2005; Pogge von Strandmann et al., 2008b), foraminifera (Hathorne and James, 2006; Misra and Froelich, 2012); soil water (Lemarchand et al., 2010; Pogge von Strandmann et al., 2012), marine pore waters (James and Palmer, 2000b); High-T vent fluids (Hathorne and James, 2006; Froelich and Misra, 2014) suspended and bedload load (James and Palmer, 2000b; Kisakurek et al., 2005; Pogge von Strandmann et al., 2006; Pogge von Strandmann et al., 2008b; Millot et al., 2010c; Pogge von Strandmann et al., 2010; Wimpenny et al., 2010b; Dellinger et al., 2014)) saprolite (Teng et al., 2010) laterite (Kisakurek et al., 2004b; Clergue et al., 2015) clays, carbonates and dust (Tsai et al., 2014; Clergue et al., 2015) Continental thermal fluids (Kisakurek et al., 2005; Pogge von Strandmann et al., 2010) MORB, chondrites and marine clastic sediments (Tomascak, 2004) loess and shales (James and Palmer, 2000a; Millot et al., 2010c) basalts (James and Palmer, 2000a; Kisakurek et al., 2004b; Wimpenny et al., 2010a; Pogge von Strandmann et al., 2013; Froelich and Misra, 2014) granites (James and Palmer, 2000a; Bottomley et al., 2003; Bryant et al., 2004; Kisakurek et al., 2004a; Lemarchand et al., 2010) and Upper continental crust (Sauzeat et al., 2015).

I.3.1 Behaviour of Li isotopes during weathering

The natural range of δ^7Li values in river waters is large; but the mean value is δ^7Li = ~23‰ (Huh et al., 1998) which is higher than all terrestrial rocks (Figure I-6). As there is no (or little) fractionation of Li isotopes during dissolution of primary minerals (Pistiner and Henderson, 2003; Wimpenny et al., 2010a), this indicates that fractionation occurs during secondary mineral formation: ^{6}Li is preferentially retained in the solid phase whilst ^{7}Li goes into solution (Huh et al.,

1998; Huh et al., 2001; Rudnick et al., 2004; Kisakurek et al., 2005). As an example, δ^7Li values of the dissolved load of the Orinoco River and its tributaries are higher than δ^7Li value of the corresponding suspended load (Figure I-7).

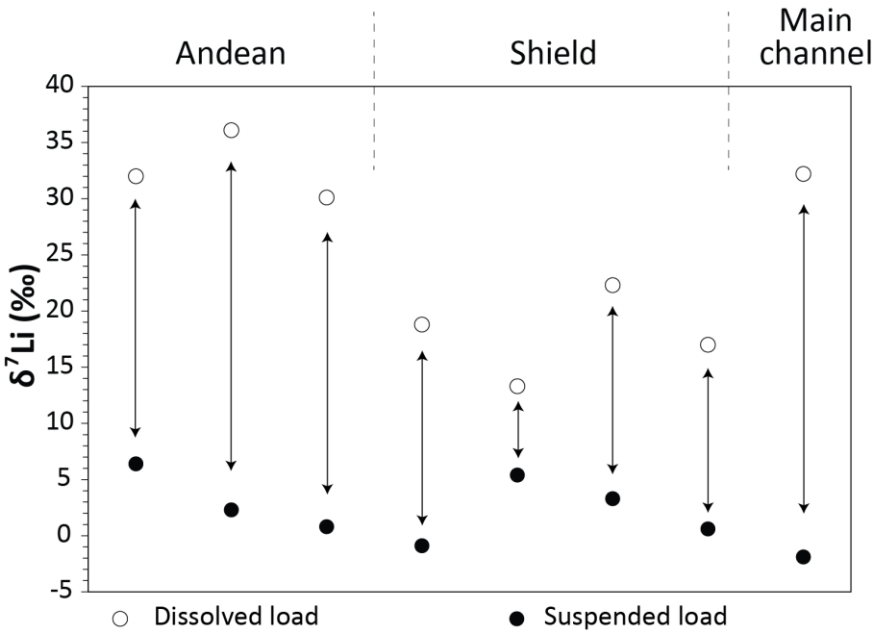

Figure I-7. δ^7Li values for river waters and suspended particulate material of the major tributaries of the Orinoco river. The suspended sediments (solid symbols) always have a lower δ^7Li value than the dissolved load (open symbols) because ^{6}Li is preferentially retained in secondary minerals during weathering. The dissolved loads of Andean tributaries (high relief, reaction limited) have a higher δ^7Li value than the Shield tributaries (low relief, transport limited). After Huh et al., 2001.

Experimental and field studies have shown that the degree of fractionation (fractionation factor) between a secondary mineral and the fluid phase, α, where $\alpha = (^7Li/^6Li)_{mineral}/(^7Li/^6Li)_{solution}$ varied depending on the mineral nature and of the temperature when the fractionation reaction occurred (Vigier et al., 2008; Millot et al., 2010b; Dellinger et al., 2014; Wimpenny et al., 2015). The α values available in the literature span a range from 0.972 to 0.999. For instance, the fractionation factor for smectite is ~0.984 (Vigier et al., 2008), for marine clays it is ~0.985 (Hathorne and James, 2006), and for illites α =0.982- 0.989 (Williams and Hervig, 2005; Weynell et al., 2017). Li is also incorporated in oxide minerals such as gibbsite (α = 0.986; Pistiner and Henderson, 2003) and/or iron oxy-hydroxides (α = 0.980; Wimpenny et al., 2010a).

Early studies on the Li isotope composition of river waters showed that differences in the δ^7Li of the dissolved load relative to the suspended load were principally a function of weathering intensity. In the Nepalese Himalaya, for example, the difference between the δ^7Li values of

the suspended load and the dissolved load in lowland rivers, characterised by more intense weathering regimes (higher temperature and low discharge), is lower than the difference at high elevations (that are likely to represent kinetically limited weathering regimes, Appendix A 3; Kisakurek et al., 2005). A number of more recent studies have focused on better quantifying the relationship between weathering intensity and δ^7Li. Chemical weathering intensity also called chemical depletion fraction (Figure I-4) is defined as the normalization of chemical weathering rates by total denudation rates in a given catchment which is independent of the drainage area (Brimhall and Dietrich, 1987; Riebe et al., 2003). Bouchez et al. (2014a) define weathering intensity as the ratio between the silicate weathering rate (W) and the total denudation rate (D) (W/D; range between 0 and 1). Using this terminology, weathering-limited weathering regimes have low W/D due to high erosion rates, whereas transport-limited weathering regimes have high W/D due to low denudation rates and increased water-rock interaction time. A plot of δ^7Li vs W/D for various rivers shows a characteristic 'boomerang' shape (Figure I-8; Dellinger et al., 2015). If the weathering intensity is high (W/D>0.1), then weathering tends to be congruent and the δ^7Li value of the dissolved load is low and close to that of the bedrock (Kisakurek et al., 2005; Millot et al., 2010c;

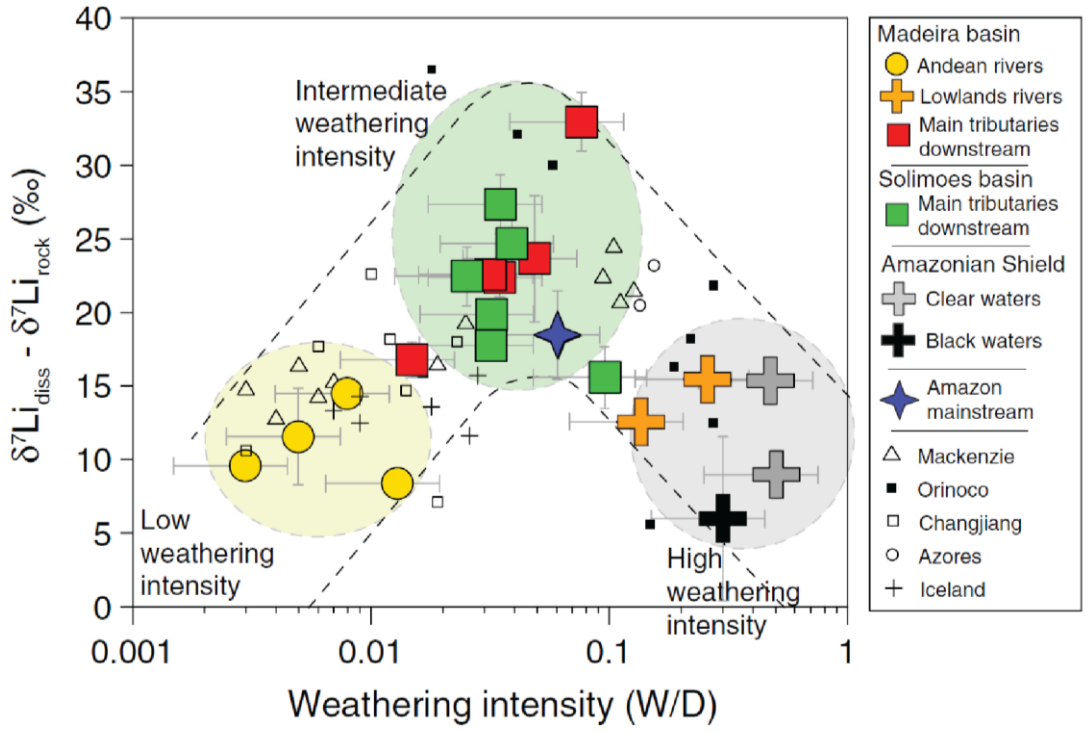

Figure I-8. The "boomerang" relationship between dissolved Li isotope composition corrected for the composition of the bedrock δ^7Li_{diss} -δ^7Li_{rock} vs. silicate weathering intensity, expressed as W/D. After Dellinger et al., 2015.

Dellinger et al., 2015). Similarly at low weathering intensity (W/D<0.01) δ^7Li values are low because silicate weathering rates are low so rivers are undersaturated with respect to secondary minerals. By contrast, δ^7Li values are highest at intermediate weathering intensities (W/D = 0.01–0.10). This is because rates of secondary mineral formation tend to be high relative to the rate of primary mineral dissolution.

I.3.2 Records of past changes in riverine δ^7Li

Over geological timescales, weathering of silicate rocks has continuously released ions into the hydrosphere which have subsequently been delivered to lakes or oceans. When the residence time of a chemical element is longer than the ocean mixing time (~200 to 1800 years; Stommel and Arons, 1959), the concentration and/or isotope composition of that element in the ocean is homogeneous. This is the case for lithium, and riverine fluxes account for ~34% of the total lithium input into the oceans (Figure I-9; Misra and Froelich, 2012; and references therein). Changes to the sources and fluxes of Li to/from the oceans have the capability to change the lithium concentration and isotope composition of seawater. Records of δ^7Li in foraminifera (for example *Orbulina universa;* Hathorne and James, 2006; Hall et al., 2005), are representative of seawater δ^7Li and can

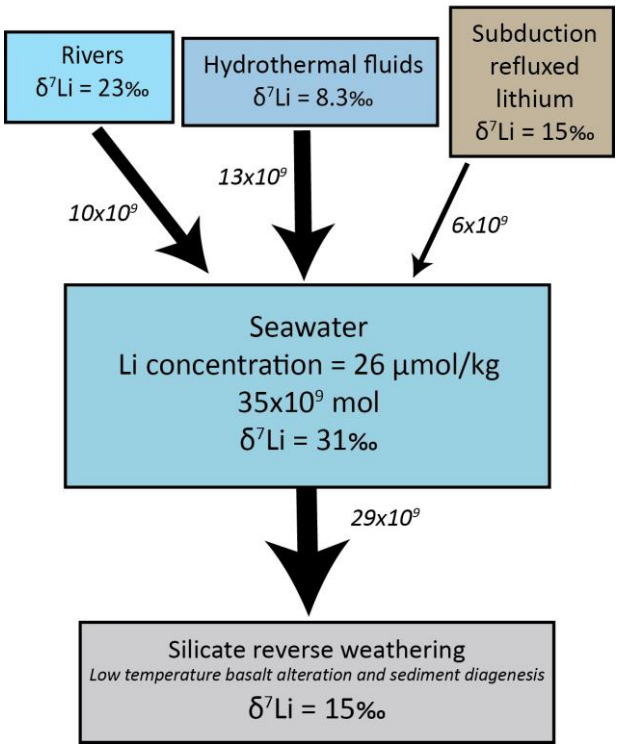

Figure I-9. Box model representing the global Li cycle. Total quantity of Li in seawater is given in mol; fluxes between reservoirs are in mol/yr. After Misra and Froelich, 2012.

be used to detect past variations. Figure I-10 shows the evolution of the Li isotope composition of seawater over the last 68 Myr (Misra and Froelich, 2012). An increase in seawater δ^7Li from ~22‰ since ~55 Ma to the ~31‰ today coincides with a reduction in global mean temperature (Froelich and Misra, 2014). Misra and Froelich (2012) suggest that this increase is due to an increase in both the weathering flux, due to higher rates of mountain building, as well as increased weathering incongruency. By contrast, Vigier and Godderis (2015) suggest that the rise in seawater δ^7Li is linked to an increase in the river flux of Li caused by a reduction in the amount of Li incorporated in clays. Finally, a study of New Zealand rivers suggests that floodplains have high riverine δ^7Li due to continued weathering of material transported from high altitude leading the authors to suggest that increasing seawater δ^7Li during the Cenozoic was the result of formation of large floodplains associated with uplift (Pogge von Strandmann and Henderson, 2015). On the other hand, the lower seawater δ^7Li that appears to coincide with the Early Eocene (Figure I-10) has been attributed to an

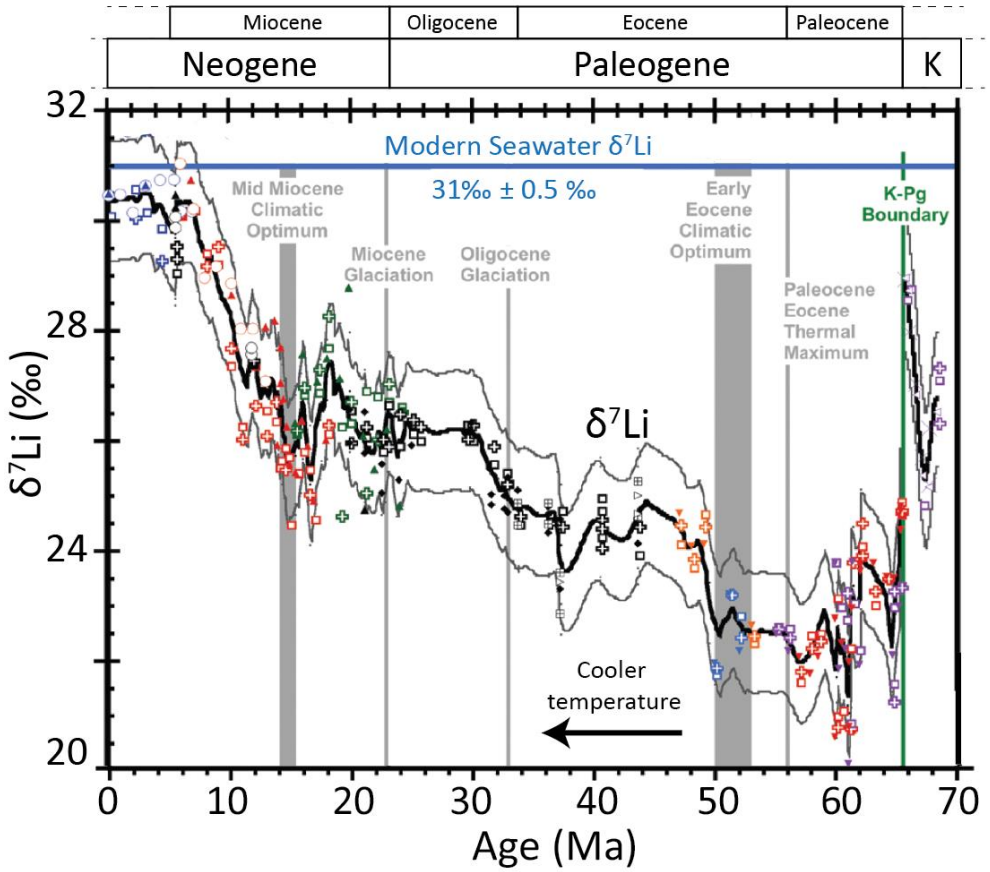

Figure I-10. Cenozoic seawater Li records for the past 68 million years (Froelich and Misra, 2014). The lithium isotope data are from both individual foram species and from bulk foram samples.Variations in seawater δ^7Li suggest different silicate weathering regimes with associated changes in CO_2 consumption. For instance, the relatively low seawater δ^7Li of ~22‰ in the late Paleocene is attributed to low rates of silicate weathering compared to today, resulting in higher temperatures because of a lower CO_2 weathering sink (Eq. I-1 and Eq. I-2).

increased contribution of Li from intensively weathered (tropical) regimes (Dellinger et al., 2014; Dellinger et al., 2015; Henchiri et al., 2016).

I.4 Magnesium isotopes as tracers of weathering processes

Magnesium (Mg), has three stable isotopes, ^{24}Mg, ^{25}Mg and ^{26}Mg, with natural abundances, respectively, of 78.99%, 10.00% and 11.01%. The relative mass difference between the isotopes is large (~4 % between ^{24}Mg and ^{25}Mg, and ~8% between ^{24}Mg and ^{26}Mg) so there are relatively large variations in $^{24}Mg/^{25}Mg$ and $^{24}Mg/^{26}Mg$ ratios under Earth surface conditions (Figure I-11). Furthermore, because Mg is a light element which has two of its three isotopes that are similar in abundance, it is ideally suited to investigation of different mass–dependent fractionation mechanisms that may operate in nature (Young and Galy, 2004).

The isotope composition of Mg is reported as $\delta^{x}Mg$ (Eq. I-5), where x is equal to 25 or 26, relative to the Mg isotope standard Dead Sea Magnesium 3 (pure magnesium metal DSM3; Galy et al., 2001):

$$\delta\,^{x}Mg = \left[\frac{\left(\frac{^{x}Mg}{^{24}Mg}\right)_{sample}}{\left(\frac{^{x}Mg}{^{24}Mg}\right)_{DSM3}} - 1\right] \times 1000 \qquad \textit{Eq. I-5}$$

The relationships between $^{25}Mg/^{24}Mg$ and $^{26}Mg/^{24}Mg$ are diagnostic of kinetic fractionation or equilibrium fractionation (Eq. I-6). The fractionation factor α is given by:

$$\alpha_{x/24} = \left(\frac{^{x}Mg}{^{24}Mg}\right)_{a} \Big/ \left(\frac{^{x}Mg}{^{24}Mg}\right)_{b} \qquad \textit{Eq. I-6}$$

Where *a* and *b* refer to either two different phases or two different materials and x is equal to either 25 or 26. The different mass-dependent fractionation laws that relate $\alpha_{25/24}$ to $\alpha_{26/24}$ are characterized by β (Eq. I-7) in the expression:

$$\alpha_{25/24} = \left(\alpha_{26/24}\right)^{\beta} \qquad \textit{Eq. I-7}$$

β values of ~0.521 are indicative of equilibrium fractionation processes, whereas β values of ~0.511 are indicative of kinetic fractionation processes (Young and Galy, 2004).

Magnesium is the fourth most abundant element in the ocean (Millero, 1974). Like Li, Mg is also a conservative element, with $[Mg]_{SW}$ = 53 mmol/kg (Carpenter and Manella, 1973), and $\delta^{26}Mg$ = -0.82‰ (Young and Galy, 2004; Pogge von Strandmann, 2008; Foster et al., 2010). The residence time of Mg in seawater is about 12.7 million years (Tipper et al., 2006b).

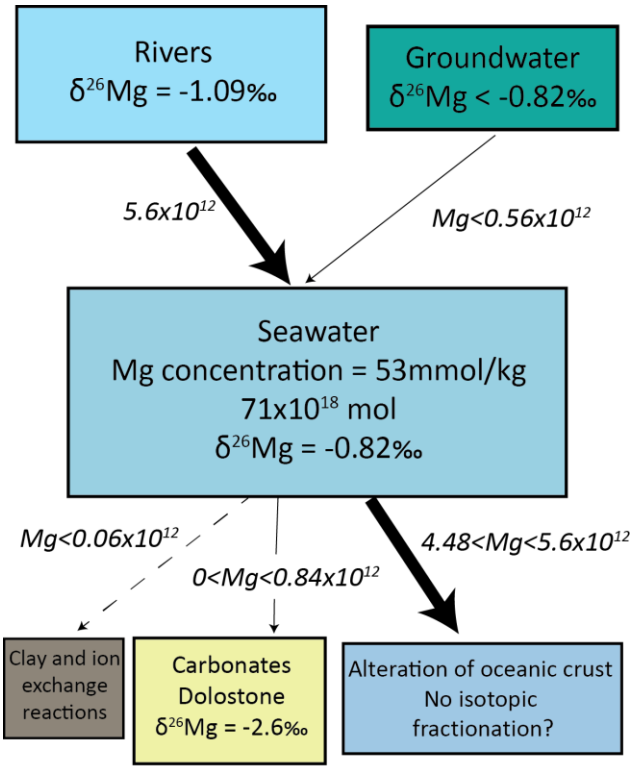

Figure I-11. Box model representing the global Mg cycle. Total quantity of Mg in seawater is given in mol; fluxes between reservoirs are in mol/yr. After Tipper et al., 2006b

I.4.1 Behaviour of magnesium isotopes during weathering

Magnesium is fluid mobile and does not undergo changes in its valence state under Earth surface conditions. However, in contrast to Li, which is not an essential plant nutrient, Mg isotopes are fractionated during uptake by vegetation (Black et al., 2008; Bolou-Bi et al., 2012).

Wheat (*Triticum aestivum L.*), for example, preferentially incorporates heavy magnesium (Black et al., 2008), and bulk trees and grass from the Vosges Mountains (France) have relatively high $\delta^{26}Mg$ (-0.41 to -0.32‰) compared to the exchangeable fraction of the soil (-0.92‰ to -0.42‰) and rainwater (-0.65‰) (Figure I-12; Bolou-Bi et al., 2012). Highest $\delta^{26}Mg$ values are found in the roots, whereas the above ground parts of the tree (wood, leaves and needles) have lower $\delta^{26}Mg$ suggesting that the lighter Mg isotopes are translocated from the

bottom to the upper part of the plant (Bolou-Bi et al., 2012). Soil solution δ^{26}Mg values also appeared to be affected by seasonal changes between May and September (by ~0.5 ‰).

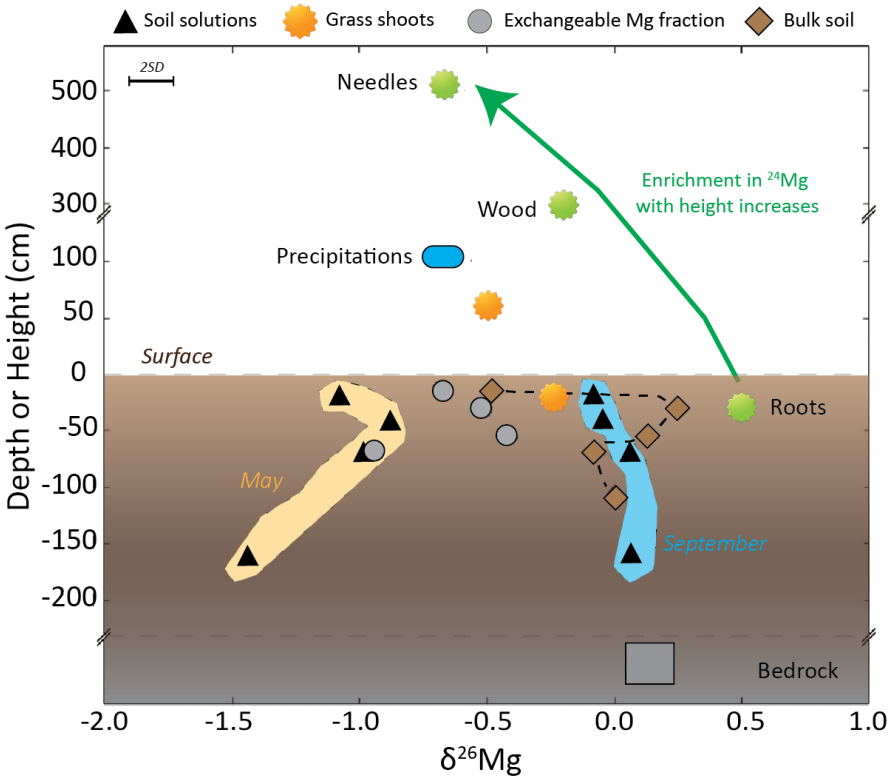

Figure I-12. Magnesium isotope composition of rainwater, plants, soil solutions, soil horizons, soil exchangeable fraction and stream water as a function of depth measured in the Gentil Sapin catchment (Bolou-Bi et al., 2012). The yellow and blue zones show the range of δ^{26}Mg soil solution in May and September respectively.

The mechanisms controlling Mg isotope fractionation during secondary mineral formation are not well understood. Rivers tend to be enriched in light Mg isotopes relative to bedrock (Tipper et al., 2006b; Brenot et al., 2008), and secondary minerals (clays, hydroxides) tend to have higher δ^{26}Mg values relative to solution, fresh rock or continental crust (Tipper et al., 2006a; Brenot et al., 2008; Li et al., 2010; Teng et al., 2010; Ryu et al., 2016). Thus secondary minerals tend to be enriched in heavy Mg and, in support of this, a comprehensive study of three soil weathering sequences in Guadeloupe shows that the δ^{26}Mg value of bulk soil and associated clays is always higher than the δ^{26}Mg value of the parent andesitic bedrock (Appendix A 5; Opfergelt et al., 2012). However, some studies suggest that some soils can have lower δ^{26}Mg relative to their parent rock (Pogge von Strandmann et al., 2008a; Ma et al., 2015). The Mg isotope composition of soils appears to be strongly controlled by the relative proportion of

Mg present in exchange positions at the mineral surface (Figure I-13; Opfergelt et al., 2012; Ma et al., 2015). Formation of clay minerals results in trapping of aqueous Mg^{2+} that has lower $\delta^{26}Mg$ in interlayer positions in the clay mineral structure preventing exchange of Mg^{2+} with the surrounding solution (Ma et al., 2015). As a result, younger soils tend to have higher bulk $\delta^{26}Mg$ values than older soils (Figure I-13).

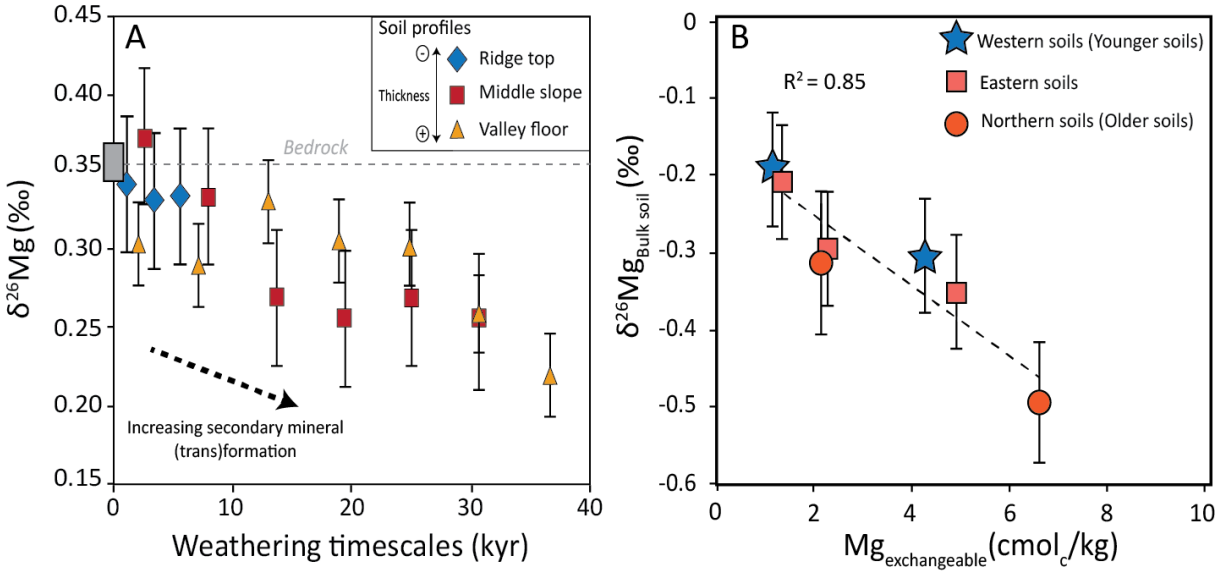

Figure I-13. $\delta^{26}Mg$ values of bulk soil against A. shale weathering timescales (Kyr) (Shale Hills catchment, Pennsylvania) and B. the amount of exchangeable Mg in bulk soil (Guadeloupe, France).Weathering durations are calculated from soil depth and regolith production rates determined by U-series disequilibrium. The negative correlation between $\delta^{26}Mg$ and exchangeable Mg suggests a retention of lighter isotopes in the soil by adsorption (modified from Opfergelt et al., 2012; Ma et al., 2015).

Carbonate rocks (magnesites, dolostones, limestones, speleothem) range in $\delta^{26}Mg$ composition from -1.1 to -5.2‰, which makes them them isotopically light compared to most other reservoirs of Mg (Young and Galy, 2004). Experimental studies of carbonate minerals (magnesite and calcite) have demonstrated that light Mg isotopes are preferentially incorporated during precipitation (Pearce et al., 2012; Mavromatis et al., 2013), whereas clays and hydroxides preferentially incorporate heavy Mg isotopes. Heavy Mg isotope enrichment during clay/hydroxide precipitation is different from other stable isotope systems (lithium, boron, silicon, nickel, calcium, strontium) that show preferential incorporation of light isotopes in secondary mineral phases. Moreover, this behaviour is also in disagreement with surface kinetic effects, bond strength and diffusion rate theories that argue in favour of enrichment of light isotopes in solids (Schauble, 2004; DePaolo, 2011). Recent studies suggest that this effect can be attributed to the speciation of Mg in

aqueous solution (Li et al., 2014; Schott et al., 2016). For instance, aqueous Mg carbonate and bicarbonate complexes with a coordination number of 5 have a shorter Mg-O bond (2.055 Å; Schott et al., 2016) than aqueous Mg^{2+} Mg-O bonds (2.08 Å, coordination number = 6; Pavlov et al., 1998) leading to an enrichment of heavy Mg isotopes in phases with the shortest Mg-O bond distance (Figure I-14). On the other hand, Mg-EDTA complexes have relatively long Mg-O bonds (2.165 Å; Pozhidaev et al., 1974) compared to aqueous Mg^{2+} Mg-O bonds, such that Mg-EDTA complexes are enriched in light Mg isotopes (Figure I-14).

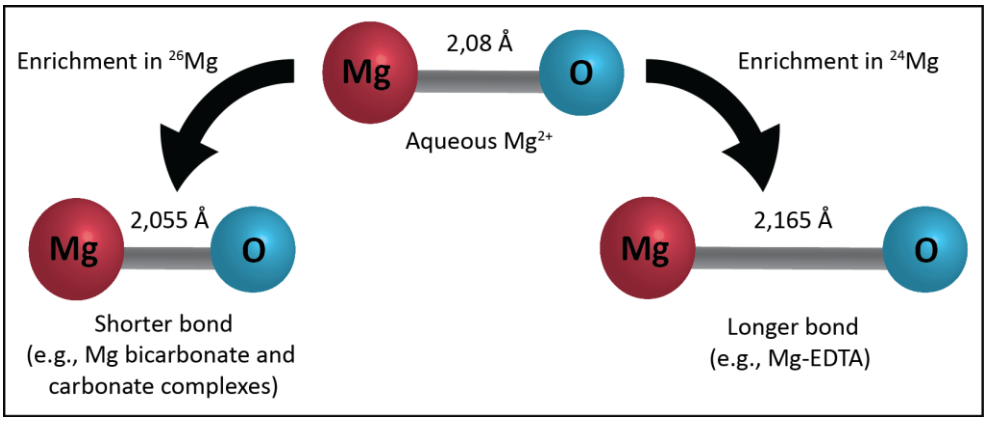

Figure I-14. Behaviour of Mg isotopes in solution according to the presence of different Mg aqueous species.

The processes that regulate the δ^{26}Mg value of river waters are complex. Some studies suggest that light Mg isotopes are preferentially released during dissolution of primary minerals at least during the early stages of dissolution, which may be a kinetic effect (Wimpenny et al., 2011; Fan et al., 2016). Dissolution of biotite also shows enrichment of ^{24}Mg in the leachate solution (Ryu et al., 2016) although, by contrast, variations in δ^{26}Mg in the leachate solution during dissolution of a granite are thought to reflect dissolution of different mineral phases that have different δ^{26}Mg (Ryu et al., 2011). Like Li, there is some evidence that the δ^{26}Mg value of river water may be controlled by weathering intensity. For instance, δ^{26}Mg values of river water in the Gentil Sapin catchment (France) appear to correlate with discharge (Figure I-15; Bolou-Bi et al., 2012). At low flow, these authors suggest that high δ^{26}Mg values are due to a strong contribution from mineral weathering from the deep saprolite ("supply-limited" weathering regime) whereas at high flow, the contribution of overland flow that is influenced by vegetation is suspected to contribute to the low δ^{26}Mg. A similar increase of ^{26}Mg in the

fluids at low discharge has also been attributed to an increased contribution of Mg from weathering from the deep saprolite in Guadeloupe and in Puerto Rico (Dessert et al., 2015; Chapela Lara et al., 2017).

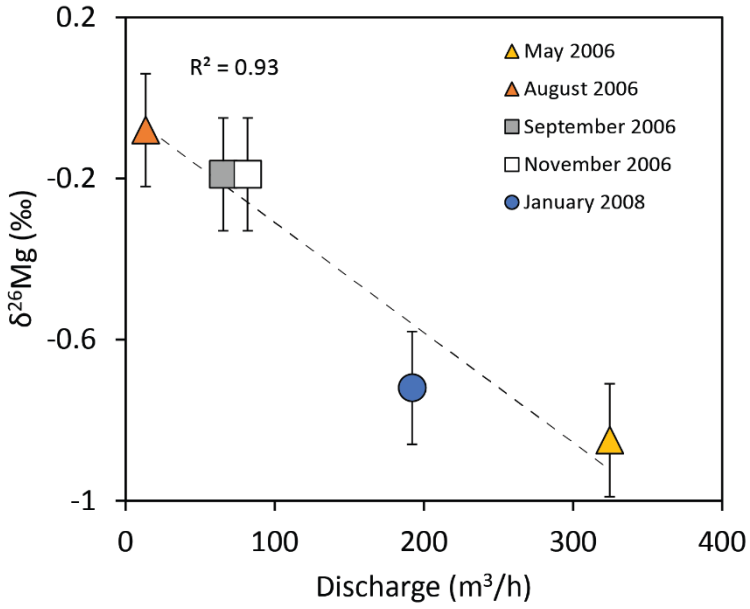

Figure I-15. Variations of stream $\delta^{26}Mg$ with discharge in the Gentil Sapin catchment. After Bolou-Bi et al. (2012).

I.4.2 Records of past changes in riverine $\delta^{26}Mg$

The chemical composition of biogenic $CaCO_3$ minerals usually reflects the composition and the conditions of the seawater in which the organisms lived (Delaney et al., 1985) and, as shown in Figure I-11, rivers are the main source of Mg to seawater. However, there is a great deal of uncertainty in the veracity of carbonates as recorders of seawater $\delta^{26}Mg$ (Chang et al., 2004; Pogge von Strandmann, 2008; Saenger and Wang, 2014; Wimpenny et al., 2014). The $\delta^{26}Mg$ value of most modern planktic and benthic foraminifera (~-4.7‰; Chang et al., 2004; Pogge von Strandmann, 2008), is significantly offset from seawater (~-0.82‰), but appears to be unaffected by environmental and biological factors including temperature, calcite saturation state, shell growth rate, the size or existence of an internally controlled calcium pool (Pogge von Strandmann, 2008). By contrast, a review of Mg isotope variability in a variety of biogenic and abiogenic carbonates suggests that there is a small temperature dependence on $\delta^{26}Mg$ of ~0.01‰ºC^{-1} (Saenger and Wang, 2014). The study also indicates that biological processes produce considerable differences between $\delta^{26}Mg_{carbonates}$ and $\delta^{26}Mg_{solution}$ in many biogenic carbonates. Despite the complex

behaviour of Mg isotopes in biogenic carbonates, there have been attempts to reconstruct the past variation in seawater $\delta^{26}Mg$ by analyses of ancient foraminifera or pelagic carbonates sediments where 90% of the Mg abundance also derived from foraminifera (Figure I-16; Higgins and Schrag, 2015; Pogge von Strandmann et al., 2014). The $\delta^{26}Mg$ of pelagic carbonates measured in the Ontong Java Plateau (site 807 ODP) and Walvis Ridge (site 1265 ODP) are similar despite differences in size fraction, location, and sedimentation rates. These values are also isotopically similar to multiple species of cleaned core-tops foraminifera (Pogge von Strandmann, 2008) consistent with the total Mg budget of the sediment being dominated by foraminiferal calcite and arguing for a representative record of $\delta^{26}Mg$ seawater in pelagic carbonates. However, despite an increase in seawater Mg/Ca (by a factor of 2-3) over the Cenozoic only small changes in $\delta^{26}Mg$ of pelagic carbonates have been recorded (Higgins and Schrag, 2015) whereas an overall decrease in seawater $\delta^{26}Mg$ value during the last ~15 million years (Figure I-16) where measured on foraminifera of different species (Pogge von Strandmann et al., 2014). This differences between $\delta^{26}Mg$ from foraminifera and pelagic carbonates clearly highlight different controls on the recorded $\delta^{26}Mg$ of these materials. The variations may also be attributed to inconsistent analytical protocols among laboratories with different instrument conditions. However, these studies suggest together that changes of Mg and $\delta^{26}Mg$ in the seawater over the Cenozoic are rather linked to a decline of the Mg sinks than variation of Mg sources from continental weathering. Decrease of dolomite formation flux or a reduction in removal of Mg from seawater in low-temperature marine clays are thus considered to be the primary controls on seawater Mg concentrations and isotope ratios (Pogge von Strandmann et al., 2014; Higgins and Schrag, 2015). However, a recent study of Mg isotopes and Mg/Ca in fossil corals by Gothmann et al. (2017) found similar $\delta^{26}Mg$ than Higgins and Schrag (2015). This study suggests that the rise of Mg/Ca is most likely due to an increase of silicate weathering or a decline in Mg uptake in marine silicate with carbonate weathering having only a secondary importance in the control of past Mg variations.

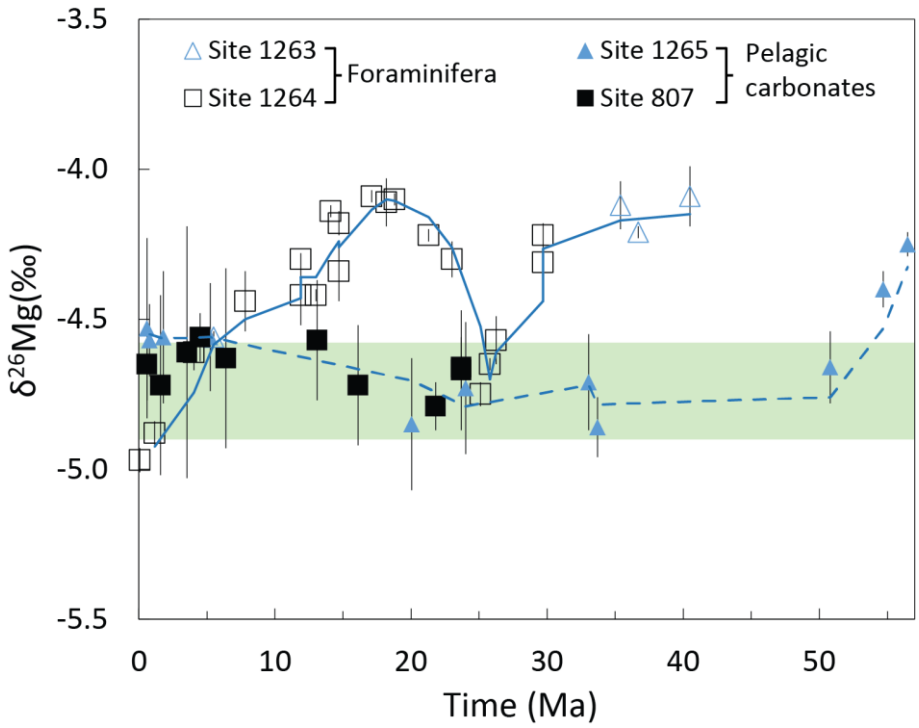

Figure I-16. Foraminifera and pelagic carbonates (size>250µm) δ^{26}Mg values from the past 56.5 Myr.Foraminifera samples are from cores of the 1263 and 1264 Ocean Drilling Program (ODP) sites, pelagic carbonates are from the 807 and 1265 ODP sites. The open squares and triangles (solid line; Pogge von Strandmann et al., 2014) vary during the last 15 Myr while the filled squares and triangles (dashed line; Higgins and Schrag, 2015) are relatively constant. Errors bar represent 2SD analytical reproducibility of the individual samples. The green band denotes the average δ^{26}Mg value (with 2SD) for a range of modern foraminifera (Pogge von Strandmann, 2008).

I.5 Thesis outline

The aim of this project is to develop the utility of Li and Mg isotopes as tracers of weathering processes in the critical zone, to better constrain the links between weathering and climate.

In support of this, we have investigated the behaviour of Li and Mg isotopes in a West Greenland fjord (Godthåbsfjord; in Chapter 3), where meltwater volume and sub-glacial weathering processes oscillate seasonally along with temperature. There is an important debate on the importance of glacial environments as a regulator of atmospheric CO_2 (Sharp et al., 1995), some argue that glacial environments induce no (or little) sequestration of CO_2 (Tranter et al., 2002). Li and Mg isotopes are both potential tracers of weathering processes and can help to solve the debate, by giving information on the chemical and physical weathering processes that operate in glaciated catchments. This study also explores the behaviour of Li and Mg isotopes during freshwater and

seawater mixing and assesses whether the terrestrial weathering signature is faithfully delivered to the ocean.

Futhermore, we have determined the response of Li and Mg isotopes to rain events in a small, highly weathered catchment (Quiock Creek) in Guadeloupe. Water samples (river, groundwater and rainwater) were collected at exceptionally high temporal resolution (Chapter 4). Differences in the behaviour of Li and Mg isotopes are interpreted in terms of plant uptake, secondary weathering products formation and ion exchange.

Finally, we have undertaken a study of the variation of Li and Mg isotopes under different hydrological regimes in the largest river in the world, the Amazon (Chapter 5). To date, there is limited information on the relationships between discharge and $\delta^{7}Li$ and $\delta^{26}Mg$ of river waters. Discharge is lower in November (low water stage) than it is in June (high water stage), which increases the residence time of water in the hydrological system and enhances the extent fluid-rock interactions. Both lithium (Li) and magnesium (Mg) isotopes respond to changes in weathering conditions such as the formation and dissolution of secondary minerals that are intimately linked to these hydrological variations. I have determined the variability of the weathering processes associated with discharge changes between the low and high water stage on Li and Mg isotopes in the main stem of the Amazon, as well as its principal tributaries.

Chapter II. Analytical methodology

This Chapter provides an overview of the sample collection and analytical procedures used in these studies. Water samples (including river waters, groundwater, soil pore waters) were collected between May 2014 and November 2015 using a variety of different approaches. These were filtered to separate the dissolved fraction from suspended particulate material, and generally preserved for analysis back in the laboratory. The chemical composition of the samples was determined principally by inductively coupled plasma mass spectrometry (ICP-MS), and Mg and Li isotope compositions were determined by multicollector ICP-MS. An overview of the different procedures and techniques is provided below.

II.1 Sample collection and preparation

II.1.1 Sample collection, preservation and field measurements

II.1.1.1 Greenland

Water samples were collected from Godthåbsfjord in Greenland in May (spring) and August (summer) 2014. To do this, an extendable plastic pole, fitted with a pre-cleaned 1 L LDPE bottle was held over the side (approximately 2 m upstream) of the ship RV SANNA (Figure II-1). Temperature,

Figure II-1. Research Vessel SANNA in Nuuk. Photo: Josephine Nymand.

turbidity (using an OBS, or Optical Backscatter Sensor), and salinity were measured directly in the fjord using a CTD profiler (Seabird SBE 19plus equipped with a Seapoint turbidity sensor) at each sampling station. The water was filtered on board the ship through 0.2 µm polyvinylidene difluoride (PVDF) filters, and stored in double bagged 1 L LDPE bottles. The bottles were refrigerated. On shore, the water samples were acidified with 500 µL of thermally-distilled (TD) concentrated HCl to prevent microbial activity and adsorption on the side of the bottles.

II.1.1.2 Guadeloupe

A total of 55 water samples comprising river water, groundwater, soil solution and throughfall were collected in the Quiock Creek catchment in Guadeloupe over a period of 21 days in October 2015 (Figure II-2). River waters (Quiock Creek) were collected on a daily basis while groundwaters, soil solution and throughfall were taken when a sufficient amount of solution was available. Soil solutions were collected from nested tension lysimeters (positioned between 61 and 1250 cm

Figure II-2. Sampling in Quiock Creek catchment: A. Throughfall collector; B. Sampling soil solution; C. Piezometers protected by a plastic cover to prevent contamination by rainwater; D. Quiock Creek: blue feature in the centre of the Creek is a venturi flume that allows measurement of discharge.

depth) equipped with porous ceramic cups. Groundwaters were collected manually using a vacuum pump from 6 piezometers positioned along a transect perpendicular to the river. Throughfall was collected in polypropylene bottles with a funnel located one meter above the ground in order to avoid soil contamination.

Temperature, conductivity and pH were directly measured in the field with a combined pH and conductivity probe (Hanna Instruments HI 98130). Fluid samples were filtered at 0.2 µm through a 47 mm cellulose acetate filter, and collected in 250 or 500 mL acid-cleaned HDPE bottles for cation analysis and in Milli-Q water (18.2 MΩ cm^{-1} H_2O) washed 30 mL bottles for anion analysis. The cation samples were acidified to pH ≈ 2 with distilled nitric acid. Alkalinity was determined by titration with 0.01 M HCl within 24 hours of sample collection.

II.1.1.3 Brazil

Samples were collected from the Amazon River basin during two research cruises in June (dry season) and November (wet season) 2015. Water samples were collected using a 7 litre horizontal Niskin-type sample bottle attached to a cable lowered at approximately 1 m depth into the river

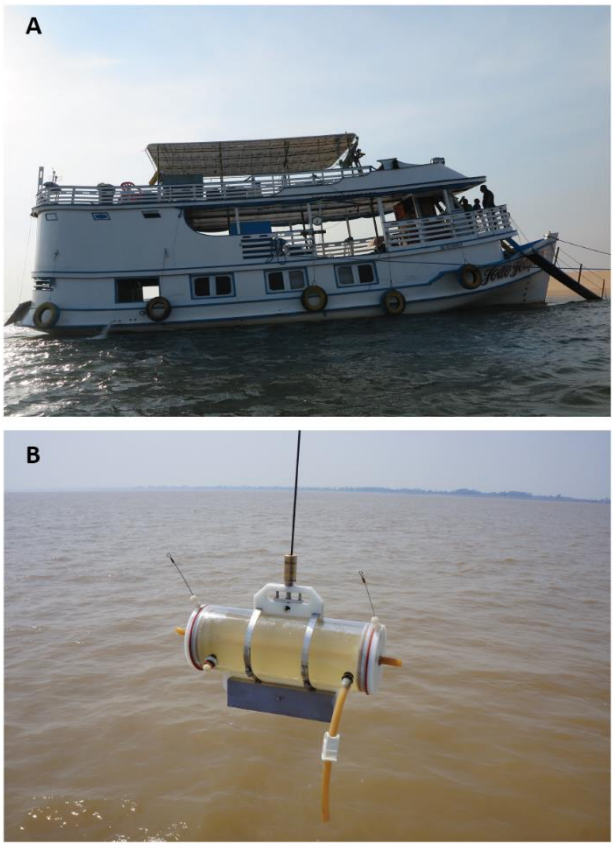

Figure II-3. A. The boat Joao Felipe II used to collect the samples; B. The horizontal water sampler.

from the boat Joao Felipe II (Figure II-3). The bottle is opened at both ends in order to take a representative sample at the depth of interest before being sealed off by a weighted trigger (or messenger) from the surface. At two locations (Obidos and Manaus), water samples were collected at discrete depths to obtain a vertical profile. On return to the surface, the water sampled was poured into an in acid-washed polypropylene container. The water samples were then filtered at 0.45 µm on board the boat using a plastic filtration unit fitted with a 142 mm membrane filter. All samples for cations analyses were acidified after the filtration by adding concentrated HCl (to a pH ≈ 2). Filters were stored in plastic bags in a freezer. Temperature and pH were measured with a pH meter using a subsample of the water freshly collected with the water sampler.

II.1.2 Digestion of suspended sediments

Suspended sediment particles were digested using a procedure based on that of Phan et al. (2015). Between 18 and 86 mg of suspended sediment was accurately weighed and placed into a weighed acid-cleaned Teflon vial. To each sample, a minimum of 10 drops of 15M HNO_3 (or 10 drops per 50 mg of sample) was added. The samples were left to reflux on a hot plate at 130 °C for at least 12 hours and then removed from the hotplate and allowed to cool. Next, a mixture of 1 mL of Romil HF and 1 mL of $HClO_4$ was added (per 50 mg of sample) and heated overnight at 130 °C. The solution was then evaporated at ~130 °C before increasing the temperature step wise to a maximum of 180°C until no more white fumes were produced. 1 mL of $HClO_4$ was then added to the residue and heated overnight at 130 °C before being dried down as described above. Sufficient 6 M TD HCl (>2 mL) was added to the residue to re-dissolve it. If undissolved material remained, the sample was dried down and treated with 15 M TD HNO_3 and 12 M TD HCl until it dissolved. The digested sample was then transferred to an acid-cleaned pre-weighed bottle and the Teflon vial was thoroughly rinsed with 6 M TD HCl and Milli-Q to make the solution up to ~30 mL. At least one blank was processed with each sample batch. The USGS standard reference material SCo-1 (Cody Shale) was also digested with each batch of samples.

In 3 samples (MAN3.40 NOV, OB1.15 JUN and MAN3.55 JUN), tiny black particles remained even after repeated acid attack. These particles were analysed by Scanning Electron Microscopy (SEM; Figure II-4), and were show to consist principally of C, O, F and Al, which is indicative of graphite.

The uncertainty of the mass of these particles is ±0.0005 g (due to very small sample sizes), which means that the uncertainty in the elemental concentrations of these samples is up to ±10%.

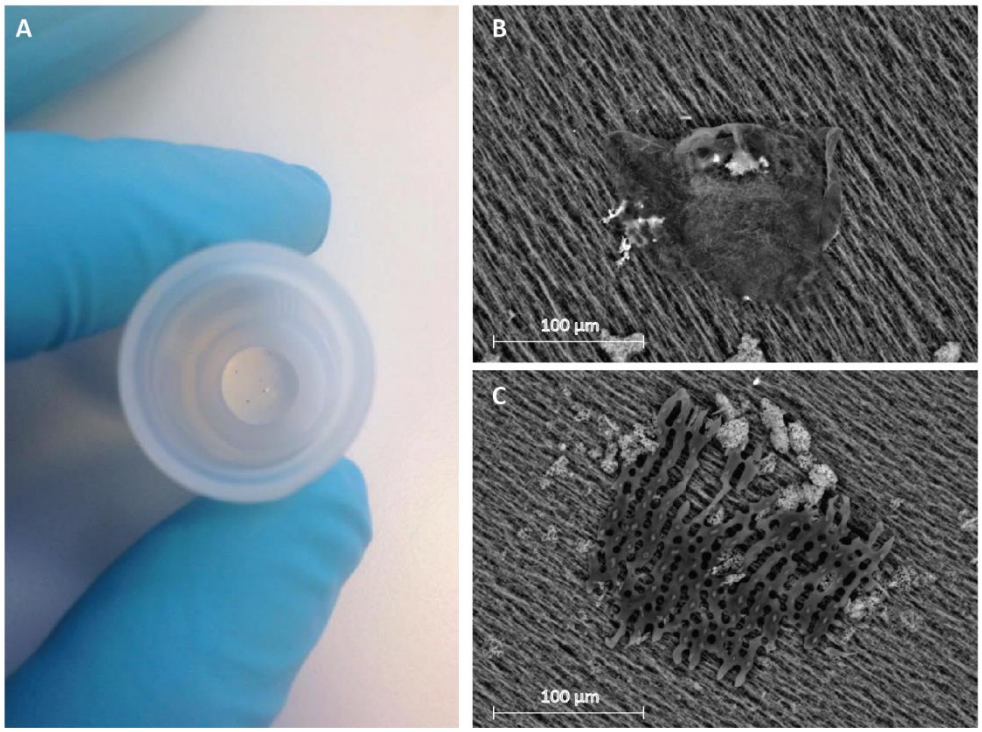

Figure II-4. A. Undissolved black particles in Teflon vial; B: SEM picture of particle in MAN3.55 JUN; C. SEM picture of particle in MAN3.45 NOV.

II.2 Elemental analysis

II.2.1 Anions

The concentrations of Cl^-, F^-, Br^- and SO_4^{2-} in Guadeloupe waters were measured by ion chromatography (Dionex ICS2500), consisting of a Dionex IP25 isocratic pump, a AS40 auto-sampler, a CD25 conductivity detector, and a LC25 chromatography oven. All waters were measured undiluted, but the certified standard reference material (IAPSO seawater) was diluted ×1500 with Milli-Q water. Analyses were calibrated using a set of synthetic multi-element standards prepared gravimetrically from high purity single element standard solutions. A drift monitor solution and several blanks were measured periodically to assess the stability of the analyte signal over time. The IAPSO seawater standard was analysed multiple times alongside the samples to assess the accuracy and precision of the analyses (Table II-1). Concentrations of F^- and Br^- are considered to be semi quantitative because their concentration is extremely low in these samples.

IAPSO seawater was analysed multiple times alongside the samples to assess the accuracy and precision of the analyses which is less than 5% for Cl^- and SO_4^{2-}.

Table II-1. Comparison between measured and certified concentrations of anions in IAPSO seawater. Standard deviation is expressed as the 95% confidence limit of the mean. Certified values are from Summerhayes and Thorpe (1996).

Sample	Anions (mmol/kg)			
	Cl^-	SO_4^{2-}	Br^-	F^-
IAPSO (n = 7)	383.4 ± 12.3	17.7 ± 2.9	0.8 ± 0.2	0.02 ± 0.03
IAPSO (certified)	385.5	18.0	1.3	0.03

II.2.2 Cations

Cation concentrations were determined by inductively coupled plasma optical emission spectrometry (ICP-OES) and ICP mass spectrometry (ICP-MS). Major cations (Na, Mg, Ca, K, B, Sr, Li) and silicon in the fjord waters were measured by ICP-OES (Thermo-Scientific iCap 6000 series) at the National Oceanography Centre Southampton (NOCS). To this end, the fjord waters were diluted 50 times with 3% TD HNO_3, and analyses were calibrated against a set of synthetic multi-element standards prepared gravimetrically from high purity single element standard solutions. A drift monitor solution and several blanks were measured periodically to assess the stability of the analyte signal over time. The IAPSO seawater standard was analysed multiple times as an unknown alongside the samples to assess the accuracy and precision of the analyses which is less than 5% (Table II-2). Additionally, two samples were duplicated (Dup GF7 and Dup I/E), the agreement between the two measurements was better than 3%.

Table II-2. Comparison between measured and certified concentrations of various elements in IAPSO seawater. Standard deviation is expressed as the 95% confidence limit of the mean. Certified values are from Summerhayes and Thorpe (1996) and Besson et al. (2014).

Sample	Major cations (mmol/kg)				Minor cations (µmol/kg)			
	Na	Mg	Ca	K	B	Sr	Li	Si
IAPSO (n = 3)	497 ± 9	55.0 ± 1.0	10.7 ± 0.1	10.8 ± 0.2	460 ± 16	92.7 ± 0.4	26.6 ± 0.3	2.1 ± 1.5
IAPSO (certified)	469 ± 5	53.1 ± 2.8	10.3 ± 0.6	10.2 ± 0.3	416	90.2	25.1	2.8

However for Na and B, the values are different from the certified values which might be the result of matrix effects that influence the analytical response (Murray et al., 2000). The low concentration

of Si in IAPSO after dilution is very close to the lowest standard value (40 ppb) which highly increase the uncertainty (>50%) of the measurements for IAPSO.

Major and minor elements in the river waters and suspended sediments from Guadeloupe and Brazil were determined by ICP-MS (Thermo X-Series II). All river waters were measured undiluted, but the mother solutions of dissolved suspended sediment were further diluted by a factor of 100 with 3% TD HNO_3. Analyses were calibrated using a set of synthetic multi-element standards prepared gravimetrically from high purity single element standard solutions. A drift monitor solution and several blanks were measured periodically to assess the stability of the analyte signal over time. Two certified standard reference material (the river water SLRS-6 and Cody Shale SCo-1) were analysed multiple times alongside the samples to assess the accuracy and precision of the analyses which is less than 5% (Table II-3).

Table II-3. Accuracy of element concentration analysis by ICP-MS. Certified values for SLRS-6 are from the NRC (National Research Council) of Canada online database and certified values for SCo-1 are from the U. S. Geological Survey online database (Gladney and Roelandts, 1988).

	Major cations (µmol/kg)								Minor cations (nmol/kg)	
	Na	Ca	Si	Mg	Al	K	B	Fe	Sr	Li
SLRS-6 (n = 8)	115 ± 4	207 ± 8	81 ± 4	84.2 ± 2.7	1.2 ± 0.1	15.5 ± 0.6	0.6 ± 0.1	1.5 ± 0.1	444 ± 19	72 ± 4
SLRS-6 (certified)	120 ± 10	219 ± 5	-	87.9 ± 2.4	1.3 ± 0.1	16.7 ± 1.4	-	1.5 ± 0.1	465 ± 3	-
	Major cations (weight %)								Minor cations (ppm)	
	Na	Ca	Si	Mg	Al	K	B	Fe	Sr	Li
SCo-1 (n = 3)	0.66 ± 0.05	1.98 ± 0.31	-	1.65 ± 0.06	7.25 ± 0.14	2.37 ± 0.08	-	3.64 ± 0.07	170 ± 12	45 ± 1
SCo-1 (certified)	0.67 ± 0.04	1.87 ± 0.14	-	1.64 ± 0.11	7.25 ± 0.11	2.30 ± 0.07	-	3.59 ± 0.13	170 ± 16	45 ± 3

II.3 Lithium isotope analysis

The lithium isotope composition of the waters and suspended particles was determined by multicollector inductively-coupled plasma-source mass spectrometry (MC-ICP-MS; Thermo Scientific Neptune Plus) after separation of Li from the sample matrix. All Li isotope work was carried out in an over-pressurized clean laboratory at the NOC, Southampton. PTFE (Savillex) columns and vials were cleaned in 50% TD HNO_3 at 120 °C overnight, and the vials were then refluxed with 12 M HCl at 120 °C overnight. Acids were thermally distilled (TD) in Teflon stills, and regularly checked for purity. Dilute acids were prepared from the TD acids by dilution with 18.2 MΩ cm^{-1} Milli-Q water, and standardised by titration against NaOH.

II.3.1 Separation of Li from the sample matrix

In order to make accurate and precise measurements of the lithium isotope composition of natural samples, Li must first be separated from the rest of the sample matrix. This was done by cation exchange chromatography. Acid-cleaned PTFE columns (6 mm in diameter, 30 mL reservoir, PTFE frit) were loaded with pre-cleaned AG50W-X12 (Bio-Rad™) cation exchange resin (James and Palmer, 2000a), to a height of 8.5 cm in 0.2 M TD HCl (Figure II-5).

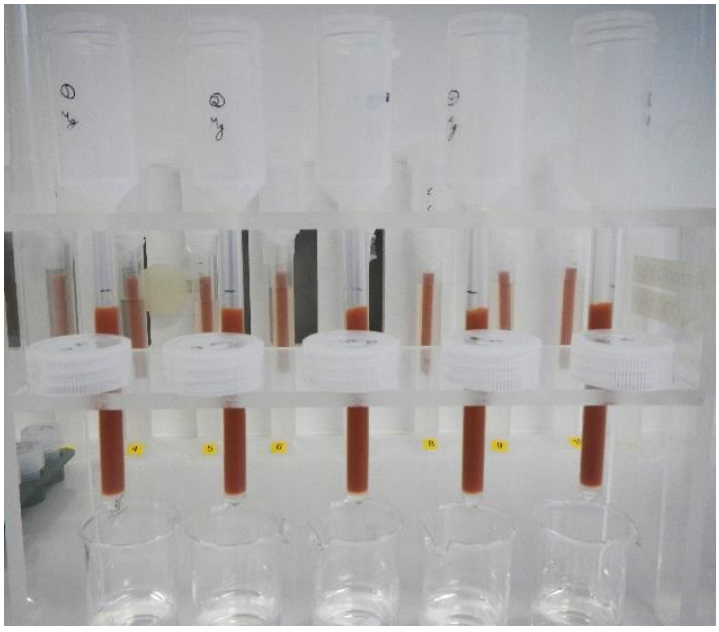

Figure II-5. Cation exchange columns filled with AG50-X12 used for purification of Li or Mg from a sample matrix.

Before starting the separation, an aliquot of each water or sediment sample equivalent to 20 ng of Li was dried down at 120 °C. The column procedure is as follows:

1. The columns were cleaned with 15 mL 6 M TD HCl and rinsed with 8 mL Milli-Q water.
2. The columns were equilibrated with 8 mL 0.2 M TD HCl and resin height was measured to check it was 8.5 cm.
3. Samples containing 20 ng Li were dissolved in 200 µL of 0.2 M TD HCl and carefully loaded onto the columns.
4. The samples were washed in with 2 x 500 µL of 0.2 M TD HCl.
5. 21 mL of 0.2 M TD HCl was discarded.
6. The Li fraction was collected in 19 mL of 0.2 M TD HCl in Savillex vials.
7. The Li fraction was dried down on a hotplate at ~120 °C.

8. The columns were cleaned with 30 mL 6 M TD HCl and rinsed with 30 mL Milli-Q water.
9. The columns were stored in 0.05 M TD HCl.

The total procedural Li blank associated with the column chemistry is 10 ± 20 pg (n = 20; measured by MC-ICP-MS) which is <0.1% of the amount of Li loaded onto the columns, and thus has a negligible effect on δ^7Li.

II.3.2 Column Calibration

To get a representative column calibration, a sea water sample (IAPSO), a lithium carbonate sample (L-SVEC), an acid-digested basalt (JB-3) and shale sample (SCo-1) were used. Each sample contained 20 ng of Li, to which 2 µg of Li (2 µL of a synthetic 1000 ppm Li ICP-MS standard solution) was added, and then dried down.

1. The columns were preconditioned by gently adding 4 mL of Milli-Q water and re-suspending the resin, equilibrated by adding 8 mL of 0.2 M TD HCl, and then the resin height was checked to be 8.5 cm.
2. The samples were re-dissolved in 200 µL of 0.2 M TD HCl and loaded onto the column.
3. The samples were washed in with 2 x 500 µL 0.2 M TD HCl.
4. 15 mL of 0.2 M TD HCl was added to the columns and then discarded.
5. The next 16 mL of 0.2 M TD HCl was collected in 2 mL or 4 mL fractions in separate vials.
6. The remaining cations were eluted with 30 mL of 6 M TD HCl and the column was then rinsed with 30 mL Milli-Q water.
7. Each 2 mL column fraction was made up to 5 mL with 0.2 M TD HCl for ICP-OES analysis. Each 4 mL fraction was directly analysed.
8. Synthetic multi-element standards were prepared, which contained Li (Aristar, 1000 ppm), Mg (VWR Prolabo, 10000 ppm) and Na (Inorganic Ventures, 10000 ppm) ICP-MS standards. A range of concentrations were used to bracket the upper and lower end of the anticipated concentration.
9. ICP-OES analysis of Li, Mg and Na was conducted. A wash solution of 0.2 M TD HCl was used.

The columns achieved good separation of Li from Na and Mg (Figure II-6). The yield of Li from the columns is >98 %.

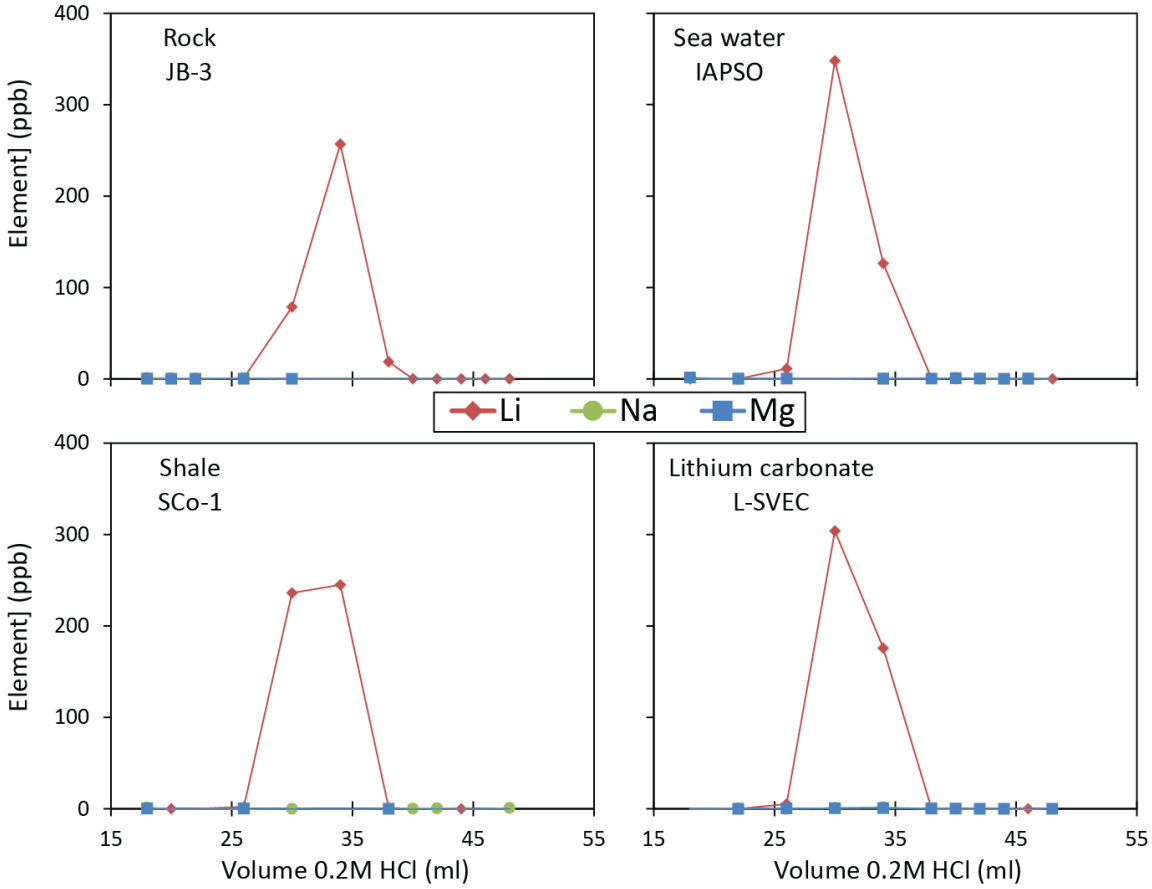

Figure II-6. Li column calibration using a sea water, lithium carbonate, shale and bedrock sample. Volume of acid eluted is plotted against element concentration in ppb.

II.3.3 Analysis of δ^7Li

II.3.3.1 Measurement of ^{7}Li/^{6}Li

Lithium isotope ratios were determined by MC-ICP-MS, at the National Oceanography Centre, Southampton. The Li fractions purified by cation exchange chromatography were re-dissolved in 3% TD HNO_3 to produce a solution with a concentration of 5 ppb Li (~4 mL). Aliquots of 1 mL were taken from each sample for analysis. Before analysis, a dip test was conducted to ensure that concentration of the sample was within ±10% of the concentration of a 5 ppb L-SVEC Li isotope standard (Flesch et al., 1973). The samples were analysed using a sample-standard bracketing technique, whereby the mass bias is determined from analysis of the ^{7}Li/^{6}Li ratio measured on the L-SVEC standard, which is analysed before and after each sample. The ^{7}Li and ^{6}Li intensity of the 3% TD HNO_3 blank solution was determined prior to analysis of each sample and standard, and then

subtracted. If the ^{7}Li intensity of the blank solution became higher than 1% of the ^{7}Li intensity of the sample/standard, the analytical run was stopped and the cones were cleaned. Samples were introduced to the plasma using a CETAC Aridus II™ desolvating nebuliser system, and typical parameters for Li isotope analyses are shown in Table II-4.

Table II-4. Settings for Li isotope analysis on the Neptune Plus.

Parameters		Parameters	
Average blank	<70 mV	Extraction voltage	2000 V
Sample and standard Li concentraton (in solution)	5 ppb	Mass resolution	Low
Average voltage ^{7}Li (5 ppb)	11 V (min 5 V max 21 V)	Wash solution	3% HNO3
No. of measurments	20	Wash time after sample	7 min
Integration time	8.389 s	Wash time after blank	1 min
Cone	Skimmer cone (X cone; Nickel)	Detector	Faraday cup L4 (^{6}Li) and H4 (^{7}Li)
Air sweep gas	6-8 L/min		

II.3.3.2 Accuracy and reproducibility of Li isotope measurements

The Li isotope composition of a reference material and a blank were determined alongside every batch of samples to ensure the efficacy of the column chemistry. In addition, a number of samples were processed through the columns several times to ensure that the column chemistry was reproducible.

The combined uncertainty on the ^{7}Li/^{6}Li ratio of the two bracketing standards (Eq. II-1), u_{LSVEC}, is:

$$u_{L-SVEC} = \frac{\sqrt{(u_{L-SVEC})^2 + (u_{L-SVEC})^2}}{2} \qquad \textit{Eq. II-1}$$

where $u_{LSVEC\,1}$ is the standard error for 20 measurements of the ^{7}Li/^{6}Li ratio on the L-SVEC standard run before the sample, and u_{LSVEC2} is the standard error for 20 measurements of the ^{7}Li/^{6}Li ratio on the L-SVEC standard run after the sample. The combined standard deviation on the δ^{7}Li value of the sample ($SD_{internal}$, Eq. II-2) is:

$$SD_{internal} = \frac{^{7}Li/\,^{6}Li_{SAMPLE}}{^{7}Li/\,^{6}Li_{L-SVEC}} \times \sqrt{\left(\frac{u_{SAMPLE}}{^{7}Li/\,^{6}Li_{SAMPLE}}\right)^2 + \left(\frac{u_{L-SVEC}}{^{7}Li/\,^{6}Li_{L-SVEC}}\right)^2} \qquad \textit{Eq. II-2}$$

Where u_{Sample} is the standard error on the ^{7}Li/^{6}Li ratio of the sample. The typical internal uncertainty is 0.1-0.2‰.

The external error of multiple measurements of a given sample or standard ($SD_{external}$, Eq. II-3) is given by the standard deviation (SD) of the replicate measurements:

$$SD_{external} = \sqrt{\frac{1}{n-1}\sum_{i=1}^{n}(x_i - \bar{x})^2} \qquad \textit{Eq. II-3}$$

Where n is the number of measurements, x_i are the measured δ^7Li values and $\bar{x}$ is the mean value of these measurements. The total uncertainty of the Li isotope measurements (Eq. II-4) is given by the combined uncertainty of the internal error and the external error:

$$2\sigma_{(internal+external)} = \sqrt{2SD_{external}^2 + 2SD_{internal}^2} \qquad \textit{Eq. II-4}$$

The accuracy (external precision) was determined by repeated measurement of IAPSO seawater, L-SVEC (purified lithium carbonate Li_2CO_3), SCo-1 and SLRS-6 (river water), the results are shown in Table II-5. The measured value of IAPSO was 30.9±0.6‰ (2SD, n = 27), which is in accordance with values reported by other groups (Figure II-7). The variation of all standard values through time for this study is shown in Figure II-8.

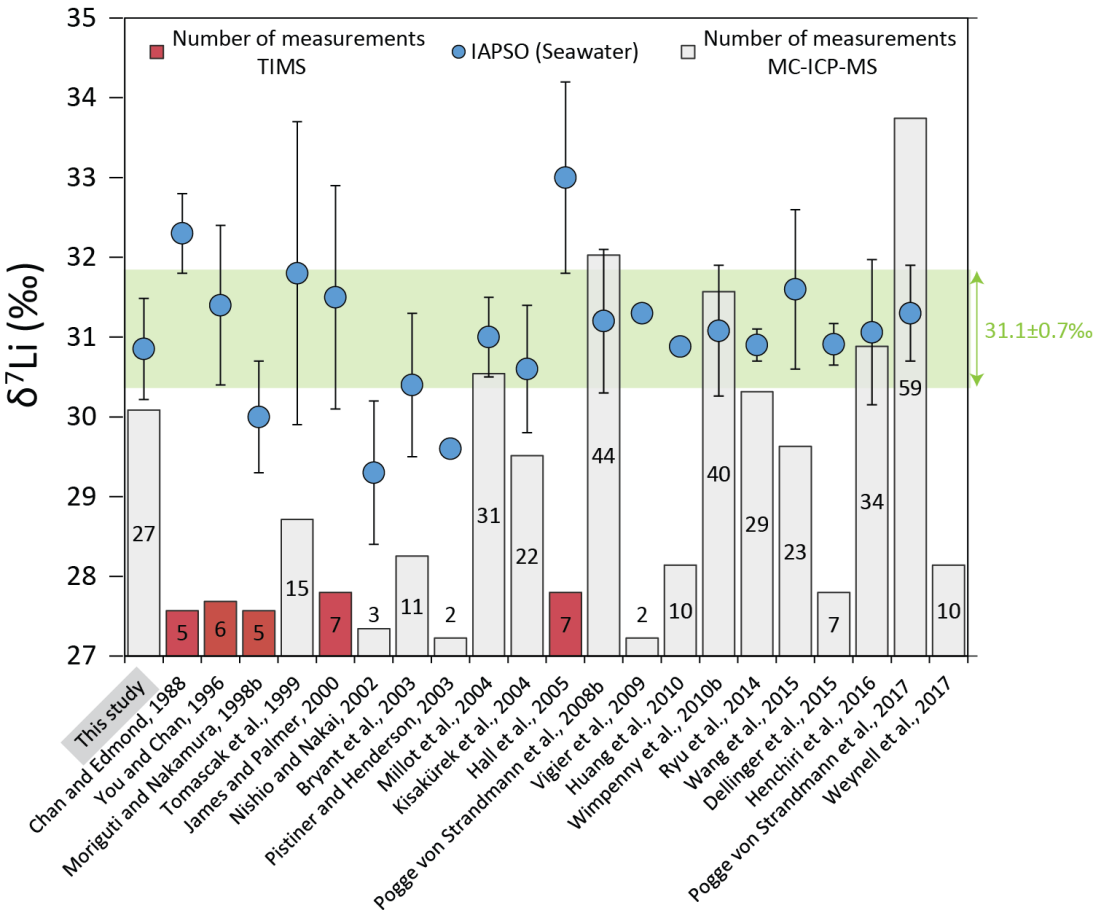

Figure II-7. Li isotope composition of IAPSO published values measured with thermal ionization mass spectrometer (TIMS) or MC-ICP-MS. The value measured in this study is highlighted by a grey shaded box. The green shaded box shows the average of all the values along with an average of all the standard deviation.

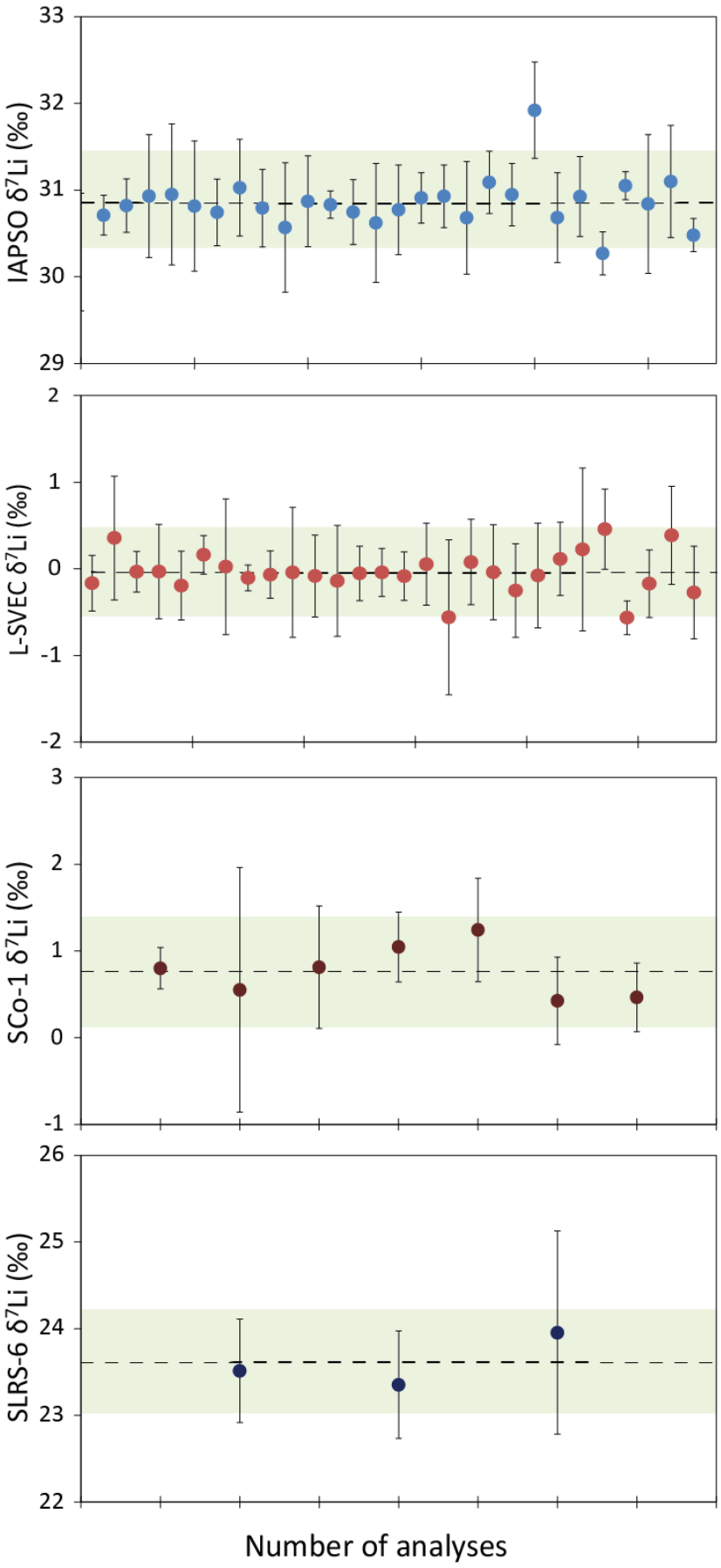

Figure II-8. δ^7Li analyses of standards measured during the course of this study. Dashed horizontal lines show the average, and the green shaded box the standard deviation (2SD) of average value. Error bars represent the internal uncertainty of an individual measurement.

Table II-5. Li isotope composition of various standards measured in this study.

Standard	Number of measurements	δ^7Li (‰)	2σ
IAPSO (Seawater)	n = 27	30.9	0.6
L-SVEC	n = 28	0.0	0.5
SLRS-6	n = 3	23.6	0.7
SCo-1	n = 7	0.8	0.6

The δ^7Li value of the Li isotope standard L-SVEC which has not been passed through columns was regularly measured to monitor instrumental stability and reproducibility. The average δ^7Li value of L-SVEC that had not been passed through columns was 0±0.5‰ (2σ, n = 101).

II.4 Magnesium Isotope Analysis

The magnesium isotope composition of the waters and suspended particles was determined by MC-ICP-MS after separation of Mg from the sample matrix. All Mg isotope work was completed in an over-pressurized clean laboratory at the NOC, Southampton. PTFE (Savillex) columns and vials were cleaned in 50% TD HNO_3 at 120 ºC overnight, and the vials were then refluxed with 12 M TD HCl at 120 ºC overnight. Dilute acids were prepared from TD acids by dilution with 18.2 MΩ cm^{-1} Milli-Q water, and standardised by titration against NaOH.

II.4.1 Separation of Mg from the sample matrix

In order to make accurate and precise measurements of the magnesium isotope composition of natural samples, Mg must first be separated from the rest of the sample matrix. This was done by cation exchange chromatography. Acid-cleaned PTFE columns (6 mm in diameter, 30 mL reservoir, PTFE frit) were loaded with pre-cleaned AG50W-X12 (Bio-Rad™) cation exchange resin (Tipper et al., 2006b; Pogge von Strandmann, 2008), to a height of 8.5 cm in 0.8 M TD HNO_3 (Figure II-5). Before starting the separation, an aliquot of each water or sediment sample equivalent to 10 µg of Mg was dried down at 120 °C. The column procedure is as follows:

1. The columns were cleaned with 4 mL 4 M TD HNO_3 and rinsed with 4 mL Milli-Q water.
2. The columns were equilibrated with 4 mL 0.8 M TD HNO_3 and resin height was measured to check it was 8.5 cm.

3. Samples containing 10 µg Mg were dissolved in 200 µL of 0.8 M TD HNO_3 and carefully loaded onto the columns.
4. The samples were washed in with 2 x 500 µL of 0.8 M TD HNO_3.
5. 50 mL of 0.8 M TD HNO_3 was eluted and discarded.
6. The Mg fraction was collected in 18 mL of 2 M TD HNO_3 in Savillex vials.
7. The Mg fraction was dried down on a hotplate at ~120 ºC.
8. The columns were cleaned with 25 mL 6 M HCl and followed by 8 mL of Milli-Q water, then cleaned with a further 8 mL 4 M TD HNO_3 followed by 8 mL Milli-Q water.
9. The columns were stored in 0.4 M TD HNO_3.

To ensure good separation from all other elements, samples were passed through the columns two times. The total procedural Mg blank associated with the column chemistry is 26 ± 20 ng (n = 26; measured by MC-ICP-MS), which is <0.01% of the amount of Mg loaded onto the columns, and thus has a negligible effect on $\delta^{26}Mg$.

II.4.2 Column Calibration

The column procedure described above was adapted from Wright (2015). The main changes were: (1) increasing the amount of Mg loaded onto the column from 2 µg to 10 µg, and (2) changes to the wash procedure to ensure complete recovery of Mg and minimise contamination from elements that cause isobaric interferences with Mg (Galy et al., 2001; Chang et al., 2003; Huang et al., 2009; Wombacher et al., 2009; An et al., 2014). The most important isobaric interferences include $^{48}Ti^{++}$, $^{48}Ca^{++}$, $^{12}C^{12}C^{+}$ on ^{24}Mg, $^{50}Ti^{++}$, $^{50}Cr^{++}$, $^{12}C^{13}C^{+}$ on ^{25}Mg, and $^{40}Ar^{12}C^{++}$, $^{52}Cr^{++}$, $^{12}C^{14}N^{+}$, $^{12}C^{13}CH^{+}$ on ^{26}Mg (Huang et al., 2009). Several column calibrations were carried out, until a Mg yield of ~100% was achieved and concentrations of all other elements were <5% of the Mg concentration. Columns were calibrated using sea water (IAPSO), an acid-digested basalt (JB-3) and riverwater (SLRS-6).

A major difficulty is the quantitative separation between Ca and Mg. To this end, it was found to be better to load a solution containing a larger amount of Mg (10 µg vs 2µg; Figure II-9 and Figure II-10). High levels of Ca were observed to shift $\delta^{26}Mg$ away from its true value (Figure II-10). However, if 10 µg of Mg were loaded onto the column, the Ca/Mg ratio of the Mg fraction was much lower, and the measured $\delta^{26}Mg$ value is equal to the expected value (Figure II-10). The final

column procedure gives a Mg yield of 100 ± 5% and concentrations of all major elements were <5% of the Mg concentration (Table II-6). A significant contribution of manganese (Mn, ~7%) was measured in the Mg fraction of two replicates of the BCR-2 basalt standard reference material (BCR-21 and BCR-22) but this had no effect on $\delta^{26}Mg$.

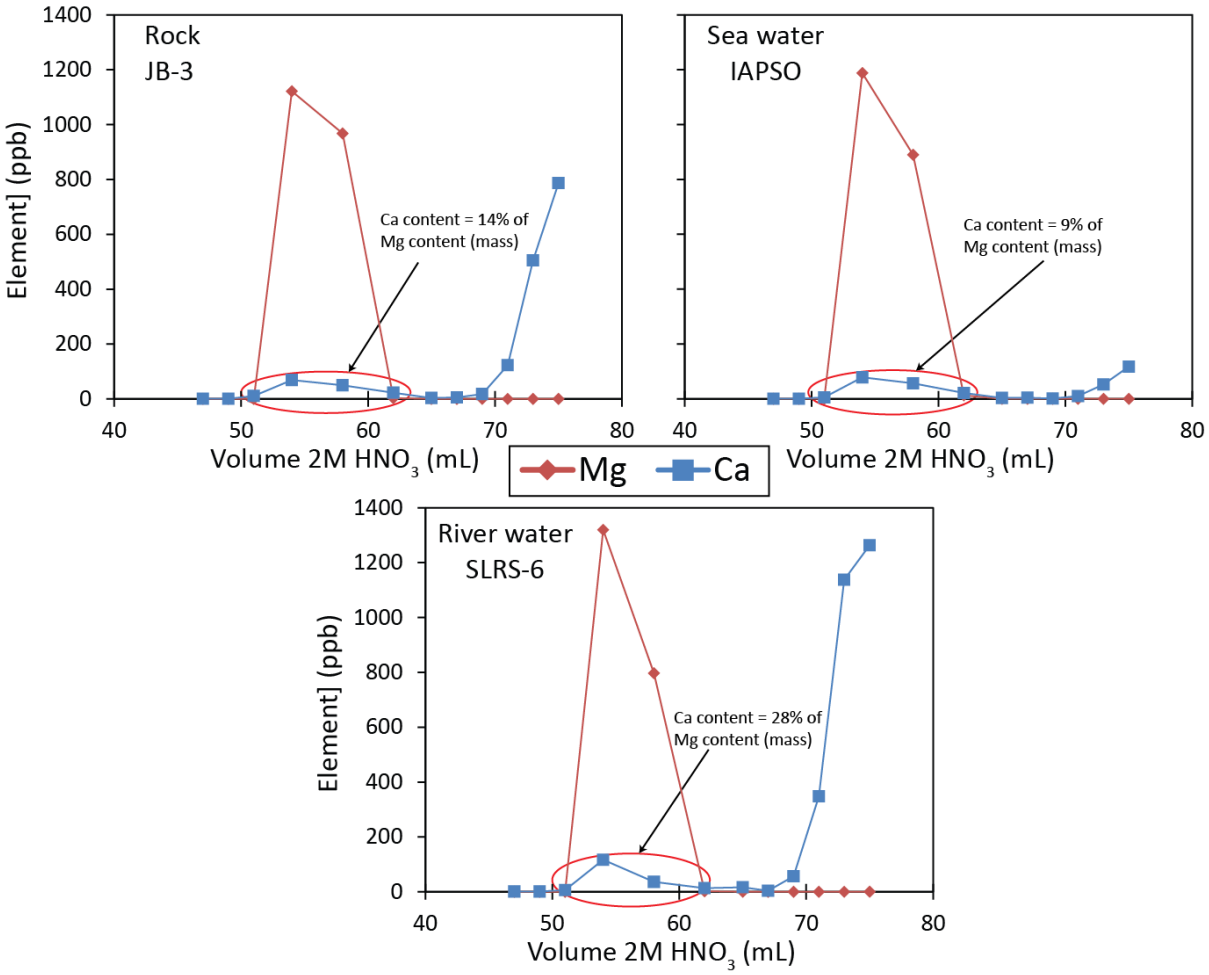

Figure II-9. Column calibration using 2µg of Mg from a sea water, river water and bedrock sample. Volume of acid eluted is plotted against element concentration in ppb.

Table II-6. Matrix element contribution compared to Mg concentration for different sample matrices.

Sample		Ca/Mg	Na/Mg	K/Mg	Al/Mg	Mn/Mg	Total
		%					
DSM-3	Pure Mg metal	0.2	0.4	0.1	0.0	-	**0.8**
IAPSO 1	Seawater	0.9	0.1	0.2	0.1	-	**1.3**
IAPSO 2	Seawater	1.2	0.3	0.2	0.1	-	**1.7**
IAPSO 3	Seawater	0.3	0.5	0.5	0.0	-	**1.4**
BCR-2 1	Basalt rock	0.8	0.2	0.2	0.1	7.3	**8.6**
BCR-2 2	Basalt rock	0.9	0.1	0.2	0.0	6.8	**8.0**

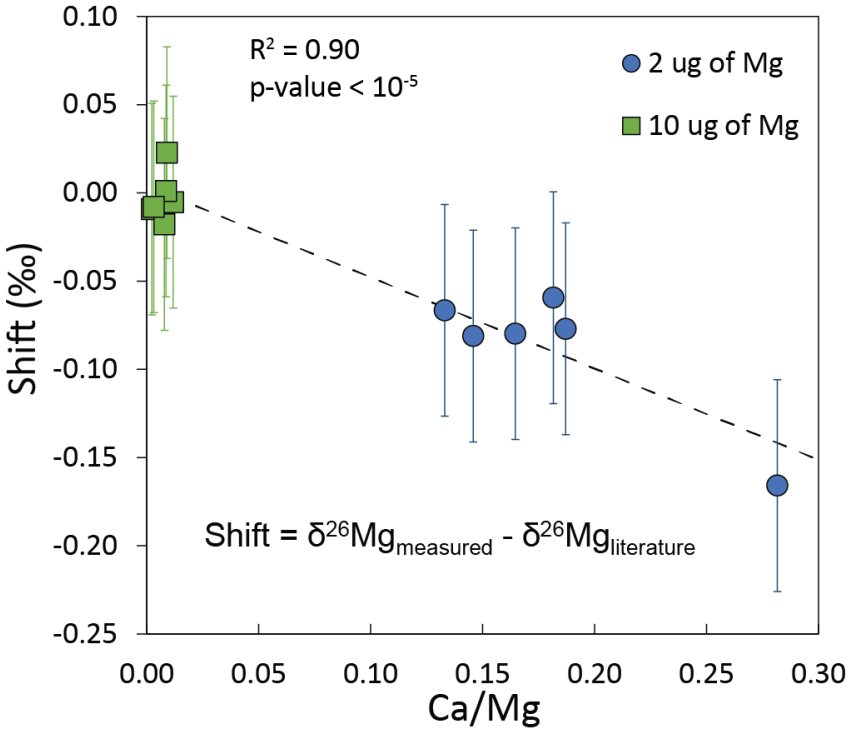

Figure II-10. Comparison of isotopic shift between samples passed with 10 µg and sample with 2 µg. The samples passed are IAPSO, DSM-3 and BCR-2.

II.4.3 Analysis of $\delta^{25}Mg$ and $\delta^{26}Mg$

II.4.3.1 Measurement of $^{25}Mg/^{24}Mg$ and $^{26}Mg/^{24}Mg$

Magnesium isotope ratios were determined by MC-ICP-MS, at the National Oceanography Centre, Southampton. The Mg fractions purified by cation exchange chromatography were re-dissolved in 3% TD HNO_3 to produce a solution with a concentration of 600 ppb Mg. Aliquots of 1 mL were taken from each sample and placed into autosampler vials ~10 minutes prior to their analysis to ensure minimal evaporation which can significantly affect the Mg isotope ratio. Before analysis, a dip test was performed to ensure that the Mg concentration of the sample was within ±10% of the concentration (600 ppb) of the bracketing standard DSM-3 (Galy et al., 2001). The samples were analysed using a sample-standard bracketing technique, whereby the mass bias is determined from analysis of the $^{25}Mg/^{24}Mg$ and $^{26}Mg/^{24}Mg$ ratio measured on the DSM-3 standard, which is analysed before and after each sample. The ^{24}Mg, ^{25}Mg and ^{26}Mg intensity of a blank solution (3% TD HNO_3) was determined prior to analysis of each sample and standard, and then subtracted. If the ^{24}Mg intensity of the blank solution became higher than 1% of the ^{24}Mg intensity of the sample/standard, the analytical run was stopped and the cones were cleaned. Samples were introduced to the plasma

using the ThermoFinnigan stable introduction system (SIS) and typical parameters for Mg isotope analyses are shown in Table II-7.

Table II-7. Settings applied during Mg isotope analysis on the Neptune Plus.

Parameters		Parameters	
Average blank ^{24}Mg	<60 mV	Extraction voltage	2000 V
Sample and standard Mg concentraton (in solution)	600 ppb	Mass resolution	Low
Average voltage ^{24}Mg (600 ppb)	14 V (min 5 V max 26 V)	Wash solution	3% HNO_3
No. of measurments	30	Wash time after sample	5 min
Integration time	8.389 s	Wash time after blank	1 min
Cone	Jet sampler cone (H cone; Nickel)	Detector	Faraday cup L3 (^{24}Mg), C (^{25}Mg) and H3 (^{26}Mg)

II.4.3.2 Accuracy and reproducibility of Mg isotope measurements

A standard reference material and a blank were processed with every batch of samples to ensure the efficacy of the column chemistry. Several samples were also processed separately through the columns at least twice to assess the reproducibility of the column chemistry.

The combined uncertainty on the ^{26}Mg/^{24}Mg ratio (or the ^{25}Mg/^{24}Mg) of the two bracketing standards, u_{DSM} (Eq. II-5), is:

$$u_{DSM} = \frac{\sqrt{(u_{DSM1})^2 + (u_{DSM2})^2}}{2} \qquad \textit{Eq. II-5}$$

where u_{DSM1} is the standard error for 30 measurements of the ^{26}Mg/^{24}Mg ratio (or ^{25}Mg/^{24}Mg ratio) on the DSM-3 standard run before the sample, and u_{DSM2} is the standard error for 30 measurements of the ^{26}Mg/^{24}Mg ratio (or ^{25}Mg/^{24}Mg ratio) on the DSM-3 standard run after the sample. The combined standard deviation on the δ^{26}Mg value of the sample ($SD_{internal}$, Eq. II-6) is:

$$SD_{internal} = \frac{{}^{X}Mg/{}^{24}Mg_{SAMPLE}}{{}^{X}Mg/{}^{24}Mg_{DSM}} \times \sqrt{\left(\frac{u_{SAMPLE}}{{}^{X}Mg/{}^{24}Mg_{SAMPLE}}\right)^2 + \left(\frac{u_{DSM}}{{}^{X}Mg/{}^{24}Mg_{DSM}}\right)^2} \qquad \textit{Eq. II-6}$$

where X refers to either 25 or 26, u_{Sample} is the standard error on the ^{25}Mg/^{24}Mg and ^{26}Mg/^{24}Mg ratio of the sample. The typical internal uncertainty of the δ^{26}Mg measurements was better than 0.03‰ and better than 0.02‰ for the δ^{25}Mg measurements.

The external error of multiple measurements of a given sample or standard ($SD_{external}$, Eq. II-7) is given by the standard deviation (SD) of the replicate measurements:

$$SD_{external} = \sqrt{\frac{1}{N-1}\sum_{i=1}^{N}(x_i - \bar{x})^2} \qquad \textit{Eq. II-7}$$

Where n is the number of measurements, x_i are the measured δ^{26}Mg values and $\bar{x}$ is the mean value of these measurements. The total uncertainty of the Mg isotope measurements (Eq. II-8) is given by the combined uncertainty of the internal error and the external error:

$$2\sigma_{(internal+external)} = \sqrt{2SD_{external}^2 + 2SD_{internal}^2} \qquad \textit{Eq. II-8}$$

The accuracy of the measurements was assessed by analysis of IAPSO seawater, DSM-3 (pure magnesium metal), SCo-1 (Cody Shale), SLRS-6 (river water) and BCR-2 (Columbia River basalt). The measured value of IAPSO was -0.82±0.05‰ (2SD, n = 18), which is in accordance with the values reported by other groups (Figure II-11). A magnesium three-isotope plot (δ^{25}Mg vs δ^{26}Mg) of all samples and the Mg standards defines a single fractionation line with a slope of 0.521 (Figure II-12),

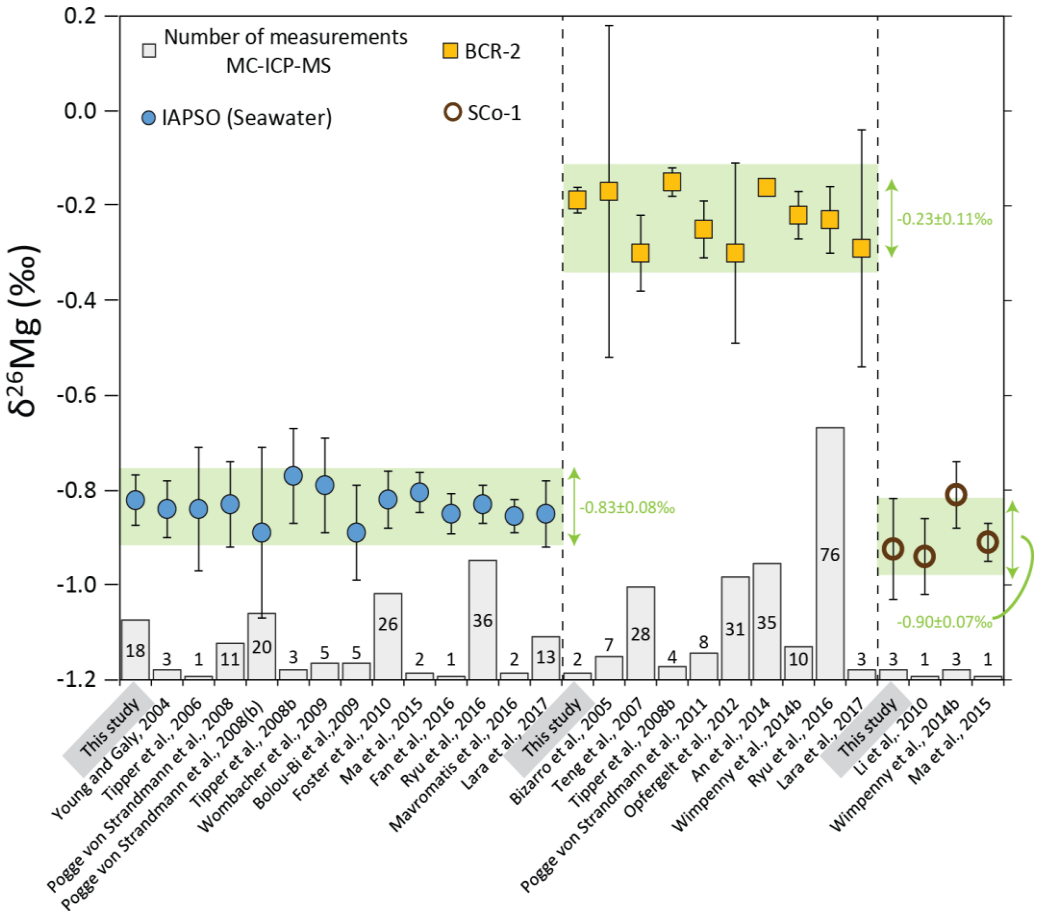

Figure II-11. Mg isotope compositions of published values for IAPSO (solid blue circles), BCR-2 (yellow squares) and SCo-1 (open brown circles).The values measured in this study are highlighted by grey shaded boxes. The green shaded boxes show the average of all the values along with an average of all the standard deviation.

consistent with the theoretical value for equilibrium fractionation of 0.521 (Young et al., 2002; Young and Galy, 2004).The variation of all standard δ^{26}Mg values through time for this study is shown in Figure II-13. The δ^{26}Mg value of the Mg isotope standards DSM-3 and CAM-1 (Cambridge-1) which have not been passed through columns were regularly measured to monitor instrumental stability and reproducibility. The average δ^{26}Mg value of DSM-3 that had not passed through columns was 0±0.09‰ (2SD, n = 155) and the average δ^{26}Mg value of CAM-1 that had not passed through columns was -2.58±0.09‰ (2SD, n = 24) which is in agreement with published values (δ^{26}Mg = −2.61±0.05‰, n = 2387) (see An and Huang (2014) and references therein).

Table II-8. Mg isotope composition of various standards measured in this study.

Standard	Number of measurements	δ^{26}Mg (‰)	2σ
IAPSO (Seawater)	n = 18	-0.82	0.05
BCR-2	n = 2	-0.19	0.03
DSM-3	n = 27	0.00	0.07
SLRS-6	n = 5	-1.22	0.03
SCo-1	n = 3	-0.92	0.11

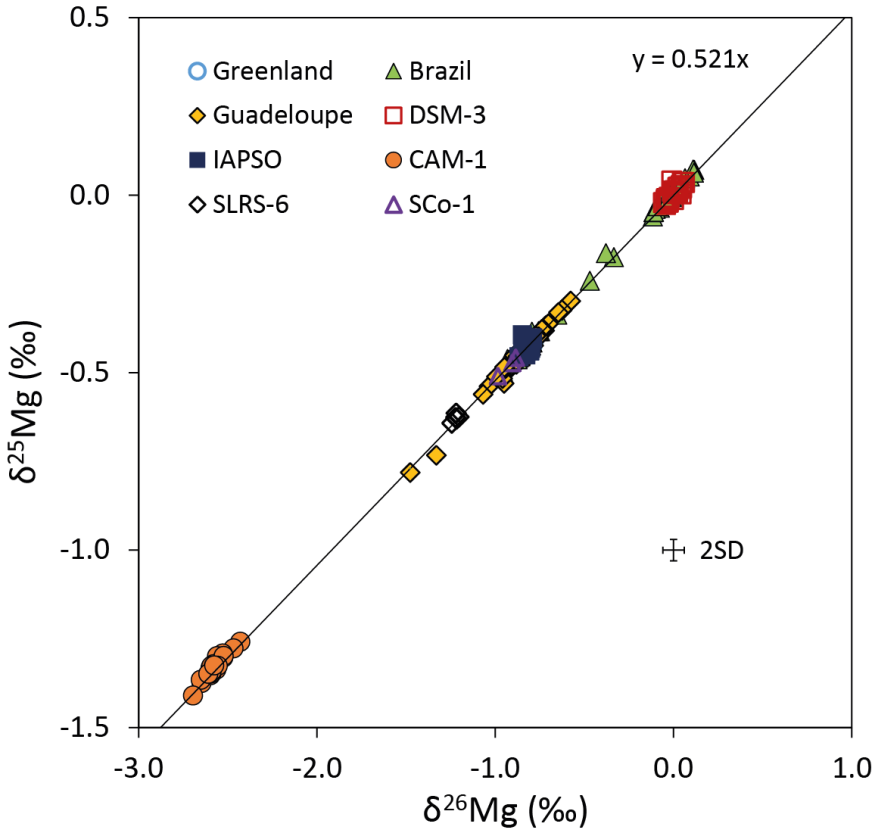

Figure II-12. Magnesium three isotope plot of all standards and samples analysed in this study. CAM-1 was not passed through columns.

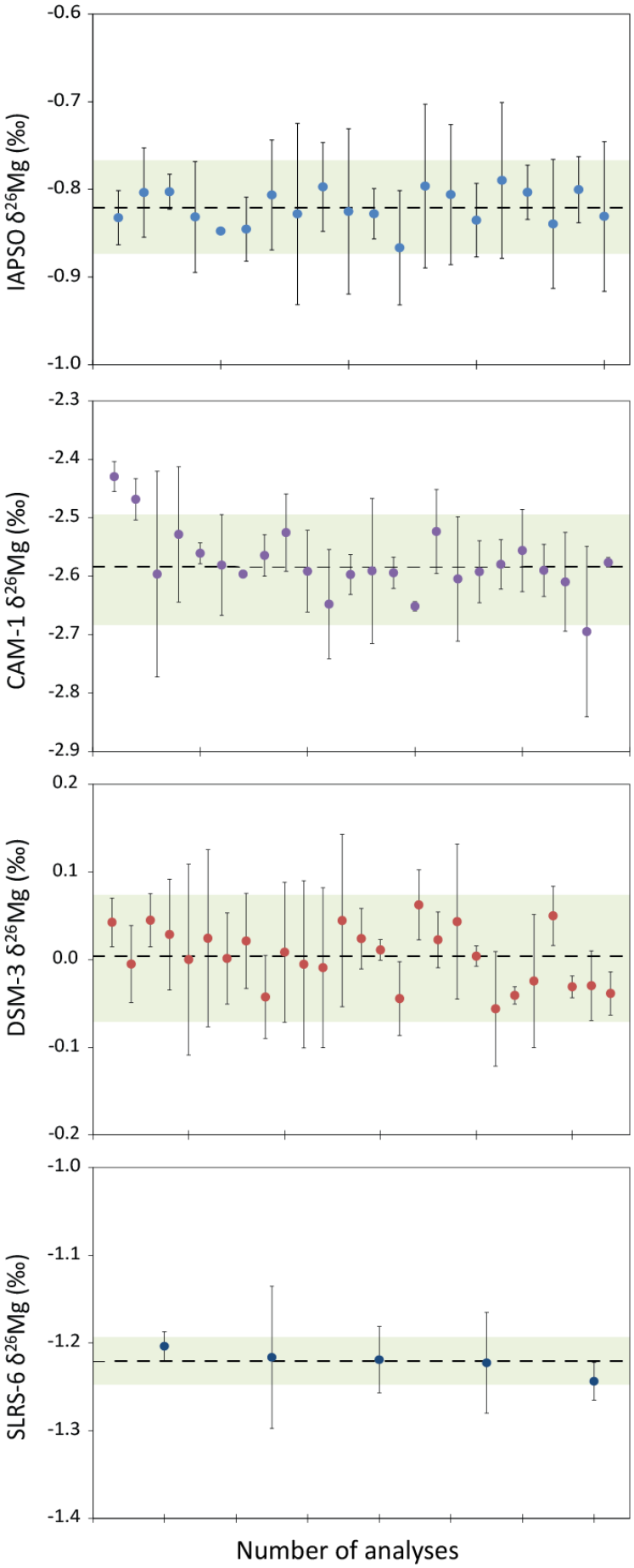

Figure II-13. δ^{26}Mg analyses of standards measured during the course of this study. Dashed horizontal lines show the average, and the green shaded box the standard deviation (2SD) of average value. Error bars represent the internal uncertainty of an individual measurement.

Chapter III. Seasonal variability in the behaviour of lithium and magnesium in a Greenlandic fjord: Implications for ocean chemistry

ABSTRACT

During glacial-interglacial cycles, differences in ice cover, ice melting, rock exposure and temperature eventually affect the chemical composition of seawater. Lithium (Li), magnesium (Mg) and Li and Mg isotopes have the potential to provide important new information on the impact of glacial weathering and estuarine mixing on the delivery of weathering products to the oceans. In glacial environments, meltwater input to glacial fjords shows distinct seasonal variations that modify the input of lithium (Li) and magnesium (Mg) to the oceans. To assess the importance of these modifications for ocean chemistry, we analysed a series of water samples collected along a transect through Godthåbsfjord (64° N, 51° W) in West Greenland, in spring (low ice melt) and summer (high ice melt). Li and Mg concentrations range from respectively, 4.1 to 23.3 µmol/kg and 9.7 to 50.5 mmol/kg and show conservative behaviour with respect to salinity whereas lithium and magnesium isotope compositions (δ^7Li, δ^{26}Mg) are largely invariant through the fjord, ranging from 29.5‰ to 31.5‰ and -0.78‰ to -0.86‰, respectively. Mass balance calculations indicate that changes in δ^{26}Mg and δ^7Li would only be detected in locations where the freshwater/seawater ratio is > 5 because concentrations of Li and Mg in ice melt are very low. As a result, even though the amount of freshwater entering the oceans at the end of the Last Glacial Maximum would have been much higher than it is today (120 to 135 m ice-equivalent sea-level lowering), this would have had minimal impact on the δ^7Li and δ^{26}Mg composition of freshwater delivered to the oceans on a global scale.

III.1 Introduction

III.1.1 Glacial weathering processes

Rates of chemical and physical weathering are controlled by a multitude of parameters, including mineral/water interaction time, rainfall (runoff), temperature, pH, mineral stability and topography. In glacial environments, rates of physical (mechanical) weathering are far higher than in temperate environments. For example, the rate of erosion in the Watson river catchment in West Greenland is ~ 1560 t/km^2/yr (Wimpenny et al., 2010b), which is up to ~200 times higher than the physical erosion rate of major non-glacial catchments such as the MacKenzie and Changjiang (Gaillardet et al., 1999a). Studies of glacier-covered alpine catchments have yielded chemical weathering rates that are far greater than the global average (Sharp et al., 1995; Jacobson et al., 2003), which has led to speculation that glacial weathering can cause significant atmospheric CO_2 drawdown (Sharp et al., 1995). In addition to the availiability of finely-ground fresh mineral, these elevated weathering rates are attribued to high flushing rates such that meltwaters remain undersaturated and reaction rates remain high (Sharp et al., 1995). However, other studies suggest that weathering in glacial environments does not necessarily involve sequestration of atmospheric CO_2 (Tranter et al., 2002), because weathering of glaciated bedrock may proceed via hydrolysis reactions (Eq. III-1) that do not consume atmospheric CO_2:

$$\underset{\textit{Pyrite}}{4FeS_2(s)} + \underset{\textit{Calcite}}{16CaCO_3(s)} + 15O_2(aq) + 14H_2O(aq) = 16Ca^{2+}(aq) + 16HCO_3^-(aq) + 8SO_4^{2-} + \underset{\textit{ferric oxyhydroxides}}{4Fe(OH)_3(s)} \qquad \textit{Eq. III-1}$$

Additionally, subglacial chemical weathering can occur as a result of reactions between the rock and CO_2 produced by root or microbial respiration, rather than atmospheric CO_2 (Tranter et al., 2002). Some models that evaluate the impact of glacial weathering processes on atmospheric CO_2 suggest that changes in the relative proportion of glacial to non-glacial weathering processes over the last 120 kyr have had little impact on levels of atmospheric CO_2 (Jones et al., 2002; Tranter et al., 2002), whereas others have suggested that glacier-covered catchments have similar or higher cation and silicon denudation rates compared to non-glaciated catchments, for the same discharge (Anderson et al., 1997). The importance of glacial environments as a regulator of atmospheric CO_2

is therefore a matter of debate, and there is a clear need to establish better tracers of weathering processes in glaciated river catchments.

III.1.2 Discharge of meltwater into the oceans

In the Northern Hemisphere, glacial meltwaters are typically discharged into a fjord, which is an estuary created by advancing glaciers. There is a growing interest in studying fjords as they play a significant role in regulating the exchange of meltwater and seawater, they harbour significant plankton communities and their sediment records provide unique information on climate evolution and glacial-interglacial cycles (Arendt et al., 2010; Mortensen et al., 2013). Mixing of glacier meltwater and seawater in a fjord may also modify the flux of dissolved solutes delivered to the oceans. For example, in a recent study in Godthåbsfjord, Western Greenland, it was demonstrated that dissolved Fe delivered into the fjord was rapidly scavenged from solution and >~97% of the sediment flux carried by meltwater runoff was physically trapped within the fjord (Hopwood et al., 2016).

The concentration and isotope composition of lithium (Li) and magnesium (Mg) have the potential to provide important information on glacial weathering processes that can be tracked over time by analysis of ancient marine sediments (Hathorne and James, 2006; Misra and Froelich, 2012; Pogge von Strandmann et al., 2014; Higgins and Schrag, 2015). This is because Li isotopes (^{6}Li and ^{7}Li) and Mg isotopes (^{24}Mg, ^{25}Mg and ^{26}Mg) are fractionated during the formation of secondary mineral phases (Huh et al., 1998; Huh et al., 2001; Pistiner and Henderson, 2003; Kisakurek et al., 2005; Tipper et al., 2008a; Opfergelt et al., 2012), or by interactions with the suspended load during transport (Pogge von Strandmann et al., 2008b; Dellinger et al., 2015; Liu et al., 2015). Additionnaly, dissolved δ^{26}Mg can also reflect the drainage of a specific bedrock lithology during continental weathering (e.g. carbonate or limestone rocks; Tipper et al., 2006b; Tipper et al., 2008), whereas this effect is limited to evaporitic rock only for δ^{7}Li (Wang et al., 2015) as silicate weathering is the major control of the dissolved Li isotope composition. For instance in Icelandic glacial rivers an increase of the dissolved δ^{7}Li associated with an increase of glacial (physical) weathering is attributed to more incongruent weathering conditions (Pogge von Strandmann et al., 2006; Vigier et al., 2009). On the contrary, in glacial river of West Greenland, the δ^{26}Mg

is not controlled by formation of secondary mineral but rather by the preferential dissolution of carbonate minerals (Wimpenny et al., 2011). The combination of Li and Mg isotopes is thus promised to be an excellent tracer of weathering processes in cold regions.

III.1.3 Past variations in the delivery of meltwaters to the ocean

The Greenland ice sheet covers 80% of the total surface area of Greenland (Vasskog et al., 2015) and 8% of the global Earth's land ice cover (Tranter, 2003). If it were to melt, it would result in a rise in global mean sea level by 7.36 m (Bamber et al., 2013). Thermomechanical (Huybrechts and de Wolde, 1999; Huybrechts et al., 2011) and mass balance models (Van As et al., 2014) suggest that the melt and runoff from the Greenland ice sheet has doubled over the past two decades (Van As et al., 2014), presumably as a result of global warming (McBean et al., 2005; Smith and Reynolds, 2005). During the Last Glacial Maximum (LGM), ~21,000 to ~18,000 years ago, eustatic sea level was ~120 to 135 m lower than it is today (Bard et al., 1990), because of increased ice volume. The Greenland ice sheet by itself was likely responsible for ~4% of the reduction in sea level (Vasskog et al., 2015). Changes in runoff and temperature between glacial-interglacial cycles are expected to induce variations in weathering and sedimentation rates at higher latitudes. To explore this idea, we have conducted a study to assess the effects of meltwater inputs on Li and Mg concentrations and isotopes in Godthåbsfjord in western Greenland. We use these data to determine the impact of glacial meltwater on the Li and Mg isotopic composition of the oceans, both today and at the LGM.

III.2 Site description and sampling

Godthåbsfjord is a 190 km long fjord located on the south west coast of Greenland at ~64°N, ~51°W (Figure III-1). The town of Nuuk is located at its mouth. It is a mountainous fjord system (Figure III-2) with a maritime-influenced polar climate that lies in the centre of an Archean complex (McGregor, 1973). This Archean complex is formed of gneiss and granite aged between 2.5 and 4 billion years (Friend and Nutman, 2005). The gneisses are dominantly pale quartzo-feldpathic gneisses that vary in composition from tonalitic to granitic (McGregor, 1973). Godthåbsfjord borders a section of the Greenland ice sheet spanning ~46 200km^2, representing 2.6% of the total Greenland ice sheet area

(Van As et al., 2014). The ice sheet extends to the coast of most of Greenland, and even into its estuaries and fjords in the winter months (Figure III-1). Freshwater inputs to Godthåbsfjord are governed by three main sources (Mortensen et al., 2011): (1) freshwater entering the surface layer of the fjord via precipitation, rivers, and streams of meteoric water and glacial meltwater; (2) subglacial freshwater that enters the fjord at depth via tidewater outlet glaciers (glacial meltwater and meteoric water); (3) glacial ice melting within the fjord (melting of icebergs and glacier termini). The mean annual freshwater discharge between 2002 and 2012 into Godthåbsfjord from the Greenland ice sheet was estimated to be 18.4 ± 5.8 Gt yr^{-1} between 2002 and 2012, whereas discharge from land surface runoff was 7.5 ± 2.1 Gt yr^{-1} (Langen et al., 2015). The hydrography of Godthåbsfjord is described in Mortensen (2011, 2013). Four types of circulation have been identified and these consist of fjord circulation driven by freshwater runoff, subglacial circulation, dense coastal inflow, and a deep tide circulation (Mortensen et al., 2011).

Water samples for this study were taken from the inner parts of the fjord (Figure III-1 and Figure III-2) in May 2014 ("spring") and August 2014 ("summer") with the Research Vessel (RV) SANNA. Sampling stations ("GF") are standard stations used by the Greenland Institute of Natural Resources

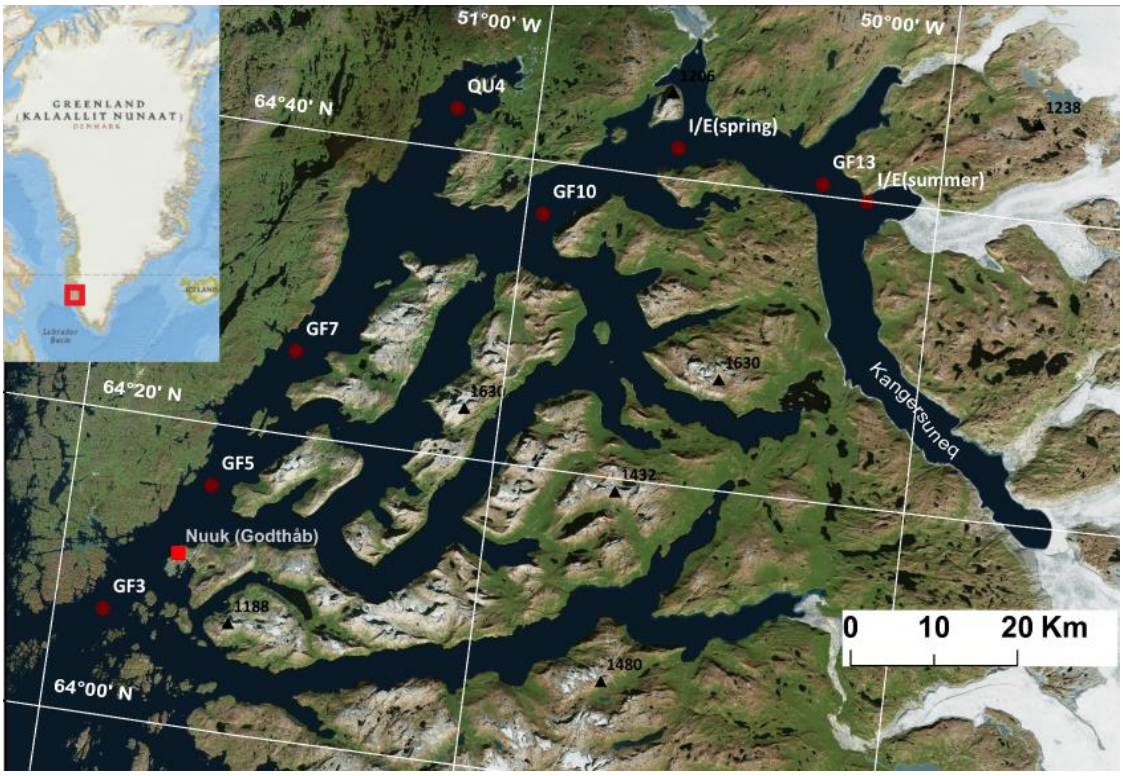

Figure III-1. Sampling stations (red dots) in Godthåbsfjord, West Greenland. I/E = Ice Edge. I/E (spring) was sampled in May while I/E (summer) was sampled in August, both as close as possible to the termini of the glaciers that enter the fjord.

(Arendt et al., 2010; Arendt et al., 2011; Mortensen et al., 2011); QU is an inlet off the main fjord and "I/E' samples refer to the Ice Edge. I/E samples were taken as close to the edge of the ice cap as possible (Figure III-1 and Figure III-2), because dense ice melange in the inner fjord makes sampling close to the glaciers logistically challenging.

Figure III-2. Station GF13 in summer. Large icebergs can be observed floating in the inner parts of the fjord but most of these melt before they reach Nuuk.

III.3 Analytical methodology

Temperature, turbidity, and salinity were measured directly in the fjord at each sampling station. Samples were filtered on board through 0.2 µm filters and acidified with 500 µL of thermally-distilled concentrated HCl to preserve them for analysis back in the laboratory. Cation concentrations of this study were determined at the National Oceanography Centre Southampton (NOCS) by inductively coupled plasma optical emission spectrometry (ICP-OES). Lithium and magnesium isotope compositions were determined by multi-collector inductively-coupled plasma-source mass spectrometry (MC-ICP-MS; Thermo Scientific Neptune), at the NOCS. A full description of the analytical methods is presented in Chapter 2.

III.4 Results

The salinity, temperature, freshwater input, turbidity and sample locations are summarized in Table III-1. Major, minor elements and isotope compositions are displayed in Table III-2.

Table III-1. Field measurements for Greenland fjord samples.

Sample	Latitude	Longitude	Temperature (°C)	Salinity (-)	Turbidity (FNU)	Freshwater (f_{FW}) (%)
Spring (May 2014)						
GF3	N 64°07'	W 51°53'	1.7	33.0	1.0	1.8
GF5	N 64°16'	W 51°40'	2.4	32.9	1.1	2.2
GF7	N 64°25.5'	W 51°30.6'	2.2	32.5	2.3	3.5
QU4	N 64°42.7'	W 51°12'	2.5	32.2	2.4	4.3
GF10	N 64°36.6'	W 50°57.5'	2.7	32.6	2.6	3.1
I/E	N 64°42'	W 50°39'	1.1	31.5	2.8	6.4
Summer (August 2014)						
GF3	N 64°07'	W 51°53'	4.7	31.6	0.5	6.1
GF5	N 64°16'	W 51°40'	6.3	27.2	1.3	19
GF7	N 64°25.5'	W 51°30.6'	7.1	23.8	1.2	29
QU4	N 64°42.7'	W 51°12'	8.8	15.1	2.0	55
GF10	N 64°36.6'	W 50°57.5'	6.2	10.8	4.8	68
GF13	N 64°40.8'	W 50°17.3'	5.8	8.1	2.9	76
I/E	N 64°40'	W 50°10.5'	5.2	8.3	4.2	75

III.4.1 In situ measurements

In spring, the samples collected in the fjord water were found to have a salinity ranging from 31.5 to 33.0. The range in temperature (1.1 to 2.7^{0}C), turbidity (1.03 to 2.84 FNU) and salinity was fairly narrow as expected prior to onset of the melt season because the fjord is mainly filled with seawater. In summer, the salinity of the water samples ranged from 8.1 (in the inner fjord) to 31.6 (in the fjord mouth), which was indicative of greater freshwater input from ice melt. The summer water temperatures were higher (4.7 to 8.8 °C) but turbidity (0.51 to 4.24 FNU) was similar to spring. The proportion of fresh meltwater proportion (f_{FW}) was estimated from the salinity (Eq. III-2) of the sample (S_{sample}), assuming that freshwater had a salinity of zero and seawater had a salinity of 33.65 (S_{SW}), which was the value measured in fjord waters from ~400m depth (Meire et al., 2015).

$$f_{FW}\ (\%) = \left[\frac{S_{SW} - S_{sample}}{S_{SW}}\right] \times 100 \qquad \textit{Eq. III-2}$$

In spring, the proportion of freshwater in the samples varied from 1.8 to 6.4%, whereas in summer it varied from 6.1 to 76%.

III.4.2 Major elements

The dissolved cation load of the fjord waters was dominated by Na^+, Mg^{2+}, Ca^{2+} and K^+ (Table III-2). Concentrations of these elements were directly proportional to salinity; in spring, the salinity variation in the samples was small so there was little variation in the concentrations of the major

elements throughout the fjord. However in summer, input of freshwater was much higher, and both salinity and major element concentrations increased towards the mouth of the fjord. Mg concentrations ([Mg]) ranged from 47.4 to 50.5 mmol/kg in spring and from 9.7 to 47.6 mmol/kg in summer (Table III-2, Figure III-3). The Mg concentration of the freshwater endmember ($[Mg]_{FW}$) was estimated to be ~272 µmol/kg (Figure III-3). The uncertainty of this value is large (± 1.1 mmol/kg), and the average value is far higher than measured concentration in glacial rivers in Greenland ([Mg] = 8.3 to 14.4 µmol/L; Wimpenny et al., 2011), Switzerland ([Mg] = 0.9 to 5.5 µmol/L; Hindshaw et al., 2011b) and ice melt from the Langjökull glacier (Iceland) ([Mg] = 6.7 µmol/L; Pogge von Strandmann et al., 2008a). Nevertheless, non-glacial rivers in Greenland had similar Mg concentrations ([Mg] = 86.3 to 775 µmol/L; Wimpenny et al., 2011), and the average of the world's largest rivers ([Mg] = ~475 µmol/L; Gaillardet et al., 1999b) was higher.

*Table III-2. Concentrations of major and minor elements, and Li and Mg isotopic compositions of Godthåbsfjord water.n.d = not determined, b.d =below detection limit (0.3 µmol/kg for Sr and Si).The 2σ is the internal uncertainty of each measurements. TdFe = total dissolvable Fe concentrations; DFe = Dissolved Fe. *Values from Hopwood et al. (2016).*

Sample	Major cations (mmol/kg)				Minor cations (µmol/kg)				Fe (nmol/L)*		Isotopic composition (‰)					
	Na	Mg	Ca	K	B	Sr	Li	Si	TdFe	DFe	δ^7Li	2σ	δ^{25}Mg	2σ	δ^{26}Mg	2σ
Spring																
GF3	441	49.3	9.7	9.4	406	82	23.1	b.d	136	< 0.1	31.0	0.2	-0.44	0.02	-0.84	0.03
GF5	434	49.5	9.7	9.3	405	82	23.0	b.d	163	5.8	31.2	0.2	-0.40	0.02	-0.81	0.03
GF7	433	49.7	9.6	9.2	396	81	22.8	b.d	247	3.5	31.2	0.2	-0.41	0.02	-0.78	0.03
QU4	420	48.6	9.4	9.0	385	79	22.3	b.d	-	-	n.d	n.d	n.d	n.d	n.d	n.d
GF10	445	50.5	9.8	9.5	403	83	23.3	b.d	247	30.9	30.3	0.2	-0.42	0.02	-0.81	0.03
I/E	413	47.4	9.0	8.8	374	78	21.8	b.d	697	8.8	30.8	0.2	-0.40	0.02	-0.79	0.02
Dup I/E	413	47.5	9.1	8.8	376	78	21.9	b.d	-	-	30.2	0.3	n.d	n.d	n.d	n.d
Summer																
GF3	422	47.6	9.2	8.9	384	80	22.3	b.d	218	< 0.1	29.8	0.2	-0.42	0.02	-0.78	0.03
GF5	368	41.8	8.1	7.6	335	69	19.5	b.d	346	5.7	31.5	0.2	-0.42	0.02	-0.79	0.03
GF7	317	37.1	7.0	6.6	282	60	16.8	b.d	437	< 0.1	30.5	0.2	-0.42	0.02	-0.82	0.02
Dup GF7	313	37.0	7.1	6.5	291	60	16.7	b.d	-	-	30.3	0.2	-0.40	0.02	-0.78	0.03
QU4	163	20.5	3.8	3.2	152	32	8.7	15.3	-	-	31.3	0.2	-0.43	0.02	-0.82	0.03
GF10	146	18.5	3.5	2.8	135	29	7.9	16.6	1840	6.3	30.8	0.2	-0.44	0.02	-0.86	0.03
GF13	102	13.6	2.5	2.0	98	21	5.7	15.3	686	< 0.1	29.7	0.2	-0.44	0.02	-0.84	0.02
I/E	68	9.7	1.8	1.3	70	b.d	4.1	18.5	1352	33.7	30.9	0.3	-0.46	0.02	-0.86	0.03

III.4.3 Minor elements

Concentrations of B, Sr and Li also increase with increasing salinity. The dissolved Li concentrations ([Li]) in our samples ranged from 21.8 to 23.3 µmol/kg in spring, and from 4.1 to 22.3 µmol/kg in summer (Table III-2 and Figure III-3). The Li concentration of the freshwater endmember ($[Li]_{FW}$) is estimated to be ~219 nmol/kg (±212 nmol/kg; Figure III-3), within the range for rivers draining into

Kangerlussaq estuary (14 to 569 nmol/L) which is also located in southwest Greenland (Wimpenny et al., 2010b). Nevertheless, this value is higher than the concentration measured in meltwater from the Langjökull icecap, in Iceland ([Li] = 2.1 nmol/L; Pogge von Strandmann et al., 2006). In contrast to Li and Mg, concentrations of Si and Fe (TdFe = Total dissolvable Fe concentrations in unfiltered samples at pH < 2 and DFe = Dissolved Fe filtrated <0.2µm) show an inverse relationship with salinity (Table III-2). The silicon concentrations ([Si]) measured in summer range from 15.3 to 18.5 µmol/kg; only the very inner parts of the fjord had Si concentrations that were higher than the detection limit.

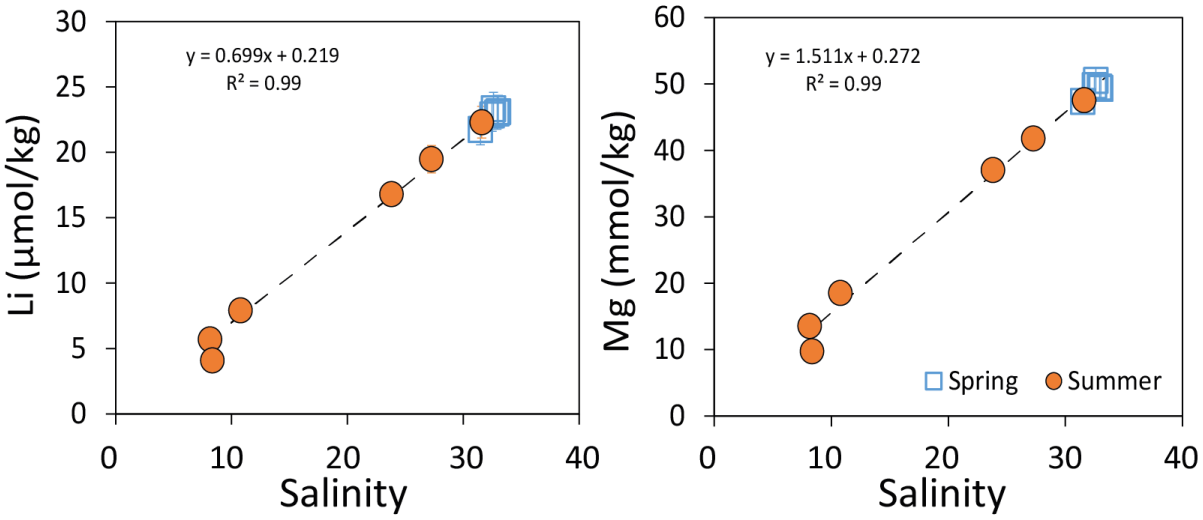

Figure III-3. [Li] and [Mg] versus salinity in Godthåbsfjord (excluding sample QU4 which is not in the fjord continuity). Blue open squares are samples taken in winter and orange circles are samples taken in summer. The uncertainty of the measurements is ± 5% for Li and Mg (error bars are smaller than the size of the symbols). The standard error of the intercept at S_{SW} = 0 is 1.1 mmol/kg for Mg and 212 nmol/kg for Li.

III.4.4 Li and Mg isotopes

The δ^7Li values of the fjord waters ranged from 30.3 to 31.2‰ in spring and from 29.5 to 31.5‰ in summer (Figure III-4). Corresponding δ^{26}Mg values ranged from -0.78 to -0.86‰ in summer and -0.79 to -0.84‰ in spring. Two samples were duplicated (Dup GF7 and Dup I/E), the agreement between the two measurements was better than 0.60‰ for δ^7Li and 0.04‰ for δ^{26}Mg (Table III-2.

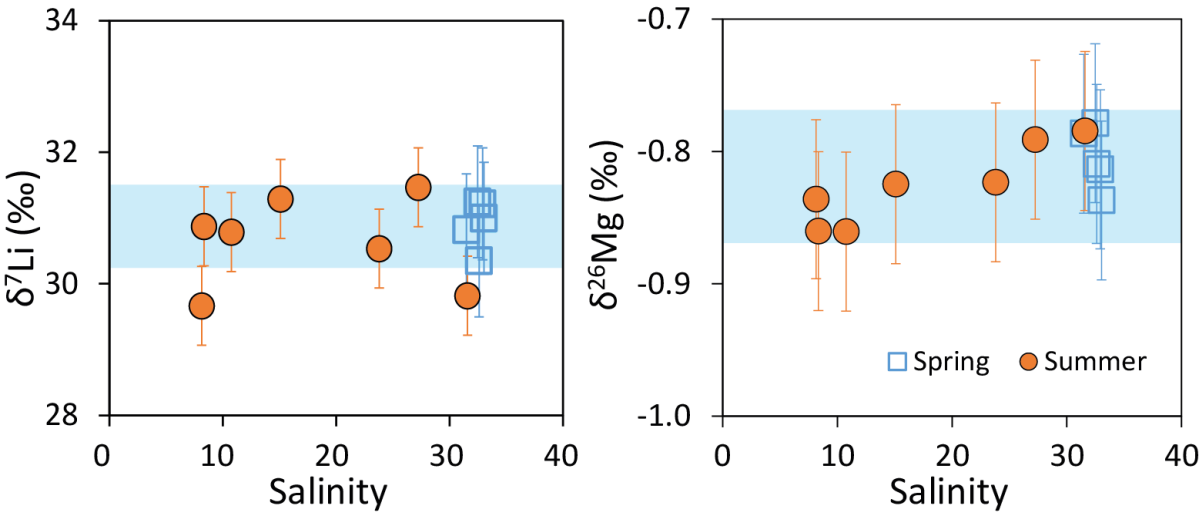

Figure III-4. Isotopic composition of lithium (δ^7Li) and magnesium (δ^{26}Mg) in summer and spring. Error bars represent the 2σ external uncertainty of the isotope analyses (0.6‰ for Li and 0.06‰ for Mg) calculated with repeated measurements of L-SVEC (δ^7Li = 0.0 ± 0.5‰ (2SD, n = 28)), DSM-3 (δ^{26}Mg = 0.00 ± 0.07‰ (2SD, n = 27)) and IAPSO (δ^7Li = 30.9 ± 0.6‰ (2SD, n = 27); δ^{26}Mg = -0.82 ± 0.05‰ (2SD, n = 18)). The blue shaded boxes show the standard deviation (2σ) around the average IAPSO seawater values.

III.5 Discussion

III.5.1 Behaviour of Li and Mg during ice melt-seawater mixing

The concentrations of Li and Mg in the fjord are directly proportional to salinity, which is indicative of conservative behaviour; i.e. their concentrations are simply controlled by the proportion of meltwater (that has low Li and Mg) and seawater (that has high Li and Mg). Conservative behaviour of Li and Mg has been observed in many other estuaries (Stoffyn-Egli, 1982; Colten and Hanor, 1984; Pogge von Strandmann et al., 2008b), although a study of the Kalix and Råne River (Sweden) indicated that in these estuaries, Li appeared to be affected by adsorption on secondary minerals (Murphy et al., 2014). The input of meltwater into the estuary was higher in the summer when temperatures are higher but, even at this time of the year, the influence of meltwater on Li and Mg concentrations was only evident in the inner parts of the fjord (Stations GF7, GF10, GF13 and I/E; Figure III-3), which is consistent with the distribution of salinity (Figure III-5; Hopwood et al., 2016). In contrast to Li and Mg, DFe shows strongly non-conservative behaviour in the estuary and removal of DFe is observed at low salinities (Figure III-6; Hopwood et al., 2016) because the increase in ionic strength destabilises Fe colloids in the meltwater causing them to form aggregates that settle out

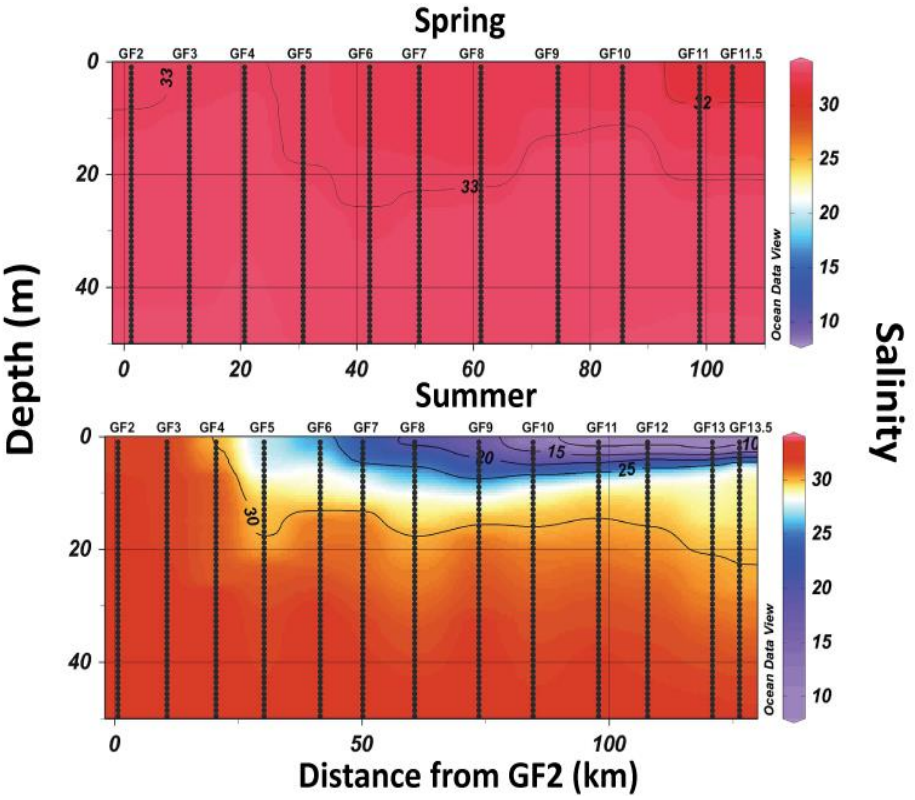

Figure III-5. Distribution of salinity in spring (May) and summer (August) in Godthåbsfjord (GF2 is the station located offshore few kilometres after GF3). After Hopwood et al., 2016.

of solution (Boyle et al., 1977; Sholkovitz et al., 1978). However, although Li can be adsorbed or incorporated in the surface of iron oxyhydroxides (Pogge von Strandmann et al., 2008b; Wimpenny et al., 2010b), and uptake of Mg by clays minerals containing Fe-oxides has also been observed (Opfergelt et al., 2012), there is no obvious evidence for uptake of Li or Mg at low salinity (Figure III-3).

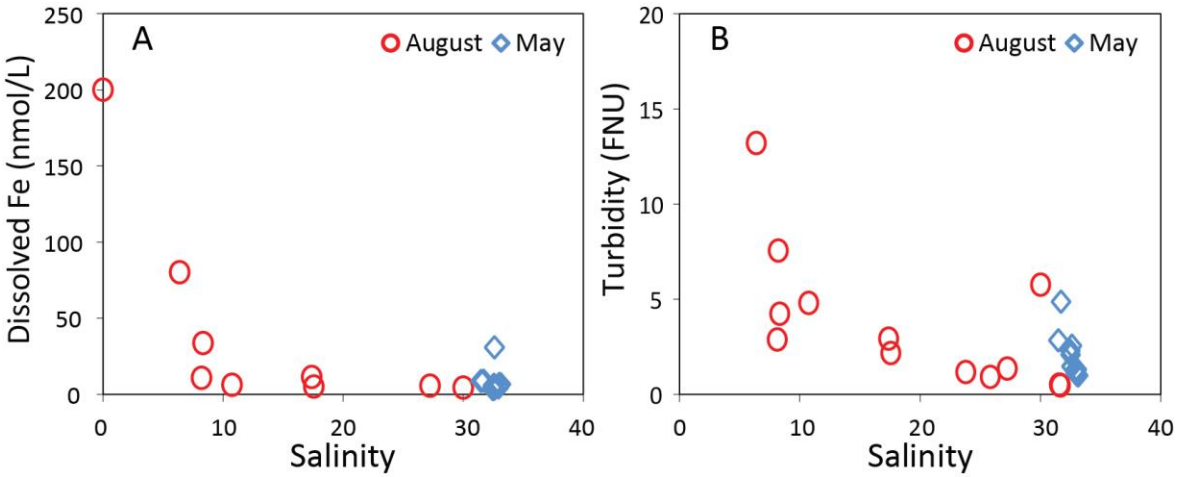

Figure III-6. A. Dissolved Fe (DFe) along the salinity gradient in Godthåbsfjord, before (May, blue diamonds) and during (August, red circles) the meltwater season. DFe is removed at low salinities due to precipitation/flocculation of iron oxides. B. Turbidity (Formazin Nephelometric Unit, FNU) follows the same trend as DFe. After Hopwood et al., 2016.

III.5.2 Behaviour of Li and Mg isotopes during ice melt-seawater mixing

Although there are clear variations in [Li] and [Mg] within the fjord, it appears that δ^7Li values are largely unaffected during the fjord mixing process, although there is a hint that δ^{26}Mg evolves towards lower values at lower salinity (Figure III-4). All of the water samples from Godthåbsfjord have Li isotope compositions that are similar to seawater, ~31‰ (James and Palmer, 2000a; Hall et al., 2005; Pogge von Strandmann et al., 2008b); most δ^{26}Mg values are also similar to seawater (~ -0.82‰; Foster et al., 2010). Analyses of waters in the same salinity range from estuaries in Iceland and the Azores give similar results within the errors (Pogge von Strandmann et al.,2008b; Figure III-7).

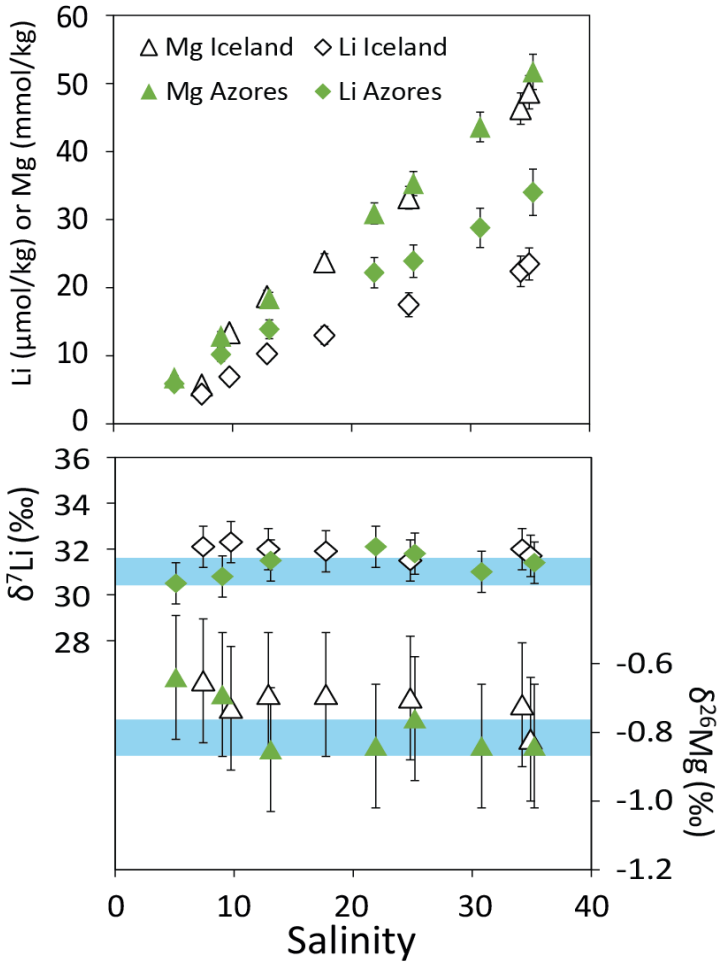

Figure III-7. Compilation of data from different estuary studies of Li and Mg concentrations and isotope compositions. The blue shaded boxes show the standard deviation (2σ) around the average IAPSO seawater values for δ^7Li and δ^{26}Mg. After Pogge von Strandmann et al. (2008b).

III.5.2.1 Li isotopes

There are three possible explanations for the lack of change in δ^7Li during fjord mixing:

1. Freshwater comes from melting of sea ice. During ice-crystal growth the major ions present in seawater (Na^+, Mg^{2+}, Ca^{2+}, K^+, Cl^-, SO_4^{2-}, CO_3^{2-}) are not incorporated into the ice crystal lattice and are rejected by the advancing ice-water interface (Petrich and Eicken, 2010). As salt is excluded from the sea ice crystal lattice, melting of sea ice introduces a freshwater component as well as salt crystals that have not been incorporated into the ice lattice (Untersteiner, 1968). The Li isotope composition of this meltwater is therefore the same as seawater, assuming there is no fractionation of Li isotopes associated with freezing/melting of water. In support of this, analyses of δ^7Li and $\delta^{26}Mg$ in meltwater from the Icelandic icecap have δ^7Li = 33.3‰ and $\delta^{26}Mg$ = -0.83‰, similar to seawater (Pogge von Strandmann et al., 2006; 2008a). This process, however, cannot explain high concentrations of dissolved Si at low salinity (Figure III-8) that have also been measured in other studies (Hopwood et al., 2016; Meire et al., 2016). As ice melt has a very low Si concentrations (e.g. in Langjökull icecap (Iceland) [Si] = 3.3 µmol/L; Pogge von Strandmann et al., 2006), this implies that Si is release during interactions between the ice sheet and the bedrock, that has high [Si] (Hopwood et al., 2016; Meire et al., 2016). Si is lost from the estuary as it is taken up by diatoms close to the glacial outflows (Meire et al., 2016). Additionally, Mortensen (2013) observed that sea ice either melts or leaves the inner part of the fjord before the onset of the summer and therefore does not influence the freshwater budget significantly.

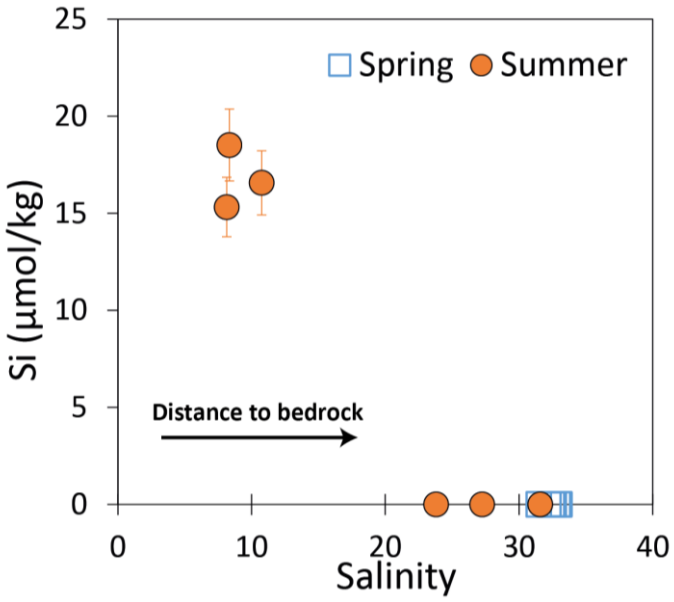

Figure III-8. [Si] (± 10%) versus salinity in Godthåbsfjord. Silicon concentrations are only detectable at low salinity at the sampling points.

2. Uptake of Li derived from meltwater, which can be assumed to have δ^7Li values similar to average of glacial river water from West Greenland (δ^7Li ≈ 26‰; Wimpenny et al., 2010a), onto the surfaces of iron oxyhydroxides that form in the subglacial environment (Eq. III-1, Section III.1.1). This process results in enrichment of ^{6}Li in the solid phase and ^{7}Li in the remaining fluid such that the δ^7Li of the meltwater is shifted to higher values, potentially close to seawater (Wimpenny et al., 2010b). However, in contrast to Fe or Si (Figure III-6 and Figure III-8), there is no obvious evidence for removal of Li at low salinities.

3. The concentration of Li in the meltwaters is so low compared to seawater, that the δ^7Li value of the fjord (δ^7Li_{fjord}, Eq. III-3) waters is dominated by seawater input. The effects of this can be assessed by mass balance:

$$\delta\ ^7Li_{Fjord} = \frac{\delta\ ^7Li_{FW} \times [Li]_{FW} \times f_{FW} + \delta\ ^7Li_{SW} \times [Li]_{SW} \times (1 - f_{FW})}{\left((1 - f_{FW}) \times [Li]_{SW}\right) + (f_{FW} \times [Li]_{FW})} \qquad \textit{Eq. III-3}$$

where [Li] is the Li concentration, *SW* and *FW* are, respectively, the seawater and freshwater endmembers, and f_{FW} and f_{SW} are the proportions of, respectively, freshwater and seawater (Eq. III-4), such that:

$$f_{FW} + f_{SW} = 1 \qquad \textit{Eq. III-4}$$

$[Li]_{SW}$ is taken to be the Li concentration at Godthåbsfjord seawater salinity (33.65) which gives $[Li]_{SW}$ ≈ 23.7 µmol/kg (Figure III-3). $[Li]_{FW}$ is the Li concentration at zero salinity (0.219 µmol/kg; Figure III-3), and δ^7Li_{SW} = 31‰. The δ^7Li value of the freshwater endmember is unknown, but is almost certainly greater than the value of the catchment bedrock (average value of ~8.5‰; Wimpenny et al., 2010a). Both this value, and the average δ^7Li value of Greenland glacial (δ^7Li ≈ 26‰; Wimpenny et al., 2010a) are considered here. The results of the mass balance calculations indicate that the low [Li] of meltwater relative to seawater means that changes in δ^7Li during the

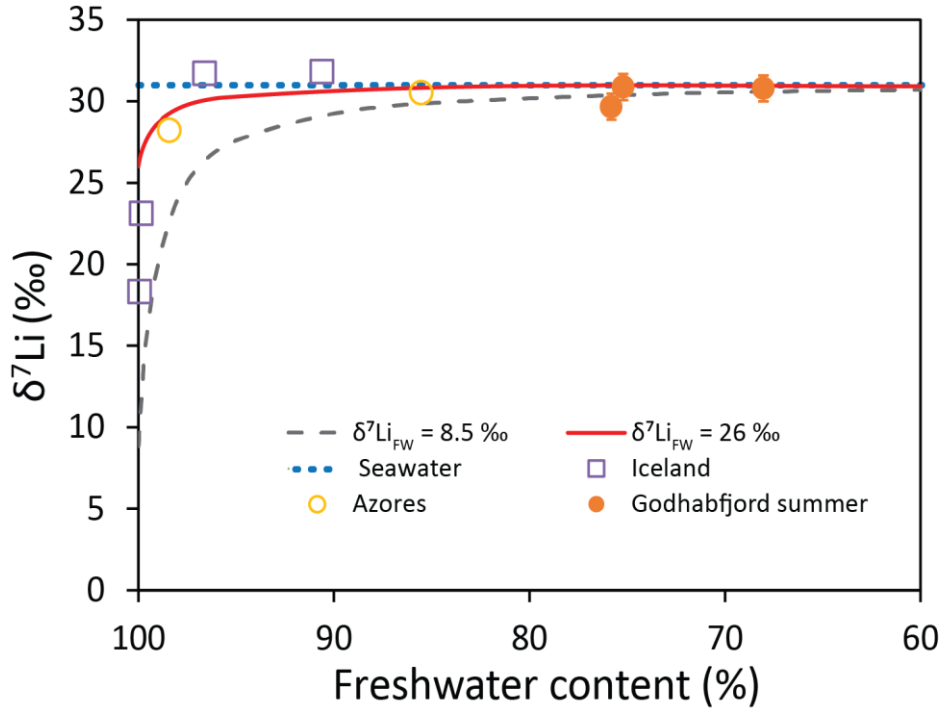

Figure III-9. Modelling of the evolution of the lithium isotope composition during seawater and freshwater mixing. Note that the effects of meltwater input can only be detected (outside the external reproducibility of the isotope measurements) when the freshwater contribution is > 85%. As all of our samples contain < 75% freshwater, no variations in δ^7Li are expected. Azores and Iceland data are from Pogge von Strandmann et al. (2008b).

mixing process are unlikely to be detected unless the proportion of freshwater is > 85% (Figure III-9) and, even in the extreme case where δ^7Li_{FW} = 8.5‰, the sample with lowest salinity can be expected to have a δ^7Li value that is only 0.6‰ lower than seawater. This is close to the uncertainty of δ^7Li analyses.

III.5.2.2 Mg isotopes

The isotope compositions of Mg are similar in summer and spring in Godthåbsfjord and are comparable to the seawater value (-0.82‰). As suggested for Li, sea ice melting is unlikely to be the reason why Mg isotopes have an isotope composition close to seawater. The expected change in $\delta^{26}Mg$ as a function of salinity (Eq. III-5) can be assessed by mass balance (Figure III-10):

$$\delta^{26}Mg_{Fjord} = \frac{\delta^{26}Mg_{FW} \times [Mg]_{FW} \times f_{FW} + \delta^{26}Mg_{SW} \times [Mg]_{SW} \times (1 - f_{FW})}{\left((1 - f_{FW}) \times [Mg]_{SW}\right) + (f_{FW} \times [Mg]_{FW})} \quad \textit{Eq. III-5}$$

where [Mg] is the Mg concentration, *SW* and *FW* are, respectively, the seawater and freshwater endmembers, and f_{FW} and f_{SW} are the proportions of, respectively, freshwater and seawater (Eq. III-6), such that:

$$f_{FW} + f_{SW} = 1$$

Eq. III-6

$[Mg]_{SW}$ is the Mg concentration at Godthåbsfjord seawater salinity (50.2 mmol/kg; Figure III-3), $[Mg]_{FW}$ is the Mg concentration at zero salinity (0.272 mmol/kg; Figure III-3) and $\delta^{26}Mg_{SW}$ = -0.82‰ (Foster et al., 2010). The $\delta^{26}Mg$ value of the freshwater endmember is unknown, but is almost certainly smaller than the value of the catchment bedrock (assuming that the bedload is representative of the bedrock, the average value is -0.4‰; Wimpenny et al., 2011). In support of this, other glacial rivers in West Greenland have $\delta^{26}Mg_{FW} = -1.12 \pm 0.06$‰ (Wimpenny et al., 2011). However, as most of the freshwater entering the fjord is provided by subglacial input (~71%) rather than surface runoff (Langen et al., 2015), this implies also a different $\delta^{26}Mg$ for subglacial runoff. Sub-glacial weathering is thought to be responsible for the preferential dissolution of easily weathered mineral phases such as carbonates (Anderson et al., 1997), and as carbonates are isotopically light ($\delta^{26}Mg$ down to -5.6‰; Wombacher et al.,2011), sub-glacial weathering is likely to produce fluids with low $\delta^{26}Mg$. Both $\delta^{26}Mg$ values (-5.6 and -0.4‰) for the freshwater endmember are considered here (Figure III-10). The results of the mass balance calculations indicate that the

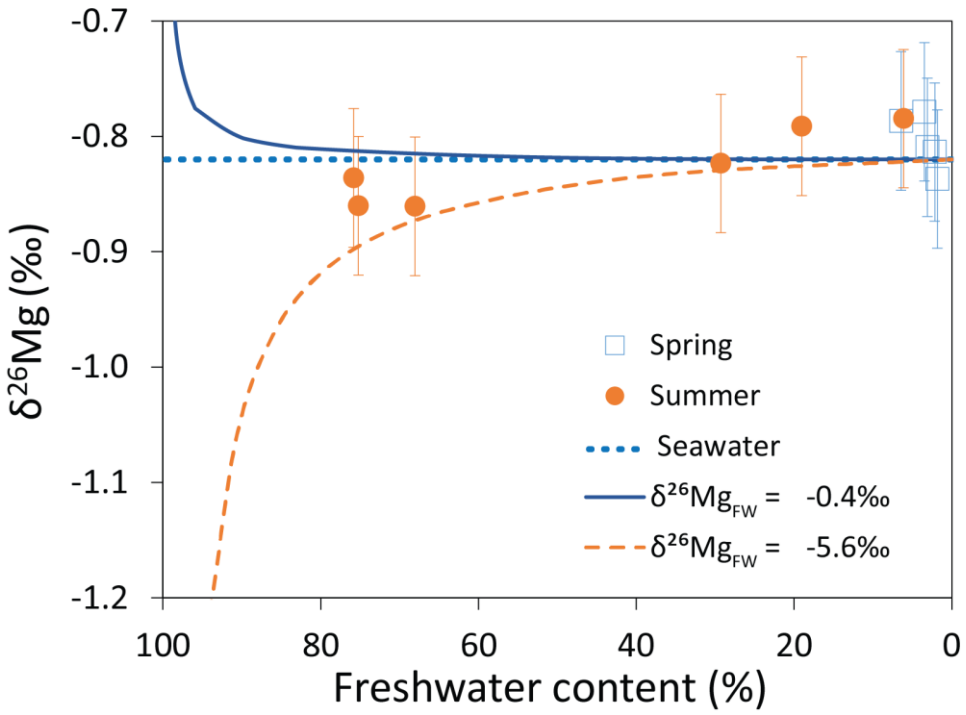

Figure III-10. Modelling of the evolution of the magnesium isotope composition during seawater and freshwater mixing. Contrary to Li the effects of meltwater input are detectable when freshwater contribution is > 80%.

low [Mg] of meltwater relative to seawater means that changes in δ^{26}Mg during the mixing process are unlikely to be detected unless the proportion of freshwater is > 80% (Figure III-10).

III.5.3 Effects of ice melt on the Li and Mg composition of seawater

As discussed in Section III.1.3, the quantity and distribution of global ice sheets has varied in the past and, for example, the extent of the ice sheets was considerably larger at the Last Glacial Maximum (LGM) than it is today (120 to 135 m ice-equivalent sea-level lowering; Clark and Mix, 2002). The potential effects of this on the Li and Mg concentration, and Li and Mg isotope composition of the ocean at the LGM are shown in Table III-3 and Figure III-11. Various scenarios are considered: (i) variations in the isotope composition of the meltwater, and (ii) variations in the volume of the ice sheets. Given that Li and Mg behave conservatively during ice melt – seawater mixing, then the concentration of Li in the oceans today is determined by the relative amount of Li (or Mg) in the ocean at the LGM (Eq. III-7), and the relative amount of Li (or Mg) added due to ice melting (Eq. III-8):

$$\text{Li in LGM ocean, } Li_{LGM} = \left(\frac{Depth_{LGM\ ocean}}{Depth_{modern\ ocean}} \times [Li]_{LGM\ ocean}\right) \qquad \textit{Eq. III-7}$$

$$\text{Li from ice melting, } Li_{Ice} = \left(\frac{Sea - Ice\ equivalent_{LGM\ ocean}}{Depth_{modern\ ocean}} \times [Li]_{Ice}\right) \qquad \textit{Eq. III-8}$$

The same equations can be used to determine the proportion of Mg in the modern ocean derived from the LGM ocean and ice melt. The δ^{7}Li (or δ^{26}Mg) value of LGM seawater can be estimated by mass balance:

$$\delta^{7}Li_{LGM\ ocean} = \frac{\delta^{7}Li_{modern\ ocean} \times (Li_{LGM} + Li_{Ice}) - \delta^{7}Li_{Ice} \times Li_{Ice}}{Li_{LGM}} \qquad \textit{Eq. III-9}$$

In all scenarios, $[Li]_{ice}$ is assumed to be 219 nmol/kg and $[Mg]_{ice}$ is assumed to be 272 µmol/kg (this study). Scenarios 1 and 2 assume that, given their long residence times in seawater, the Li and Mg concentration of LGM seawater was the same as it is today. Scenarios 3 and 4 consider that the Li and Mg concentration in the LGM ocean was higher than it is today because of the reduction in the volume of the oceans, consistent with higher concentrations of chlorine in LGM sediment pore waters (Adkins and Schrag, 2001). Scenarios 1 and 2, and Scenarios 3 and 4 differ only with the

isotope composition of the freshwater input used (8.5‰ and -5.6‰ for Li and Mg respectively, for the scenario 1 and 3; 26‰ and -0.4‰ for Li and Mg respectively, for the scenario 2 and 4).

Table III-3. Evolution of the isotope composition of the ocean between LGM and present according to four different scenarios of seawater and meltwater mixing.

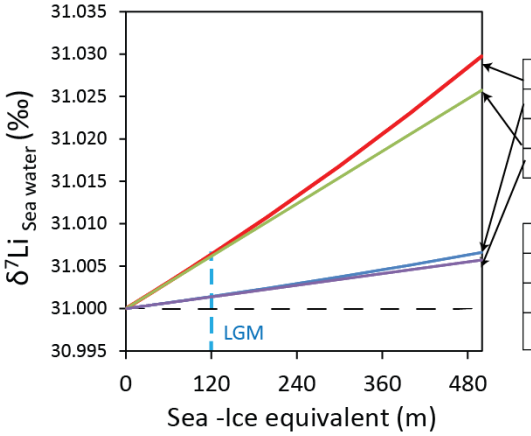

	Parameters	$\delta^7Li_{LGM\ Sea}$ (‰) 120 m Sea-Ice equivalent	$\delta^7Li_{LGM\ Sea}$ (‰) 135 m Sea-Ice equivalent
Li Scenario 1	δ^7Li_{Fw} = 8.5‰, $[Li]_{LGM\ Sea}=[Li]_{Sea}$	31.006	31.007
Li Scenario 2	δ^7Li_{Fw} = 26‰, $[Li]_{LGM\ Sea}=[Li]_{Sea}$	31.001	31.002
Li Scenario 3	δ^7Li_{Fw} = 8.5‰, $[Li]_{LGM\ Sea}\neq[Li]_{Sea}$	31.006	31.007
Li Scenario 4	δ^7Li_{Fw} = 26‰, $[Li]_{LGM\ Sea}\neq[Li]_{Sea}$	31.001	31.002
	Parameters	$\delta^{26}Mg_{LGM\ Sea}$ (‰) 120 m Sea-Ice equivalent	$\delta^{26}Mg_{LGM\ Sea}$ (‰) 135 m Sea-Ice equivalent
Mg Scenario 1	$\delta^{26}Mg_{Fw}$ = -5.6‰, $[Mg]_{LGM\ Sea}=[Mg]_{Sea}$	-0.82	-0.82
Mg Scenario 2	$\delta^{26}Mg_{Fw}$ = -0.4‰, $[Mg]_{LGM\ Sea}=[Mg]_{Sea}$	-0.82	-0.82
Mg Scenario 3	$\delta^{26}Mg_{Fw}$ = -5.6‰, $[Mg]_{LGM\ Sea}\neq[Mg]_{Sea}$	-0.82	-0.82
Mg Scenario 4	$\delta^{26}Mg_{Fw}$ = -0.4‰, $[Mg]_{LGM\ Sea}\neq[Mg]_{Sea}$	-0.82	-0.82

Our calculations show that the reduction in ice melt input into the oceans at the LGM has minimal impact of the Li and Mg concentration, and Li and Mg isotope composition of seawater. Despite a decrease in the volume of ocean of between ~3.3% and ~3.7%, and higher Li and Mg concentrations than today, ranging from 26.87 to 26.98 µmol/L and 54.78 to 55.01 mmol/L respectively, the isotope composition of Li and Mg in the LGM ocean is indistinguishable from the δ^7Li and $\delta^{26}Mg$ values of seawater today. We estimate that δ^7Li can vary by up to +0.007‰ and $\delta^{26}Mg$ by up to +0.001‰ which is negligible and indistinguishable from the modern seawater values (δ^7Li = 31.2 ± 0.9‰; Pogge von Strandmann et al., 2008b; and $\delta^{26}Mg$ = -0.82 ± 0.1‰; Foster et al., 2010).

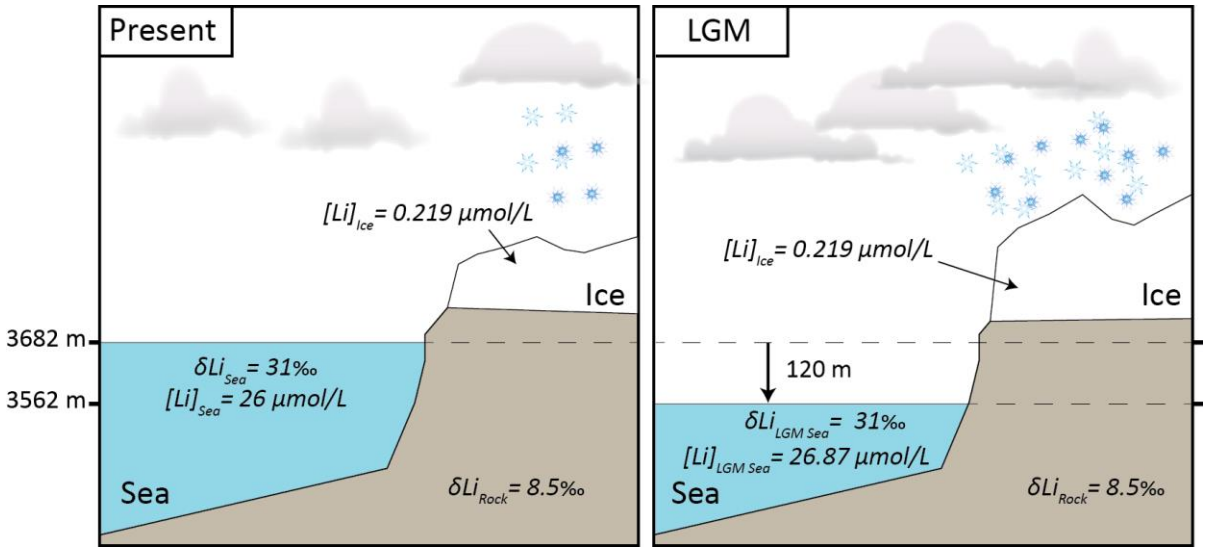

Figure III-11. Cartoon illustrating how δ^7Li and [Li] changes between LGM and the present according to Scenario 3 (see Table III-3).

III.6 Conclusions

Godthåbsfjord is characterised by marked changes in the concentrations of Li and Mg that can be explained by mixing between a low [Li] and low [Mg] freshwater endmember and a high [Li] and high [Mg] seawater endmember. Inputs of freshwater are higher in summer than in winter due to melting of the Greenland ice cap. However, freshwater input has little impact on $\delta^{26}Mg$ and $\delta^{7}Li$ in the fjord; $\delta^{26}Mg$ and $\delta^{7}Li$ values are generally within uncertainty of the seawater value. The influence of meltwater input on $\delta^{7}Li$ and $\delta^{26}Mg$ can only be detected at very high freshwater/seawater ratios (> 5) as a result of the low Li and Mg concentrations in freshwater. Although there is evidence for near-quantitative removal of Fe by flocculation of Fe-colloids at low salinities, this has no effect on $\delta^{26}Mg$ and $\delta^{7}Li$ and there is no evidence for uptake of Li and Mg onto mineral surfaces. While the quantity of meltwater entering the oceans at the LGM was much higher than it is today, we estimate that this resulted in no significant changes to seawater $\delta^{26}Mg$ and $\delta^{7}Li$ values. This suggests that variations in $\delta^{26}Mg$ and $\delta^{7}Li$ values of ancient seawater preserved in marine sediments cannot be explained by glaciations and sea level changes.

Chapter IV. The response of Li and Mg isotopes to rain events in a highly-weathered catchment

ABSTRACT

Storms are responsible for up to ~50 % of total annual rainfall on tropical islands and result in rapid increases in discharge from rivers. Storm events are, however, notoriously under-sampled and their effects on weathering rates and processes are poorly constrained. To address this, we have undertaken high-frequency sampling of the small instrumented Quiock Creek catchment, a Critical Zone Observatory located in Guadeloupe, over a period of 21 days, encompassing several storm events. Chemical and isotopic (Li and Mg) analyses of different critical zone reservoirs (throughfall, soil pore water, groundwater and river water) are used to assess the interactions between rock, water and secondary minerals. The Li concentrations and δ^7Li values of these different reservoirs range from 14 to 95 nmol/kg and 1.8 to 16.8‰, respectively. After several rain events, the average δ^7Li value (13.3‰) of soil solutions from the lower part of the soil profile (> ~150 cm below the surface) was unchanged, whereas in the upper part of the profile δ^7Li values increased by ~2 - 4‰ due to increased contribution from throughfall. By contrast, the δ^{26}Mg value of soil waters in the upper part of the soil profile were not significantly affected by the rain events with an average value of -0.90‰. The δ^{26}Mg values of the different fluid reservoirs are generally close to the value of throughfall (-0.97 and -0.84‰), but higher δ^{26}Mg values (up to -0.58‰) are measured in the deeper parts of the soil profile, and groundwaters that have a long residence time have lower δ^{26}Mg values (down to -1.48‰). These higher and lower values are attributed to, respectively, adsorption/desorption of light Mg isotopes on/from the surface of clay minerals. The Li isotope composition of the river was ~9.3‰, with a Li concentration of 60 µmol/kg, but during a storm these values decreased to, respectively, 7.8‰ and 40 µmol/kg. This change in δ^7Li is consistent with an increased contribution of Li from the soil solution. Considered together, our data provide first-order constraints on the behaviour of Li and Mg isotopes during storm events in tropical climates.

IV.1 Introduction

Weathering processes drive soil and landscape formation, soil nutrient cycling and they control the delivery of chemical elements from the continents to the oceans (Gaillardet et al., 1999b; Millot et al., 2002). The chemical composition of river waters is also strongly influenced by hydrology (Maher, 2011); in some rivers element concentrations do not vary with discharge, so elemental fluxes are determined primarily by the water flux, whereas in other rivers, element concentrations decrease with increasing discharge indicating that dilution is the principal control and elemental fluxes remain constant (Godsey et al., 2009). Concentration-discharge relationships have been suggested to be controlled by: water saturation in the soil (Godsey et al., 2009); the interplay between fluid residence time, the kinetics of water-rock interactions, and thermodynamic constants (Maher, 2011); exchange reactions (Clow and Mast, 2010); and mixing between different types of subsurface water bodies (Calmels et al., 2011) or between tributaries (Bouchez et al., 2017). During extreme hydrological events such as storms, chemical weathering fluxes are likely to be highly dependent on changes in water residence time (Benettin et al., 2017), as well as on the mobilization of “old pockets” of subsurface/deep water that has a distinct chemical composition linked to its long residence time. Even in small, relatively homogeneous catchments, sampling of rivers (e.g. weekly or monthly) provides only a snapshot of the water-rock interactions. Storm events are often undersampled although they can contribute up to 50% of the total annual water export over very short periods of time (Larsen and Simon, 1993). In areas where the hydrological cycle is greatly variable, high-frequency sampling is thus needed to fully evaluate weathering fluxes and gain better insight into weathering processes and their relation to the catchment hydrology (Wohl et al., 2012; Floury et al., 2017).

Isotopic tracers that are sensitive to chemical weathering processes can be used to help understand the controls on concentration-discharge relationships. Many studies have highlighted the potential of lithium (Li) and magnesium (Mg) isotopes to characterise the variety of weathering processes occurring in the environment (Teng et al., 2010; Pogge von Strandmann et al., 2012; Tipper et al., 2012a). These isotope systems can be used to evaluate plant uptake (Bolou-Bi et al., 2012) and the source of dissolved solutes (Kisakurek et al., 2005; Weynell et al., 2017), as well as the importance

of mineral (trans)formations (Ryu et al., 2014; Ma et al., 2015). Li and Mg isotopes are also fractionated during the formation of secondary minerals (Opfergelt et al., 2012; Henchiri et al., 2014; Trostle et al., 2014; Clergue et al., 2015; Dellinger et al., 2015; Dessert et al., 2015; Henchiri et al., 2016; Chapela Lara et al., 2017) and are thus well suited to trace water-rock interactions in weathering systems. Here, we investigate the Li and Mg isotope composition of fluids from a small catchment in Guadeloupe (Quiock Creek) during a stormy period of one month. Throughfall, soil solution, river waters and groundwater were sampled to assess the effects of hydrological changes on Li and Mg isotopes. We show that Li and Mg isotopes are fractionated by different mechanisms in this highly weathered catchment, and that the Li and Mg isotope signatures of the river waters are principally controlled, respectively, by precipitation of secondary minerals, and throughfall inputs and mineral-fluid exchange reactions.

IV.2 Site description

Quiock Creek catchment (16°17'N, 61°70'W) is located on Basse-Terre Island, the volcanic part of the Guadeloupe archipelago in the French West Indies (Figure IV-1), and covers an area of ~8 hectares. The catchment is a Critical Zone Observatory (CZO), part of the "Observatoire de l'Eau et de l'éRosion aux Antilles" (ObsERA), which is operated by INSU-CNRS (OZCAR, the French National Research Infrastructure of CZOs) and the "Institut de Physique du Globe de Paris" (IPGP), and it is devoted to the study of weathering and erosion of volcanic islands under tropical climate conditions. Quiock Creek is a small tributary of the Bras-David River, which is located in primary tropical rainforest in the Guadeloupe National Park. Rainfall variation is high in Basse-Terre and varies with the strength of the Northeast trade winds and topography (Figure IV-1). The mean annual temperature and throughfall rate (the quantity of rainfall that reaches the ground having passed through the subaerial vegetation) are, respectively, 25 °C and 3079 $mm.yr^{-1}$ and the rate of infiltration is relatively fast, ~0.1-1 $mm.s^{-1}$ (Guérin, 2015). Climate is characterised by two seasons: a dry season, from January to June, and a cyclonic wet season, from July to December. Wet seasons are associated with intense rainfall events initiated by tropical depressions and cyclones (Zahibo et al., 2007) that significantly contribute to the water budget. The rate of evapotranspiration is around

63% (Clergue et al., 2015). Mean annual discharge ranges between 9.9 m^3/h and 10.3 m^3/h (Clergue et al., 2015; Guérin, 2015), which is five times lower than the Bras-David river (~50.4 m^3/h; Lloret et al., 2011). The subsurface of Quiock Creek catchment hosts an unconfined aquifer (i.e. it is connected to the atmosphere) with a porosity of ~2% and a permeability of ~10^{-6} m/s (Guérin, 2015). During storm flow Quiock Creek discharge increases in proportion to the rainfall rate, whereas during drought flow the discharge decreases as a power law with time. This behaviour shows that the Quiock Creek aquifer acts as a non-linear filter between precipitation inputs and river discharge (Guérin, 2015), which suggests that Quiock Creek is mostly fed by groundwater. This is also supported by the fact that the creek flows throughout most of the year, even after long periods of drought (Guérin, 2015). In turn, the catchment is relatively unaffected by overland flow due to its smooth topography and the fast infiltration rate (Guérin, 2015).

Quiock Creek catchment is underlain by Pleistocene andesitic pyroclastic deposits that are usually covered by >15 meters of highly-weathered ferralitic regolith (Clergue et al., 2015). The deep regolith isolates groundwater and vegetation from the bedrock. The mineralogy, chemistry and

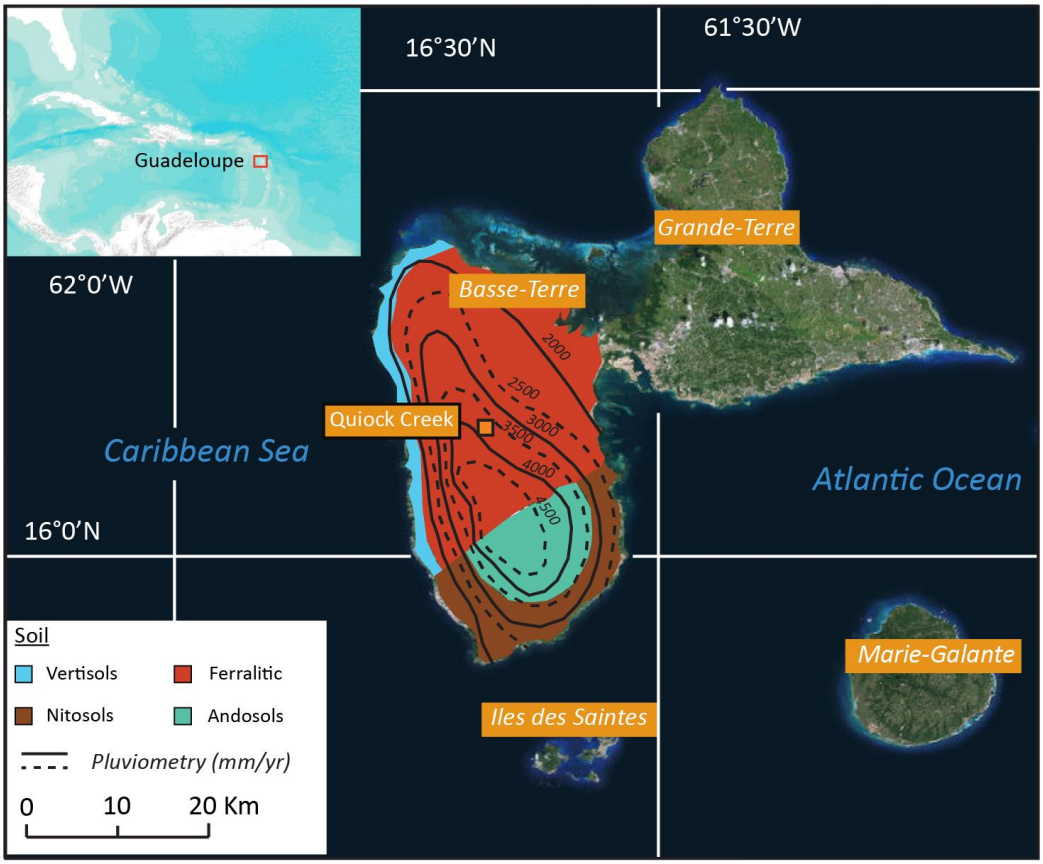

Figure IV-1. Location of Quiock Creek catchment (orange square; 16°17'N, 61°60'W) in Guadeloupe with isohyets (adapted from Lloret et al., 2010) and simplified map of Guadeloupe soils (adapted from Colmeet-Daage and Bernard, 1979).

resistivity of the regolith shows little variation with depth (Guérin, 2015). The bulk regolith is highly weathered and is composed of 95 wt.% of secondary mineral phases with clays (mostly halloysite and kaolinite) accounting for 70 wt.% of the secondary minerals; the remaining 30% mainly consists of Fe(III)-hydroxides and gibbsite (Buss et al., 2010). Primary minerals consist of quartz (0–8 wt%), feldspar (0–4 wt.%) and volcanic dust from Monserrat (~3 wt.%). The upper 30 cm of the profile is slightly enriched in quartz and feldspars (dominantly orthoclase) due to deposition of Saharan dust, the main terrestrial dust source to Guadeloupe (Buss et al., 2010; Clergue et al., 2015). The dust flux is highest between the months of June and October (Graham and Duce, 1979). The regolith is strongly depleted in soluble cations compared to the bedrock (Buss et al., 2010) and supports a dense tropical rainforest that has a mean litter flux of 7.8 t ha^{-1} yr^{-1}.

IV.3 Methodology

IV.3.1 Sample collection and elemental analyses

A total of 55 water samples comprising throughfall, soil solution, river water and groundwater were collected in Quiock Creek catchment over a period of 21 days in October 2015 (Figure IV-2). Soil solution and groundwater reservoirs were emptied after each sampling to allow the “stagnant” water to be removed and replaced by “fresh” water for the next sample collection. Soil solution reservoirs were emptied on 18/09/2015, 18 days before the first sampling date (Day 1, 06/10/2015), but the groundwater reservoirs were not emptied prior to the first sampling date. Temperature, conductivity and pH were directly measured in the field with a combined pH and conductivity probe (Hanna Instruments HI 98130). Fluid samples were filtered at 0.2 µm-porosity through a cellulose acetate filter, and collected in 250 or 500 mL acid-cleaned HDPE bottles for cation analysis and in Milli-Q water (18.2 MΩ cm^{-1} H_2O) washed 30 mL bottles for anion analysis. The cation samples were acidified to pH ≈ 2 with distilled nitric acid. Alkalinity was determined by titration with 0.01 M HCl within 24 hours of sample collection.

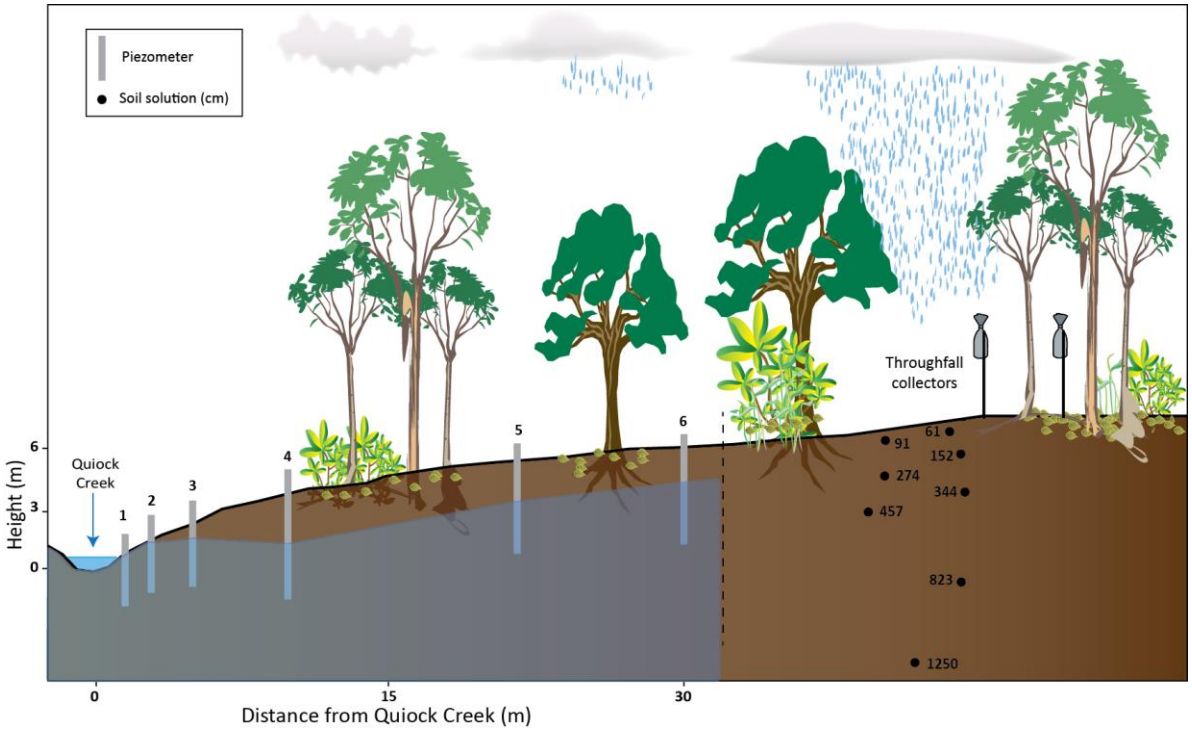

Figure IV-2. Schematic diagram showing the samples collected in Quiock Creek catchment. Depth of soil solution samples are shown as centimetres below the soil surface.

Major and minor cation (Na, Ca, Mg, K, Al, B, Fe, Sr, Li) and silicon concentrations were measured by inductively-coupled plasma-source mass spectrometry (ICP-MS; Thermo X-Series II) at the National Oceanography Centre Southampton (NOCS). Analyses were calibrated using a set of synthetic multi-element standards prepared gravimetrically from high purity single element standard solutions. The certified standard reference material SLRS-6 (river water) and IAPSO seawater were analysed multiple times (n = 8) alongside the samples to assess the accuracy of the analyses, which is ± 5% of the certified values. Anion (Cl and SO_4) concentrations were measured by ion chromatography (Dionex ICS2500) and calibrated using a set of synthetic multi-element standards prepared gravimetrically from high purity single element standard solutions. IAPSO seawater was analysed multiple times (n = 7) alongside the samples to assess the accuracy of the analyses, which is ± 5% of the certified values.

IV.3.2 Li and Mg isotope analyses

For Li isotope analysis, an aliquot of each water sample equivalent to 20 ng of Li was dried down and re-dissolved in 0.2 M HCl and loaded onto a cation exchange column filled with BioRad AG50W-X12 cation exchange resin to separate Li from the sample matrix (James and Palmer, 2000a). Lithium isotope ratios were determined by multi-collector inductively-coupled plasma-source mass

spectrometry (MC-ICP-MS; Thermo Scientific Neptune Plus) using a sample-standard bracketing technique (Flesch et al., 1973), at NOCS. The Li isotope composition of samples is expressed as δ^7Li (‰), which is given by:

$$\delta\ ^7Li = \left[\frac{\left(\frac{^7Li}{^6Li}\right)_{sample}}{\left(\frac{^7Li}{^6Li}\right)_{L-SVEC}} - 1\right] \times 10^3 \qquad \textit{Eq. 10}$$

where L-SVEC is the Li isotope standard reference material (Flesch, 1973). The external reproducibility of the Li isotope analyses was assessed by repeated measurement of IAPSO seawater (δ^7Li = 30.9±0.6‰; (2σ, n=27)), L-SVEC (δ^7Li = 0.0 ± 0.5‰ (2σ, n = 28)), and SLRS-6 river water (δ^7Li = 23.6 ± 0.7‰ (2σ, n = 3)).

For Mg isotope analysis, an aliquot of each water sample equivalent to 10 µg of Mg was dried down and re-dissolved in 0.8 M HNO_3 and loaded onto a cation exchange column filled with BioRad AG50W-X12 cation exchange resin to separate Mg from the sample matrix (Tipper et al., 2006b; Pogge von Strandmann, 2008). Magnesium isotope ratios were determined by MC-ICP-MS (Thermo Scientific Neptune Plus) using a sample-standard bracketing technique. The Mg isotope composition of samples is expressed as δ^xMg (where x is ^{25}Mg or ^{26}Mg), which is given by:

$$\delta\ ^xMg = \left[\frac{\left(\frac{^xMg}{^{24}Mg}\right)_{sample}}{\left(\frac{^xMg}{^{24}Mg}\right)_{DSM-3}} - 1\right] \times 10^3 \qquad \textit{Eq. 11}$$

where DSM-3 is the Mg isotope standard (Galy et al., 2001). The external reproducibility of the measurements was determined by repeated analysis of IAPSO seawater (δ^{26}Mg = -0.82 ± 0.05‰ (2σ, n = 18)), DSM-3 (δ^{26}Mg = 0.00 ± 0.07‰ (2σ, n = 27)), and SLRS-6 river water (δ^{26}Mg = -1.22 ± 0.03‰ (2σ, n = 5)).

IV.3.3 Hydrological measurements

Precipitation, discharge and water table data for the 21-day sampling period are shown in Figure IV-3. Additional data, for the period between 18/09/2015 (when the soil solution reservoirs were first emptied) and 06/10/2015 are given in the Appendix B 1. Rainfall was measured using a tipping-bucket rain gauge. Discharge was measured using a Venturi Flume (19 x 26.6 x 250 cm) together

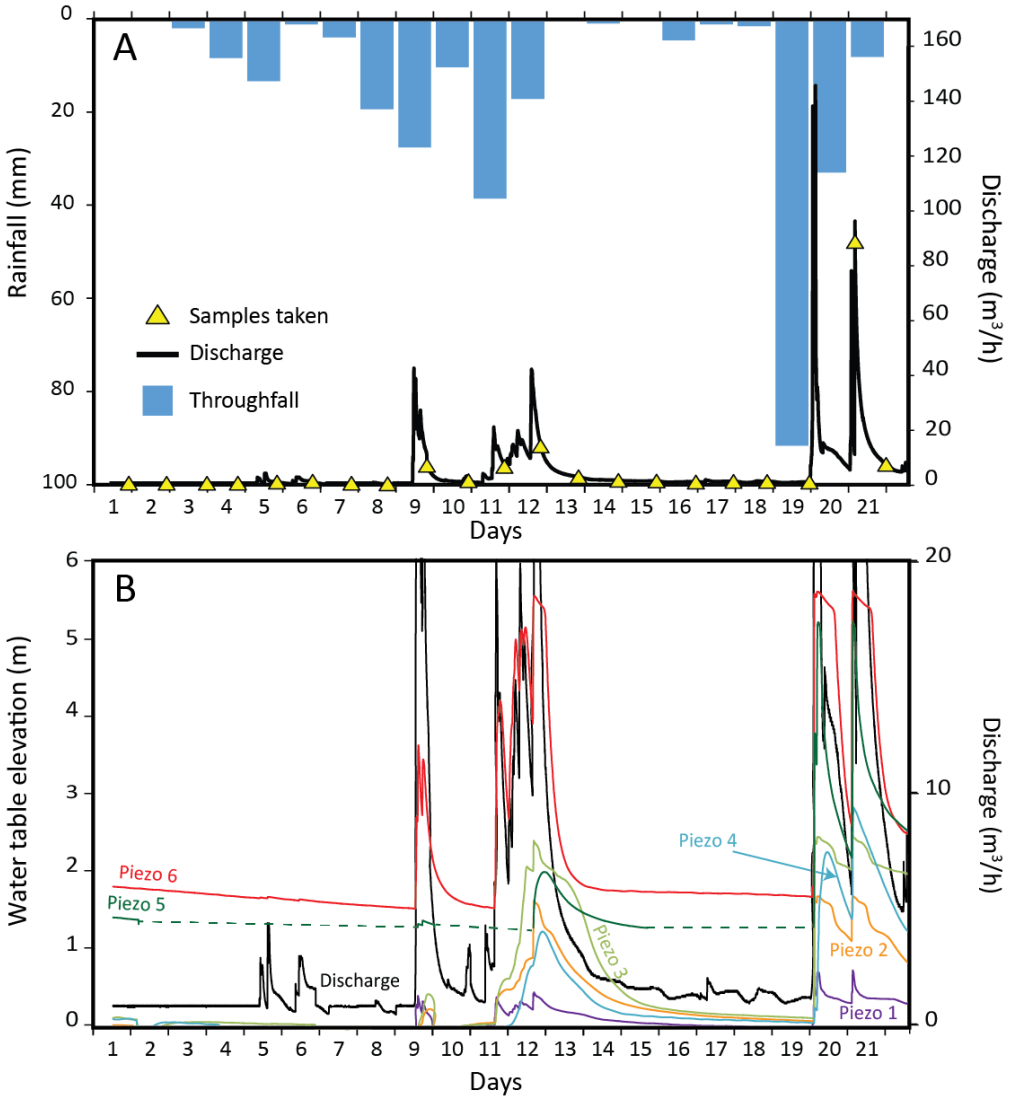

Figure IV-3. A. Precipitation and discharge of Quiock Creek. B. Water table elevation and discharge during the period of study. Data are from the ObsERA website (http://webobsera.ipgp.fr/).

with a pressure sensor (CS451, Campbell Scientic) that measured the water height (or stage) to a precision of ±0.7 mm (Guérin, 2015). Water table elevation is reported relative to the river elevation so a value of zero means that the water table is below the river elevation, but water is present. The water table elevation was determined with a pressure sensor connected to a data logger (Campbell Scientic, CR800) placed approximatively 15 cm above the bottom of the piezometer.

IV.4 Results

Sample terminology is described in Table IV-1**Error! Reference source not found.**.Temperature, pH, conductivity and alkalinity data are summarized in Table IV-2. Major and minor element and Total Dissolved Solids (TDS) concentrations are displayed in Table IV-3. Li and Mg isotope measurements are summarized in Table IV-4.

Table IV-1. Sample terminology

Sample	Description	X	Y
L X.Y	Lysimeter/Soil solution	Depth (61 to 1250 cm)	Collection day (1 or 18)
Th X	Throughfall	Location	-
Piezo X.Y	Piezometer/Groundwater	Location (1 to 6)	Collection day (1, 4, 8 or 9)
QC Y	Quiock Creek/River water	-	Collection day (1 to 21)

IV.4.1 Hydrological data in-situ measurements, alkalinity and TDS

Levels of discharge and precipitation in the catchment during the sampling campaign are shown in Figure IV-3. The year 2015 was drier than usual, with a mean throughfall input of ~2509 mm in 2015 compared to an average of 3079 mm/yr between 2011 and 2013 (Clergue et al., 2015). Similarly, the mean discharge in 2015 was ~5.2m^3/h compared to ~10 m^3/h between 2011 and 2013. During the one-month period of this study, 283.6 mm of rain entered the catchment, corresponding to 12.5% of the total annual rain input in 2015. A series of large rain events occurred starting on days 4, 8, 11 and 19 of the sampling period (Figure IV-3). Three of these rain events noticeably increased the discharge in Quiock Creek (days 9, 11 and 19), and they also increased the elevation of the water table (Figure IV-3 A and B). Highest rainfall (92 mm) occurred on day 19, generating a peak discharge of 145 m^3/h. Because of previously dry conditions, the rainfall event on day 4 only triggered a small response in river discharge and water table (Figure IV-3 A and B).

The temperature of the river water samples ranged from 23.7 to 25.5°C, conductivity ranged from 35 to 56 µS/cm, pH ranged from 4.9 to 5.6, TDS concentrations ranged from 18 to 24 ppm and alkalinity was <10 µeq/L. All of these parameters showed a slight tendency to decrease with increasing discharge. Groundwater samples by comparison had generally higher pH (4.8 to 6.5), higher conductivity (48 to 109 µS/cm) and a wider range of alkalinity (5 to 1108 µeq/L) and TDS (21 to 97 ppm) values. The temperature of the groundwater samples (24.1 to 25.9°C) was close to that of the river water samples. The soil solutions were characterised by generally lower pH (4.5 to 5.5), TDS (15 to 25 ppm) and alkalinity (5 to 22 µeq/L) compared to the groundwater samples. The pH and conductivity of the throughfall samples were close to those of the soil solutions (respectively, 5.9 and 42 µS/cm), but the throughfall samples had higher alkalinity and lower TDS.

IV.4.2 Composition of the dissolved load

The accuracy of the analyses for major ions can be estimated from the electrical balance (E.B., Eq. 12), where cations and anions are expressed as meq/L:

$$\text{Electrical Balance (E.B., \%)} = \frac{\text{Sum cations} - \text{Sum anions}}{\text{Sum cations} + \text{Sum anions}} \times 100 \qquad \textit{Eq. 12}$$

The electrical balance was within ±10% and for most samples it was within ±5% (Figure IV-4). This indicates that there is no significant contribution to the geochemical composition of the waters from any species not reported in Table IV-3 (Appelo and Postma, 2004). Additionally, TDS extrapolated from conductivity measurements made in the field were well correlated to TDS measurements made in the laboratory indicating that the chemical composition of the samples was preserved between collection and analysis (Figure IV-4).

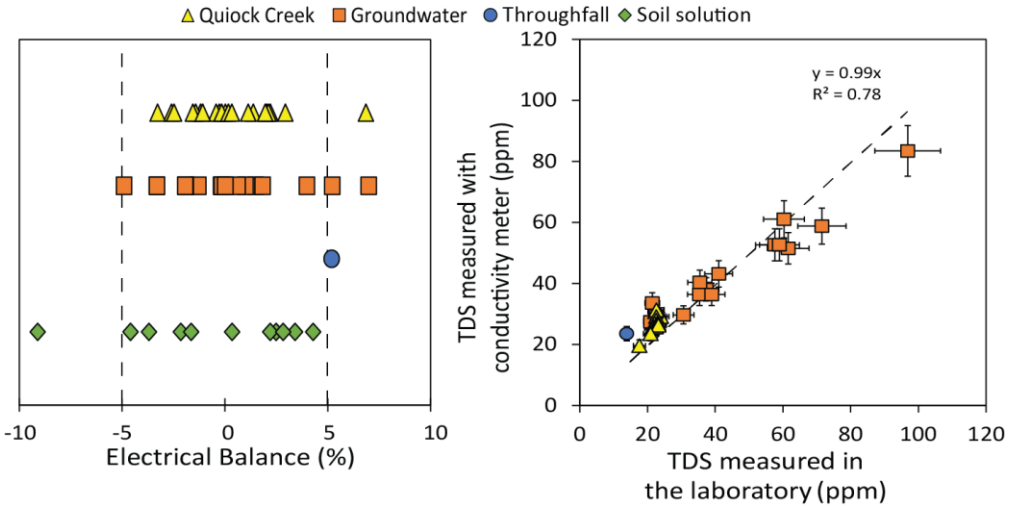

Figure IV-4. Electrical balance and TDS measured with conductivity meter vs TDS measured in the laboratory (± 10%) for Quiock Creek samples.

The major ion data of the catchment waters are plotted in a Piper diagram (Piper, 1953) in Figure IV-5. The two throughfall samples were chloride and sodium rich, showing a strong seawater influence, but they had higher Ca and K concentrations (18 - 21 µmol/kg for Ca and 31 - 67 µmol/kg for K) compared to rain water (3 - 8 µmol/L for Ca and 3 - 5 µmol/L for K; Dessert et al., 2015). Soil solutions were also chloride and sodium rich and their alkalinity (up to 22 µeq/L) and Mg content (11 - 43 µmol/kg) were variable. Quiock Creek samples contained higher proportions of Na and Cl compared to throughfall samples, and their chemical composition was very constant throughout the sampling campaign. Groundwater samples contained proportionally higher calcium and

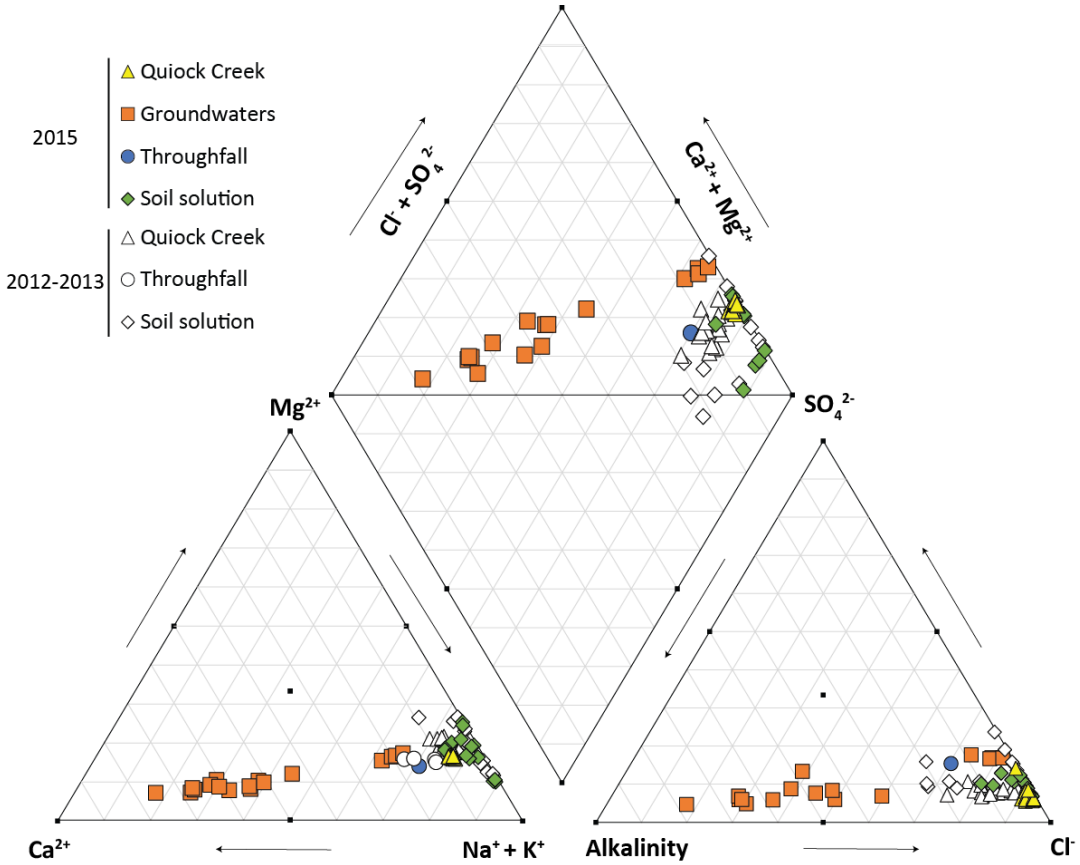

Figure IV-5. Piper diagram showing the relative abundance of anions and cations in samples from Quiock Creek catchment. Data for water samples collected in 2012-2013 (white symbols) are from Clergue et al. (2015).

alkalinity than the other water samples and tend to become more enriched in chloride and sodium with decreasing distance from the river. The compositions of all of the samples were similar to those measured in 2012-2013 (Clergue et al., 2015) with the exception of the alkalinities of the soil solutions and Quiock Creek samples, which had higher alkalinity in 2012-2013 (11 - 66 µeq/L).

Concentrations of TDS, Si, Li and Mg in Quiock Creek are plotted versus discharge in Figure IV-6. Most of these variables showed a linear, slightly inverse relationship with discharge (Q), in a log-log plot indicating that there is a power-law relationship (e.g. for Si, $[Si] = aQ^b$, where a and b are constants and b is the power-law exponent) between concentration and discharge (Godsey et al., 2009). A slope of 0 would indicate that concentrations remain constant despite changes in discharge (so-called "chemostatic behaviour"; Godsey et al., 2009), whereas a slope of -1 indicates that solute concentration become more dilute as discharge increases (concentration scales as 1/Q).

Table IV-2. Field measurements and alkalinity data for Quiock Creek catchment samples. n.d = not determined, b.d = below detection limit. Discharge data are from the ObsERA website (http://webobsera.ipgp.fr/).

Sample	Day	Date	Distance to river (m)	Temperature (°C)	pH	Conductivity (µS/cm)	Alkalinity (µeq/L)
Soil solution							
L91.18	18	23/10/2015	-	n.d	4.9	n.d	b.d
L152.1	1	06/10/2015	-	n.d	5.2	n.d	18
L152.18	18	23/10/2015	-	n.d	5.2	n.d	5
L274.1	1	06/10/2015	-	n.d	4.9	n.d	b.d
L274.18	18	23/10/2015	-	n.d	4.7	n.d	b.d
L344.1	1	06/10/2015	-	n.d	4.8	n.d	b.d
L344.18	18	23/10/2015	-	n.d	4.5	n.d	b.d
L457.1	1	06/10/2015	-	n.d	5.5	n.d	22
L457.18	18	23/10/2015	-	n.d	5.2	n.d	9
L823.1	1	06/10/2015	-	n.d	5.1	n.d	8
L823.18	18	23/10/2015	-	n.d	4.8	n.d	b.d
Throughfall							
Th1	11	16/10/2015	-	25.4	5.9	42	67
Th3	11	16/10/2015	-	25.4	5.9	42	28
Groundwaters							
Piezo 1.1	1	06/10/2015	1.0	24.9	6.1	92	597
Piezo 1.4	4	09/10/2015	1.0	24.8	6.5	77	297
Piezo 1.8	8	13/10/2015	1.0	24.5	6.0	68	254
Piezo 2.1	1	06/10/2015	2.4	25.3	5.6	49	28
Piezo 2.4	4	09/10/2015	2.4	25.9	5.3	60	13
Piezo 2.8	8	13/10/2015	2.4	24.6	4.9	48	15
Piezo 2.9	9	14/10/2015	2.4	24.6	4.8	49	5
Piezo 3.1	1	06/10/2015	4.5	24.5	6.3	105	691
Piezo 3.8	8	13/10/2015	4.5	24.5	6.4	109	529
Piezo 3.9	9	14/10/2015	4.5	24.7	5.8	72	187
Piezo 4.1	1	06/10/2015	9.4	24.2	6.4	149	1108
Piezo 4.8	8	13/10/2015	9.4	24.1	6.0	94	566
Piezo 4.9	9	14/10/2015	9.4	24.4	5.6	65	238
Piezo 5.1	1	06/10/2015	21.2	24.4	6.3	94	579
Piezo 6.1	1	06/10/2015	29.8	24.2	5.7	65	315
Piezo 6.8	8	13/10/2015	29.8	n.d	n.d	n.d	n.d
Piezo 6.9	9	14/10/2015	29.8	24.7	5.6	53	214
Sample	**Day**	**Date**	**Discharge (m^3/h)**	**Temperature (°C)**	**pH**	**Conductivity (µS/cm)**	**Alkalinity (µeq/L)**
Quiock Creek							
QC1	1	06/10/2015	0.8	25.5	5.5	53	b.d
QC2	2	07/10/2015	0.8	25.3	5.5	48	1
QC3	3	08/10/2015	0.8	25.5	5.6	52	8
QC4	4	09/10/2015	0.8	25	5.5	52	7
QC5	5	10/10/2015	1.2	25	5.6	49	5
QC6	6	11/10/2015	1.5	24.7	5.3	55	b.d
QC7	7	12/10/2015	0.8	24.9	5.3	56	b.d
QC8	8	13/10/2015	0.5	24.4	5.3	52	10
QC9	9	14/10/2015	7.3	24.7	5.1	48	6
QC10	10	15/10/2015	1.7	24.8	5.2	50	3
QC11	11	16/10/2015	6.9	24.5	5.1	48	5
QC12	12	17/10/2015	14.3	24.2	5.1	45	1
QC13	13	18/10/2015	3.1	23.7	5.2	46	2
QC14	14	19/10/2015	1.8	23.8	5.2	46	b.d
QC15	15	20/10/2015	1.6	23.9	5.2	47	5
QC16	16	21/10/2015	1.2	24.7	5.3	48	7
QC17	17	22/10/2015	1.5	25	5.5	48	1
QC18	18	23/10/2015	1.4	24.1	5.1	48	b.d
QC19	19	24/10/2015	1.2	24.2	5.2	47	0.1
QC20	20	25/10/2015	88.8	24.3	4.9	35	b.d
QC21	21	26/10/2015	7.7	24.5	4.9	42	0.4

Table IV-3. Concentrations of major and minor elements in soil solution, groundwater, throughfall and Quiock Creek itself.
n.d = not determined, b.d = below detection limit. TDS = Total Dissolved Solids, calculated as the sum of cation, anion and Si concentrations in ppm*

Sample	µmol/kg										nmol/kg		TDS*
	Cl^-	SO_4^{2-}	Na^+	Ca^{2+}	Si	Mg^{2+}	K^+	Al	B	Fe	Sr	Li	
Soil solution													
L61.1	n.d	n.d	142	7.5	86	18.0	3.0	5.3	2.4	b.d	53	47	-
L61.18	n.d	n.d	207	11.3	67	25.6	4.5	6.7	3.6	b.d	76	54	-
L91.1	n.d	n.d	185	4.5	92	18.3	3.1	3.3	1.5	b.d	19	69	-
L91.18	264	9.3	230	6.1	68	24.2	4.1	3.9	2.1	b.d	21	57	19
L152.1	206	11.7	145	5.4	45	19.4	2.1	3.2	0.8	b.d	14	29	15
L152.18	207	12.3	179	3.7	52	24.4	1.9	4.6	1.0	b.d	13	34	15
L274.1	244	12.5	168	1.2	65	20.4	2.9	9.3	2.4	b.d	15	68	16
L274.18	253	14.4	204	2.4	78	24.5	3.6	9.4	2.8	b.d	21	84	18
L344.1	388	15.0	247	1.0	75	42.8	7.1	12.7	2.3	b.d	16	71	25
L344.18	360	17.1	255	1.6	87	42.6	7.8	11.4	2.4	b.d	18	81	24
L457.1	184	11.4	178	1.2	102	9.9	3.5	5.5	0.8	b.d	10	79	16
L457.18	195	14.8	202	1.8	106	11.5	3.8	5.3	1.0	b.d	13	88	17
L823.1	264	16.6	231	1.5	113	14.0	14.2	6.5	0.9	b.d	14	80	21
L823.18	271	18.5	253	1.6	106	15.4	15.3	6.6	1.0	b.d	14	77	21
L1250	n.d	n.d	220	2.8	153	24.8	34.9	1.8	0.9	b.d	12	95	-
Throughfall													
Th1	n.d	7.1	123	20.9	18	18.4	66.7	2.9	3.0	0.6	64	14	-
Th3	144	15.4	121	18.2	26	13.6	30.6	2.5	3.0	0.5	55	14	14
Groundwater													
Piezo 1.1	259	25.9	222	302	58	30.6	3.2	2.5	1.5	3.7	232	50	62
Piezo 1.4	278	23.0	197	178	60	22.3	2.4	0.6	1.4	1.7	160	47	41
Piezo 1.8	285	16.4	198	145	68	20.8	2.5	0.9	1.4	0.2	151	55	37
Piezo 2.1	255	29.8	209	40	69	26.2	6.8	10.8	2.1	5.9	88	47	23
Piezo 2.4	260	27.3	198	32	68	25.8	5.9	3.9	1.9	3.2	119	56	21
Piezo 2.8	261	27.1	196	30	69	25.7	5.6	3.5	1.9	6.5	95	50	22
Piezo 2.9	259	26.3	201	27	64	26.8	5.5	9.7	2.0	5.3	100	54	21
Piezo 3.1	295	35.1	305	322	41	54.2	5.3	7.5	1.3	4.5	187	31	71
Piezo 3.8	328	25.6	254	284	41	40.3	3.9	3.0	1.3	2.4	179	29	60
Piezo 3.9	335	18.6	233	116	44	31.2	4.2	8.3	1.5	0.6	121	37	35
Piezo 4.1	248	31.5	252	534	40	48.2	1.5	1.1	2.3	0.2	99	36	97
Piezo 4.8	269	20.0	208	270	48	31.1	1.5	2.2	1.8	1.1	77	45	58
Piezo 4.9	261	22.0	194	132	48	25.4	1.0	2.1	1.4	4.2	51	44	35
Piezo 5.1	259	25.4	209	279	43	33.7	0.5	4.2	1.3	3.5	127	92	59
Piezo 6.1	231	25.3	197	148	43	23.0	4.1	1.8	1.7	2.2	90	37	39
Piezo 6.8	n.d	n.d	190	193	47	26.7	3.8	n.d	1.9	n.d	133	35	
Piezo 6.9	174	29.3	170	112	48	20.9	4.2	11.9	2.4	2.8	85	32	31
Quiock Creek													
QC1	334	10.0	257	12.8	89	27.0	9.0	2.1	1.6	0.3	57	55	23
QC2	333	9.8	258	13.1	90	27.5	6.2	2.0	1.6	0.2	67	55	23
QC3	336	9.6	260	13.1	91	27.8	6.5	2.1	1.5	0.3	64	56	23
QC4	350	11.0	261	14.0	88	28.4	6.7	2.5	1.7	0.3	79	56	24
QC5	326	13.5	247	13.3	83	27.5	9.3	3.4	1.8	0.4	68	56	23
QC6	332	12.5	241	12.7	80	26.7	8.3	3.4	1.8	0.4	64	52	22
QC7	335	11.0	246	13.0	86	27.1	7.5	4.0	1.7	0.4	65	53	23
QC8	327	10.5	240	13.0	83	26.6	7.5	3.0	1.7	0.4	64	53	23
QC9	328	11.3	255	11.5	82	26.4	7.0	3.3	1.7	0.4	60	59	23
QC10	317	13.8	255	13.6	81	27.8	8.1	4.9	1.9	0.7	78	60	23
QC11	319	10.7	250	11.8	79	26.7	6.1	3.8	1.7	0.6	60	57	22
QC12	307	11.8	249	12.1	69	27.9	4.9	3.8	1.8	0.6	66	58	21
QC13	321	9.3	251	12.1	77	27.6	4.8	1.8	1.6	0.2	62	55	22
QC14	325	9.9	261	13.1	87	28.9	5.4	1.8	1.6	0.2	75	62	22
QC15	326	9.9	257	12.4	90	28.4	5.2	2.6	1.5	0.2	63	56	23
QC16	326	10.1	262	12.8	92	28.4	5.4	1.8	1.5	0.2	66	58	23
QC17	328	10.1	263	13.3	91	28.3	6.3	2.3	1.6	0.2	78	61	23
QC18	330	11.0	271	12.6	92	28.8	6.5	2.6	1.6	0.4	58	54	23
QC19	330	10.4	269	12.8	98	29.3	5.8	2.2	1.5	0.3	65	58	23
QC20	226	18.3	201	10.9	61	22.0	4.8	8.0	2.0	1.5	56	41	18
QC21	297	13.2	245	11.3	73	26.6	4.3	2.1	1.7	0.3	61	51	21

Table IV-4. Li and Mg isotope compositions in soil solution, groundwater, throughfall and Quiock Creek itself.
n.d = not determined. 2σ is the internal uncertainty of the sample

Sample	δ^{7}Li (‰)	2σ	δ^{25}Mg (‰)	2σ	δ^{26}Mg (‰)	2σ
Soil solution						
L61.1	6.1	0.5	-0.53	0.01	-0.95	0.00
L61.18	9.0	0.5	-0.54	0.03	-1.04	0.05
L91.1	2.7	0.2	-0.50	0.03	-0.94	0.05
L91.18	6.4	0.3	-0.48	0.01	-0.91	0.03
L152.1	7.7	0.5	-0.42	0.02	-0.78	0.04
L152.18	9.5	0.1	-0.48	0.04	-0.88	0.00
L274.1	9.1	0.1	-0.46	0.05	-0.82	0.04
L274.18	8.6	0.1	-0.41	0.03	-0.79	0.05
L344.1	10.4	0.5	-0.41	0.07	-0.77	0.06
L344.18	9.8	0.3	-0.37	0.01	-0.72	0.02
L457.1	7.0	0.1	-0.32	0.01	-0.63	0.01
L457.18	6.4	0.6	-0.36	0.03	-0.70	0.06
L823.1	4.5	0.1	-0.30	0.00	-0.58	0.02
L823.18	5.3	0.2	-0.32	0.03	-0.63	0.07
L1250	1.8	0.0	-0.33	0.01	-0.65	0.03
Throughfall						
Th1	13.6	0.2	-0.50	0.01	-0.97	0.02
Th3	13.0	0.0	-0.45	0.00	-0.84	0.04
Groundwater						
Piezo 1.1	11.3	0.1	-0.52	0.04	-0.96	0.06
Piezo 1.4	10.9	0.4	n.d	n.d	n.d	n.d
Piezo 1.8	9.7	0.2	-0.43	0.08	-0.81	0.04
Piezo 2.1	9.2	0.7	-0.48	0.02	-0.91	0.04
Piezo 2.4	10.7	0.1	n.d	n.d	n.d	n.d
Piezo 2.8	9.5	0.2	n.d	n.d	n.d	n.d
Piezo 2.9	8.0	0.1	-0.43	0.05	-0.84	0.06
Piezo 3.1	15.6	0.4	-0.49	0.01	-0.94	0.02
Piezo 3.8	16.8	0.0	n.d	n.d	n.d	n.d
Piezo 3.9	12.6	1.3	-0.45	0.00	-0.89	0.07
Piezo 4.1	16.5	0.5	-0.78	0.02	-1.48	0.01
Piezo 4.8	15.1	0.3	n.d	n.d	n.d	n.d
Piezo 4.9	12.6	0.3	-0.56	0.02	-1.07	0.01
Piezo 5.1	16.4	0.2	-0.73	0.09	-1.33	0.10
Piezo 6.1	16.4	0.3	-0.51	0.03	-0.99	0.05
Piezo 6.8	16.6	0.2	n.d	n.d	n.d	n.d
Piezo 6.9	16.6	0.3	-0.48	0.05	-0.95	0.04
Quiock Creek						
QC1	8.6	0.3	-0.38	0.01	-0.72	0.02
QC2	9.8	0.4	-0.38	0.02	-0.73	0.05
QC3	9.2	0.1	-0.38	0.01	-0.73	0.01
QC4	8.7	0.2	n.d	n.d	n.d	n.d
QC5	9.1	0.6	n.d	n.d	n.d	n.d
QC6	9.8	0.1	-0.44	0.03	-0.85	0.06
QC7	9.7	0.4	n.d	n.d	n.d	n.d
QC8	9.9	0.1	-0.41	0.01	-0.77	0.02
QC9	9.2	0.1	-0.41	0.06	-0.80	0.05
QC10	10.0	0.2	-0.38	0.00	-0.74	0.03
QC11	9.5	0.1	n.d	n.d	n.d	n.d
QC12	9.1	0.1	-0.45	0.01	-0.87	0.01
QC13	8.8	0.3	-0.43	0.01	-0.84	0.01
QC14	9.2	0.3	n.d	n.d	n.d	n.d
QC15	9.5	0.1	n.d	n.d	n.d	n.d
QC16	9.0	0.2	-0.43	0.03	-0.84	0.03
QC17	8.8	0.0	n.d	n.d	n.d	n.d
QC18	8.7	0.1	n.d	n.d	n.d	n.d
QC19	9.3	0.0	n.d	n.d	n.d	n.d
QC20	7.7	0.2	-0.40	0.01	-0.76	0.03
QC21	7.2	0.6	-0.40	0.06	-0.77	0.06

All concentration-discharge plots had a slope of slightly less than zero (between -0.09 and -0.03) suggesting that Quiock Creek behaves almost chemostatically for most of the major elements. However, Li and Mg had a weaker relationship with discharge (R^2=0.23 and 0.47, respectively; Figure IV-6), and showed chemostatic behaviour only at low discharge.

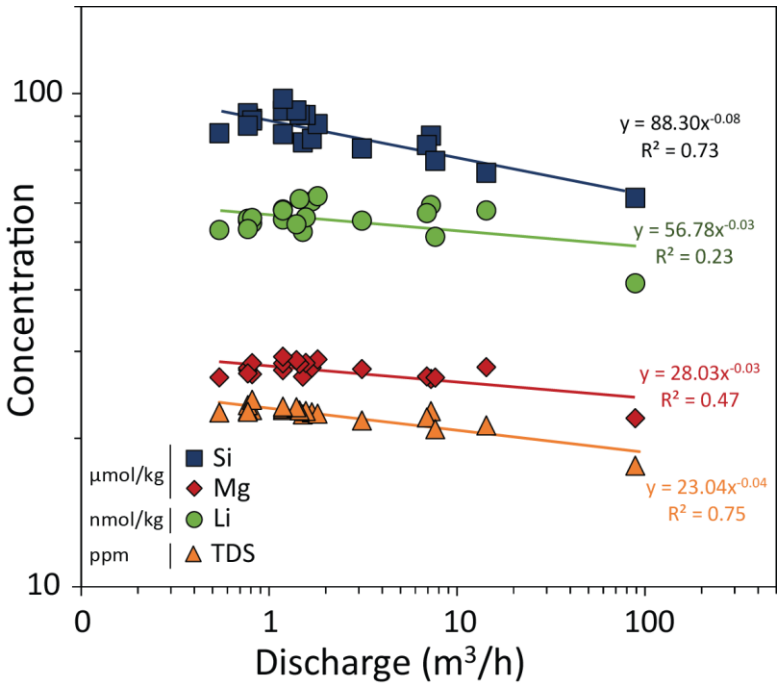

Figure IV-6. Si, Total Dissolved Solid (TDS), Mg and Li concentration in Quiock Creek as a function of discharge.

IV.4.3 Li and Mg, and their isotopes

IV.4.3.1 [Li] and δ^7Li

The Li concentration and isotope composition of the water samples are plotted together in Figure IV-7A. Different critical zone reservoirs had very different dissolved Li concentrations ([Li]) and δ^7Li values, and the overall range was, respectively, between 14 to 95 nmol/kg and 1.8 to 16.8‰. Throughfall contained relatively low [Li], averaging ~14 nmol/kg, and had δ^7Li values of ~13.3‰. By contrast, the soil solutions (taken on Day 1 and Day 18, before and after rain events) generally had the highest Li concentrations of all of the reservoirs (29 to 95 nmol/kg), and lowest δ^7Li values (1.8 to 10.4‰) (Figure IV-7A and Figure IV-8). Soil solution data were consistent with other measurements of soil solutions in Quiock Creek catchment ([Li] = 41-121 nmol/kg and δ^7Li = 4.6 to 8.9‰; Clergue et al., 2015). [Li] and δ^7Li were variable in the upper 300 cm of the soil profile, whereas [Li] increased with depth and δ^7Li decreased with depth in the deeper part of the profile

(>300 cm). There was little difference in either the Li concentration or the δ^7Li value of soil solutions sampled before and after the rain events.

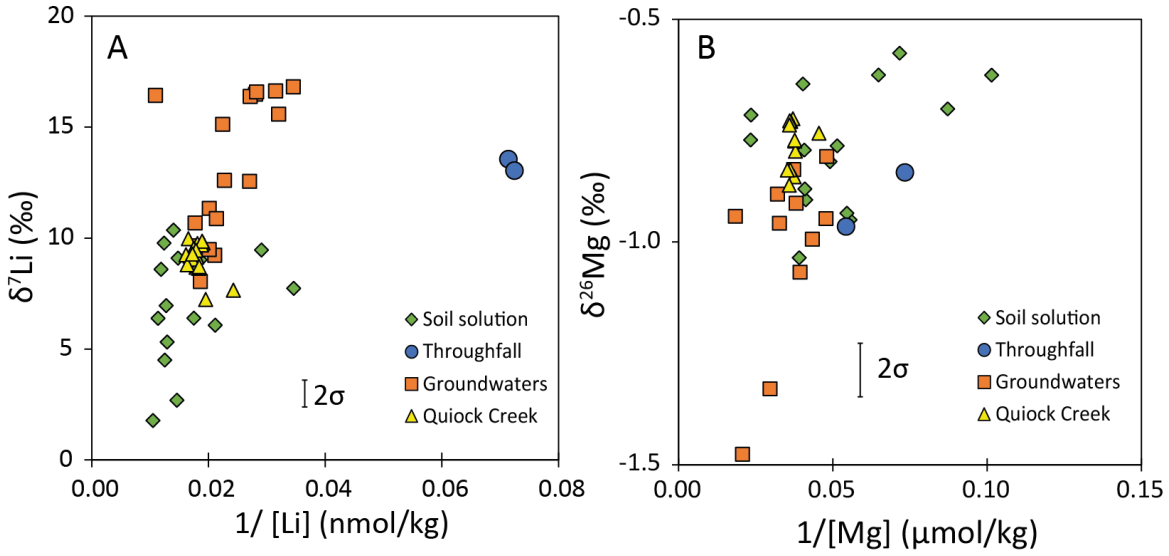

Figure IV-7. A. [Li] and δ^7Li values of the dissolved load in Quiock Creek catchment. B. [Mg] and δ^{26}Mg values of the dissolved load in Quiock Creek catchment The error bars represent the external error (2σ); the external error on the Li and Mg concentration are smaller than the symbols.

Groundwaters generally have highest δ^7Li values (up to 21‰), but generally lower [Li] than the soil solutions (29 to 92 nmol/kg; Figure IV-7A and Figure IV-9A). Significantly higher Li concentrations (~288 to 3026 nmol/L) were found in shallow and deep groundwater in the Colombia River Basalts (Liu et al., 2015). Lithium concentrations increased towards the river whereas δ^7Li values decreased from ~16‰ 30 m away from the river channel to ~9‰ close to the river (Figure IV-9B). The groundwater sample from Piezo 5 had much higher [Li] than the rest of the samples (92 nmol/kg compared to ~35 nmol/kg at the adjacent sampling site, Piezo 6), but its δ^7Li value was similar to samples recovered from Piezo 6. While the Li concentrations in samples collected on different days were similar in all the piezometers, their δ^7Li values varied by up to 4‰ (e.g. Piezo 3 and 4). By contrast, all of the groundwater samples from Piezo 6 had very consistent Li concentrations (35 ± 5 nmol/kg; n = 3) and δ^7Li values (16.5 ± 0.3‰; n = 3).

The Li content of the river waters (~55 nmol/kg) was generally lower than the soil solutions, and was also relatively low compared to the world's major rivers ([Li] = ~215 nmol/L; Huh et al., 1998) but comparable to other rivers draining basaltic tropical catchments (Henchiri et al., 2014). δ^7Li values (7.2 to 10‰) were similar to those measured in a previous sampling campaign in Quiock

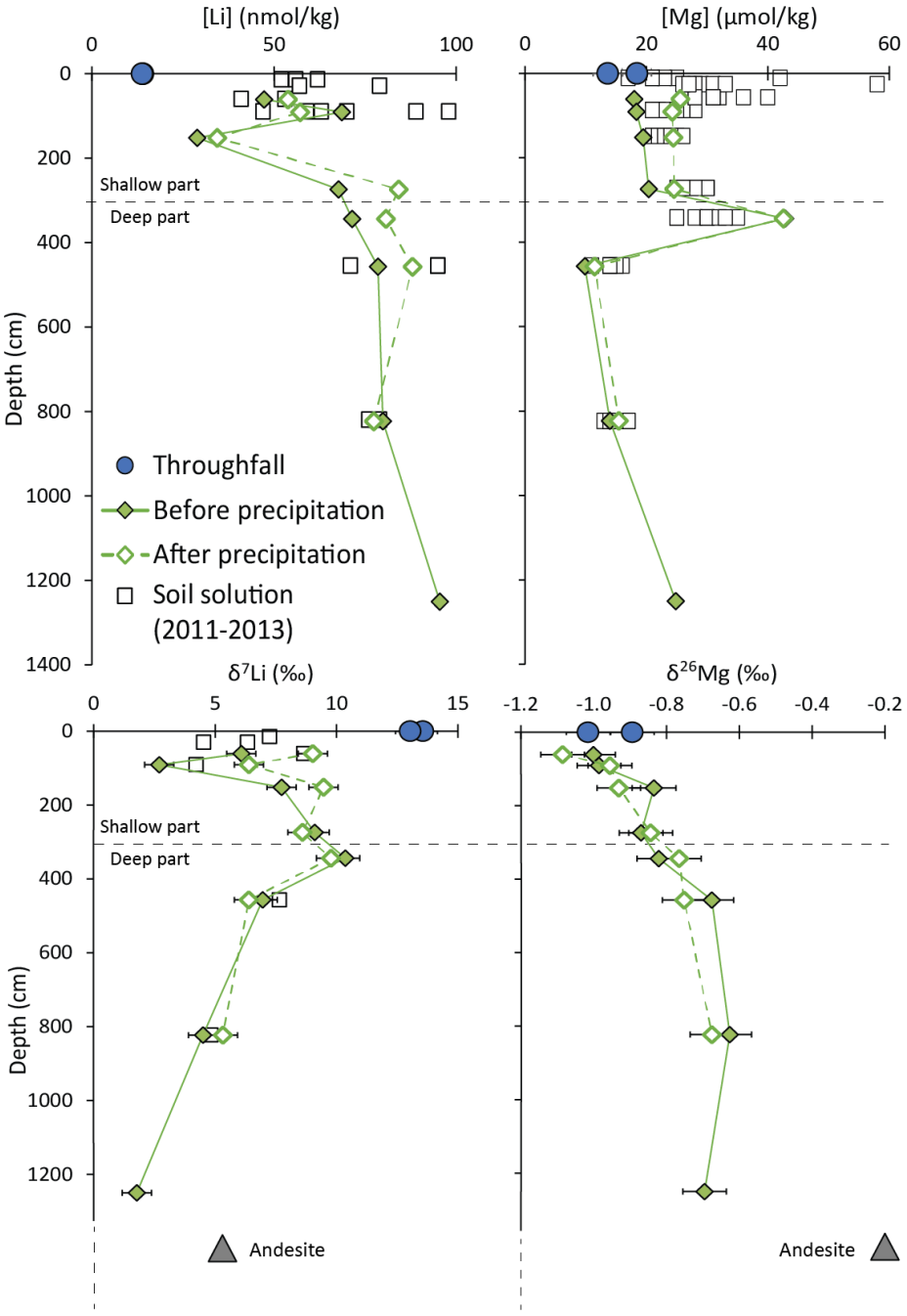

Figure IV-8. Li and Mg concentrations and isotope compositions of soil solutions taken before (Day 1) and after (Day 18) several rain events. Data for soil solution (collected in 2011-2013) are from Clergue et al. (2015), δ^{7}Li and δ^{26}Mg values for andesite are from Clergue et al. (2015) and Dessert et al. (2015). Error bars show the external error (0.6‰, 2σ).

Creek (δ^{7}Li = 8 to 9.3‰ (n = 4), (Clergue et al., 2015)) and other highly-weathered catchments (1-16‰; Dellinger et al., 2015 and references therein) and volcanic islands (e. g. Martinique δ^{7}Li = 4.9 to 20.6‰; Rad et al., 2013). However, Martinique rivers can be strongly affected by hydrothermal inputs (that have δ^{7}Li = ~1.6‰; Rad et al., 2013), whereas Quiock Creek is not affected by hydrothermal inputs (Clergue et al., 2015). Li concentrations tended to slightly decrease with increasing discharge (Figure IV-6) but there was no relationship between discharge and δ^{7}Li values

(Figure IV-10A). However, two samples (QC20 and QC21) measured during and a day after a storm event had relatively low [Li] and δ^7Li ([Li] = ~40 nmol/kg and δ^7Li = ~7.4‰).

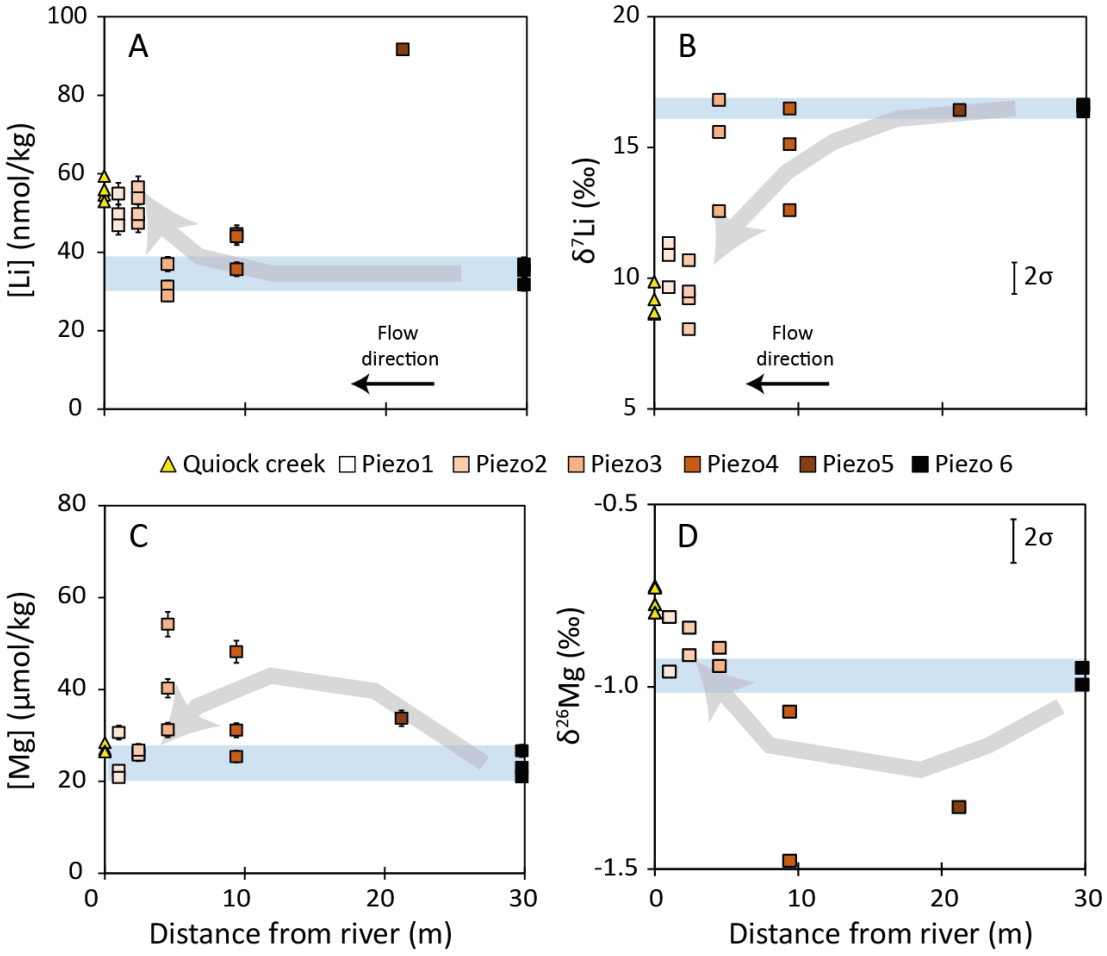

Figure IV-9. Evolution of groundwater [Li] and [Mg] (± 5%), δ^7Li and δ^{26}Mg versus distance to the river. Along this specific profile, groundwater from the Quiock Creek aquifer feeds Quiock Creek (Guérin, 2015). The blue shaded boxes highlight Piezo 6 samples likely represent river baseflow (see section IV.4.3.1). The grey shaded arrows show the general trend of the data points. Error bars show the external reproducibility of the isotope analyses (2σ).

IV.4.3.2 [Mg] and δ^{26}Mg

The Mg concentration and Mg isotope composition of the catchment samples are plotted together in Figure IV-7B. The Mg concentrations of the two throughfall samples were similar (18 µmol/kg and 14 µmol/kg) but their corresponding δ^{26}Mg values were slightly different (-0.97 and -0.84‰; Figure IV-7B) but close to the value for seawater (-0.82‰; Foster et al., 2010; Ryu et al., 2016). The δ^{26}Mg values of the throughfall samples are similar to values measured in rainwater in Guadeloupe (-0.87 ± 0.05‰ and -0.86 ± 0.11‰; Dessert et al., 2015), and in openfall precipitation in Puerto Rico (-1.10 to -0.92‰; Chapela Lara et al., 2017).

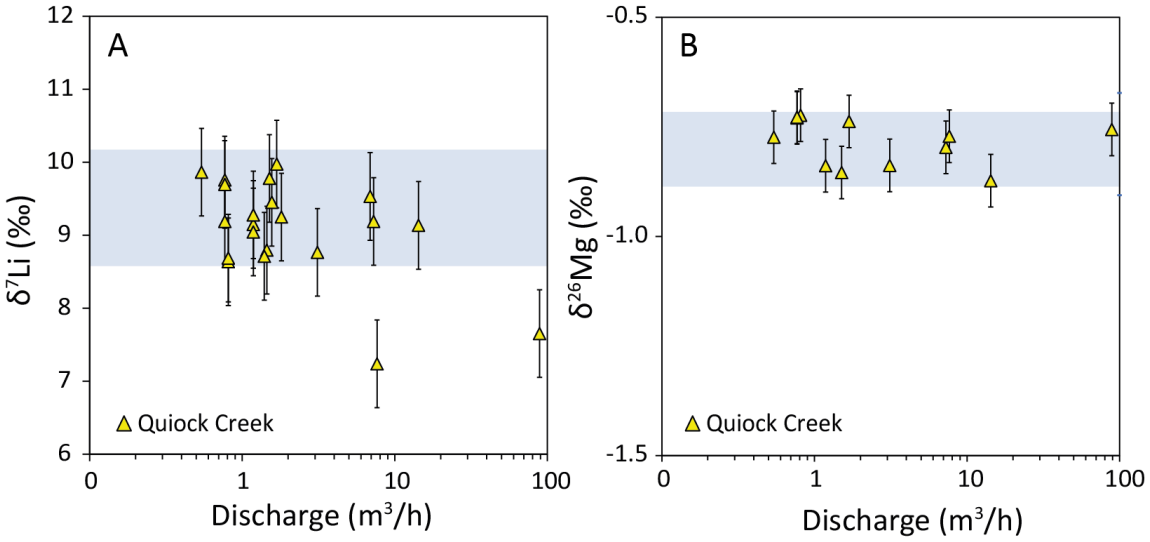

Figure IV-10. A. δ^7Li values vs discharge. B. δ^{26}Mg values vs discharge, the blue shaded boxes show the range of δ^7Li and δ^{26}Mg measured before the storm (QC20 and QC21 excluded from the average). Error bars show the external error.

The concentration of Mg in the soil solutions (10 to 43 µmol/kg) was generally lower than the Mg concentration of throughfall, and the soil solutions generally have higher δ^{26}Mg (-1.04 to -0.58‰; Figure IV-7B and Figure IV-8) compared to other reservoirs. The Mg concentrations were within the range of those previously measured in Quiock Creek catchment (11-32 µmol/L; Clergue et al. (2015)), and in soil solutions from Puerto Rico (6 to 68 µmol/L; Chapela Lara et al., 2017). There was no clear trend between [Mg] and depth, but δ^{26}Mg values increased progressively from -1.04‰ at the surface to -0.65‰ at 1250 cm. This pattern of increasing soil solution δ^{26}Mg with depth has also been observed in soil profiles from California (from -0.99‰ at the surface to -0.43‰ at the base of the profile; Tipper et al., 2010) and Puerto Rico (from -0.78‰ at the surface to -0.22‰ at the base of the profile; Chapela Lara et al., 2017). Soil solutions sampled on Day 18 have higher [Mg] in the upper part of the profile, compared to the samples measured on Day 1, whereas in the deeper part of the profile there was no obvious change in [Mg]. The δ^{26}Mg values of soil pore waters were generally identical within analytical uncertainty between Day 1 and Day 18.

Groundwaters sampled before and after a significant rain event (Day 1 and 9) had the lowest δ^{26}Mg values (from -1.48 to -0.81‰) and the highest Mg concentrations (from 21 to 54 µmol/kg) compared to any of the other Quiock Creek fluids (Figure IV-7B and Figure IV-9C and D). The range of δ^{26}Mg measured in the groundwaters was comparable with other reported groundwaters (-1.70 to 0.23‰; (Teng, 2017). There was no obvious change in groundwater Mg concentration with

distance from the river channel, but [Mg] decreased by 10-23 µmol/kg after the significant rain event on Day 9, reaching values similar to the throughfall concentration. Similarly, there was no obvious change in δ^{26}Mg with distance from the river channel (Figure IV-9D). However, three samples taken from piezometers 4 and 5 (Piezo 41, Piezo 49 and Piezo 51) had significantly lower δ^{26}Mg (-1.48 to -1.07‰) compared to any of the other samples. The Mg concentrations and δ^{26}Mg values of groundwaters from Piezo 6 (respectively, 21 to 27 µmol/kg and -0.99 to -0.95‰) were relatively stable throughout the sampling period but the δ^{26}Mg values of all of the other groundwater samples increased by 0.05 to 0.41‰ after the rainfall event, towards the value measured in throughfall.

Mg concentrations of samples from Quiock Creek ranged between 22 and 29 µmol/kg. δ^{26}Mg values showed a limited range, from -0.87 to -0.72‰, and there was no obvious relationship between either [Mg] or δ^{26}Mg with discharge (Figure IV-6 and Figure IV-10B) even at very high discharge. These δ^{26}Mg values were lighter than those measured in other Guadeloupe rivers (-0.59 and -0.43‰; Dessert et al., 2015), but within the range measured in the world's largest rivers (-0.52 to -1.70‰; Tipper et al., 2006), and rivers in Puerto Rico (-0.57 to 0.01‰), with the exception of one sample (δ^{26}Mg = -0.74‰) that was sampled when discharge was extremely high (Chapela Lara et al., 2017).

IV.4.4 Sea salt contribution

The chemical composition of river water was determined by inputs from several sources, including sea salt and dust delivered in precipitation. The contribution from sea salts can be assessed through analysis of the Cl content, assuming that all of the Cl in the river water comes from sea salt (Stallard and Edmond, 1981), and that Cl shows conservative behaviour in the system. Thus, for Li:

$$[Li]_{Sea} = \left(\frac{Li}{Cl}\right)_{Sea} \times [Cl]_X \qquad \textit{Eq. 13}$$

where $(Li/Cl)_{sea}$ = 0.05 (Dessert et al., 2015) and X is either the soil solution, groundwater, or river water. The fraction of Li derived from sea salt in the different fluid reservoirs is given in Table IV-5. The sea salt contribution in throughfall was determined using the seawater Li/Na ratio and the sample Na concentration instead, because Cl was not determined for sample Th1 (Keene et al.,

1986; Clergue et al., 2015). The majority of the Na, and most of the Mg, in all of the fluid reservoirs (throughfall, soil solutions, groundwater and river water) has a marine origin, whereas Li was mainly provided by other sources.

Table IV-5. Elemental contribution (%) of sea salts in Quiock Creek catchment fluids where $(Mg/Cl)_{sea}$ = 0.1, $(Ca/Cl)_{sea}$ = 0.02, $(K/Cl)_{sea}$ = 0.02 and $(Na/Cl)_{sea}$ = 0.86 (Dessert et al., 2015).

X	Amount derived from sea salt (%)									
	Li		Mg		Ca		K		Na	
	Min	Max	Min	Max	Min	Max	Min	Max	Min	Max
Soil solution	10	33	85	100	76	100	35	100	83	100
Throughfall	44	48	77	100	13	16	4	9	94	100
Groundwaters	13	52	51	100	1	19	75	100	83	100
Quiock Creek	24	29	100	100	41	57	70	100	96	100

IV.5 Discussion

IV.5.1 Sources of Li and Mg in Quiock Creek catchment

The isotope compositions of Mg and Li are plotted with elemental ratios (Mg/Ca and Li/Na, respectively) in Figure IV-11 and Figure IV-12 to help characterize the possible sources of Mg and Li in the catchment. The use of elemental ratios permits better comparison between the fluids as they

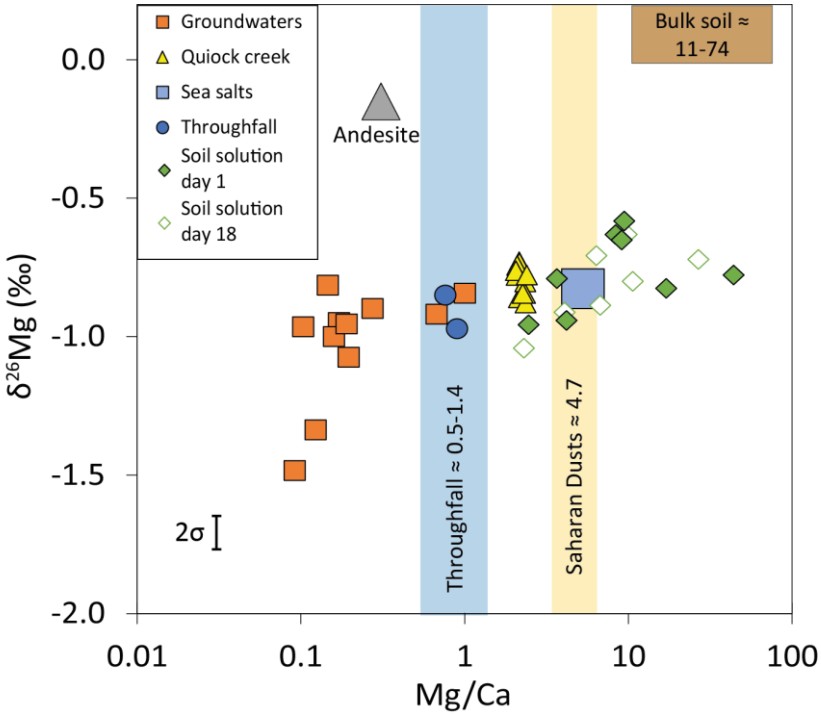

Figure IV-11. $\delta^{26}Mg$ versus Mg/Ca for fluids in Quiock Creek catchment. Bedrock (andesite) and bulk soil $\delta^{26}Mg$ are from Dessert et al. (2015) and Mg/Ca ratios used for throughfall (blue box), bulk soil (brown box) and Saharan dusts (yellow box) are from Clergue et al. (2015).

are unaffected by dilution and evaporation processes (Gaillardet et al., 1999b). Mg and Ca are both soluble alkaline earth elements that are susceptible to be taken up by plants. However, in volcanic settings, Mg is more likely to be incorporated into secondary clays or adsorped on clay mineral surfaces (Tipper et al., 2006a, 2008a). Figure IV-11 shows that the Mg/Ca ratios of different reservoirs of Mg in the catchment can be very variable but the Mg isotope composition of the river waters and most of the groundwaters is within the range of throughfall and sea salt, consistent with the results of sea salt contribution reported in Table IV-5. However, groundwater samples from Piezo 41, Piezo 49 and Piezo 51 have much lower δ^{26}Mg that cannot be explained by mixing between any of the potential Mg reservoirs analysed in this study. We investigate the possible causes if these low δ^{26}Mg values in Section IV.5.3.

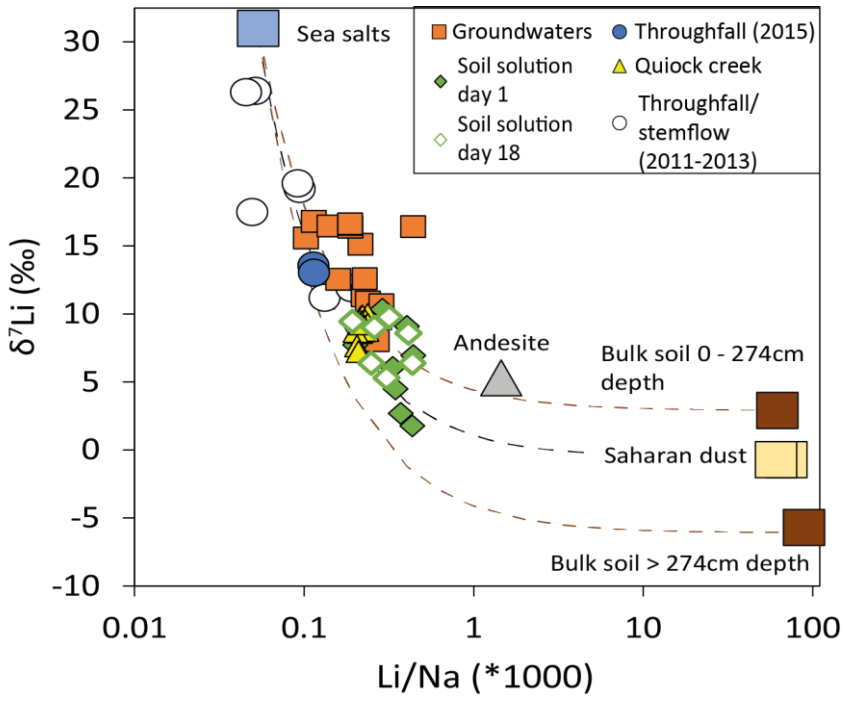

Figure IV-12. δ^7Li versus Li/Na for all fluids from Quiock Creek catchment. δ^7Li values for andesite, throughfall/stemflow (collected in 2011-2013), and bulk soils are from Clergue et al. (2015). Dashed lines represent the theoretical mixing trend between seawater and dust or bulk soils. The external error of the δ^7Li values is smaller than the symbols.

Li and Na are both soluble alkali metals and are not essential nutrients, so they can be expected to act similarly during weathering. However, Na is generally not incorporated into secondary minerals whereas Li can be significantly enriched in clays and oxy-hydroxides (Sawhney, 1972; Millot et al., 2010c; Dellinger et al., 2015). Figure IV-12 shows that most of the Quiock Creek fluids have Li/Na

and δ^7Li values that are intermediate between sea salts that have low Li/Na and high δ^7Li and Saharan dust or bulk soil that have much lower δ^7Li and higher Li/Na (Clergue et al., 2015). However, many of the samples have higher δ^7Li than predicted by simple binary mixing, which can likely be attributed to uptake of Li into secondary mineral phases (Huh et al., 1998; Huh et al., 2001; Rudnick et al., 2004; Kisakurek et al., 2005).

IV.5.2 Controls on the Li and Mg isotope composition of throughfall and soil solutions

IV.5.2.1 Li and Mg isotopes in throughfall

The δ^7Li values of the two throughfall samples (13 and 13.6‰) are much lower than that of sea salt (δ^7Li = ~31‰), suggesting that there is additional input of Li from a source with lower δ^7Li. The source of this Li is most likely to be leaching of Saharan dust located on the canopy, which has δ^7Li = -0.7‰ (Clergue et al. (2015). Assuming that no fractionation of Li isotopes occurs during dust dissolution (Pistiner and Henderson, 2003; Wimpenny et al., 2010a), then mass balance considerations indicate that approximately 50% of the Li in throughfall comes from Saharan dust, consistent with estimations of the sea salt contribution (44-48%; Table IV-5). Note, however, that this estimate is specific to our sampling period, as at other times of the year, the dust contribution has been reported to be lower (as low as 25%; Clergue et al. (2015)).

The δ^{26}Mg values of the two throughfall samples differ by 0.13‰, just outside of the uncertainty of the analyses. This difference is unlikely to be due to differences in dust input, as no difference in δ^7Li is observed in the throughfall samples. The variation of δ^{26}Mg in the throughfall could be due to differences in inputs of Mg from leaching of dust on the canopy. While plants are overall enriched in heavy Mg isotopes compared to the soil solution, the transfer of Mg from the roots to the leaves fractionates Mg isotopes, such that the upper part of the plant has lower δ^{26}Mg (Bolou-Bi et al., 2010; Bolou-Bi et al., 2012). Sample Th1 has lower δ^{26}Mg and higher [K] compared to sample Th3 (Table IV-3); high concentrations of K in rainfall and throughfall are indicative of input of K from vegetation (Riotte et al., 2014). By contrast, vegetation inputs have little effect on δ^7Li (Lemarchand et al., 2010; Clergue et al., 2015).

IV.5.2.2 Li isotopes in soil solution

Soil solution δ^7Li decreases with depth (from 10.4 to 1.8‰) and the δ^7Li value of bulk soil also decreases with depth (from 0.6 to -13.5‰; Clergue et al., 2015). The change in the δ^7Li value of the bulk soil has been attributed to increased dust input to the upper part of the soil profile (Clergue et al., 2015). In the soil solutions, however, the proportion of Li derived from sea salt does not decrease significantly with depth (Figure IV-13A), suggesting that changes in δ^7Li in the soil solution must be principally controlled by weathering processes rather than atmospheric inputs. However, in the upper part of the soil profile (above 152 cm depth), the δ^7Li value of the soil solution increases after the rain events, whereas the Li/Na ratio decreases (Figure IV-8 and Figure IV-13B). This is consistent with increased input of Li from throughfall that has relatively high δ^7Li and low Li/Na. The soil solution δ^7Li in the upper part of the profile appears to be much more influenced by throughfall inputs compared to the deeper part of the soil profile despite significant changes in hydrological conditions during the sampling period.

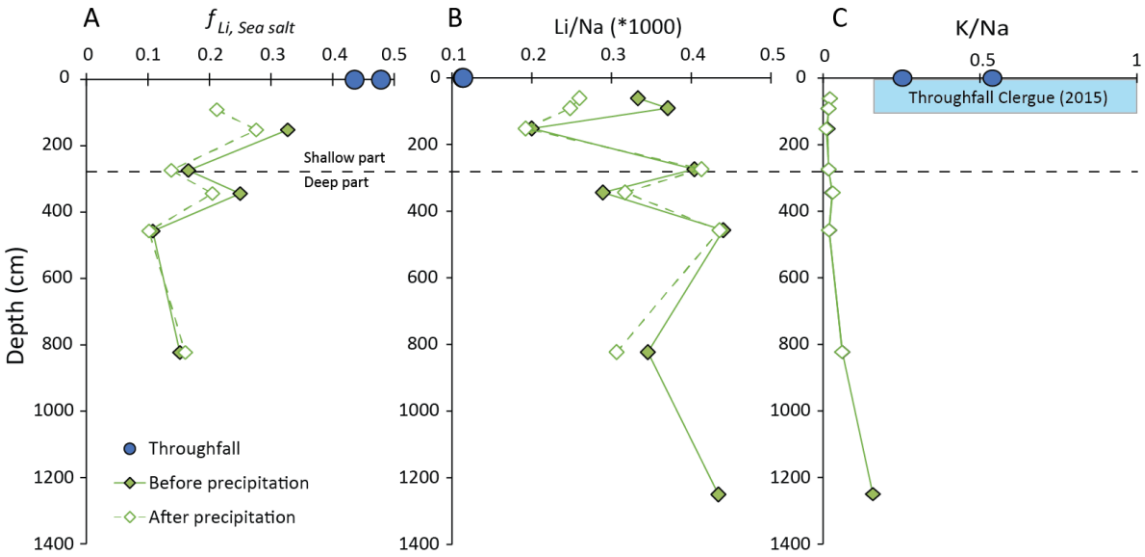

Figure IV-13. A. Fraction of Li derived from sea salts in the soil solutions. B and C. Evolution of soil solution Li/Na and K/Na with depth before and after rainfall events. C. The blue shaded box shows the range of K/Na in throughfall samples measured by Clergue et al. (2015).

IV.5.2.3 Mg isotopes in the soil solution

In contrast to Li, almost all of the Mg in the soil solution is delivered by atmospheric inputs (Table IV-5), which is consistent with the high depletion of Mg in the soil of the catchment (Clergue et al., 2015). Nevertheless, the δ^{26}Mg values of the soil solutions increase slightly with depth in the soil

profile; this cannot be attributed to simple mixing between throughfall and Mg derived from the bulk soil (Figure IV-11), suggesting that Mg isotope fractionation must occur during weathering. As all of the Cl in the soil solution comes from throughfall, and Cl is conservative during water transfer into the soil, changes in the Mg/Cl ratio of the soil solution can be used to identify whether the soils are a source or a sink of Mg. Figure IV-14 suggests that Mg is removed from the soil solution in the deeper part of the soil profile, and this leads to an increase in δ^{26}Mg. The change in δ^{26}Mg must reflect preferential incorporation of light Mg isotopes into secondary mineral phases, or preferential adsorption of light Mg isotopes, in the deeper part of the soil profile. In Guadeloupe, soils tend to be enriched in heavy Mg isotopes compared to the fluids (Opfergelt et al., 2012; Dessert et al., 2015), which suggests that secondary minerals are enriched in heavy, not light, Mg isotopes. However, several studies have shown that cation exchange can lead to preferential uptake of light Mg isotopes onto mineral surfaces, increasing the δ^{26}Mg value of Mg that remains in solution (Jacobson et al., 2010; Opfergelt et al., 2012; Ma et al., 2015). Therefore, it seems likely that cation exchange occurs in the deepest part of the profile where the longer residence time of the water allows dissolved Mg to adsorb on the clay surfaces.

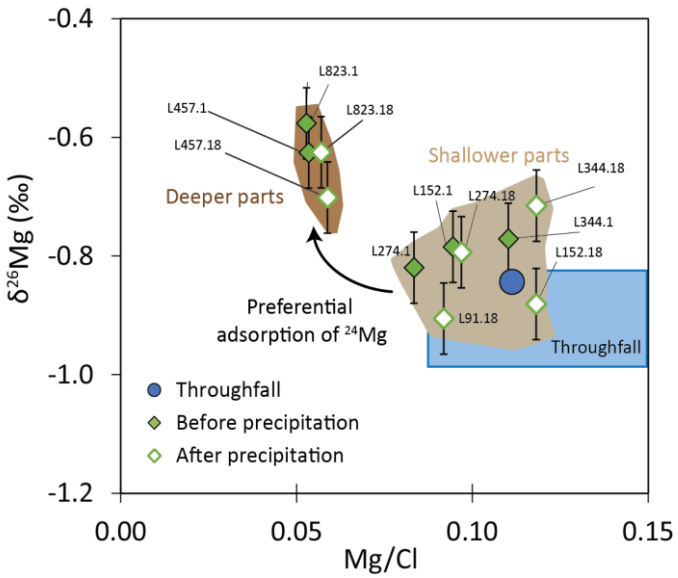

Figure IV-14. Mg/Cl versus δ^{26}Mg in the soil solution before and after rainfall events. The figure highlights the removal of Mg from the solution in the deeper part of the profile together with an increase of δ^{26}Mg. The blue shaded box shows the throughfall/stemflow composition (Clergue et al., 2015).

Mg may also potentially be affected by vegetation uptake. The soil solutions have much lower K/Na than the throughfall (Figure IV-13C), which is indicative of uptake of K (and by analogy uptake of

Mg) by plants (Jobbagy and Jackson, 2001). However, this appears to have limited impact on the δ^{26}Mg value of the soil solutions, consistent with results from a previous study (Chapela Lara et al., 2017). Despite dense vegetation cover and tight nutrient cycles in tropical rainforests (Wood et al., 2009), the δ^{26}Mg of soil solutions therefore appears to be unaffected by plant uptake if atmospheric inputs of Mg are high. This is a major difference with more temperate mountainous areas where lower δ^{26}Mg in soil water has been attributed to preferential uptake of the heavy Mg isotopes by plants (Uhlig et al., 2017).

IV.5.3 Weathering processes in groundwaters

The Li isotopic signature of groundwaters cannot be explained by simple mixing of Li from bulk soil or rock, and throughfall, as discussed in Section IV.5.1. The δ^{7}Li value of the groundwaters (8 to 16.8‰) is significantly higher than the δ^{7}Li value of the bulk soil (δ^{7}Li = 2.9‰ above 274 cm and -6.1‰ below 274 cm on average; Clergue et al., 2015) and, because primary minerals are almost totally absent from the soil (Buss et al., 2010), the δ^{7}Li value of the groundwaters must be linked to dissolution and precipitation of secondary mineral phases. After a rain event, the Li/Na ratio of the groundwaters increases, whereas the δ^{7}Li value of the groundwaters decreases (by 1.5 to 3.6‰ in Piezo 1, 2, 3 and 4; Figure IV-15). This cannot be attributed to input of Li from sea salt, implying that a ^{6}Li-enriched reservoir of Li in the catchment is produced during rain events, either through enhanced dissolution of secondary minerals, or through suppressed secondary mineral formation, or through injection of previously isolated pockets of water enriched in ^{6}Li through interactions with secondary minerals before the rain event.

To further explore the possibility of a change in the rate of secondary mineral dissolution during a rain event, the saturation states of the groundwaters with respect to different secondary mineral phases were calculated with the PHREEQC program (Parkhurst and Appelo, 2013) using the measured concentration data, field pH and temperature. PHREEQC calculates mineral stability in terms of the saturation index (SI). If SI > 0, the solution is supersaturated and the mineral may precipitate, whereas if SI < 0, the mineral is likely to dissolve. The groundwater SI for the principal constituents of the soil, kaolinite (halloysite), gibbsite and goethite (Buss et al., 2010), are shown in Figure IV-16. All of these mineral phases are oversaturated in the Quiock Creek groundwaters, so

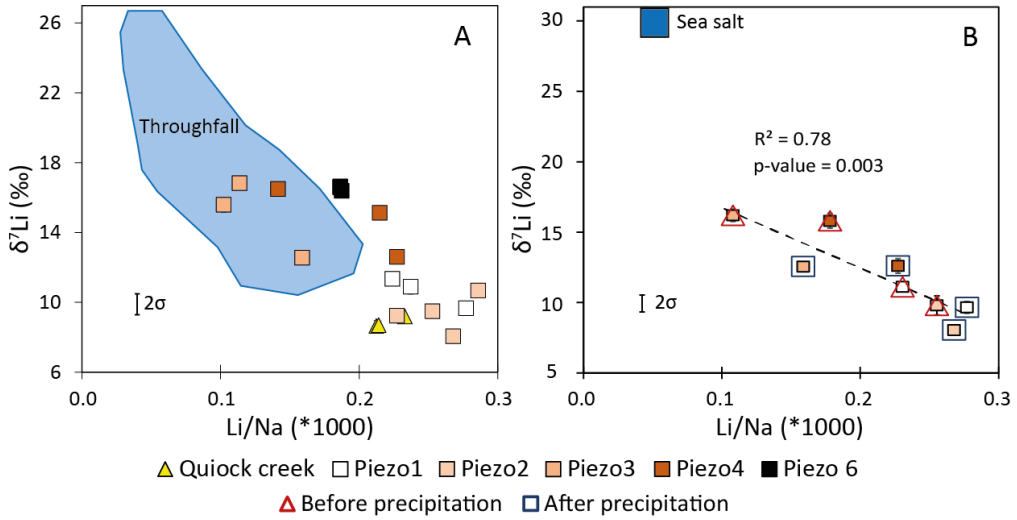

Figure IV-15. A. Relationship between δ^7Li vs Li/Na for the dissolved load in groundwaters and Quiock Creek samples sampled on Day 1, 4, 8, and 9 (Piezo 5 is not shown). The blue shaded areas show the throughfall/stemflow composition (Clergue et al., 2015). B. Li/Na versus δ^7Li in groundwaters before and after precipitation. The red open triangles show the average value for samples collected on Day 1 and 8 while the blue open squares show the values measured after a significant rain event at Day 9.

changes in δ^7Li most likely controlled by changes in the rate of secondary mineral precipitation. After a rain event, the SI of all of the secondary mineral phases decreases, consistent with lower rates of secondary mineral precipitation and thus lower δ^7Li (Figure IV-16).

The majority of the groundwater samples have a Mg isotope composition similar to the groundwaters sampled in Piezo 6 (δ^{26}Mg = -0.95 to -0.99‰). The δ^{26}Mg value of these groundwaters was invariant over time, suggesting that they have a long residence time and this represent the baseflow contribution to Quiock Creek. Two samples, Piezo 41 and Piezo 51, have significantly lower δ^{26}Mg values (respectively, -1.48 and -1.33‰). These samples contained 'stagnant' water, as the piezometers were not emptied prior to sampling (see Section IV.3.1). The low δ^{26}Mg values could be linked to (1) release of Mg to groundwater from solid phases, (2) uptake or release of Mg by plants; (3) cation exchange with mineral surfaces. Because soils and bedrock tend to be enriched in heavy Mg isotopes in Guadeloupe, addition of Mg with low δ^{26}Mg cannot be attributed to dissolution of mineral phases. In support of hypothesis 2, these samples have much lower K/Cl and higher Mg/Cl and Mg/K ratios compared to the other groundwater samples (Figure IV-17). Potassium is an essential nutrient that is highly concentrated in plant tissues (Bowen, 1979; Riotte et al., 2014). The potential effects of vegetation on K and Mg in groundwaters include

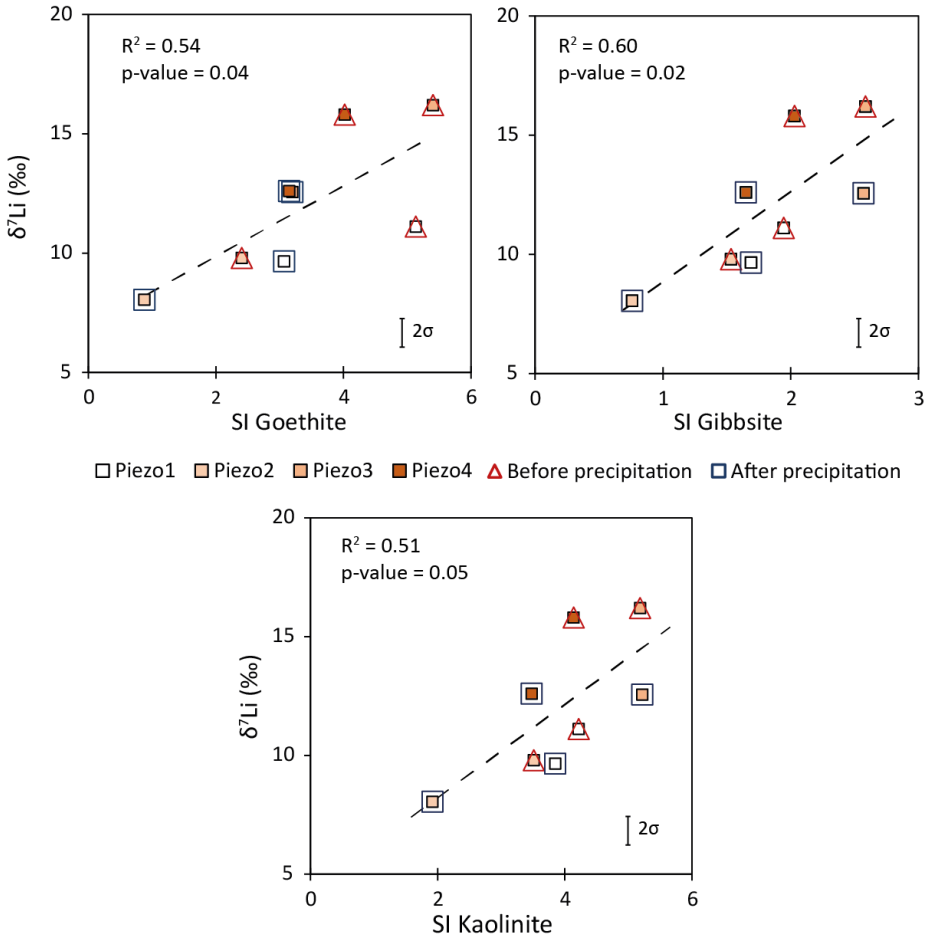

Figure IV-16. δ^7Li vs saturation index (SI) of goethite, gibbsite and kaolinite in groundwaters. The red open triangles show the average value for samples collected on Day 1, 4 and 8 while the blue open squares show the value measured after a significant rain event at Day 9.

leaching of leaves that increases the K content of throughfall relative to sea salt and slightly decreases $\delta^{26}Mg$ due to preferential leaching of light Mg isotopes from the upper part of the plant (Bolou-Bi et al., 2010; Bolou-Bi et al., 2012); uptake of K, but not Mg, by plants; or removal of K associated with addition of Mg with lighter $\delta^{26}Mg$ values. The two first patterns concur with analyses of soil solutions discussed in Section IV.5.2.3, which suggests that groundwaters can be also affected by plant uptake. However, the lower K/Cl (Figure IV-17B) is inconsistent with reduced plant uptake which would have increased [K] relative to [Cl] (Jobbagy and Jackson, 2001). Therefore, it seems most likely that the low $\delta^{26}Mg$ groundwaters acquire Mg through cation exchange (hypothesis 3). During adsorption the lighter Mg isotopes are preferentially fixed (Ma et al., 2015), therefore, desorption of Mg from secondary minerals can be expected to enrich the solution in light isotopes. These 'stagnant' groundwater samples have high [Ca]; despite its similar charge, Ca^{2+} has a higher ionic radius and a lower hydrated radius than Mg^{2+}, so it is preferentially adsorbed on clay

surfaces (Udo, 1978; Appelo and Postma, 2004). As Ca^{2+} concentrations increase with increasing residence time, previously adsorbed light Mg isotopes are released increasing then Mg concentration and reducing the $\delta^{26}Mg$ value of the groundwater.

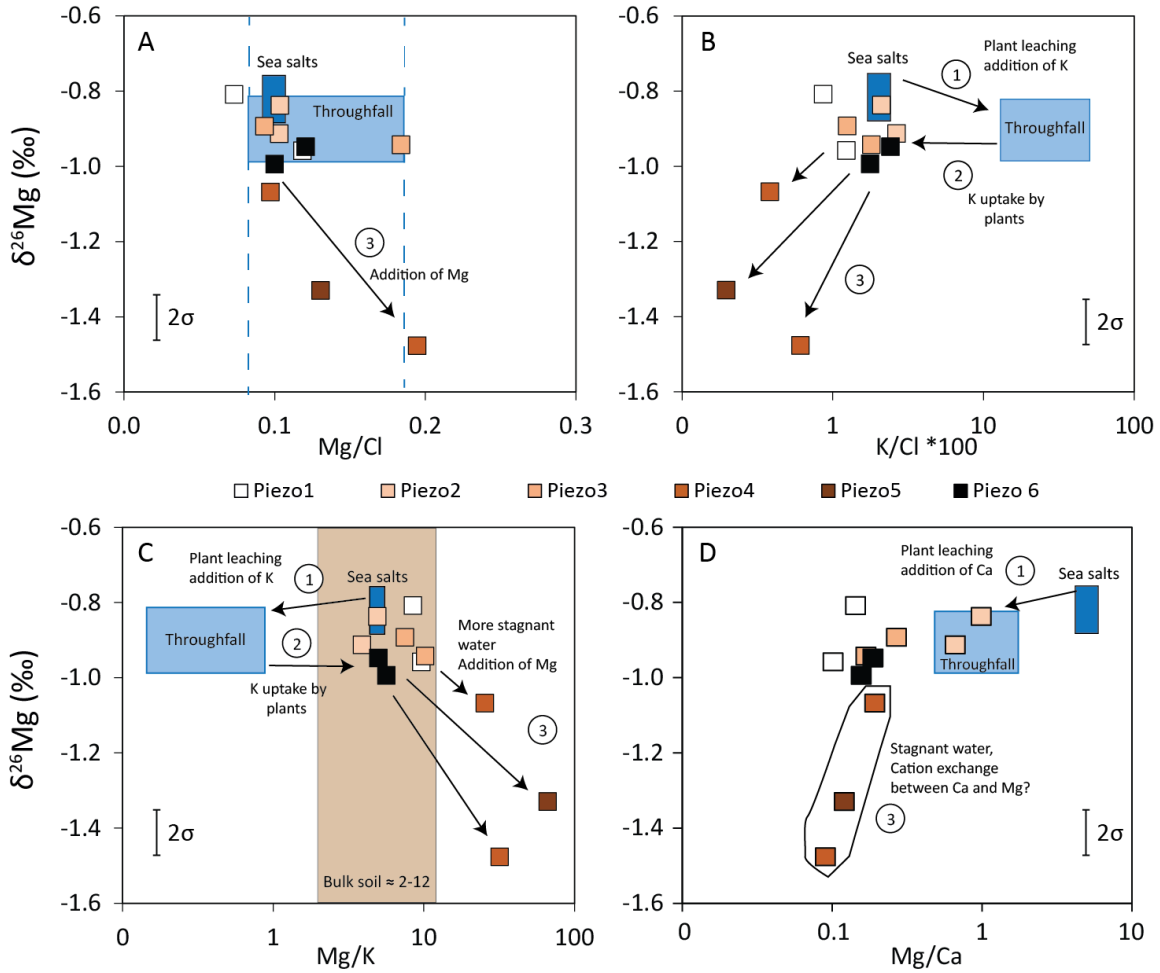

Figure IV-17. A. Relationship between $\delta^{26}Mg$ vs Mg/Cl, B. $\delta^{26}Mg$ vs K/Cl, C. $\delta^{26}Mg$ vs Mg/K and D. $\delta^{26}Mg$ vs Mg/Ca for the dissolved load in groundwaters. The light blue shaded box shows the throughfall composition while the dark blue shaded box shows the sea salt composition. Three different patterns are observed to explain change in K and Mg content together with $\delta^{26}Mg$.

IV.5.4 Temporal variations in the Mg and Li isotopic compositions of Quiock Creek waters

As the soils in Quiock Creek catchment are highly weathered, and there is limited contact with the bedrock as the soils are thick, river waters can be expected to become more dilute during storm events. However, there was in fact little variation in element concentrations with discharge in this study, even though discharge varied by two orders of magnitude (Figure IV-6). At the highest discharge, [Li] and [Mg] were slightly lower (by ~25%) than expected for chemostatic behaviour,

which implies that solute production is kinetically-limited at high discharge (Maher, 2011). This is consistent with the high permeability of the catchment (10^{-6}m/s or ~30m/yr; (Guérin, 2015), which means that water residence time is relatively short.

In contrast to previous studies conducted in Guadeloupe and Puerto Rico (both tropical catchments), we find no evidence for increased river water δ^{26}Mg at low discharge, which has been attributed to an increased contribution of Mg from weathering from the deep saprolite at low flow (Dessert et al., 2015; Chapela Lara et al., 2017). This is likely related to the very high depletion of Mg and the absence of easily-weathered primary mineral phases in the soil (Buss et al., 2010). By contrast, the δ^{7}Li value of the river water decreased by, on average, ~2‰ after the largest rain even and remained low afterwards (Figure IV-3 and Figure IV-7B). The decrease in δ^{7}Li is most likely due to either input of Li from isolated pockets of soil solution with lower δ^{7}Li that are flushed out during rain events or a decrease in rates of secondary mineral precipitation.

On a first order, the Li isotope composition of Quiock Creek ($\delta^{7}Li_{QC}$) is controlled by mixing between Li derived from the soil solution and Li derived from groundwater:

$$\delta^{7}Li_{QC} = \delta^{7}Li_{Soil\ solution} \times f_{Soil\ solution} + \delta^{7}Li_{Groundwater} \times f_{Groundwater} \quad \textit{Eq. 14}$$

$$f_{Soil\ solution} + f_{Groundwater} = 1 \quad \textit{Eq. 15}$$

where $\delta^{7}Li_{Soil\ solution}$ and $\delta^{7}Li_{Groundwater}$ are the average isotope composition of the soil solution and groundwater respectively, and $f_{Soil\ solution}$ and $f_{Groundwater}$ represent, respectively, the flux of Li derived from the soil solution and groundwater. Hence:

$$f_{Soil\ solution} = \frac{\delta^{7}Li_{QC} - \delta^{7}Li_{Groundwater}}{\delta^{7}Li_{Soil\ solution} - \delta^{7}Li_{Groundwater}} \quad \textit{Eq. 16}$$

Assuming that $\delta^{7}Li_{Soil\ solution}$ = 6.9‰ and $\delta^{7}Li_{Groundwater}$ = 13.2‰, we calculate that 52 to 73% of the Li in Quiock Creek came from the soil solution before the storm, whereas after the storm this increased to 89 to 95% (Figure IV-18). Thus, the decrease in δ^{7}Li was most likely due to increased input of Li from soil solution that has lower δ^{7}Li and was flushed out during the rain event.

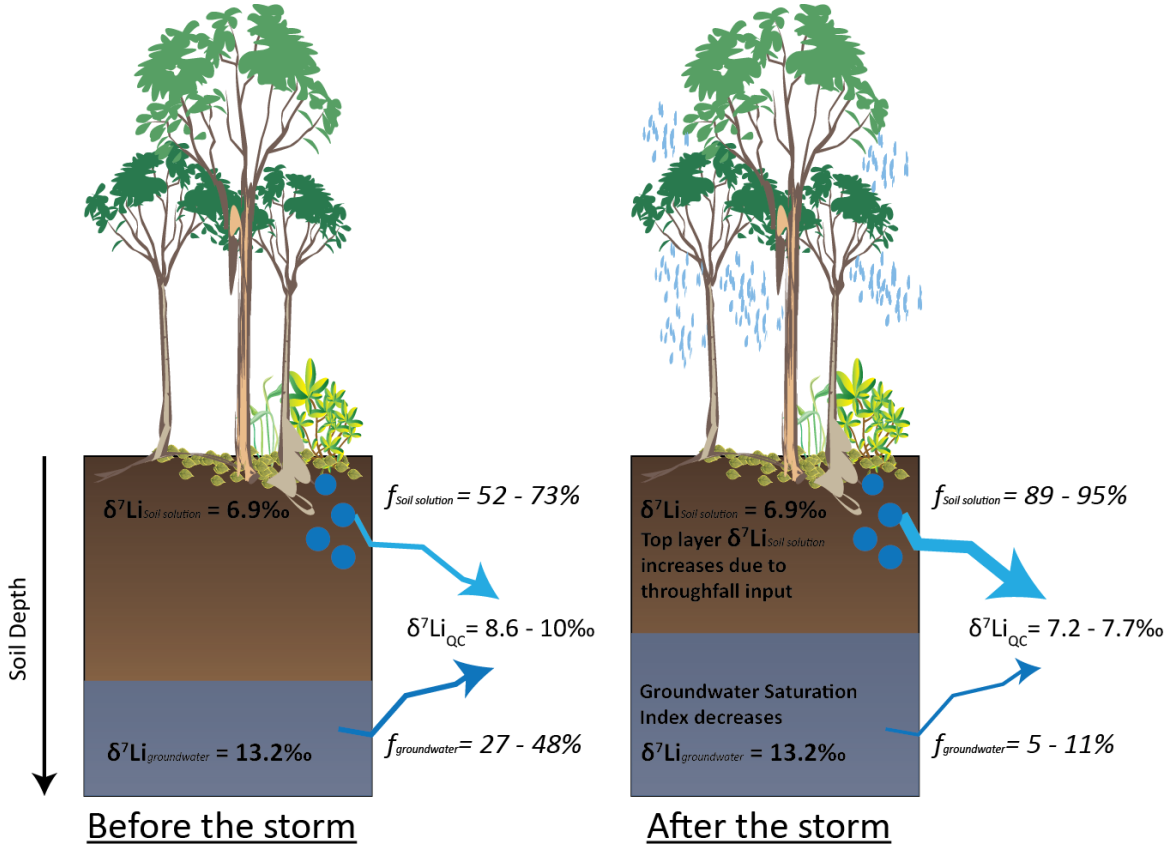

Figure IV-18. Summary of the dissolved Li flux and δ^7Li evolution before and after a storm event.

IV.6 Conclusions

This study highlights that, even in a highly-weathered catchment that drains single lithology, there can be significant differences in the Li and Mg isotope compositions of different critical zone reservoirs. Isotope signals are strongly affected by atmospheric inputs of Mg and Li, but they are also controlled by interactions with soil and bedrock. Li isotope compositions are mostly influenced by preferential incorporation of ^{6}Li into secondary minerals, whereas Mg isotope compositions mainly reflect input of Mg from sea salts although adsorption or desorption of light Mg isotopes to/from mineral surfaces can occur in waters that have a relatively long residence time. δ^7Li values of groundwaters can quickly decrease even after a single rain event and this is likely due to lower rates of precipitation of secondary minerals. A rapid decrease in δ^7Li in Quiock Creek after a storm event is attributed to increased input of Li from soil solutions that have lower δ^7Li compared to groundwater. Atmospheric inputs of Li increase the δ^7Li of soil solutions after rain events only in the upper part of the soil profile. δ^{26}Mg values show little change during hydrological events,

because most of the Mg in Quiock Creek catchment is supplied by throughfall and Mg is not significantly impacted by plant uptake.

Chapter V. Influence of hydrological variations in the lithium and magnesium isotopic composition of the Amazon River

ABSTRACT

The volume of water and suspended sediment delivered to the Atlantic Ocean by the Amazon River, which supplies ~20% of the freshwater input to the ocean, varies significantly over the annual cycle. As past variations in the lithium (Li) and magnesium (Mg) isotopic composition of seawater are usually interpreted in terms of variations in weathering fluxes, and/or weathering intensity, it is crucial to assess the present-day weathering variations to better interpret $\delta^{7}Li$ and $\delta^{26}Mg$ records. In support of this, we have sampled the dissolved and suspended load of the Amazon River and its principal tributaries during both high water stage (HW) in June and low water stage (LW) in November. The $\delta^{7}Li$ value of the dissolved load was higher at low discharge than it was at high discharge ($\delta^{7}Li_{LW} - \delta^{7}Li_{HW}$ = 0.7 to 8.7‰) both in the main stem of the Amazon and its tributaries, but there is little difference in the $\delta^{26}Mg$ value of the dissolved phase ($\delta^{26}Mg_{LW} - \delta^{26}Mg_{HW}$ = -0.10 to 0.49‰). The Li and Mg isotope composition of the suspended material did not change significantly between the HW and LW stages. The higher $\delta^{7}Li$ in the dissolved phase during the LW stage is likely due to increased input of Li from the floodplains that form along the banks of the Amazon and some of its tributaries (Madeira and Negro River). Water stored on the floodplains has a relatively long residence time, resulting in significant formation of secondary minerals that preferentially incorporate ^{6}Li increasing the $\delta^{7}Li$ value of Li that remains in solution. By contrast, variations between LW and HW stages in the Mg isotopic composition of river water are insignificant suggesting that retention of Mg in the floodplains is insignificant.

V.1 Introduction

The dissolved solids and suspended sediments that are carried by large rivers are the witnesses of continental weathering processes that strongly control the chemical oceanic budget (Gaillardet et al., 1999a; Gaillardet et al., 1999b). In the Amazon basin, important seasonality discharge variation is associated with significant changes in the quantity and composition of weathering products (Stallard and Edmond, 1983; Guyot et al., 2007; Hughes et al., 2013; Bouchez et al., 2014b; Moquet et al., 2016). These changes have been attributed to changes in silicate weathering rates (Mortatti and Probst, 2003), and/or to simple mixing tributaries processes in term of water and weathering products (Moquet et al., 2016; Bouchez et al., 2017; Torres et al., 2017). One way to distinguish these different mechanisms is by the analysis of isotopic tracers such as lithium (Li) and magnesium (Mg) isotopes that are sensitive to changes in weathering processes (Teng et al., 2010; Pogge von Strandmann et al., 2012; Tipper et al., 2012a). Lithium is mainly present in silicate minerals and the Li isotopic composition of river water appears to be independent of catchment lithology (Kisakurek et al., 2005) and biological processes (Lemarchand et al., 2010). While Li is usually a trace constituent of rock and water, Mg is a major component of many rocks and fluids (Teng, 2017). The Mg isotopic composition of river water is sensitive to bedrock lithology (Tipper et al., 2006b) and biological processes can fractionate Mg isotopes toward lighter values by preferential uptake of ^{26}Mg (Black et al., 2008; Bolou-Bi et al., 2010; Bolou-Bi et al., 2012). Both Li and Mg are strongly fractionated during the formation of secondary minerals and, as a result, the Li and Mg isotopic composition of river water can reflect weathering intensity within the catchment (Bouchez et al., 2014a; Dellinger et al., 2015; Dessert et al., 2015).

The isotopic signal of Li and Mg obtained during weathering is eventually transferred to seawater which acts as a global “database” of present and paleo-weathering conditions. To date, past variations of δ^7Li and $\delta^{26}Mg$ recorded in foraminifera, carbonates and corals show a net increase in seawater δ^7Li (~ 9‰) but little change in seawater $\delta^{26}Mg$ over the last 60 million years (Hathorne and James, 2006; Misra and Froelich, 2012; Higgins and Schrag, 2015; Gothmann et al., 2017). Although the mechanisms that cause these variations are still debated for Li (Misra and Froelich, 2012; Pogge von Strandmann and Henderson, 2015; Vigier and Godderis, 2015) and Mg (Pogge von

Strandmann et al., 2014; Higgins and Schrag, 2015; Gothmann et al., 2017), most studies suggest that a reduction in silicate weathering intensity associated with global cooling of the Earth's surface must play an important role. In this study, we have determined the Li and Mg isotopic composition of the dissolved phases and suspended particulate material in both the main stem of the Amazon and its principal tributaries (Solimões, Negro, Madeira, Trombetas and Tapajós), for both HW and LW stages. We use these data to assess the effects of discharge changes in Li and Mg isotopes on seawater composition and consequently for the interpretation of paleo-climatic and paleo-oceanic studies.

V.2 Study area

The studied area covers the Amazon River and five of its principal tributaries, the Solimões, Negro, Madeira, Trombetas and Tapajós rivers. The Amazon River is the largest world river in terms of water discharge and basin drainage area (5.9×10^6 km^2; Callède et al., 2010). It supplies ~17% of the water (Callède et al., 2010) and ~7% of the total dissolved load flux (Moquet et al., 2016) exported from the continents to the oceans. Geologically, the Amazon Basin is mainly composed of igneous (mostly andesites and granodiorites) and sedimentary rocks and can be divided in three main domains according to distinctive soils, lithology, climate and vegetation: 1. the Andes and Andean forelands (25% of the basin); 2. the Guiana and Brazilian cratonic shields (51% of the basin); 3. the central Amazon floodplain or lowland (24% of the basin; Moquet et al., 2016; Stallard and Edmond, 1983). This study focuses in the central Amazon region, which is bounded by the Guiana and Brazilian shields to the north and south respectively (Figure V-1). The sampled region corresponds to the lowland area (a zone of subsidence) with weak slope, a relief below 500 m and is covered by Tertiary and Quaternary lacustrine and alluvial deposits (Stallard and Edmond, 1983). Highest discharge usually occurs between April and July, and during the low water stage the water level of the river decreases by some 7 to 10 m in the main stem (Richey et al., 1989; Appendix C 1). The central Amazon (lowland) is associated to floodplain lakes (várzeas) along the main channel of the Solimões and Amazon Rivers, which are connected or isolated from the main stem depending on the water stage (Richey et al., 1989). Around 30% of the Amazon water discharge transits

through these floodplains (Richey et al., 1989; Bonnet et al., 2008), and they are also an important sink of suspended particulate material (Dunne et al., 1998; Moreira-Turcq et al., 2004; Bourgoin et al., 2007; Vauchel et al., 2017). The residence time of the sediments trapped within the floodplains is much higher than it is for material in the main channel (Dosseto et al., 2006), which increases the extent of fluid-sediment interactions (Viers et al., 2005; Guyot et al., 2007; Frings et al., 2016). Water is stored on the floodplains between December-January and May-June as the water stage in the Amazon River rises, and it is exported from the floodplains into the main channel between ~July and November as the water stage falls (Bonnet et al., 2008). Bonnet et al. (2008) estimated that the water residence time within the floodplain is around 5 months.

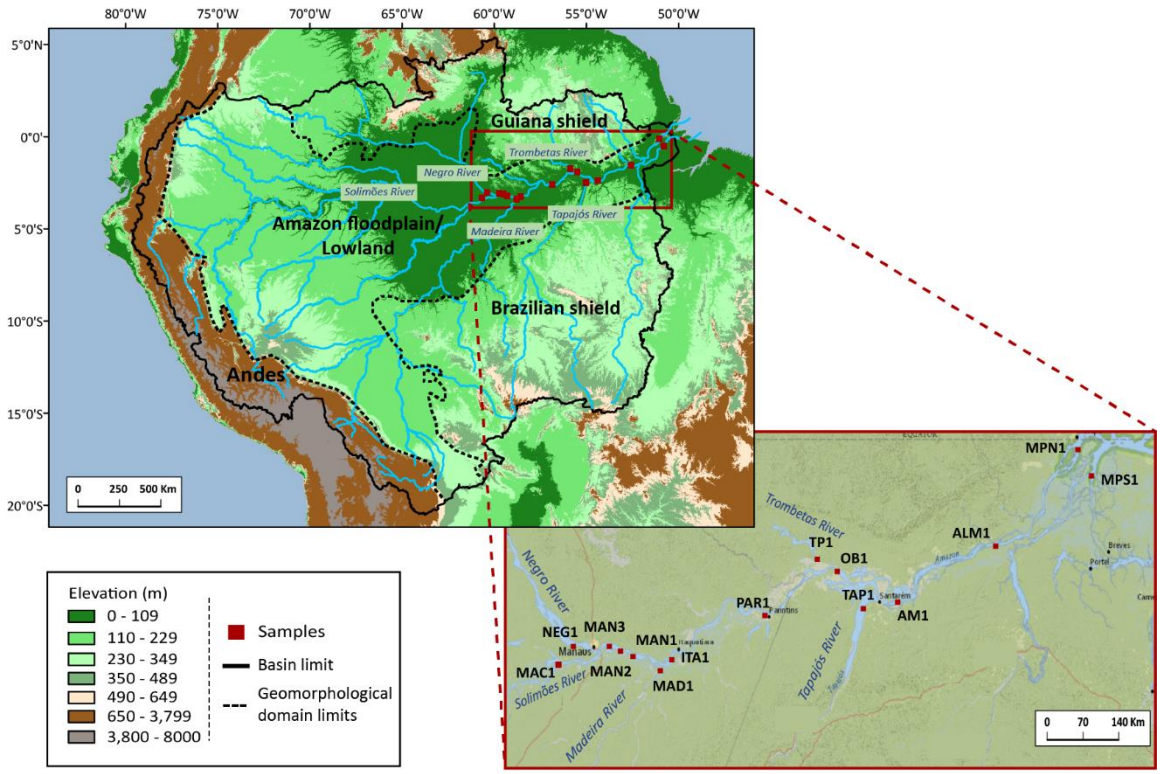

Figure V-1. Amazon basin morphological units and map of the Amazon River and its tributaries showing the sampling locations (red squares). Two profiles at Óbidos (OB1) and Manaus (MAN3) were made to collect water and sediment at different depths. Samples were collected in 2015 during both high and low water stage. Watershed limit, hydrography network and elevation are derived from the SO-HYBAM website (http://www.ore-hybam.org).

Suspended sediments in the Amazon River mainly consist of T-O-T clays (i.e. clays composed of 2 tetrahedral silicate sheets and 1 octahedral hydroxide sheet), mainly smectite (50%), illite and chlorite (30%). Kaolinite, which is a T-O clays, is also present (~20%) (Guyot et al., 2007). The

Solimões and Madeira rivers, which originate from the Andes, are the principal source (<90%) of suspended sediments in the main stem of the Amazon River (Filizola and Guyot, 2009). Both of these tributaries principally carry T-O-T structure clays. The Tapajós, Trombetas and Negro rivers contribute less than 10% of the total suspended sediment flux and mostly have a high kaolinite content (up to 98% in the Negro) and minor T-O-T structure clays (Guyot et al., 2007). These sediments are highly depleted in cations (Stallard and Edmond, 1983; Gaillardet et al., 1997).

V.3 Material and methods

The sample collection procedure and analytical methodologies used in this study are described in detail in Chapter II. Briefly, river water and suspended sediment samples were collected along a ~1350 km transect (Figure V-1) along the Amazon floodplain, from Manacapuru (sample MAC1) in the south to Macapá (samples MPS1 and MPN1) in the north. The 35 water samples and 31 sediment samples were collected from the Amazon River basin at 15 different locations during two research cruises in June (low water stage; LW) and November (high water stage; HW) 2015. Additional samples were also collected in January (start of the HW stage) and August (end of the HW stage) at Óbidos (sample OB1) but also in December (end of the LW stage) for MPS1 and MPN1 (Figure V-2). Water profiles in Óbidos (OB1.30 and 60) and Manaus (MAN3.15, 30 and 45) were only taken in the LW stage contrary to sediment profiles that were taken during both HW and LW stages. All river water and suspended sediments were sampled against the flow direction while temperature and pH were measured in-situ. Discharge and sediment concentration data used here were from the HYBAM observatory website (http://www.ore-hybam.org; Figure V-2). River waters were filtered in-situ at 0.45 µm through a 142 mm diameter membrane filter and then acidified for cation analysis. The suspended sediments retained on the filter were stored in plastic bags in a freezer. Cation concentrations in water samples were determined at the Eidgenössische Technische Hochschule Zürich (ETHZ) by inductively coupled plasma mass spectrometry (ICP-MS), and cation concentrations in sediment samples at the National Oceanography Centre Southampton (NOCS).

Lithium and magnesium isotope compositions were determined by multi-collector inductively-coupled plasma-source mass spectrometry (MC-ICP-MS; Thermo Scientific Neptune), at the NOCS.

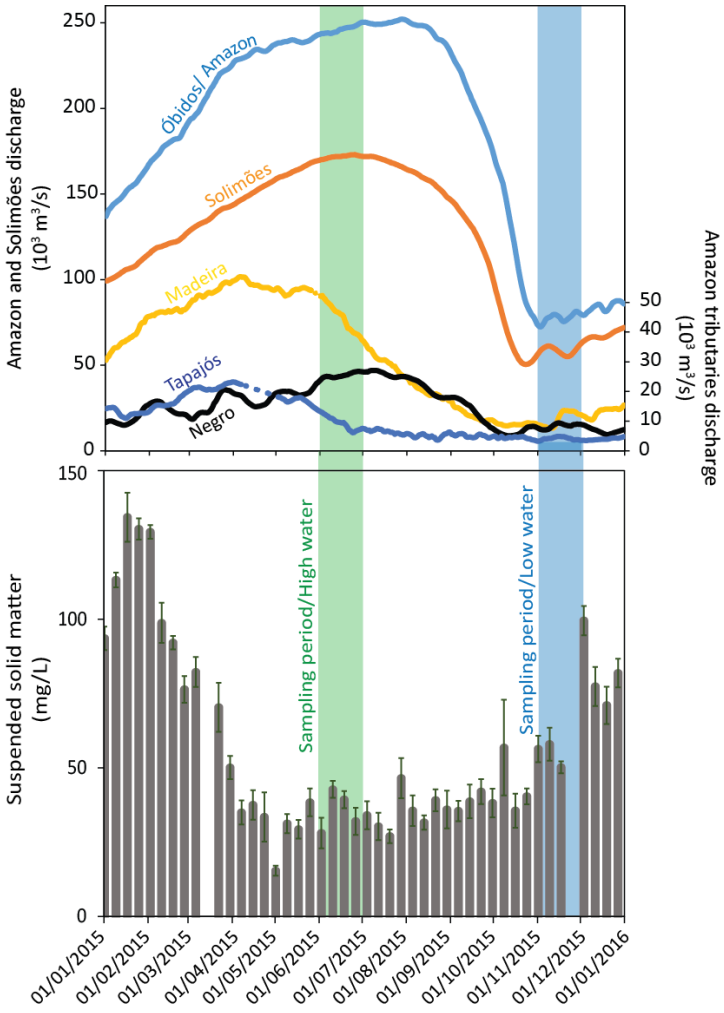

Figure V-2. Top panel: daily water discharge of the Amazon River at Óbidos and its tributaries during 2015. Lower panel: satellite derived suspended sediment concentrations from Óbidos. Data are from: SO-HYBAM website – (http://www.ore-hybam.org).

V.4 Results

V.4.1 In situ measurements and discharge

In the Amazon River and its tributaries, the range of temperature (27.4 to 32.3°C) and pH (4.6 to 8.6) was fairly narrow in both the HW and LW stages (Table V-1). Nevertheless, during the LW stage, temperature and pH were slightly higher than they were in the HW stage. The Negro River (NEG1) had the lowest pH, similar to previous measurements for this tributary (Gaillardet et al., 1997; Aucour et al., 2003; Dellinger et al., 2015), and analyses of other organic-rich rivers like the Congo

*Table V-1 Field measurements for the Amazon River and its tributaries (Solimões, Negro, Madeira, Trombetas and Tapajós rivers). Samples are shown in order of increasing distance from the ocean. Discharge data are from the SO-HYBAM website (http://www.ore-hybam.org). *estimated discharges (see text).*

Sample	River name	Longitude (°W)	Latitude (°S)	Distance inland (km)	Depth (m)	Date	Discharge 10^3 m^3/s	Temp (°C)	pH	Date	Discharge 10^3 m^3/s	Temp (°C)	pH
										Dec-15			
MPN1	Amazonas	50.81	0.11	220	1					09/12/2015	216*	29.3	7.4
MPS1	Amazonas	51.06	0.52	220	1					09/12/2015	216*	29.8	7.5
						Jun-15 High water				*Nov-15 Low water*			
ALM1	Amazonas	52.58	1.56	450	1	30/06/2015	258*	-	6.9	11/12/2015	89*	30.6	8.6
AM1	Amazonas	54.39	2.40	650	1	12/06/2015	254*	28.9	6.8	17/11/2015	81*	30.4	7.4
TAP1	Tapajos	55.03	2.49	720	1	11/06/2015	10	30.2	6.9	17/11/2015	5	30.0	6.7
OB1	Amazonas	55.51	1.93	760	1	14/06/2015	246	28.2	7.0	18/11/2015	76	31.4	7.3
TP1	Trombetas	55.88	1.75	790	1	14/06/2015	-	29.0	6.1	19/11/2015	-	32.3	6.6
PAR1	Amazonas	56.85	2.59	923	1	16/06/2015	246	27.4	6.8	21/11/2015	77	30.8	7.1
ITA1	Amazonas	58.57	3.25	1130	1	18/06/2015	241*	28.4	6.8	23/11/2015	77*	30.8	7.0
MAD1	Madeira	58.79	3.42	1150	1	18/06/2015	44	28.9	6.7	23/11/2015	13	31.9	7.3
MAN1	Amazonas	59.29	3.21	1200	1	19/06/2015	198*	-	6.7	24/11/2015	64*	30.9	7.0
MAN2	Amazonas	59.52	3.13	1230	1	19/06/2015	198*	-	6.9	24/11/2015	64*	29.2	7.2
MAN3	Amazonas	59.73	3.06	1250	1	20/06/2015	199*	-	6.4	25/11/2015	66*	30.4	7.0
MAC1	Solimoes	60.67	3.33	1350	1	21/06/2015	173	28.2	6.9	26/11/2015	66	29.5	7.2
NEG1	Negro	60.40	3.05	1310	1	22/06/2015	26	29.9	4.6	27/11/2015	9	32.6	5.3
Profile													
OB1.30	Amazonas	55.51	1.93	760	30	13/06/2015	245	28.6	7.0	18/11/2015	76	30.3	7.3
OB1.60	Amazonas	55.51	1.93	760	60	13/06/2015	245	28.4	7.1	18/11/2015	76	30.3	7.4
MAN3.15	Amazonas	59.73	3.06	1250	15	20/06/2015	198*	-	6.5	25/11/2015	66*	30.6	7.0
MAN3.30	Amazonas	59.73	3.06	1250	30	20/06/2015	198*	-	6.7	25/11/2015	66*	30.0	7.0
MAN3.45	Amazonas	59.73	3.06	1250	45	19/06/2015	199*	28.7	6.7	25/11/2015	66*	31.4	7.0
MAN3.60	Amazonas	59.73	3.06	1250	60	19/06/2015	199*	28.9	6.6	25/11/2015	66*	31.3	7.1

Basin (Dupré et al., 1996). Similarly to hydrological data from 1983-2012 (Moquet et al., 2016), the maximum monthly discharges of the Tapajós (TAP1), Madeira (MAD1), Solimões and Negro (NEG1) Rivers occurred in March, April, June and July, respectively (the discharge in Trombetas was not determined; Figure V-2). At Óbidos, the discharge was maximum (~252.10^3 m^3/s) between June and August 2015 while the lowest discharge (~72.10^3 m^3/s) was measured in November. The discharges of MAN1, MAN2, MAN3, ITA, AM1, ALM1, MPN1 and MPS1 were estimated by summing the discharge of the main stem and the discharge of the tributary, assuming that evaporation is negligible. The November discharge of the Amazon at OB1 was 31% lower than the discharge observed in June, but this decrease of discharge can be up to 48% in TAP1. The suspended sediments concentration ranged between 15 to 135 mg/L and had minimum concentration during the HW stage (Figure V-2).

V.4.2 Major element concentration

V.4.2.1 Dissolved load

Solute concentrations (Na, Ca, Mg, K, Al, Fe, Sr and Li) are displayed in Table V-2. The Amazon River waters (including the Solimões) were dominated by Ca^{2+} (104 - 238 µmol/L), followed by Na^{+} (55 –

Table V-2. Concentration of major elements, Al and Li (± 10%) in the Amazon and its tributaries in the dissolved phase. TZ^+ = Total cation concentrations (µeq/L).*

Water samples	µmol/L					nmol/L	TZ^+*	µmol/L					nmol/L	TZ^+*
	Na^+	Ca^{2+}	Mg^{2+}	K^+	Al	Li		Na^+	Ca^{2+}	Mg^{2+}	K^+	Al	Li	
								Dec-15						
MPN1								163	155	64	23	0.1	76	600
MPS1								144	151	56	23	0.4	89	556
	Jun-15 High water							*Nov-15 Low water*						
ALM1	70	150	46	23	0.5	49	484	174	183	64	28	0.3	56	697
AM1	69	156	44	24	0.5	95	492	171	186	62	27	0.2	80	693
TAP1	22	16	12	16	2.2	24	92	28	25	30	16	0.4	26	156
OB1	64	145	37	23	1.1	90	450	140	166	50	23	0.1	87	571
TP1	50	22	13	23	2.3	49	143	59	16	9	16	0.4	24	124
PAR1	69	175	38	22	0.4	102	516	180	217	68	22	0.2	136	773
ITA1	78	191	46	23	0.5	99	575	100	146	36	22	0.1	89	464
MAD1	69	108	66	31	0.3	135	448	199	187	156	37	0.2	210	886
MAN1	55	121	29	16	1.9	57	372	102	117	34	18	0.6	76	423
MAN2	85	214	43	20	0.9	75	619	112	163	38	22	0.1	91	514
MAN3	70	153	41	21	1.0	102	480	112	104	37	18	0.9	68	396
MAC1	94	238	53	25	0.2	91	700	182	222	63	24	0.2	114	775
NEG1	10	5	3	6	5.2	23	31	15	3	4	10	2.8	20	39
Profile														
OB1.30								191	213	68	24	0.3	148	778
OB1.60								170	183	61	23	0.2	137	681
MAN3.15								147	155	46	20	1.0	120	570
MAN3.30								174	195	56	24	0.7	148	700
MAN3.45								162	184	52	21	0.7	144	656
MAN3.60								-	-	-	-	-	-	-
	Jan-15							*Aug-15*						
OB1	163	247	80	27	0.2	160	819	114	168	53	24	0.3	112	555

182 µmol/L) and Mg^{2+} (29 – 68 µmol/L). In the tributaries, sodium and potassium were the most abundant cations in the Negro and Trombetas (TP1) rivers while the composition of Tapajós and Madeira rivers was not dominated by any cation. Sodium concentrations are higher at the LW stage (average 144 µmol/), than they are at the HW stage (average 73 µmol/L) in the Amazon River. A significant increase of the mean Mg^{2+} concentration was also observed in the Madeira at the LW stage (156 µmol/L, compared to 66 µmol/L at HW) and Tapajós rivers (30 µmol/L compared to 12 µmol/L at HW). The concentrations of the cations were in the range of previous measurements made between 2001-2012 in the Solimões, Madeira (MAD1), Negro (NEG1), Óbidos and Tapajós (TAP1) rivers (Gaillardet et al., 1997; Dosseto et al., 2006; Hughes et al., 2013; Dellinger et al., 2015; Moquet et al., 2016), close to Parintins (PAR1) (Dosseto et al., 2006) and in the Trombetas (TP1) River (Dosseto et al., 2006; Dellinger et al., 2015). There was no obvious change in the dissolved cation composition with depth during the LW stage at MAN3 and OB1. The total cationic charge ($TZ^+=Na^+ + K^+ + 2Ca^{2+} + 2Mg^{2+}$) in the Amazon floodplain was higher in the LW stage (39 to 886 µeq/L; average = 501 µeq/L) compared to the HW stage (31 to 700 µeq/L; average = 416 µeq/L). In both stages the total cationic charge was within the range measured in other lowlands rivers (294 to 743 µeq/L; Moquet et al., 2011).

V.4.2.2 Chemical composition of the suspended sediments

Table V-3 shows the relative proportions of major elements in the surface suspended sediment; concentrations of these elements were within the range of those previously reported in the Amazon River and its tributaries (Gaillardet et al., 1997; Dosseto et al., 2006; Viers et al., 2008; Dellinger et al., 2014). The sediments carried by the Amazon main stem were principally composed of Al (5.75 to 15.10 wt %) and Fe (2.54 to 7.68 wt %), followed by K (1.37 to 3.54 wt %) and Na (0.12 to 1.58 wt %). For all the samples, there were no clear changes of the elemental composition between the LW and HW stages, and there was little change in chemical composition with depth in the Amazon River at MAN3 and OB1.

The chemical index of alteration (CIA; Nesbitt and Young, 1982) can be used to evaluate the extent of silicate weathering (Eq. V-1):

$$CIA\ (wt\ \%) = \frac{Al_2O_3}{Al_2O_3 + CaO^* + Na_2O + K_2O} \times 100\ (molar\ proportions) \qquad \textit{Eq. V-1}$$

The CIA reflects the proportion of Al_2O_3 to labile oxides (CaO* is the amount of Ca only derived from silicate weathering), and therefore higher values are representative of more intensely weathered materials (Nesbitt and Young, 1982). Similarly to Viers et al. (2008), CaO* is assumed to be equal to CaO if CaO ≤ Na_2O. CIA values of between 30 - 55 are indicative of unweathered silicates (basalts, granites and granodiorites), while a value of 100 indicates the complete removal of labile oxides

Table V-3. Elemental composition of the suspended sediments in the Amazon and the Negro River during high and low water stage. CIA = Chemical index of alteration.

Sediment samples	Weight %						ppm		CIA	Weight %						ppm		CIA
	Na	Ca	Mg	K	Al	Fe	Sr	Li		Na	Ca	Mg	K	Al	Fe	Sr	Li	
	Jun-15 High water									*Nov-15 Low water*								
ALM1	0.77	0.71	0.89	2.40	9.34	4.42	155	59	71	0.73	0.68	0.84	2.38	9.41	4.19	144	58	71
OB1	0.92	0.72	0.87	2.39	8.91	4.07	163	58	69	0.97	0.83	1.04	2.64	11.33	4.48	181	61	72
PAR1	0.88	0.35	0.78	2.41	9.26	3.71	135	60	72	0.98	0.77	0.98	2.51	10.00	4.28	166	57	70
ITA1	0.82	0.86	0.91	2.23	8.71	4.45	170	52	69	0.75	0.77	0.85	2.02	9.26	4.06	167	50	72
MAN1	1.04	1.11	1.03	2.46	10.32	5.12	198	51	69	1.06	1.02	1.03	2.24	9.97	4.43	199	49	70
MAN3	1.39	1.40	1.55	3.54	15.10	7.68	211	66	70	-	-	-	-	-	-	-	-	-
NEG1	0.12	0.07	0.15	1.37	8.04	5.14	42	16	84	0.26	0.15	0.27	1.55	10.43	3.09	56	24	84
Profile																		
OB1.15	0.86	0.65	0.78	1.56	6.85	3.08	152	47	67	0.73	0.88	0.92	2.31	9.65	4.14	142	54	68
OB1.30	1.01	0.77	0.81	2.07	7.51	3.64	167	46	60	0.95	0.76	0.87	2.19	9.68	3.89	168	51	68
OB1.30	1.07	0.79	0.66	1.81	6.20	3.00	165	36	60	0.99	0.79	0.90	2.20	9.18	3.95	172	52	64
OB1.60	1.11	0.77	0.59	1.83	5.75	2.65	168	31	59	0.76	0.60	0.70	1.72	7.21	3.07	133	40	59
MAN3.15	1.30	1.18	1.07	2.50	10.04	5.05	209	46	69	0.99	0.99	0.90	1.85	8.25	3.83	183	41	71
MAN3.30	1.55	1.33	0.88	2.23	7.63	3.46	251	34	66	1.01	1.02	0.93	1.92	8.35	3.89	186	42	71
MAN3.45	1.47	1.26	0.91	2.36	7.72	3.68	234	36	63	1.30	1.16	0.90	1.79	7.50	3.48	217	36	70
MAN3.60	1.58	1.28	0.83	1.82	6.75	3.09	255	30	61	1.20	0.88	0.58	1.67	5.32	2.54	185	22	70
	Jan-15									*Aug-15*								
OB1	0.83	0.64	0.99	2.62	10.03	4.20	150	61	71	0.84	0.76	0.92	2.29	9.05	4.12	160	54	70

from the parent rocks (Nesbitt and Young, 1982). CIA values calculated for the surface suspended sediments in the Amazon main stem ranged between 68.9 and 72.4 (Table V-3) and values were similar in both hydrological stages. These measurements were within the range of previously calculated CIA values in the Solimões (68 – 71; Viers et al., 2008). However, at deeper depths the CIA of suspended sediments was always lower than the CIA of sediments sampled close to the surface (Table V-3). The Negro River has significantly higher CIA values with an average of 84.

V.5 Li and Mg isotopes in the dissolved phase

V.5.1 [Li] and δ^7Li

Concentrations of Li in the HW stage ranged from 14 to 135 nmol/L and the average [Li] in the main stem of the Amazon River was 85 nmol/L (Figure V-3). In the LW stage, Li concentrations were slightly higher (20 to 210 nmol/L), and the average [Li] in the main stem of the Amazon River was 88 nmol/L. These concentrations were similar to those measured previously in rivers in the Amazon floodplain (Gaillardet et al., 1997; Huh et al., 1998; Dellinger et al., 2015). Highest Li concentrations (135 nmol/L in HW and 210 nmol/L in LW) and the biggest variations were measured in the Madeira

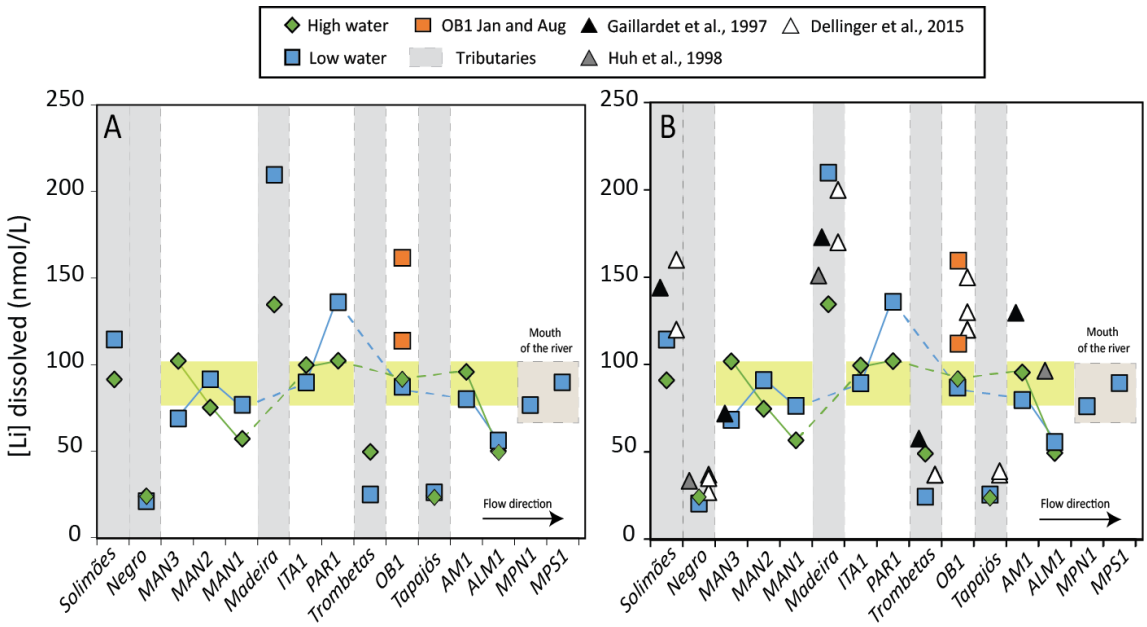

Figure V-3. A. Li concentration of the dissolved load in the in the Amazon River and its tributaries. B. Comparison with other published values. Tributaries are highlighted by grey shaded boxes. The yellow shaded box shows the average [Li] (±10%) for the main stem of the Amazon River in both the HW and LW stages. Sampling locations are linked with a solid line when they are adjacent; otherwise they are linked with a dashed line.

River (MAD1). By contrast, there was little change in the Li concentrations in the Negro, Tapajos and Trombetas tributaries, and these have relatively low Li concentrations (20 - 49 nmol/L).

The δ^7Li values of the dissolved load ranged from 1 to 30.3‰ (Figure V-4; Table V-4). In the HW stage, the δ^7Li of samples collected from the main stem of the Amazon River ranged from 11.2 to 17.8‰ (average 16.3‰), whereas in the LW stage δ^7Li values generally increased and ranged from 18.5 to 23.7‰ (average 21.5‰). At Óbidos, the δ^7Li value was similar in June and August (HW stage, respectively 16.7 and 16.5‰) and in January and November (LW stage, 22.2 and 23.2‰, respectively). The average difference in the δ^7Li value of the dissolved load between the LW and the HW stages was about 6.6‰, with the exception of sample MAN3 that did not show any significant change. The Madeira River had the highest δ^7Li of all the water samples in both the HW and the LW stages (respectively, 21.7 and 30.3‰) and also showed the biggest variation (8.7‰). When considering the whole Amazon River at different hydrological stages, the variation in δ^7Li was greatest for the downstream sites with change >15.5‰ (HW stage ALM1 vs LW stage MPN1; Figure V-4). The Negro River had the lowest δ^7Li (1 and 7.7‰ in the HW and the LW stages, respectively). A similar range of δ^7Li has previously been reported for the Amazon Basin (1.2 to 32.9‰; Dellinger et al. (2015), although the highest δ^7Li value for the lowland rivers (~16‰) was lower than

Table V-4. Li and Mg isotope compositions in the dissolved phase at the different sampling locations. The 2σ is the total internal uncertainty of each measurement.

Water samples	‰											
	δ^7Li	2σ	δ^{25}Mg	2σ	δ^{26}Mg	2σ	δ^7Li	2σ	δ^{25}Mg	2σ	δ^{26}Mg	2σ
							Dec-15					
MPN1							26.7	0.4	-0.42	0.06	-0.79	0.06
MPS1							25.5	0.2	-0.41	0.02	-0.80	0.03
	Jun-15 High water						*Nov-15 Low water*					
ALM1	11.2	0.7	-0.38	0.03	-0.79	0.03	-	-	-	-	-	-
AM1	16.4	1.3	-0.42	0.03	-0.80	0.02	23.7	0.6	-0.42	0.00	-0.81	0.03
TAP1	14.5	0.8	-0.24	0.04	-0.47	0.07	-	-	-0.50	0.01	-0.96	0.02
OB1	16.7	0.6	-0.38	0.01	-0.75	0.00	23.2	0.4	-0.42	0.04	-0.81	0.07
TP1	9.6	0.7	-0.17	0.03	-0.33	0.04	-	-	-	-	-	-
PAR1	16.5	0.5	-0.42	0.01	-0.80	0.07	22.6	0.8	-0.40	0.01	-0.79	0.04
ITA1	15.9	1.3	-0.46	0.02	-0.93	0.02	21.2	0.3	-0.44	0.03	-0.83	0.03
MAD1	21.7	0.4	-0.34	0.02	-0.65	0.03	30.3	0.3	-0.41	0.01	-0.80	0.02
MAN1	13.2	0.2	-0.45	0.02	-0.86	0.06	-	-	-	-	-	-
MAN2	14.6	0.5	-0.41	0.02	-0.80	0.02	20.1	0.1	-0.44	0.00	-0.85	0.00
MAN3	17.8	0.9	-0.38	0.02	-0.76	0.00	18.5	0.5	-0.42	0.02	-0.82	0.01
MAC1	15.6	0.3	-0.47	0.08	-0.93	0.10	-	-	-	-	-	-
NEG1	1.0	1.0	-0.16	0.03	-0.38	0.08	7.7	0.3	-	-	-	-
Profile												
OB1.30							22.6	0.1	-0.42	0.00	-0.81	0.02
OB1.60							23.5	0.3	-0.42	0.01	-0.80	0.04
MAN3.15							17.9	0.2	-0.43	0.06	-0.83	0.07
MAN3.30							19.8	0.1	-0.42	0.06	-0.84	0.03
MAN3.45							20.0	0.1	-0.45	0.00	-0.86	0.05
MAN3.60							20.4	0.2	-0.42	0.01	-0.81	0.00
	Jan-15						*Aug-15*					
OB1	22.2	0.0	-0.43	0.03	-0.82	0.02	16.5	0.4	-0.46	0.01	-0.88	0.02

measured in this study. Huh et al. (1998) reported δ^7Li values of 21.6±1.3‰ at the mouth of the Amazon River, and 10.5±1.3‰ for the Negro River (Figure V-4). During the LW stage, there was no significant variation in δ^7Li with depth at Óbidos (average = 21.6‰); this was also the case in the HW stage (Dellinger et al., 2015). At Manaus, water samples collected between 1 to 15 m depth had lower δ^7Li (average = 18.2‰) compared to samples collected from 30, 45 and 60 m depth (from 19.8 to 20.4‰; Table V-4).

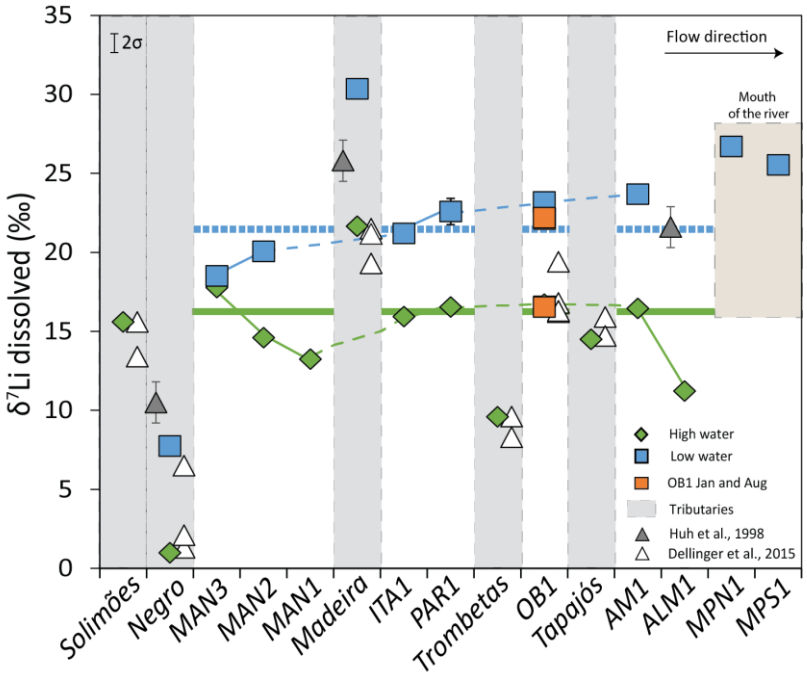

Figure V-4. δ^7Li values of the dissolved load in the Amazon River and its tributaries plotted with previous measurements of δ^7Li. Tributaries are highlighted by grey shaded boxes. The green solid line and blue dotted line show the average δ^7Li for the main stem of the Amazon River in the HW and the LW stage, respectively. Sampling locations are linked with a solid line when they are adjacent; otherwise they are linked with a dashed line. Error bars show the external error (0.6‰, 2σ) of the isotope analyses calculated with repeated measurements of L-SVEC (δ^7Li = 0.0 ± 0.5‰ (2SD, n = 28)), and IAPSO (δ^7Li = 30.9 ± 0.6‰ (2SD, n = 27).

V.5.2 [Mg] and δ^{26}Mg

The dissolved [Mg] varied from 3 to 156 µmol/L (Figure V-5; Table V-2). In the main stem of the Amazon River, Mg concentrations were on average slightly higher in the HW stage than in the LW stage (49 vs 42 µmol/L, respectively), although [Mg] was slightly higher during the LW stage after the confluence with the Trombetas tributary (samples OB1, AM1 and ALM1). Concentrations of Mg in the tributaries Negro, Trombetas and Solimões did not show any significant change between the HW and the LW stages, but some variations were observed in the Madeira River and Tapajós River,

with Mg concentrations increasing by 90 and 18 µmol/L respectively in the LW stage (Figure V-5). Negligible variations of [Mg] in the main stem of the Amazon and its tributaries have also been reported in other studies (Mortatti and Probst, 2003; Hughes et al., 2013; Moquet et al., 2016). Compared to a previous study, the dissolved [Mg] measured in Madeira River was high (up to 156 µmol/L), however significant increase in Mg concentrations of up to 70 µmol/L have also been reported in this river (Hughes et al., 2013).

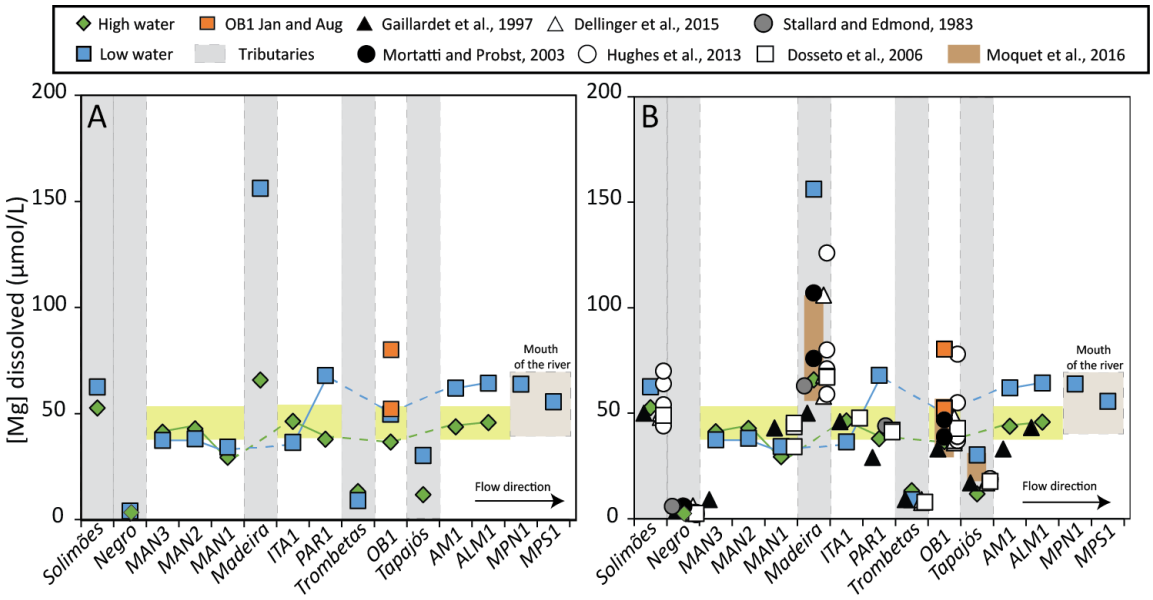

Figure V-5. A. Mg concentration of the dissolved load in the in the Amazon River and its tributaries. B. Comparison with other published values. Tributaries are highlighted by grey shaded boxes. The yellow shaded box shows the average [Mg] (±10%) for the main stem of the Amazon River in both the HW and the LW stages. Sampling locations are linked with a solid line when they are adjacent; otherwise they are linked with a dashed line.

Mg isotope analyses of the Amazon River have previously been reported for two stations close to PAR1 and ALM1 (Figure V-6) during the high water stage, and gave δ^{26}Mg between -1.03 and -0.87‰, averaging at -0.95‰ (Tipper et al., 2006b). In comparison, the δ^{26}Mg of the dissolved load of the main stem of the Amazon River determined in this study ranged from -0.93 to -0.75‰ (average = -0.81‰) during the high water stage and from -0.85 to -0.79‰ (average = -0.82‰) during the low water stage (Figure V-6, Table V-4; excluding samples MPN1 and MPS1). Over the course of a year, the δ^{26}Mg value of dissolved Mg at Óbidos only varied by 0.13‰ (Figure V-6). However, the range in δ^{26}Mg was higher in the tributaries of the Amazon River, -0.96 to -0.33‰. The Tapajós had the lowest δ^{26}Mg (-0.96‰) and the Trombetas River and the Negro River had the highest values (-0.33‰ and -0.38‰, respectively). The values for the Trombetas and Negro were

amongst the highest values recorded in the world's largest rivers (Tipper et al., 2006b). Only the Tapajós and Madeira tributaries were analysed for both hydrological stages and both appear to be slightly enriched in lighter Mg isotopes during the LW stage. There is no significant variation in dissolved δ^{26}Mg with depth at Óbidos and Manaus (OB1 average = -0.80‰ and MAN3 = -0.81 to -0.86‰).

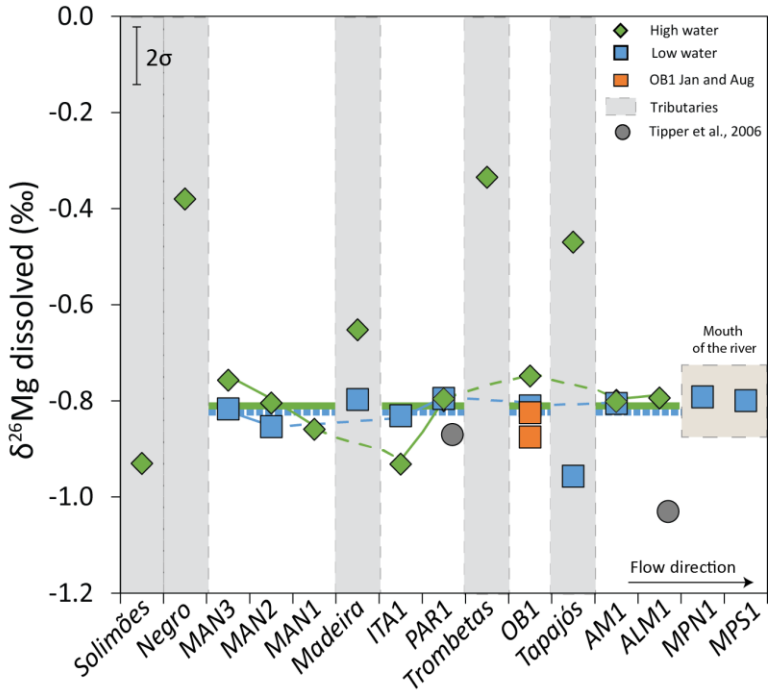

Figure V-6. δ^{26}Mg values of the dissolved load in the Amazon River and its tributaries plotted with previous measurements of δ^{26}Mg. Tributaries are highlighted by grey shaded boxes. The green solid line and blue dotted line show the average δ^{26}Mg for the main stem of the Amazon River in the HW and the LW stage, respectively. Sampling locations are linked with a solid line when they are adjacent; otherwise they are linked with a dashed line. Error bar show the external error (0.06‰, 2σ) of the isotope analyses calculated with repeated measurements of DSM-3 (δ^{26}Mg = 0.00 ± 0.07‰ (2SD, n = 27)) and IAPSO (δ^{26}Mg = -0.82 ± 0.05‰ (2SD, n = 18)).

V.6 Li and Mg in the suspended sediments

V.6.1 δ^{7}Li and δ^{26}Mg in surface suspended sediments

In the main stem of the Amazon River, concentrations of Li in surface suspended sediments collected during the HW stage were in average about 58 ppm and during the LW stage Li concentrations were 55 ppm (Table V-3 and Figure V-7). Li concentrations were similar to the mean [Li] measured for other large rivers (50±10 ppm; Dellinger et al., 2014), but they were lower than previously measured at Óbidos (Dellinger et al., 2014; Figure V-7). The highest [Li] (66 ppm) was

measured at MAN3 after the confluence with the Negro River, which had suspended sediments with much lower [Li] (16-24 ppm). The Li content of the suspended sediments in the Negro measured in this study was lower than reported previously for this river (44 ppm; Dellinger et al., 2015). There were no variations in the Mg concentration between HW and LW stages of the suspended sediments, and Mg concentrations were on average about 0.90 wt % in the HW stage and 0.95 wt % in the LW stage. These values were within the range of those reported previously at stations MAN1, PAR1 and OB1 during the HW stage (0.92 - 0.99 wt %; Dosseto et al., 2006) and for the Solimões River (1.03±0.09 wt %; Dosseto et al., 2006; Viers et al., 2008). Highest Mg concentrations were measured at MAN3 ([Mg] = 1.55 wt %) and the lowest concentrations were measured at NEG1 ([Mg] = 0.15 - 0.27 wt %; Figure V-7).

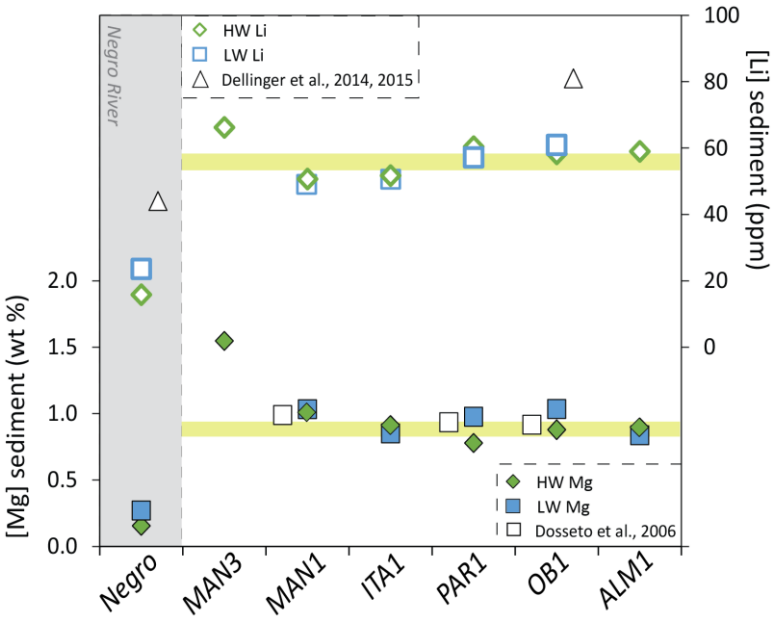

Figure V-7. Li and Mg concentration of surface suspended sediments in the main stem of the Amazon River and the Negro River. The yellow shaded boxes show the average values for the Amazon River.

The δ^{26}Mg values of surface suspended sediments of the Amazon River ranged from -0.12 to 0.09‰ (average = -0.02‰) during the HW stage and from -0.03 to 0.01‰ (average = -0.01‰) during the LW stage (Table V-5 and Figure V-8A). There was no significant change in δ^{26}Mg between the stages, with the exception of sample PAR1, which decreased by 0.11‰ in the LW stage. The δ^{26}Mg values of the suspended sediments were close to the δ^{26}Mg values of bedrocks present in the Amazon basin like andesite (-0.15±0.07‰; Dessert et al., 2015) and diorite/granodiorite (δ^{26}Mg = -0.31 to

Table V-5. Li and Mg isotope compositions in the suspended sediments at the different sampling locations. The 2σ is the total internal uncertainty of each measurement.

Sediment samples	‰											
	δ^7Li	2σ	δ^{25}Mg	2σ	δ^{26}Mg	2σ	δ^7Li	2σ	δ^{25}Mg	2σ	δ^{26}Mg	2σ
	Jun-15 High water						*Nov-15 Low water*					
ALM1	-2.3	0.5	0.01	0.02	0.01	0.01	-2.7	0.2	0.01	0.02	0.00	0.00
OB1	-1.7	0.3	0.00	0.01	0.00	0.01	-2.6	0.2	0.01	0.02	0.01	0.02
PAR1	-1.4	0.8	0.05	0.00	0.09	0.01	-2.6	0.4	0.00	0.04	-0.02	0.07
ITA1	-2.6	0.1	-0.01	0.01	-0.04	0.02	-1.9	0.6	0.01	0.02	0.01	0.04
MAN1	-2.1	0.5	-0.04	0.02	-0.08	0.04	-1.6	0.1	0.00	0.01	-0.03	0.00
MAN3	-2.9	0.4	-0.06	0.02	-0.12	0.03	-	-	-	-	-	-
NEG1	-4.1	0.3	-0.01	0.01	-0.01	0.00	-3.6	0.4	-0.02	0.04	-0.04	0.02
Profile												
OB1.15	-1.7	0.9	0.00	0.03	-0.03	0.05	-3.0	0.1	0.05	0.01	0.06	0.02
OB1.30	-1.6	0.6	0.00	0.04	-0.02	0.03	-2.0	0.3	0.07	0.01	0.12	0.02
OB1.30	-0.7	0.2	0.00	0.01	-0.03	0.00	-1.5	0.3	0.07	0.05	0.11	0.04
OB1.60	-0.6	0.5	-0.03	0.06	-0.09	0.05	-2.0	0.6	0.06	0.05	0.11	0.07
MAN3.15	-1.9	0.4	-0.02	0.03	-0.07	0.05	-1.3	0.6	0.03	0.00	0.04	0.00
MAN3.30	-0.5	0.8	-0.04	0.01	-0.10	0.06	-2.2	0.2	0.01	0.04	0.01	0.01
MAN3.45	-1.1	0.5	-0.05	0.02	-0.11	0.06	-1.9	0.6	0.01	0.00	-0.02	0.05
MAN3.60	-0.4	0.5	-0.05	0.02	-0.11	0.03	0.2	0.1	0.01	0.01	-0.01	0.05
	Jan-15						*Aug-15*					
OB1	-1.9	0.0	0.01	0.01	0.01	0.01	-2.7	0.2	0.00	0.05	-0.01	0.10

0.04‰; Teng, 2017) but they were significantly higher than shale (e.g. SCo-1 δ^{26}Mg = -0.90±0.07‰; this study, Chapter 2) or δ^{26}Mg values of the corresponding dissolved phase, as observed in other river systems (Wimpenny et al., 2011; Tipper et al., 2012b).

The δ^7Li values of the surface suspended sediments in the main stem of the Amazon River ranged from -2.9 and -1.4‰ (average = -2.4‰) during the HW stage and from -2.7 to -1.6‰ (average = -

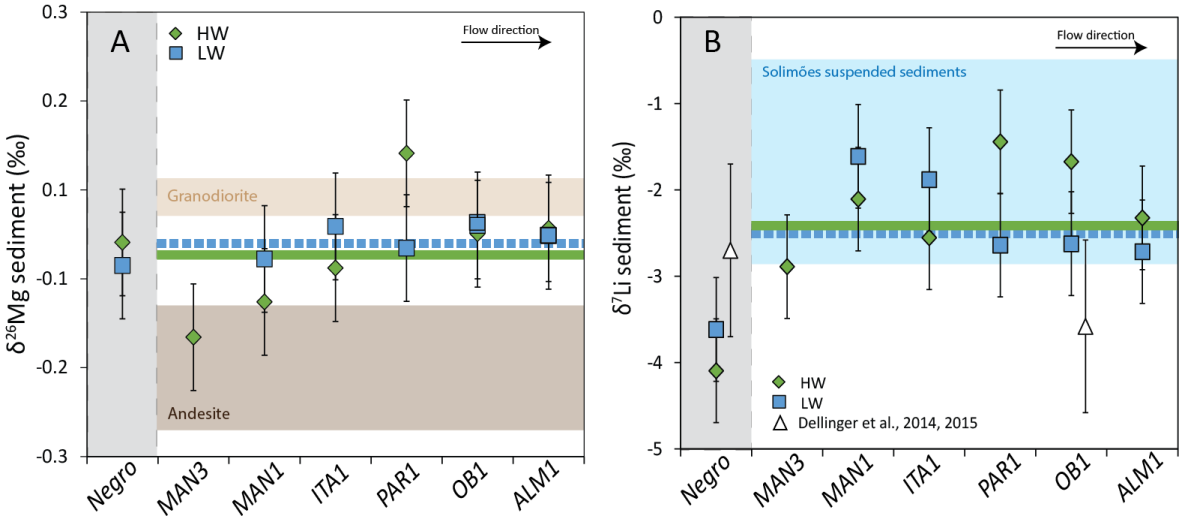

Figure V-8A. δ^{26}Mg values and B. δ^7Li of the suspended load for the main stem of the Amazon River and the Negro River. The brown shaded boxes show the standard deviation around the average granodiorite and andesite rock δ^{26}Mg values. The blue shaded box shows the standard deviation around the average surface suspended sediment value of the Solimões (Dellinger et al., 2014). The green solid lines and blue dotted lines show the average of δ^{26}Mg and δ^7Li calculated in the Amazon River in both HW and LW stages. Error bars represent the external error (2σ).

2.5‰) during the LW stage (Table V-5 and Figure V-8B). Thus, like $\delta^{26}Mg$, there were no significant variations in the $\delta^{7}Li$ values of the suspended between the HW and the LW stages. The $\delta^{7}Li$ values of the suspended sediments were lighter than the $\delta^{7}Li$ values of bedrocks present in the Amazon basin like andesite (5.3‰; Clergue et al., 2015), diorite/granodiorite ($\delta^{7}Li$ = -0.8 to 2.3‰; James and Palmer, 2000; Sun et al., 2016) and shale (e.g. SCo-1 $\delta^{7}Li$ = 0.80±0.6‰; this study, Chapter 2). The Negro River had distinctly lower $\delta^{7}Li$ for the suspended sediments (-3.6 and -4.1‰) compared to the main stem. The $\delta^{7}Li$ values of the suspended sediments were in the range of those measured previously in large rivers (-1.5±1‰; Dellinger et al., 2014). However, while previous measurements of surface $\delta^{7}Li$ in the Madeira and Solimões rivers (-2.90 and -2.60‰ respectively; Dellinger et al., 2014) were similar to this study, the Negro and Óbidos rivers had significantly different values with $\delta^{7}Li$ = -2.7 and -3.6‰ respectively (Dellinger et al., 2014; Dellinger et al., 2015).

V.6.2 Variation in $\delta^{7}Li$ and $\delta^{26}Mg$ in suspended sediments with depth

The [Li] in the suspended sediments was similar at Óbidos and Manaus, and was similar in both the HW and the LW stages. At both stations, there was an overall slight decrease in [Li] with depth, by up to 27 ppm at Óbidos and 36 ppm at Manaus. The Mg concentration of the suspended sediments also decreased slightly with depth, by up to 0.72 wt % (in the HW stage) at Manaus and up to around 0.32 wt % at Óbidos (Figure V-9).

At Óbidos, the $\delta^{7}Li$ value of the suspended sediments increased slightly with depth, from -3‰ at the surface to -1.5‰ close to the river bed in the LW stage, and from -1.7‰ at the surface to -0.6‰ close to the river bed in the HW stage. At Manaus the $\delta^{7}Li$ value of the suspended sediments also increased slightly with depth, but there was no obvious change in $\delta^{7}Li$ between the HW and the LW stage. The $\delta^{26}Mg$ values of the suspended sediments in the two profiles were higher in the LW stage than they were in the HW stage, at both sites (Figure V-9). There was no obvious change in the $\delta^{26}Mg$ value of the suspended sediments with depth, at either site.

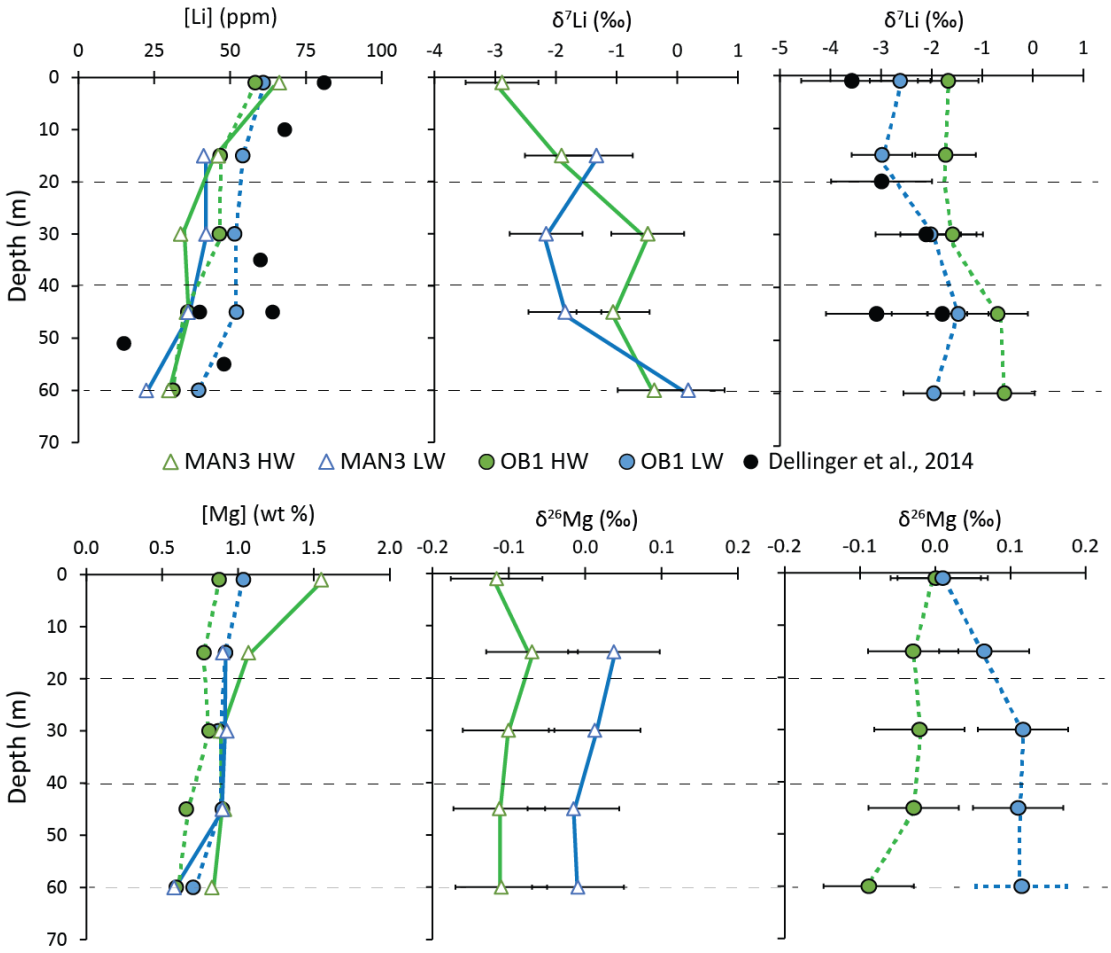

Figure V-9. Profiles of [Li] and δ^7Li (first row), and with [Mg] and δ^{26}Mg (second row) in suspended sediments from Óbidos and Manaus. The error bars represent the external error (2σ).

V.7 Discussion

V.7.1 Li and Mg isotope signatures of the suspended sediments: Tracers of sources and dynamics.

The CIA values of the surface suspended sediments from the Amazon River (Table V-3) are higher than the CIA of unweathered rocks (~50; Nesbitt and Markovics, 1997) consistent with materials that have lost soluble elements such as Na and K during the weathering process (Nesbitt and Young, 1982). The chemical composition of the sediments does not change along the Amazon system in either hydrological stage despite the influence of suspended particles from tributaries that have sediments with different elemental compositions like the Madeira River (Viers et al., 2008; Dellinger et al., 2014). The δ^7Li and δ^{26}Mg values of the suspended sediments are generally lighter and heavier respectively than the catchment bedrock values (δ^7Li = -0.8 to 5.3‰ and δ^{26}Mg = -0.9 to

0.04‰) which supports other studies that indicate that secondary mineral phases are preferentially enriched in light Li isotopes and heavy Mg isotopes (Teng et al., 2010; Pogge von Strandmann et al., 2012). Additionally, the δ^7Li and δ^{26}Mg values of surface sediments do not vary with hydrological stages or with distance along the river (upstream to downstream samples) which suggests that the suspended sediments are not further weathered in the Amazon River. Rather, the suspended sediments provide a record of the weathering history of the basin on long timescales (Gaillardet et al., 1999a; Dosseto et al., 2006; Bouchez et al., 2012; Dellinger et al., 2014).

There are clear differences in the Li and Mg compositions of the suspended sediments sampled at OB1 and MAN3 as a function of depth, and also between the HW and LW stages. [Li] and [Mg] decrease with increasing depth (R^2 = 0.94-0.99;Figure V-10), which can be attributed to enrichment of coarse-grained material with a high proportion of albite and quartz at the bottom of the Amazon River, and a lower proportion of fine-grained clays that are relatively enriched in Li and Mg (Bouchez et al., 2011; Dellinger et al., 2014). By contrast, there were no clear variations in δ^7Li and δ^{26}Mg with depth for both profiles (Figure V-10). We estimate the degree of weathering by comparing the Na and the Al content in the suspended sediments (Figure V-11). Na is a soluble element whereas Al is relatively immobile, so the Al/Na ratio of sedimentary materials will increase with increased weathering intensity (Nesbitt and Young, 1982). Figure V-11 clearly shows that δ^7Li decreases with increased weathering intensity and, additionally, the δ^7Li of the sediments increases from the

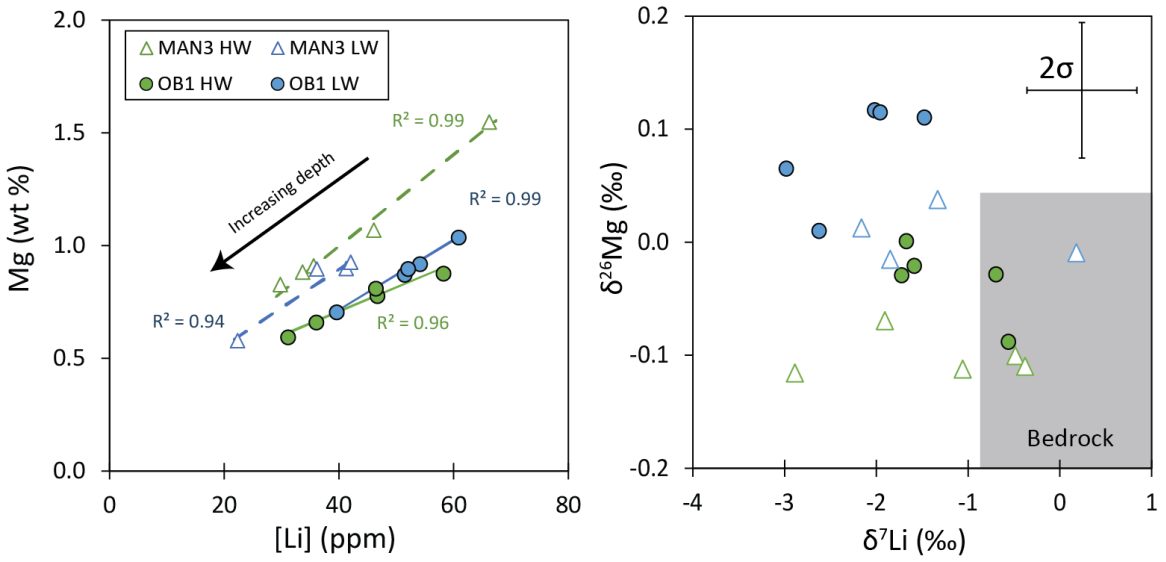

Figure V-10. Comparison between the [Li] and [Mg] and the δ^7Li and δ^{26}Mg of the suspended sediments in the Óbidos and Manaus profile The grey shaded box shows the compilation of δ^7Li and δ^{26}Mg values for the bedrocks.

surface of the river to the river bed implying that the surface waters contain more weathered material (Figure V-9). This is consistent with results reported by Dellinger et al. (2014), for a profile at Óbidos, and with our CIA calculations that are higher close to the surface. At Óbidos, sediments sampled in June had higher δ^7Li and lower Al/Na which suggests that during HW stage the Amazon River (at Óbidos) carries less weathered and/or coarser sediments which is consistent with the high discharge that is capable of transporting heavier material. Similar behaviour has been observed in the Madeira River where fine-grained, clay rich materials were predominantly transported during the low water stage (Bouchez et al., 2014b). This behaviour was not observed at Manaus or in the Solimões (Bouchez et al., 2014b), which suggests that the sediment nature is mainly controlled by sediment inputs from the Madeira River. This is consistent with results reported by Vauchel et al. (2017), indicating that the Madeira River can contribute up to 50% of the sediments present in the

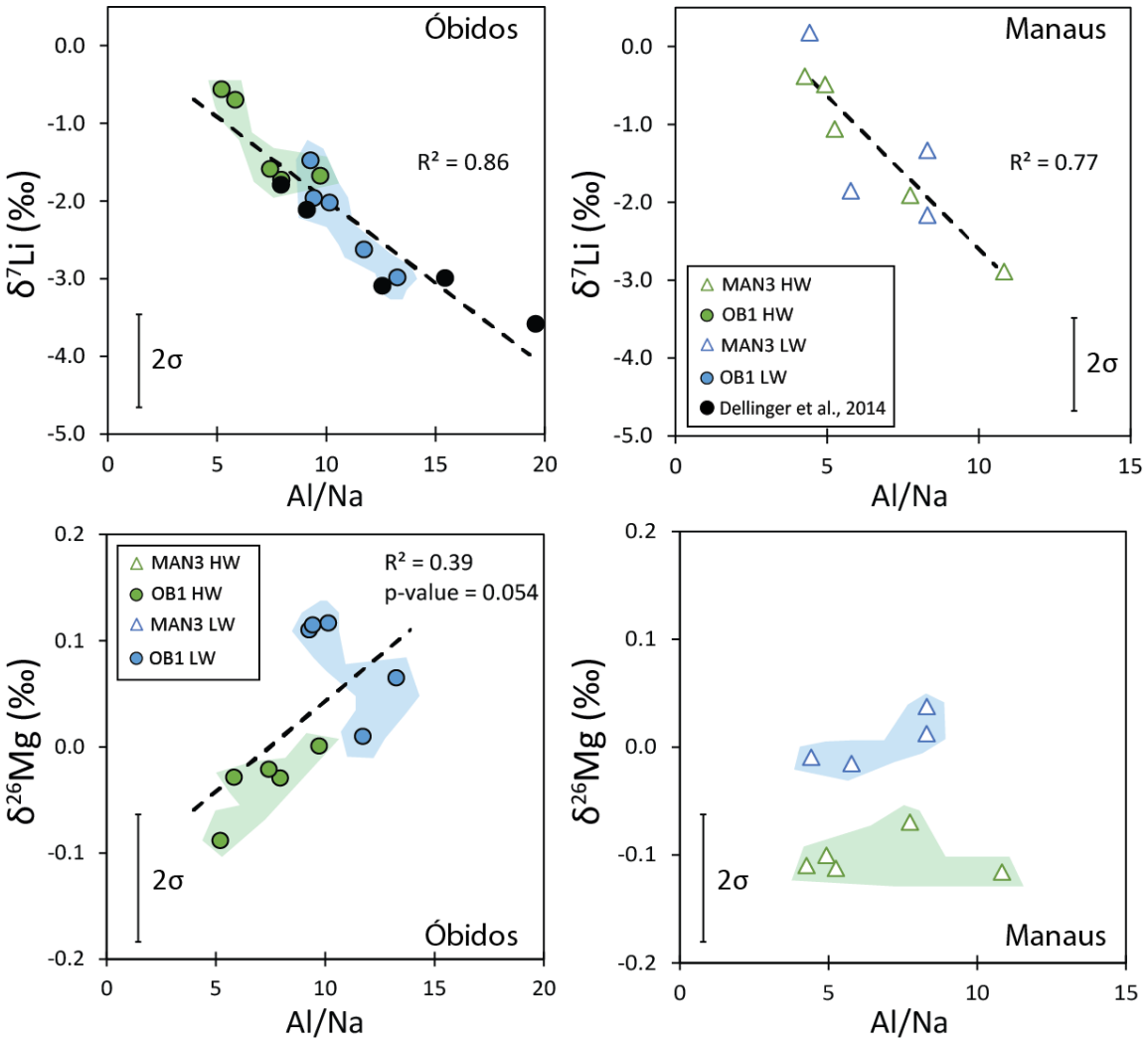

Figure V-11. Al/Na vs δ^7Li and δ^{26}Mg for the two full-depth profiles sampled in June and in November.

main Amazon stem. During the LW stage, at Óbidos, the sediments carried by the river have higher Al/Na and higher $\delta^{26}Mg$ which suggests that more weathered materials enriched in heavy Mg isotopes compared to the bedrock (Tipper et al., 2006a; Brenot et al., 2008) are transported at low discharge. This is consistent with our previous conclusions made with $\delta^{7}Li$ in sediments at Óbidos.

V.7.2 Li and Mg composition of the Amazon River: Tracers of weathering intensity in Amazonian tributaries

The $\delta^{26}Mg$ and $\delta^{7}Li$ of the dissolved phase of the Amazon River are respectively lighter and heavier than the $\delta^{26}Mg$ and $\delta^{7}Li$ of suspended sediments consistent with preferential uptake of heavy Mg isotopes and light Li isotopes by secondary minerals (Huh et al., 2001; Kisakurek et al., 2005; Tipper et al., 2006a; Brenot et al., 2008; Opfergelt et al., 2012; Dellinger et al., 2014). There is positive correlation between [Mg] and [Li] in the Amazon River (R^2 = 0.77 - 0.81), but no correlation between $\delta^{7}Li$ and $\delta^{26}Mg$ (Figure V-12). This suggests that additional other processes, in addition to secondary mineral formation, regulate $\delta^{26}Mg$ and/or $\delta^{7}Li$ (Teng et al., 2010; Pogge von Strandmann et al., 2012; Tipper et al., 2012a).

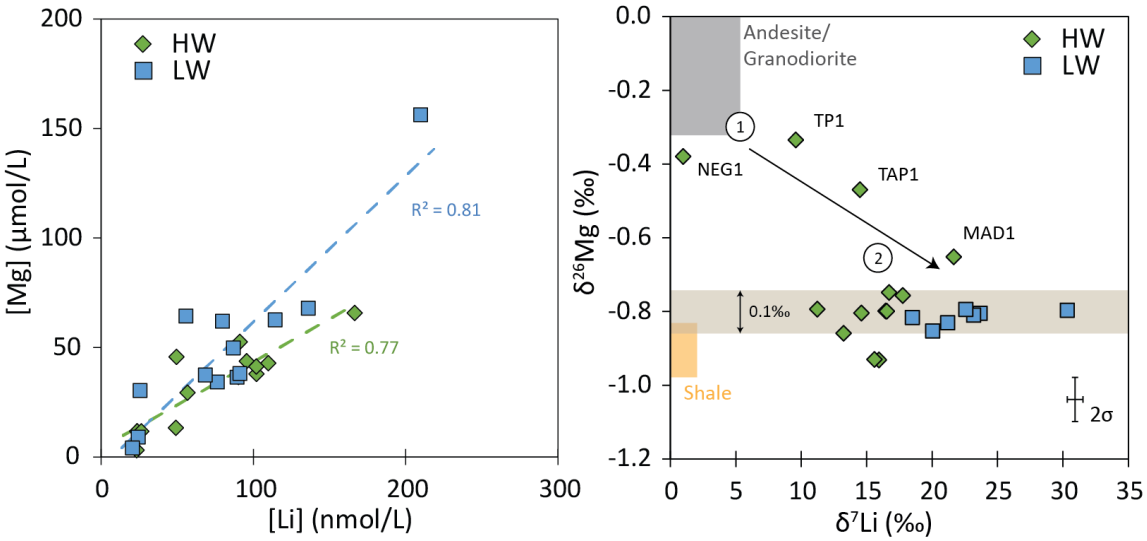

Figure V-12. Comparison between [Li] and [Mg] and $\delta^{7}Li$ and $\delta^{26}Mg$ in the dissolved load of the Amazon River and its tributaries. The brown shaded box shows the $\delta^{26}Mg$ in the main stem of the Amazon River.1.High weathering intensity; 2.Intermediate weathering intensity.

The Mg isotope composition of the tributaries were always heavier than $\delta^{26}Mg$ values in the main channel during the HW stage (Figure V-12). Heavier $\delta^{26}Mg$ can be attributed to a higher proportion of Mg from weathering of silicate minerals, that have high $\delta^{26}Mg$ (like andesite or granodiorites),

than from carbonate or shale weathering, as carbonates and shales tend to be relatively enriched in light Mg isotopes ($\delta^{26}Mg$ = -5.57 to -0.9‰, Teng, 2017), or from seawater aerosols that have $\delta^{26}Mg$ = -0.82‰ (Foster et al., 2010). However, the $\delta^{26}Mg$ of the Negro, Trombetas and Tapajós tributaries ($\delta^{26}Mg_{Trib}$) needs to be corrected from atmospheric inputs to estimate the $\delta^{26}Mg$ due to weathering of continental crust ($\delta^{26}Mg_{cont}$). The proportions of Mg derived from atmospheric contributions, f_{atm}, is assumed to be 0.07 in the Tapajós, 0.21 in the Trombetas and 0.22 in the Negro (Gaillardet et al., 1997). We make the assumption that the $\delta^{26}Mg$ value of the atmospheric input ($\delta^{26}Mg_{atm}$) is similar to the sea water value (-0.82‰) and therefore we can calculate the $\delta^{26}Mg_{cont}$ using Eq. V-2:

$$\delta^{26}Mg_{Trib} = \delta^{26}Mg_{atm} \times f_{atm} + \delta^{26}Mg_{cont} \times (1 - f_{atm}) \qquad \textit{Eq. V-2}$$

$\delta^{26}Mg_{cont}$ is -0.26‰, -0.21‰ and -0.44‰ for the Negro, Trombetas and Tapajós respectively. These values are close to those of andesites/granodiorites ($\delta^{26}Mg$ = -0.31 to 0.04‰), which suggests that weathering is more congruent in these tributaries. Interestingly, during the HW stage samples NEG1, TP1, TAP1 and MAD1 show a negative relationship between $\delta^{26}Mg$ and $\delta^{7}Li$ consistent with preferential incorporation of the light isotopes of Li and the heavy isotopes of Mg in secondary minerals (Figure V-12). This negative relationship may be indicative of high weathering intensity (high $\delta^{26}Mg$ and low $\delta^{7}Li$) and intermediate weathering intensity (low $\delta^{26}Mg$ and high $\delta^{7}Li$).

V.7.3 Importance of floodplains as a source and/or sink of Li and Mg

Crucially, the lowlands of the Amazon River contain significant areas of floodplains that play a major role in the storage of sediments and water (Dunne et al., 1998; Seyler and Boaventura, 2003; Bourgoin et al., 2007; Bouchez et al., 2012; Frings et al., 2014). Water retained on the floodplains has a long residence time, promoting the formation of secondary minerals that potentially drives the $\delta^{7}Li$ value of the dissolved phase towards higher values (Dellinger et al., 2015; Pogge von Strandmann and Henderson, 2015). The potential control of secondary mineral precipitation or dissolution on $\delta^{7}Li$ can be assessed by its relationship with Li/Na ratio in the Amazon River or its tributaries (MAD1 and NEG1; Figure V-13). Na is generally not incorporated in the secondary minerals products whereas Li is assimilated, and secondary minerals carry most of the Li in the

Amazon River (Sawhney, 1972; Millot et al., 2010c; Dellinger et al., 2015). Figure V-13 shows that at low discharge the δ^7Li of water from a given sampling station is high (and Li/Na is low) while at high discharge δ^7Li is low and Li/Na increases. This suggests that at low discharge there is an increase in precipitation of secondary minerals that preferentially incorporate ^{6}Li driving the δ^7Li of the fluid phase towards higher values. Therefore, it seems likely that the changes in δ^7Li are associated with increased input of Li from floodplains during the LW stage. Moreover, during the LW stage, the sampling stations towards the mouth of the river (from MAN3 to MPN1/MPS1) became progressively enriched in heavy Li isotopes (an increase of 7 - 8.2‰) consistent with an increased contribution from the floodplains. This is consistent with a study in New Zealand that shows that the transfer of water from regions of high uplift to regions of low uplift (similar to the passage from the Andes to the Amazon lowlands) results in increased riverine δ^7Li values, up to 35‰ (Pogge von Strandmann and Henderson, 2015). Similarly, in the Okavango Delta in Southern Africa, enrichment of heavy Si isotopes in the dissolved phase has been attributed to inputs of water from seasonal floodplains where light Si isotopes were preferentially incorporated in clays (Frings et al., 2014).

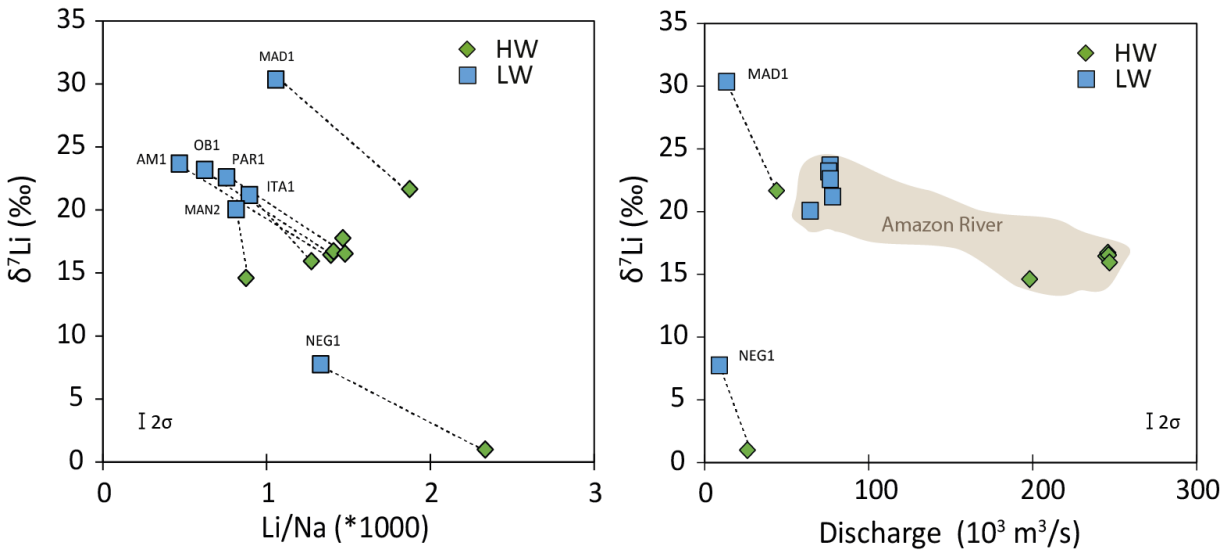

Figure V-13. Li/Na ratios and discharges versus δ^7Li in the Amazon River and its tributaries (Negro and Madeira).

As the water stage falls (between the end of August and January) the floodplains contribute to the water of the main stem (Bonnet et al., 2008) and thus increase the δ^7Li and decrease the Li/Na at the lower water stage. This phenomenon is highlighted by comparing the data for Óbidos with the

Amazon River δ^7Li values measured at different hydrological stages (Figure V-14). The δ^7Li of water from the floodplains must be >26‰ to be able to drive the δ^7Li value measured at MPN1/MPS1 (at the mouth of the Amazon) towards 26‰ in December (Figure V-14). This is very likely given that floodplains can drive the riverine δ^7Li up to ~35‰ in New Zealand (Pogge von Strandmann and Henderson, 2015).

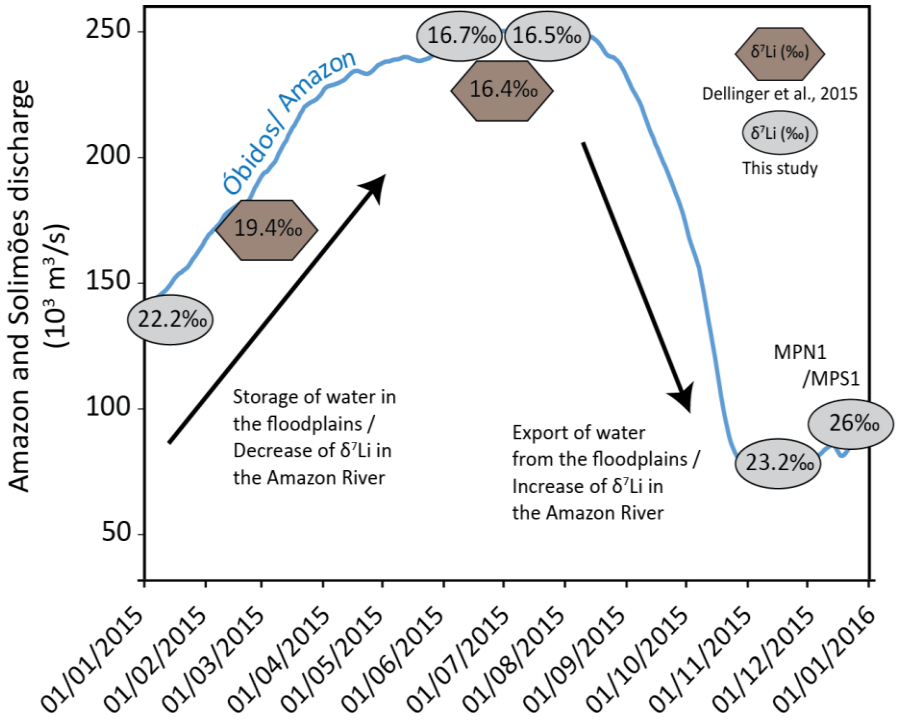

Figure V-14. Dissolved δ^7Li for different periods of the hydrological cycle in the Amazon River. The discharge at Óbidos is represented by the blue line while the δ^7Li are represented by ellipses (this study) or hexagons (Dellinger et al., 2015). The increase of δ^7Li is linked with input of Li with high δ^7Li from floodplains.

The relationship between Li/Na and δ^7Li as a function of discharge (and so floodplain inputs) measured at Óbidos shows a clockwise hysteresis (Figure V-15). While hysteresis between the TDS and discharge has been attributed to a lag in the flux of material entering via tributaries (Moquet et al., 2016), this does not appear to be the case for Li isotopes. This is because the δ^7Li value of Li added to the system at low discharge must be higher than ~16‰ to influence the composition of the Amazon River. Only the Madeira River respects this requirement with δ^7Li = 21.7-30.3‰. Increased input of Li from the Madeira River could account for the δ^7Li values measured in November, but it cannot explain the increase of δ^7Li in the Amazon River before the confluence and in the Negro River. However, the decrease in Li/Na between June and August (at the same discharge) without change in δ^7Li (Figure V-15) indicates that there is a decrease of the relative

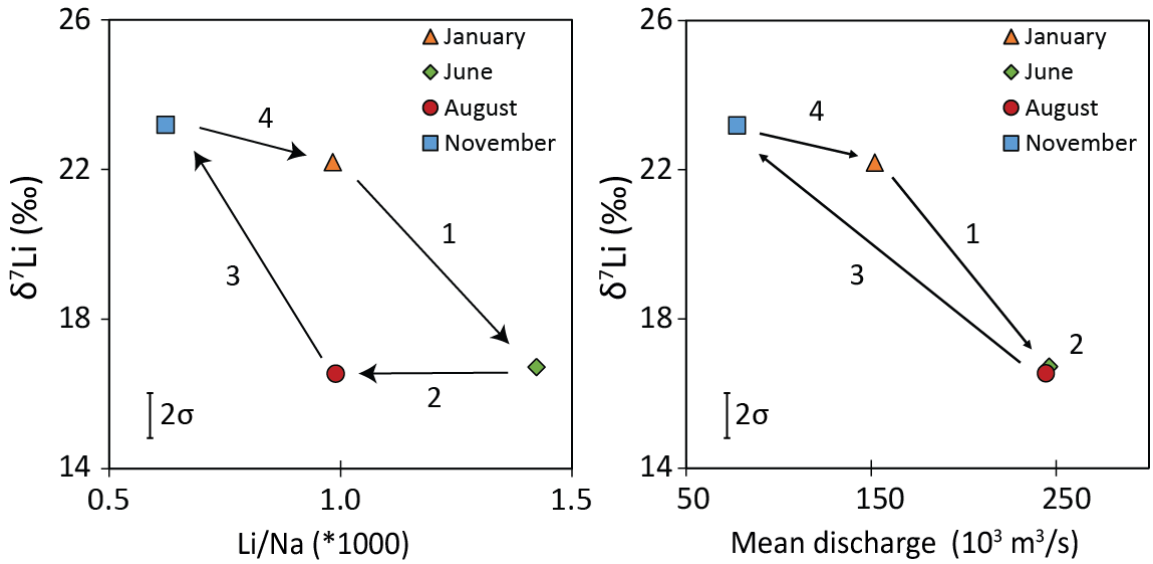

Figure V-15. Li/Na ratios and discharges versus δ^7Li measured at Óbidos in January, June, August and November in 2015. 1. As water level rises, floodplains are flooded with runoff with relatively low δ^7Li and low Li/Na; 2. Li/Na decreases while δ^7Li is unchanged highlighting a decreased influence of the Madeira and Negro rivers with high Li/Na; 3. Export of water from the floodplains with high δ^7Li and lower Li/Na; 4. Increased contribution from the Madeira and Negro rivers and slight decrease of floodplain inputs.

contribution from the Negro and Madeira rivers which have a higher Li/Na (2.72 and 1.95 respectively) than the Solimões (Li/Na = 0.97).

The δ^{26}Mg of the Amazon main stem by contrast does not show any change with hydrological variations. The most likely reason for the lack of change in δ^{26}Mg is due to the mass balance budget of the Mg fluxes. The amount of Mg incorporated in secondary minerals on the floodplains would not be sufficient to drive the δ^{26}Mg of the dissolved phases toward lighter values. The average [Li] of the Amazon main stem is ~0.2% the average of [Mg] and therefore is more strongly influenced by secondary mineral formation. However, during the LW stage δ^{26}Mg decreased from -0.47 to -0.96‰ at TAP1 and -0.65 to -0.80‰ at MAD1. The Madeira River showed the biggest increase of δ^7Li (8.7‰) during LW stage and also the highest δ^7Li in the Amazon lowlands which must be the result of higher secondary mineral formation. This phenomenon could have therefore been sufficient to affect the δ^{26}Mg values of the dissolved phase. By contrast, the Tapajos River has lower [Mg] (1-30 µmol/L) and lower discharge (i.e. lower Mg flux) than the Amazon main stem and therefore is more influenced by floodplain inputs during the LW stage. The behaviour of the dissolved Mg is consistent with the stability of the chemical composition of river sediments that show no significant loss or gain of Mg during weathering in floodplains (Bouchez et al., 2012).

V.7.4 Implications for the modern seawater budget and past records of seawater δ^7Li and δ^{26}Mg

The riverine inputs of Li and Mg from the Amazon main stem (average of ALM1, AM1, OB1, PAR1 and ITA1 values) to the ocean are much higher in the HW stage (686 x 10^6 mol/yr and 325 x 10^9 mol/yr respectively) compared to the LW stage (225 x 10^6 mol/yr and 141 x 10^9 mol/yr respectively) and these fluxes also have different δ^7Li (21.5‰ at LW and 16.3‰ at HW) but not δ^{26}Mg. Given the importance of the Amazon River as a source of dissolved solids to the ocean (Gaillardet et al., 1999b; Moquet et al., 2016), these variations need to be taken into account to better constrain the isotope budget of Li and Mg of the modern ocean (Huh et al., 1998; Tipper et al., 2006b). The average Li flux at each hydrological stage (assuming that LW and HW are 6 months each) is 456 x 10^6 mol/yr corresponding to ~18% of the total Li flux into the ocean (Huh et al., 1998), while the δ^7Li of this flux is ~19‰, ~3‰ lower than previously assumed (Huh et al., 1998). The average Mg flux of both the LW and HW stages is 233 x 10^9 mol/yr, similar to previous studies (Tipper et al., 2006b; Moquet et al., 2016) but the δ^{26}Mg is ~-0.81‰ which is significantly higher than previous measurements (-0.95‰; Tipper et al., 2006b).

Past records have shown an increase of seawater δ^7Li over the Cenozoic (Hathorne and James, 2006; Misra and Froelich, 2012) but there appears to be little variation in seawater δ^{26}Mg (Higgins and Schrag, 2015; Gothmann et al., 2017). This would be consistent with an increase in the area of floodplains that have the capability to drive the dissolved phase toward high δ^7Li with no change in dissolved δ^{26}Mg.

V.8 Conclusions

We have measured the Li and Mg isotopes in sediment and dissolved phases at low and high hydrological stages in the Amazon River and its tributaries. The δ^7Li and δ^{26}Mg values for the dissolved load are always, respectively, heavier and lighter than those of the corresponding suspended load supporting a preferential enrichment of ^{6}Li and ^{26}Mg in secondary minerals. The surface suspended sediments did not display any variations of δ^7Li and δ^{26}Mg at the different hydrological stages and there were no systematic changes in δ^7Li and/or δ^{26}Mg along the course of

the Amazon main stem. However, analyses of sediments from depth profiles show higher $\delta^{7}Li$ and lower $\delta^{26}Mg$ in HW stages which may reflect the transport of less weathered and/or coarser sediments at high discharge.

The comparison of $\delta^{7}Li$ and $\delta^{26}Mg$ in the dissolved phase can be used to trace weathering intensity in the Amazon tributaries but not in the Amazon main stem as the $\delta^{26}Mg$ values of the fluid are invariant. In the Amazon main stem, the dissolved $\delta^{7}Li$ values increases by ~5‰ during the LW stage which is best explained by an increased contribution of Li from floodplains where high rates of secondary formation drive the $\delta^{7}Li$ of the fluids toward higher values but leave the $\delta^{26}Mg$ values of the dissolved phase unchanged. Consequently, the riverine $\delta^{7}Li$ might indicate the efficiency of the continents to deliver cations to the ocean which regulate the atmospheric CO_2.

Chapter VI. Conclusions

VI.1 Motivation

Lithium and magnesium isotopes provide critical information as to fluid-rock interactions and silicate weathering rates (Huh et al., 1998; Kisakurek et al., 2005; Tipper et al., 2006b; Pogge von Strandmann et al., 2008a; Bouchez et al., 2013; Dellinger et al., 2015; Dessert et al., 2015), soil formation (Rudnick et al., 2004; Opfergelt et al., 2012), and paleo-weathering conditions (Misra and Froelich, 2012; Gothmann et al., 2017). Lithium is mainly present in silicate minerals and the Li isotopic composition of river water appears to be independent of catchment lithology (Kisakurek et al., 2005) and biological processes (Lemarchand et al., 2010). While Li is usually a trace constituent of rock and water, Mg is a major component of many rocks and fluids (Teng, 2017). The Mg isotopic composition of river water is sensitive to bedrock lithology (Tipper et al., 2006b) and biological processes that fractionate Mg isotopes due to preferential uptake of ^{26}Mg (Black et al., 2008; Bolou-Bi et al., 2010; Bolou-Bi et al., 2012). Both Li and Mg are strongly fractionated during the formation of secondary minerals and, as a result, the Li and Mg isotopic composition of river water can reflect weathering intensity within the catchment (Bouchez et al., 2014a; Dellinger et al., 2015; Dessert et al., 2015).

The aim of this PhD was to evaluate the mechanisms controlling δ^7Li and $\delta^{26}Mg$ in the dissolved and solid phases during weathering under different environmental and hydrological conditions. Studies were undertaken in Greenland, Guadeloupe and Brazil, to assess:

- The implications for ocean chemistry of seasonal variations in inputs of lithium and magnesium to a fjord (Greenland).
- The response of Li and Mg isotopes to rain events in a highly-weathered catchment (Guadeloupe)
- The influence of hydrological variations on the lithium and magnesium isotopic composition of the Amazon River (Brazil).

VI.2 Variability in $\delta^{7}Li$ and $\delta^{26}Mg$ in weathering products

A total of 362 samples and standards were measured in this study, including 167 Mg isotope and 195 Li isotope analyses. The variation of $\delta^{7}Li$ and $\delta^{26}Mg$ in different weathering reservoirs is shown in Figure VI-1.

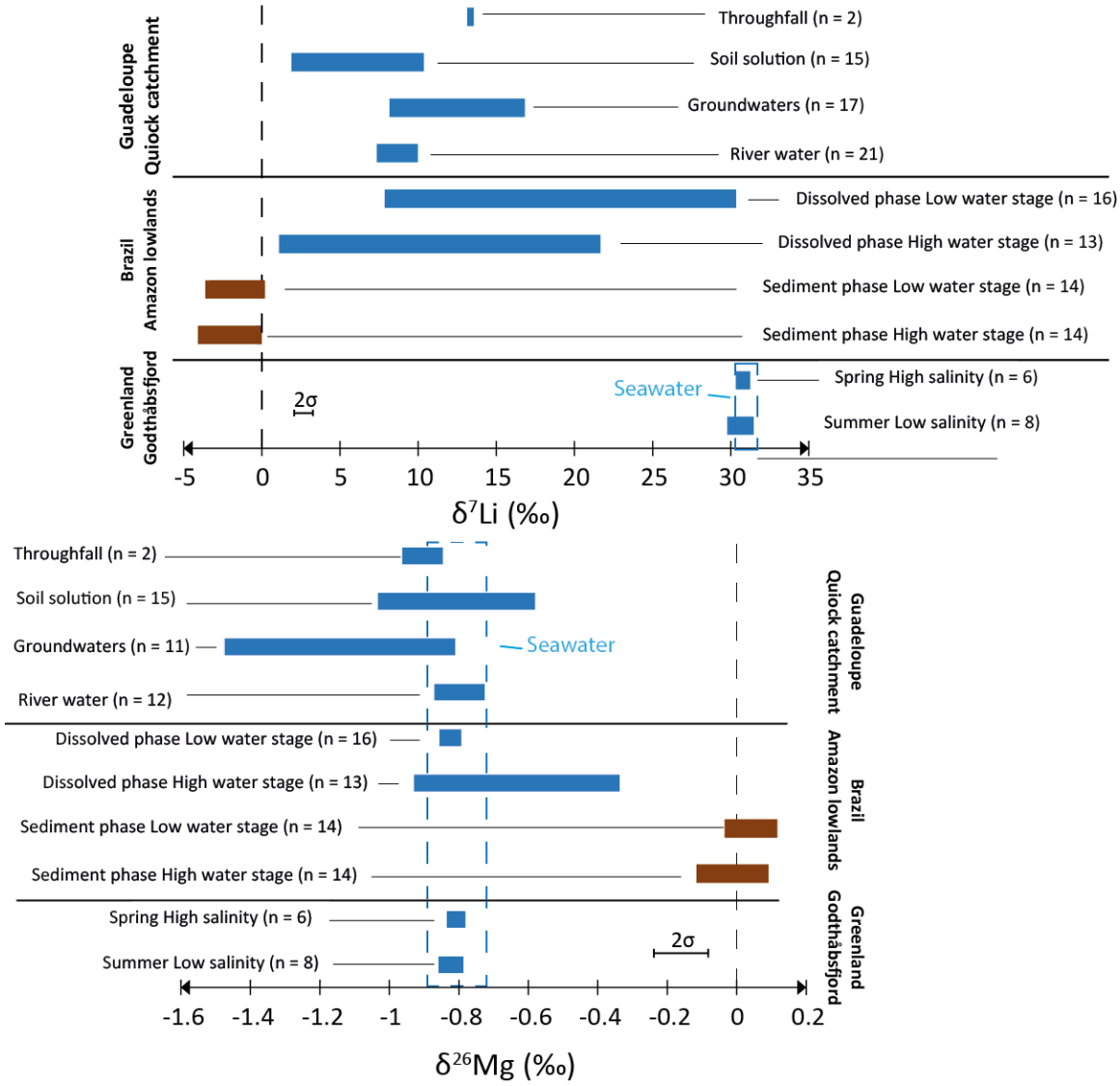

Figure VI-1. Isotope composition of Li and Mg in weathering products from Guadeloupe, Brazil and Greenland. The blue dashed lines show the standard deviation (2σ) around the average IAPSO seawater value.

$\delta^{7}Li$ values of fluids ranges from 1 to 31.5‰. The range in $\delta^{7}Li$ reflects mixing of solutions with different $\delta^{7}Li$, fractionation of Li isotopes due to the formation of secondary mineral that are enriched in ^{6}Li (Huh et al., 2001; Kisakurek et al., 2005), and the dissolution of rocks or secondary minerals (Tang et al., 2007). The Li isotopic composition of suspended sediments in the Amazon

lowlands by contrast shows limited variability, but the sediments tend to have relatively low δ^7Li values consistent with a preferential incorporation of ^{6}Li in secondary minerals.

Fluid δ^{26}Mg values ranged from -1.48 to -0.33‰, which encompasses the range of δ^{26}Mg values observed in the world's largest rivers (Tipper et al., 2006b). Most of the rivers sampled in this study have δ^{26}Mg values that are similar to seawater (-0.82‰; Foster et al., 2010; Ryu et al., 2016). However, shifts in δ^{26}Mg away from seawater or rock sources are due either to Mg isotope fractionation during secondary mineral formation (which drives the fluid towards lower δ^{26}Mg values) (Tipper et al., 2006a; Brenot et al., 2008), or to adsorption/desorption of Mg to/from mineral surfaces that preferentially adsorb light Mg isotopes (Opfergelt et al., 2012; Ma et al., 2015). The Mg isotopic composition of suspended sediments measured in the Amazon lowlands is consistent with preferential incorporation of heavy Mg isotopes in secondary minerals.

If both Li and Mg isotopes are principally fractionated by secondary mineral formation, a negative correlation between δ^7Li and δ^{26}Mg is expected because secondary minerals preferentially incorporate light Li isotopes but heavy Mg isotopes (Teng et al., 2010; Pogge von Strandmann et al., 2012; Tipper et al., 2012a). However, no negative correlation was observed in this study (Figure VI-2). The causes of the δ^{26}Mg and δ^7Li variability in the different catchments is more complex, as summarised below.

VI.3 Principal findings

VI.3.1 Greenland / Chapter 3

δ^7Li and δ^{26}Mg values were determined along a 190 km long fjord (Godthåbsfjord) to evaluate the impact of glacial meltwater (high ice melt in summer and low in spring) on weathering processes and to assess the behaviour of the Li and Mg concentrations and isotopes during mixing between seawater and meltwater. The δ^7Li values of the fjord waters ranged from 30.3 to 31.2‰ in spring and from 29.5 to 31.5‰ in summer, and the corresponding δ^{26}Mg values ranged from -0.78 to -0.86‰ in summer and -0.79 to -0.84‰ in spring. Even in summer, when the range in salinity was wide (8 to 33), there was very little variability in δ^7Li and δ^{26}Mg. Despite evidence for removal of Fe due to flocculation of colloids at low salinities, there was no evidence for removal of Li and Mg.

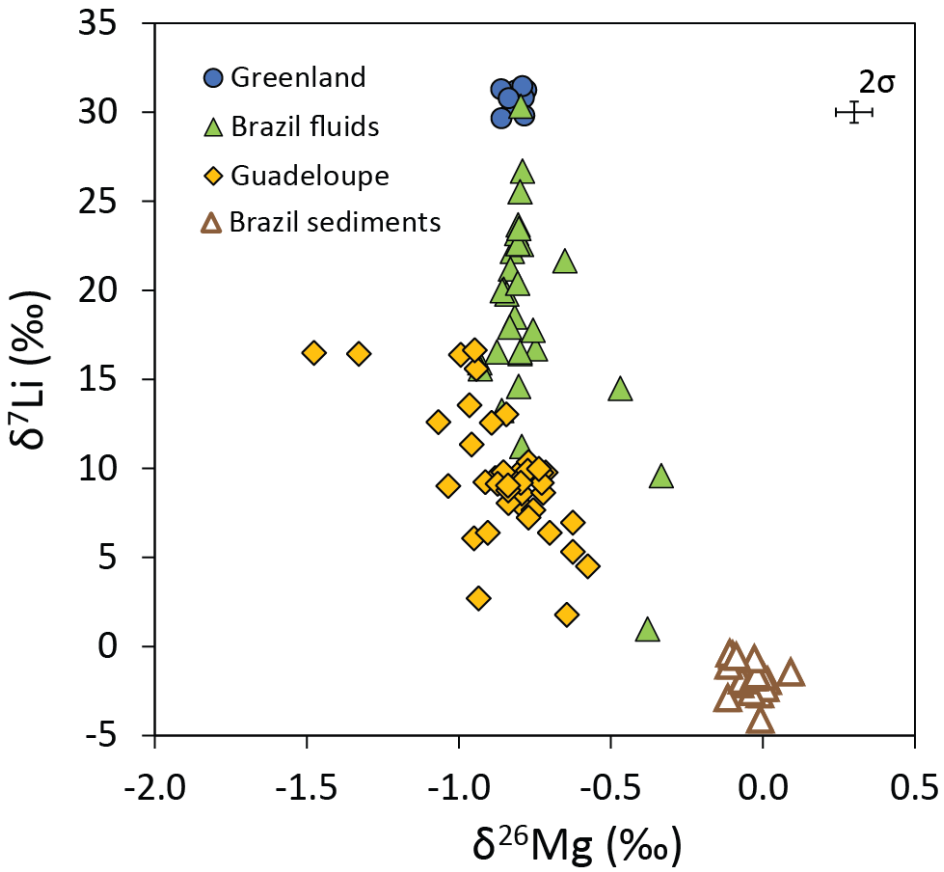

Figure VI-2. Comparison between δ^7Li and δ^{26}Mg in the dissolved load of the Godthåbsfjord, Quiock catchment and the Amazon lowlands. Error bars represent the 2σ external uncertainty of the isotope analyses (0.6‰ for Li and 0.06‰ for Mg) based on repeated measurements of L-SVEC (δ^7Li = 0.0 ± 0.5‰ (2SD, n = 28)), DSM-3 (δ^{26}Mg = 0.00 ± 0.07‰ (2SD, n = 27)) and IAPSO (δ^7Li = 30.9 ± 0.6‰ (2SD, n = 27); δ^{26}Mg = -0.82 ± 0.05‰ (2SD, n = 18)).

Because of the very low Li and Mg concentrations in the meltwater, the influence of melt water input on δ^7Li and δ^{26}Mg can only be detected at very high freshwater/seawater ratios (>5). These results suggest that records of seawater δ^{26}Mg and δ^7Li preserved in marine sediments cannot be explained by glaciations and changes in sea level.

VI.3.2 Guadeloupe / Chapter 4

The variability of Li (δ^7Li = 1.8 to 16.8‰) and Mg (δ^{26}Mg = -1.48 to -0.58‰) isotopes in Quiock Creek catchment highlights that, even in a highly-weathered catchment that drains a single lithology, several factors can impact the δ^7Li and δ^{26}Mg of the different fluids. The Mg isotope compositions of the soil waters, groundwater and the river itself mainly reflect input of Mg from sea salts as well as adsorption or desorption of Mg from mineral surfaces that preferentially adsorb light Mg isotopes. There was little evidence for Mg isotope fractionation due to plant uptake despite the dense vegetation, and there was little change in δ^{26}Mg during hydrological events. By contrast the

Li isotope compositions of the fluids is mainly influenced by preferential incorporation of light Li isotopes into secondary minerals. δ^7Li in the Quiock Creek rapidly decreased after a storm event due to increased input of Li from soil solutions input that have relatively low δ^7Li. δ^7Li values of groundwaters also decreased after a single rain event, most likely due to decreased rates of precipitation of secondary minerals. This has important implications for understanding the complex relationships between runoff and chemical weathering rates (Maher, 2011), and suggests that discharge has profound influences on rates of secondary mineral precipitation.

VI.3.3 Brazil / Chapter 5

The study of the Amazon River shows that hydrological regime can be an important control on chemical and isotopic fluxes delivered to the ocean. While surface suspended sediments did not display any variations of δ^7Li and δ^{26}Mg with hydrological stage, and there were no systematic changes in δ^7Li and/or δ^{26}Mg along the course of the Amazon main stem, the δ^7Li value of the dissolved load was higher at low discharge than it was at high discharge ($\delta^7Li_{LW} - \delta^7Li_{HW}$ = 0.7 to 8.7‰) both in the main stem of the Amazon and its tributaries. By contrast, there was little difference in the δ^{26}Mg value of the dissolved phase ($\delta^{26}Mg_{LW} - \delta^{26}Mg_{HW}$ = -0.10 to 0.49‰). These changes are best explained by an increased contribution of Li from the floodplains that border the Amazon River and the principal tributaries. As a result of long residence times on the floodplain, rates of secondary formation are high driving the δ^7Li of the fluids towards higher values but leaving δ^{26}Mg unchanged. Thus increases in seawater δ^7Li but unchanged seawater δ^{26}Mg over the Cenozoic may potentially be explained by increased inputs of Li and Mg from floodplains (Dellinger et al., 2015; Pogge von Strandmann and Henderson, 2015).

This thesis highlights that temporal variations in continental weathering processes can be monitored with weathering tracers like Li and Mg isotopes that respond quickly to changes in weathering processes (secondary mineral formation, adsorption/desorption, mixing of waters). Indeed, the use of Li and Mg isotopes together have the potential to describe most of the processes occurring in the critical zone, biological vs non-biological processes, silicate vs carbonate

weathering and therefore can be utilized to accurately identify the major controls on weathering rates at Earth's surface.

Appendices

Appendix A

Appendix A 1. Roots growing in cracks within rocks in French Polynesia (Tahiti). Although the roots may damage the rock structure, they can also prevent erosion by keeping the rock or secondary rock material in place.

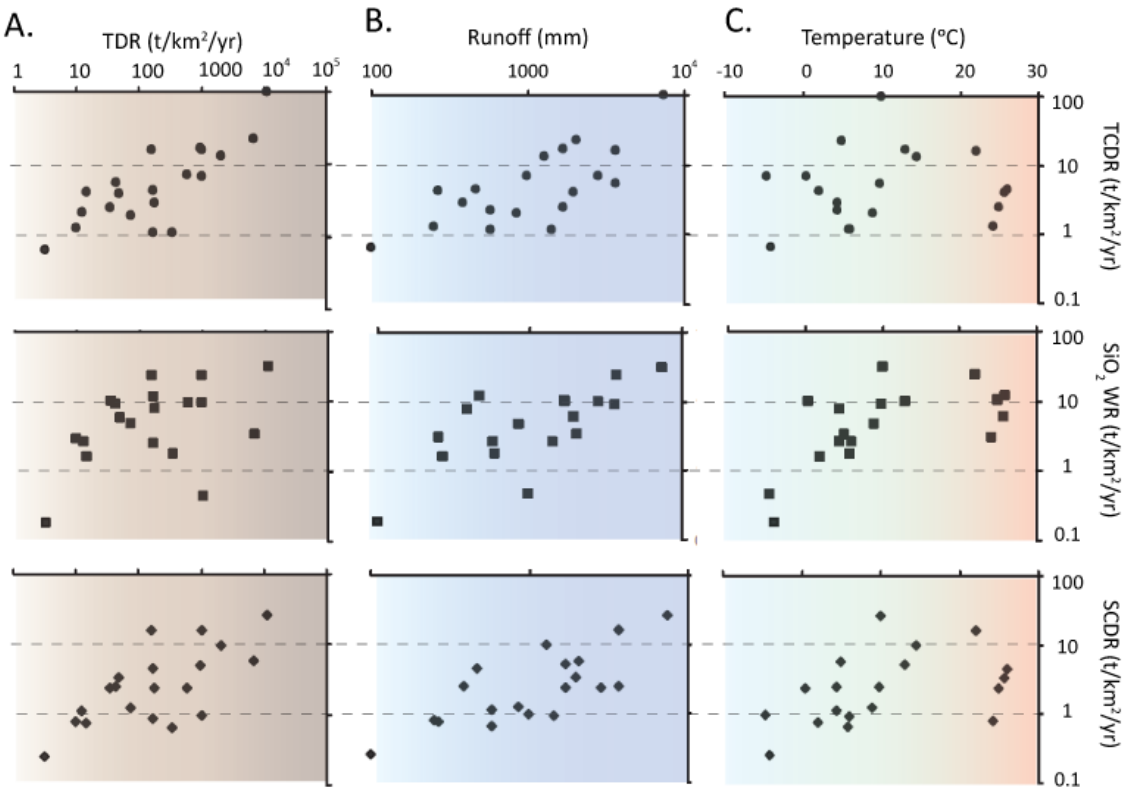

Appendix A 2. Evolution of TCDR (total cation denudation rate, circles), SCDR (silicate cation denudation rate, squares), and SiO_2 WR (SiO_2 weathering rate) with TDR (A, total denudation rates), runoff (B) and temperature (C) in shields, sub-montane and alpine catchments. Temperature shows little correlation with TCDR but distinct relationships with SCDR and SiO_2 WR. The lower silicate weathering rates at high temperature and low runoff are associated with a transport-limited weathering regimes (limited amount of fresh minerals). After West et al., 2005.

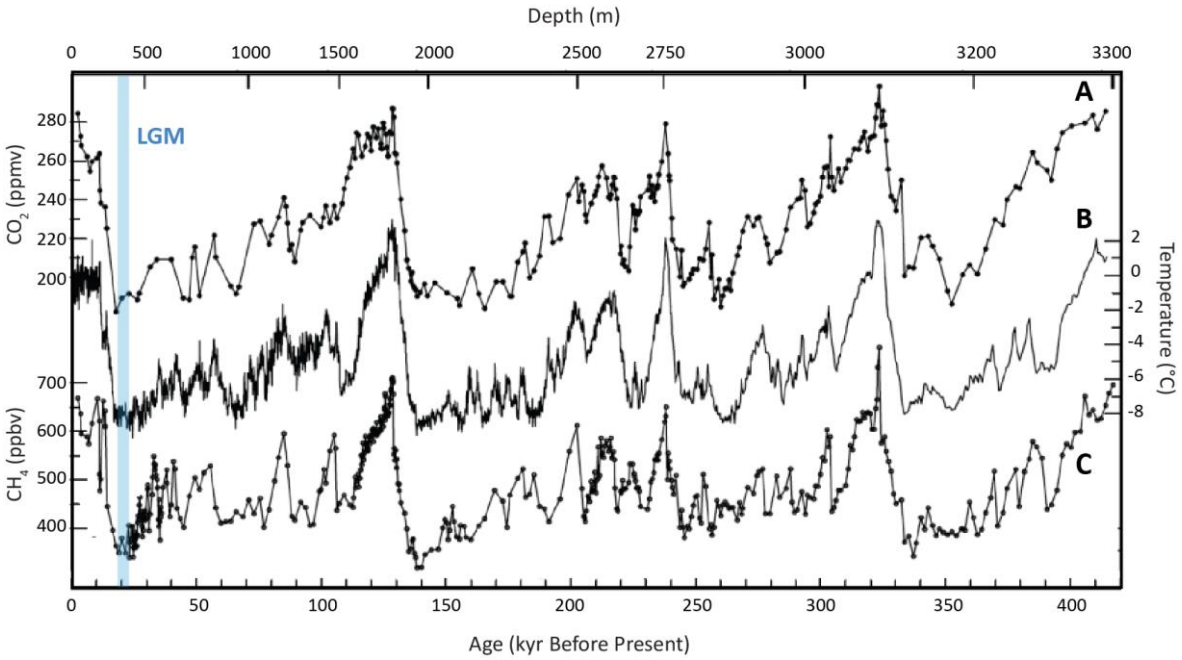

Appendix A 4. Vostok time series. Variation with respect to time of: a, CO_2; b, Temperature of the atmosphere c, CH_4. The atmospheric CO_2 at the last glacial maximum (LGM), about 21 ka BP was ~200 ppm, while the pre-industrial value for the current interglacial is ~280 ppm. After Petit et al., 1999.

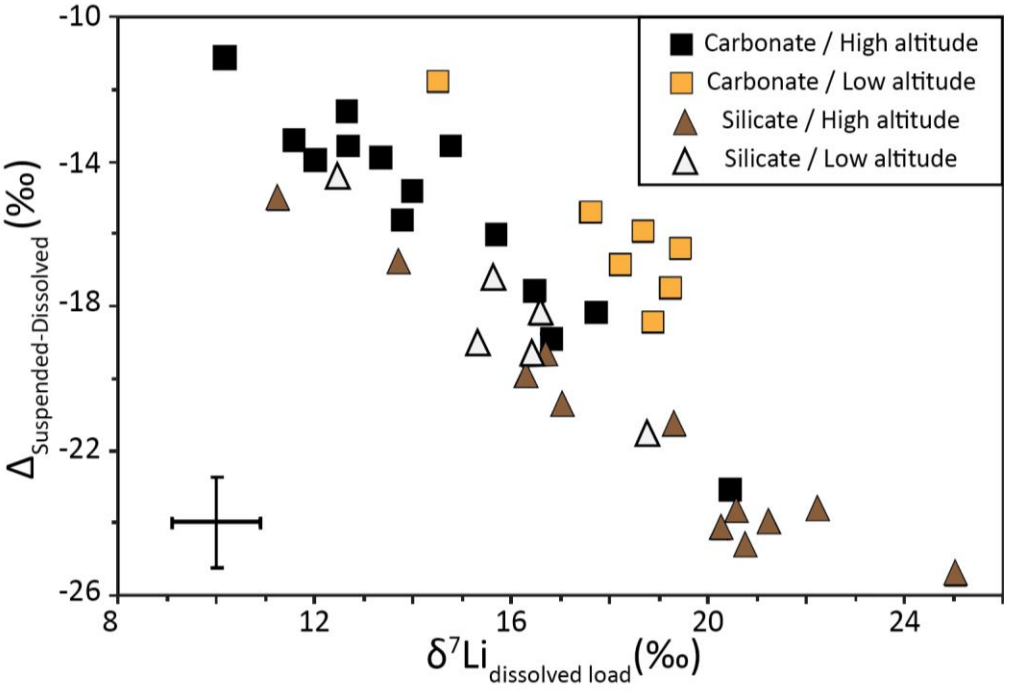

Appendix A 3. Difference between the δ^7Li value of suspended sediments and the δ^7Li value of dissolved load ($\Delta_{Suspended-Dissolved}$) of Himalayan rivers. Silicate-dominated catchments at high altitude (2000–4000 m) show the highest degree of fractionation between the dissolved load and conjugate suspended sediment. However, at low altitude (550–1300 m), where weathering is more intense, the fractionation decreases. The external errors are shown bottom left (from Kisakurek et al., 2005).

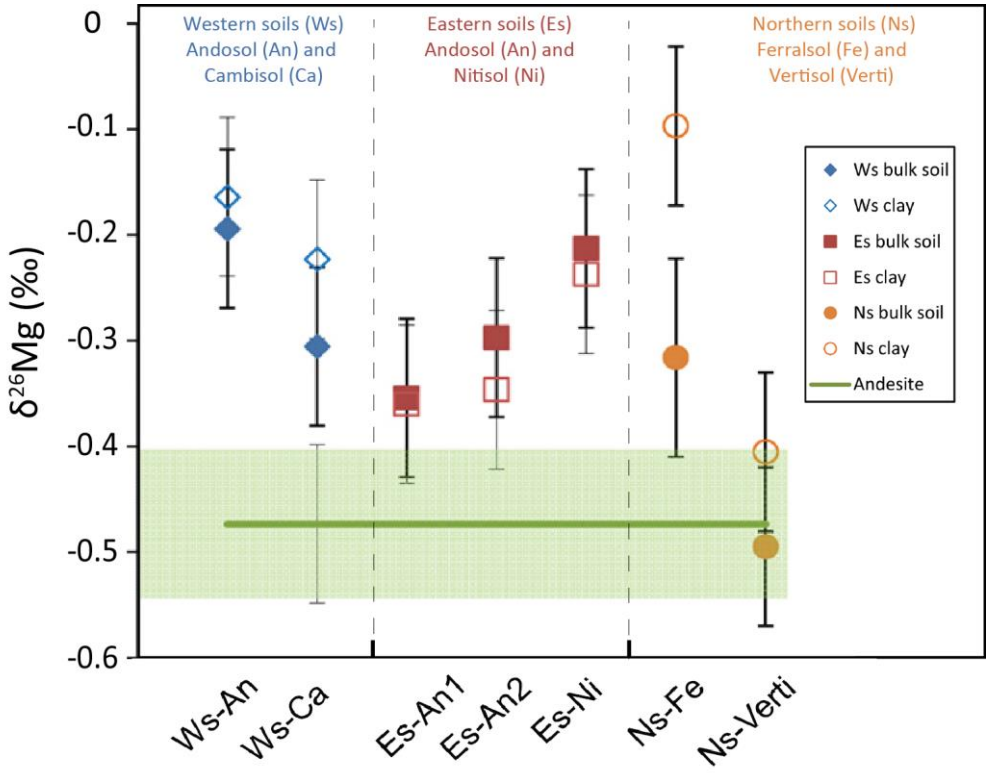

Appendix A 5. Magnesium isotope composition (‰) of bulk soil (solid symbols) and clay fraction (open symbols) relative to the parent rock (solid line with uncertainty shaded) in three soil sequences from Guadeloupe. After Opfergelt et al,. 2012.

Appendix B

We reported the hydrological conditions of Quiock Creek catchment since the first emptying of the soil solution reservoirs in Appendix B 1. A description of these conditions is necessary to accurately interpret the soil solution and groundwater chemistry of the sample collected during the first day of the campaign. Briefly, during this period a relatively small input of rainfall entered the catchment (~36.4 mm during 18 days) and therefore the water table elevation decreased and discharge was relatively low (maximum of 12m^3/h the 28/09/15). The Piezo 1, 2 and 3 water table were below the river elevation at the beginning of the study.

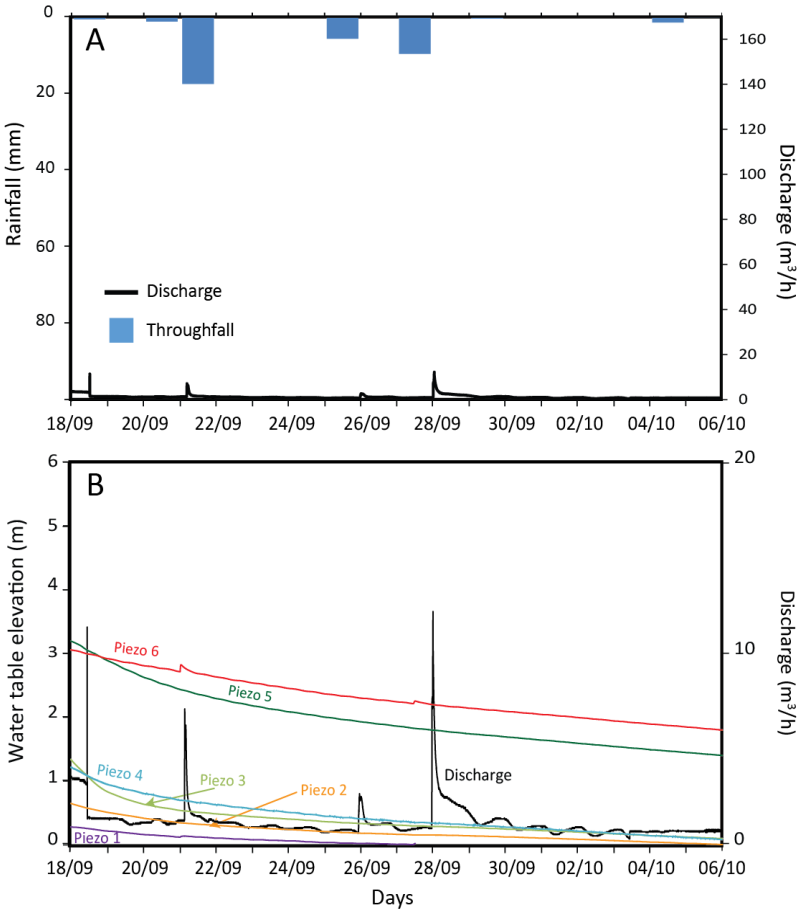

Appendix B 1. A. Precipitation and discharge of Quiock Creek. B. Water table elevation and discharge from the 18/09/2015 until the beginning of the sampling campaign. All the discharge and water elevation data are derived from the ObsERA website (https://morpho.ipgp.fr/Obsera).

Appendix C

The Amazon River is fed by 3 different types of waters (Stallard and Edmond, 1983; Appendix C 1A and B): ‘‘white waters’’ characterized by higher level of suspended sediments, dissolved material and conductivity (Solimões and Madeira rivers); ‘‘black waters’’ with the lowest conductivities, pH and suspended matter and the highest humic acid content (Negro River); ‘‘clear waters’’ with low suspended sediments, conductivity and nutrient concentrations (e.g. Tapajós and Trombetas rivers).

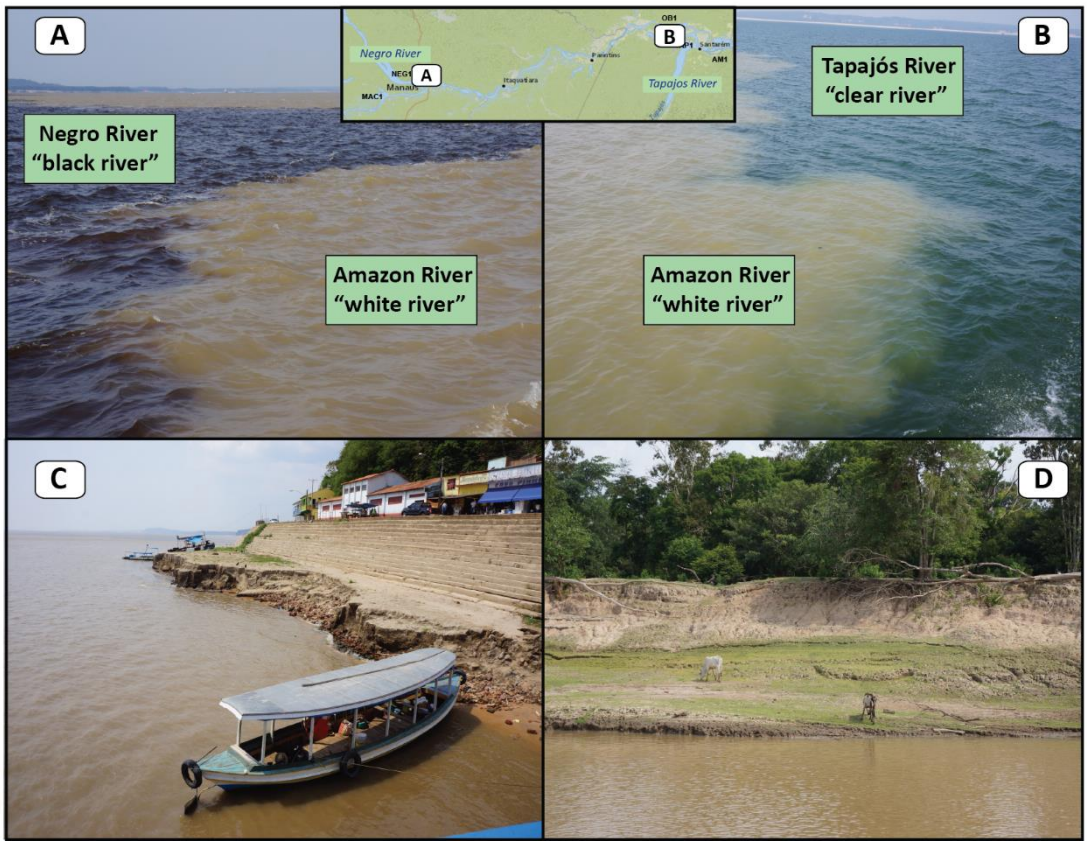

Appendix C 1. A. Confluence of the Negro River and Solimões River; B. Confluence of the Tapajós River and the Amazon River; C. and D. During the LW stage, lower discharge reduces the surface area in contact with water. In both pictures the stage of the main stem is 7-10 m lower than it is in the wet stage. Photos are from Chantal Freymond.

References

Adkins, J.F. and Schrag, D.P. (2001) Pore fluid constraints on deep ocean temperature and salinity during the last glacial maximum. Geophys. Res. Lett. 28, 771-774.

An, Y.J. and Huang, F. (2014) A review of Mg isotope analytical methods by MC-ICP-MS. J. Earth Sci. China 25, 822-840.

An, Y.J., Wu, F., Xiang, Y.X., Nan, X.Y., Yu, X., Yang, J.H., Yu, H.M., Xie, L.W. and Huang, F. (2014) High-precision Mg isotope analyses of low-Mg rocks by MC-ICP-MS. Chem. Geol. 390, 9-21.

Anderson, S.P., Drever, J.I. and Humphrey, N.F. (1997) Chemical weathering in glacial environments. Geology 25, 399-402.

Appelo, C.A.J. and Postma, D. (2004) Geochemistry, groundwater and pollution. CRC press.

Arendt, K.E., Nielsen, T.G., Rysgaard, S. and Tonnesson, K. (2010) Differences in plankton community structure along the Godthabsfjord, from the Greenland ice sheet to offshore waters. Mar. Ecol. Prog. Ser. 401, 49-62.

Arendt, K.E., Dutz, J., Jonasdottir, S.H., Jung-Madsen, S., Mortensen, J., Moller, E.F. and Nielsen, T.G. (2011) Effects of suspended sediments on copepods feeding in a glacial influenced sub-Arctic fjord. J. Plankton Res. 33, 1526-1537.

Aucour, A.M., Tao, F.X., Moreira-Turcq, P., Seyler, P., Sheppard, S. and Benedetti, M.F. (2003) The Amazon River: behaviour of metals (Fe, Al, Mn) and dissolved organic matter in the initial mixing at the Rio Negro/Solimões confluence. Chem. Geol. 197, 271-285.

Bamber, J.L., Griggs, J.A., Hurkmans, R.T.W.L., Dowdeswell, J.A., Gogineni, S.P., Howat, I., Mouginot, J., Paden, J., Palmer, S., Rignot, E. and Steinhage, D. (2013) A new bed elevation dataset for Greenland. Cryosphere 7, 499-510.

Bard, E., Hamelin, B., Fairbanks, R.G. and Zindler, A. (1990) Calibration of the ^{14}C timescale over the past 30,000 years using mass spectrometric U–Th ages from Barbados corals. Nature 345, 405-410.

Benettin, P., Soulsby, C., Birkel, C., Tetzlaff, D., Botter, G. and Rinaldo, A. (2017) Using SAS functions and high-resolution isotope data to unravel travel time distributions in headwater catchments. Water Resources Research 53, 1864-1878.

Berner, E.K. and Berner, R.A. (1996) Global environment: water, air, and geochemical cycles. Prentice Hall, New York.

Berner, R.A., Lasaga, A.C. and Garrels, R.M. (1983) The carbonate-silicate geochemical cycle and its effect on atmospheric carbon-dioxide over the past 100 million years. Am. J. Sci. 283, 641-683.

Besson, P., Degboe, J., Berge, B., Chavagnac, V., Fabre, S. and Berger, G. (2014) Calcium, Na, K and Mg concentrations in seawater by inductively coupled plasma-atomic emission epectrometry: applications to IAPSO seawater reference material, hydrothermal fluids and synthetic seawater solutions. Geostand. Geoanal. Res. 38, 355-362.

Bizzarro, M., Baker, J.A., Haack, H. and Lundgaard, K.L. (2005) Rapid timescales for accretion and melting of differentiated planetesimals inferred from ^{26}Al-^{26}Mg chronometry. Astrophys. J. Letters 632, L41.

Black, J.R., Epstein, E., Rains, W.D., Yin, Q.Z. and Casey, W.H. (2008) Magnesium-isotope fractionation during plant growth. Environ. Sci. Technol. 42, 7831-7836.

Bolou-Bi, E.B., Vigier, N., Brenot, A. and Poszwa, A. (2009) Magnesium isotope compositions of natural reference materials. Geostand. Geoanal. Res. 33, 95-109.

Bolou-Bi, E.B., Poszwa, A., Leyval, C. and Vigier, N. (2010) Experimental determination of magnesium isotope fractionation during higher plant growth. Geochim. Cosmochim. Acta 74, 2523-2537.

Bolou-Bi, E.B., Vigier, N., Poszwa, A., Boudot, J.P. and Dambrine, E. (2012) Effects of biogeochemical processes on magnesium isotope variations in a forested catchment in the Vosges Mountains (France). Geochim. Cosmochim. Acta 87, 341-355.

Bonnet, M.P., Barroux, G., Martinez, J.M., Seyler, F., Moreira-Turcq, P., Cochonneau, G., Melack, J.M., Boaventura, G., Maurice-Bourgoin, L., León, J.G., Roux, E., Calmant, S., Kosuth, P., Guyot, J.L. and Seyler, P. (2008) Floodplain hydrology in an Amazon floodplain lake (Lago Grande de Curuaí). J. Hydrol. 349, 18-30.

Bottomley, D.J., Chan, L.H., Katz, A., Starinsky, A. and Clark, I.D. (2003) Lithium isotope geochemistry and origin of Canadian shield brines. Ground Water 41, 847-856.

Bouchez, J., Lupker, M., Gaillardet, J., France-Lanord, C. and Maurice, L. (2011) How important is it to integrate riverine suspended sediment chemical composition with depth? Clues from Amazon River depth-profiles. Geochim. Cosmochim. Acta 75, 6955-6970.

Bouchez, J., Gaillardet, J., Lupker, M., Louvat, P., France-Lanord, C., Maurice, L., Armijos, E. and Moquet, J.-S. (2012) Floodplains of large rivers: Weathering reactors or simple silos? Chem. Geol. 332-333, 166-184.

Bouchez, J., von Blanckenburg, F. and Schuessler, J.A. (2013) Modeling novel stable isotope ratios in the weathering zone. Am. J. Sci. 313, 267-308.

Bouchez, J., Gaillardet, J. and von Blanckenburg, F. (2014a) Weathering intensity in lowland river basins: from the andes to the amazon mouth. Procedia Earth Planet. Sci. 10, 280-286.

Bouchez, J., Galy, V., Hilton, R.G., Gaillardet, J., Moreira-Turcq, P., Pérez, M.A., France-Lanord, C. and Maurice, L. (2014b) Source, transport and fluxes of Amazon River particulate organic carbon: Insights from river sediment depth-profiles. Geochim. Cosmochim. Acta 133, 280-298.

Bouchez, J., Moquet, J.S., Espinoza, J.C., Martinez, J.M., Guyot, J.L., Lagane, C., Filizola, N., Noriega, L., Hidalgo Sanchez, L. and Pombosa, R. (2017) River mixing in the Amazon as a driver of concentration-discharge relationships. Water Resources Research 53, 8660-8685.

Bourgoin, L.M., Bonnet, M.-P., Martinez, J.-M., Kosuth, P., Cochonneau, G., Moreira-Turcq, P., Guyot, J.-L., Vauchel, P., Filizola, N. and Seyler, P. (2007) Temporal dynamics of water and sediment exchanges between the Curuaí floodplain and the Amazon River, Brazil. J. Hydrol. 335, 140-156.

Bowen, H.J.M. (1979) Environmental chemistry of the elements. Academic Press, London, UK.

Boyle, E.A., Edmond, J.M. and Sholkovitz, E.R. (1977) Mechanism of iron removal in estuaries. Geochim. Cosmochim. Acta 41, 1313-1324.

Brenot, A., Cloquet, C., Vigier, N., Carignan, J. and France-Lanord, C. (2008) Magnesium isotope systematics of the lithologically varied Moselle river basin, France. Geochim. Cosmochim. Acta 72, 5070-5089.

Bridge, J.S. and Demicco, R.V. (2008) Earth surface processes, landforms and sediment deposits. Cambridge University Press, Cambridge.

Brimhall, G.H. and Dietrich, W.E. (1987) Constitutive mass balance relations between chemical composition, volume, density, porosity, and strain in metasomatic hydrochemical systems: results on weathering and pedogenesis. Geochim. Cosmochim. Acta 51, 567-587.

Bryant, C.J., McCulloch, M.T. and Bennett, V.C. (2003) Impact of matrix effects on the accurate measurement of Li isotope ratios by inductively coupled plasma mass spectrometry (MC-ICP-MS) under "cold" plasma conditions. J. Anal. At. Spectrom. 18, 734-737.

Bryant, C.J., Chappell, B.W., Bennett, V.C. and McCulloch, M.T. (2004) Lithium isotopic compositions of the New England Batholith: correlations with inferred source rock compositions. Geol. Soc. Am. Spec. 389, 199-214.

Buss, H., White, A., Dessert, C., Gaillardet, J., Blum, A. and Sak, P. (2010) Depth profiles in a tropical volcanic critical zone observatory: Basse-Terre, Guadeloupe, in: Torres-Alvarado, I.S., Birkkle, P. (Ed.), Proceedings of the 13th International Conference on Water–Rock Interaction. Taylor & Francis Group, London, UK.

Calmels, D., Galy, A., Hovius, N., Bickle, M., West, A.J., Chen, M.-C. and Chapman, H. (2011) Contribution of deep groundwater to the weathering budget in a rapidly eroding mountain belt, Taiwan. Earth Planet. Sci. Lett. 303, 48-58.

Camuffo, D. (1995) Physical weathering of stones. Sci. Total Environ. 167, 1-14.

Carpenter, J.H. and Manella, M.E. (1973) Magnesium to chlorinity ratios in seawater. J. Geophys. Res. 78, 3621-3626.

Chan, L.H. and Edmond, J.M. (1988) Variation of lithium isotope composition in the marine-environment: a preliminary report. Geochim. Cosmochim. Acta 52, 1711-1717.

Chang, V.T.C., Makishima, A., Belshaw, N.S. and O'Nions, R.K. (2003) Purification of Mg from low-Mg biogenic carbonates for isotope ratio determination using multiple collector ICP-MS. J. Anal. At. Spectrom. 18, 296-301.

Chang, V.T.C., Williams, R.J.P., Makishima, A., Belshawl, N.S. and O'Nions, R.K. (2004) Mg and Ca isotope fractionation during $CaCO_3$ biomineralisation. Biochem. Biophys. Res. Commun. 323, 79-85.

Chapela Lara, M., Buss, H.L., Pogge von Strandmann, P.A.E., Schuessler, J.A. and Moore, O.W. (2017) The influence of critical zone processes on the Mg isotope budget in a tropical, highly weathered andesitic catchment. Geochim. Cosmochim. Acta 202, 77-100.

Chen, T.C., Yeung, M.R. and Mori, N. (2004) Effect of water saturation on deterioration of welded tuff due to freeze-thaw action. Cold. Reg. Sci. Technol. 38, 127-136.

Clark, P.U. and Mix, A.C. (2002) Ice sheets and sea level of the Last Glacial Maximum. Quat. Sci. Rev. 21, 1-7.

Clergue, C., Dellinger, M., Buss, H.L., Gaillardet, J., Benedetti, M.F. and Dessert, C. (2015) Influence of atmospheric deposits and secondary minerals on Li isotopes budget in a highly weathered catchment, Guadeloupe (Lesser Antilles). Chem. Geol. 414, 28-41.

Clow, D.W. and Mast, M.A. (2010) Mechanisms for chemostatic behavior in catchments: Implications for CO_2 consumption by mineral weathering. Chem. Geol. 269, 40-51.

Colbourn, G., Ridgwell, A. and Lenton, T.M. (2015) The time scale of the silicate weathering negative feedback on atmospheric CO_2. Global Biogeochem. Cycles 29, 583-596.

Colmeet-Daage, F. and Bernard, Z. (1979) Contribution à l'Atlas des départements d'Outre-mer : Guadeloupe. Carte des sols de la Guadeloupe, Grande-Terre, Marie-Galante. Carte des pentes et du modelé de la Guadeloupe, Grande-Terre, Marie-Galante. ORSTOM, Antilles.

Colten, V.A. and Hanor, J.S. (1984) Variations in dissolved lithium in the Mississippi River and Mississippi River estuary, Louisiana, USA, during low river stage. Chem. Geol. 47, 85-96.

Delaney, M.L., W.H.Bé, A. and Boyle, E.A. (1985) Li, Sr, Mg, and Na in foraminiferal calcite shells from laboratory culture, sediment traps, and sediment cores. Geochim. Cosmochim. Acta 49, 1327-1341.

Dellinger, M., Gaillardet, J., Bouchez, J., Calmels, D., Galy, V., Hilton, R.G., Louvat, P. and France-Lanord, C. (2014) Lithium isotopes in large rivers reveal the cannibalistic nature of modern continental weathering and erosion. Earth Planet. Sci. Lett. 401, 359-372.

Dellinger, M., Gaillardet, J., Bouchez, J., Calmels, D., Louvat, P., Dosseto, A., Gorge, C., Alanoca, L. and Maurice, L. (2015) Riverine Li isotope fractionation in the Amazon river basin controlled by the weathering regimes. Geochim. Cosmochim. Acta 164, 71-93.

DePaolo, D.J. (2011) Surface kinetic model for isotopic and trace element fractionation during precipitation of calcite from aqueous solutions. Geochim. Cosmochim. Acta 75, 1039-1056.

Dessert, C., Lajeunesse, E., Lloret, E., Clergue, C., Crispi, O., Gorge, C. and Quidelleur, X. (2015) Controls on chemical weathering on a mountainous volcanic tropical island: Guadeloupe (French West Indies). Geochim. Cosmochim. Acta 171, 216-237.

Dixon, J.L., Hartshorn, A.S., Heimsath, A.M., DiBiase, R.A. and Whipple, K.X. (2012) Chemical weathering response to tectonic forcing: A soils perspective from the San Gabriel Mountains, California. Earth Planet. Sci. Lett. 323, 40-49.

Dosseto, A., Bourdon, B., Gaillardet, J., Allègre, C.J. and Filizola, N. (2006) Time scale and conditions of weathering under tropical climate: study of the Amazon basin with U-series. Geochim. Cosmochim. Acta 70, 71-89.

Dunne, T., Mertes, L.A., Meade, R.H., Richey, J.E. and Forsberg, B.R. (1998) Exchanges of sediment between the flood plain and channel of the Amazon River in Brazil. Geological Society of America Bulletin 110, 450-467.

Dupré, B., Gaillardet, J., Rousseau, D. and Allègre, C.J. (1996) Major and trace elements of river-borne material: the Congo Basin. Geochim. Cosmochim. Acta 60, 1301-1321.

Eby, G.N. (2004) Principles of environmental geochemistry. Thomson-Brooks/Cole, Pacific Grove, CA. ; London.

Egli, M., Dahms, D. and Norton, K. (2014) Soil formation rates on silicate parent material in alpine environments: Different approaches–different results? Geoderma 213, 320-333.

Fan, B., Zhao, Z.-Q., Tao, F., Li, X., Tao, Z., Gao, S. and He, M. (2016) The geochemical behavior of Mg isotopes in the Huanghe basin, China. Chem. Geol. 426, 19-27.

Filizola, N. and Guyot, J.L. (2009) Suspended sediment yields in the Amazon basin: an assessment using the Brazilian national data set. Hydrol. Processes 23, 3207-3215.

Flesch, G., Anderson, A. and Svec, H. (1973) A secondary isotopic standard for $^{6}Li/^{7}Li$ determinations. Int. J. Mass Spectrom. Ion Phys. 12, 265-272.

Floury, P., Gaillardet, J., Gayer, E., Bouchez, J., Tallec, G., Ansart, P., Koch, F., Gorge, C., Blanchouin, A. and Roubaty, J.-L. (2017) The potamochemical symphony: new progress in the high-frequency acquisition of stream chemical data. Hydrol Earth Syst Sc 21, 6153.

Foster, G.L., Pogge von Strandmann, P.A.E. and Rae, J.W.B. (2010) Boron and magnesium isotopic composition of seawater. Geochem. Geophys. Geosyst. 11.

Friend, C.R.L. and Nutman, A.P. (2005) New pieces to the Archaean terrane jigsaw puzzle in the Nuuk region, southern West Greenland: steps in transforming a simple insight into a complex regional tectonothermal model. J. Geol. Soc. 162, 147-162.

Frings, P.J., De La Rocha, C., Struyf, E., van Pelt, D., Schoelynck, J., Hudson, M.M., Gondwe, M.J., Wolski, P., Mosimane, K., Gray, W., Schaller, J. and Conley, D.J. (2014) Tracing silicon cycling in the Okavango Delta, a sub-tropical flood-pulse wetland using silicon isotopes. Geochim. Cosmochim. Acta 142, 132-148.

Frings, P.J., Clymans, W., Fontorbe, G., De La Rocha, C.L. and Conley, D.J. (2016) The continental Si cycle and its impact on the ocean Si isotope budget. Chem. Geol. 425, 12-36.

Froelich, F. and Misra, S. (2014) Was the late Paleocene-early Eocene hot because earth was flat? An ocean lithium isotope view of mountain building, continental weathering, carbon dioxide, and Earth's Cenozoic climate. Oceanography 27, 36-49.

Gaillardet, J., Dupré, B., Allègre, C.J. and Négrel, P. (1997) Chemical and physical denudation in the Amazon River basin. Chem. Geol. 142, 141-173.

Gaillardet, J., Dupré, B. and Allègre, C.J. (1999a) Geochemistry of large river suspended sediments: silicate weathering or recycling tracer? Geochim. Cosmochim. Acta 63, 4037-4051.

Gaillardet, J., Dupré, B., Louvat, P. and Allègre, C.J. (1999b) Global silicate weathering and CO_2 consumption rates deduced from the chemistry of large rivers. Chem. Geol. 159, 3-30.

Galy, A., Belshaw, N.S., Halicz, L. and O'Nions, R.K. (2001) High-precision measurement of magnesium isotopes by multiple-collector inductively coupled plasma mass spectrometry. Int. J. Mass Spectrom. 208, 89-98.

Garrels, R.M., Mackenzie, F.T. and Hunt, C. (1975) Chemical cycles and the global environment: assessing human influences. William Kaufmann Inc., Los Altos, California.

Gladney, E.S. and Roelandts, I. (1988) Compilation of elemental concentration data for USGS BHVO-1, MAG-1, QLO-1, RGM-1, SCo-1, SDC-1, SGR-1 and STM-1. Geostandard Newsletter 12, 253-362.

Godsey, S.E., Kirchner, J.W. and Clow, D.W. (2009) Concentration-discharge relationships reflect chemostatic characteristics of US catchments. Hydrol. Processes 23, 1844-1864.

Gothmann, A.M., Stolarski, J., Adkins, J.F. and Higgins, J.A. (2017) A Cenozoic record of seawater Mg isotopes in well-preserved fossil corals. Geology 45, 1039-1042.

Graham, W.F. and Duce, R.A. (1979) Atmospheric pathways of the phosphorus cycle. Geochim. Cosmochim. Acta 43, 1195-1208.

Griffiths, R.P., Baham, J.E. and Caldwell, B.A. (1994) Soil solution chemistry of ectomycorrhizal mats in forest soil. Soil Biol. Biochem. 26, 331-337.

Grotzinger, J.P. and Jordan, T.H. (2014) Understanding Earth, 7th ed. W.H. Freeman and Company, New York.

Guérin, A. (2015) Dynamique de l'écoulement dans un aquifère non confiné. Université Paris Diderot (Doctoral dissertation).

Guyot, J.L., Jouanneau, J.M., Soares, L., Boaventura, G.R., Maillet, N. and Lagane, C. (2007) Clay mineral composition of river sediments in the Amazon Basin. Catena 71, 340-356.

Hall, J.M., Chan, L.H., McDonough, W.F. and Turekian, K.K. (2005) Determination of the lithium isotopic composition of planktic foraminifera and its application as a paleo-seawater proxy. Mar. Geol. 217, 255-265.

Hathorne, E.C. and James, R.H. (2006) Temporal record of lithium in seawater: A tracer for silicate weathering? Earth Planet. Sci. Lett. 246, 393-406.

Heimsath, A.M., Dietrich, W.E., Nishiizumi, K. and Finkel, R.C. (1997) The soil production function and landscape equilibrium. Nature 388, 358-361.

Henchiri, S., Clergue, C., Dellinger, M., Gaillardet, J., Louvat, P. and Bouchez, J. (2014) The influence of hydrothermal activity on the Li isotopic signature of rivers draining volcanic areas. Geochemistry of the Earth's Surface Ges-10 10, 223-230.

Henchiri, S., Gaillardet, J., Dellinger, M., Bouchez, J. and Spencer, R.G.M. (2016) Riverine dissolved lithium isotopic signatures in low-relief central Africa and their link to weathering regimes. Geophys. Res. Lett. 43, 4391-4399.

Higgins, J.A. and Schrag, D.P. (2015) The Mg isotopic composition of Cenozoic seawater- evidence for a link between Mg-clays, seawater Mg/Ca, and climate. Earth Planet. Sci. Lett. 416, 73-81.

Hindshaw, R.S., Tipper, E.T., Reynolds, B.C., Lemarchand, E., Wiederhold, J.G., Magnusson, J., Bernasconi, S.M., Kretzschmar, R. and Bourdon, B. (2011) Hydrological control of stream water chemistry in a glacial catchment (Damma Glacier, Switzerland). Chem. Geol. 285, 215-230.

Hopwood, M.J., Connelly, D.P., Arendt, K.E., Juul-Pedersen, T., Stinchcombe, M., Meire, L., Esposito, M. and Krishna, R. (2016) Seasonal changes in Fe along a glaciated Greenlandic fjord. Front. Earth Sci. 4.

Huang, F., Glessner, J., Ianno, A., Lundstrom, C. and Zhang, Z.F. (2009) Magnesium isotopic composition of igneous rock standards measured by MC-ICP-MS. Chem. Geol. 268, 15-23.

Hughes, H.J., Sondag, F., Santos, R.V., Andre, L. and Cardinal, D. (2013) The riverine silicon isotope composition of the Amazon Basin. Geochim. Cosmochim. Acta 121, 637-651.

Huh, Y., Chan, L.H., Zhang, L. and Edmond, J.M. (1998) Lithium and its isotopes in major world rivers: implications for weathering and the oceanic budget. Geochim. Cosmochim. Acta 62, 2039-2051.

Huh, Y., Chan, L.H. and Edmond, J.M. (2001) Lithium isotopes as a probe of weathering processes: Orinoco River. Earth Planet. Sci. Lett. 194, 189-199.

Huybrechts, P. and de Wolde, J. (1999) The dynamic response of the Greenland and Antarctic ice sheets to multiple-century climatic warming. J. Clim. 12, 2169-2188.

Huybrechts, P., Goelzer, H., Janssens, I., Driesschaert, E., Fichefet, T., Goosse, H. and Loutre, M.F. (2011) Response of the Greenland and Antarctic ice sheets to multi-millennial greenhouse warming in the Earth system model of intermediate complexity LOVECLIM. Surveys in Geophysics 32, 397-416.

Jacobson, A.D., Blum, J.D., Chamberlain, C.P., Craw, D. and Koons, P.O. (2003) Climatic and tectonic controls on chemical weathering in the New Zealand Southern Alps. Geochim. Cosmochim. Acta 67, 29-46.

Jacobson, A.D., Zhang, Z.F., Lundstrom, C. and Huang, F. (2010) Behavior of Mg isotopes during dedolomitization in the Madison Aquifer, South Dakota. Earth Planet. Sci. Lett. 297, 446-452.

James, R.H. and Palmer, M.R. (2000a) The lithium isotope composition of international rock standards. Chem. Geol. 166, 319-326.

James, R.H. and Palmer, M.R. (2000b) Marine geochemical cycles of the alkali elements and boron: the role of sediments. Geochim. Cosmochim. Acta 64, 3111-3122.

Jobbagy, E.G. and Jackson, R.B. (2001) The distribution of soil nutrients with depth: global patterns and the imprint of plants. Biogeochemistry 53, 51-77.

Jones, I.W., Munhoven, G., Tranter, M., Huybrechts, P. and Sharp, M.J. (2002) Modelled glacial and non-glacial HCO_3^-, Si and Ge fluxes since the LGM: little potential for impact on atmospheric CO_2 concentrations and a potential proxy of continental chemical erosion, the marine Ge/Si ratio. Global Planet. Change 33, 139-153.

Keene, W.C., Pszenny, A.A.P., Galloway, J.N. and Hawley, M.E. (1986) Sea-salt corrections and interpretation of constituent ratios in marine precipitation. J Geophys Res-Atmos 91, 6647-6658.

Kisakurek, B., James, R.H. and Harris, N.B.W. (2004a) Utility of lithium isotopes as tracers of continental weathering processes. Geochim. Cosmochim. Acta 68, A420-A420.

Kisakurek, B., Widdowson, M. and James, R.H. (2004b) Behaviour of Li isotopes during continental weathering: the Bidar laterite profile, India. Chem. Geol. 212, 27-44.

Kisakurek, B., James, R.H. and Harris, N.B.W. (2005) Li and δ^7Li in Himalayan rivers: proxies for silicate weathering? Earth Planet. Sci. Lett. 237, 387-401.

Langen, P.L., Mottram, R.H., Christensen, J.H., Boberg, F., Rodehacke, C.B., Stendel, M., van As, D., Ahlstrom, A.P., Mortensen, J., Rysgaard, S., Petersen, D., Svendsen, K.H., Adalgeirsdottir, G. and Cappelen, J. (2015) Quantifying energy and mass fluxes controlling Godthabsfjord freshwater input in a 5 km simulation (1991-2012). J. Clim. 28, 3694-3713.

Larsen, M.C. and Simon, A. (1993) A rainfall intensity-duration threshold for landslides in a humid-tropical environment, Puerto Rico. Geografiska Annaler. Series A, Physical Geography 75, 13-23.

Lasaga, A.C., Soler, J.M., Ganor, J., Burch, T.E. and Nagy, K.L. (1994) Chemical weathering rate laws and global geochemical cycles. Geochim. Cosmochim. Acta 58, 2361-2386.

Lemarchand, E., Chabaux, F., Vigier, N., Millot, R. and Pierret, M.C. (2010) Lithium isotope systematics in a forested granitic catchment (Strengbach, Vosges Mountains, France). Geochim. Cosmochim. Acta 74, 4612-4628.

Li, W.Q., Beard, B.L., Li, C.X. and Johnson, C.M. (2014) Magnesium isotope fractionation between brucite [$Mg(OH)_2$] and Mg aqueous species: implications for silicate weathering and biogeochemical processes. Earth Planet. Sci. Lett. 394, 82-93.

Li, W.Y., Teng, F.Z., Ke, S., Rudnick, R.L., Gao, S., Wu, F.Y. and Chappell, B.W. (2010) Heterogeneous magnesium isotopic composition of the upper continental crust. Geochim. Cosmochim. Acta 74, 6867-6884.

Li, Y., Zhang, Q.W., Wan, G.J., Huang, R.G., Piao, H.C., Bai, L.Y. and Li, L. (2006) Physical mechanisms of plant roots affecting weathering and leaching of loess soil. Sci. China, Ser. D Earth Sci. 49, 1002-1008.

Liu, X.-M., Wanner, C., Rudnick, R.L. and McDonough, W.F. (2015) Processes controlling δ^7Li in rivers illuminated by study of streams and groundwaters draining basalts. Earth Planet. Sci. Lett. 409, 212-224.

Lloret, E. (2010) Dynamique du carbone dans des petits bassins versants tropicaux, Exemple de la Guadeloupe PhD Thesis Université Paris Diderot.

Lloret, E., Dessert, C., Gaillardet, J., Alberic, P., Crispi, O., Chaduteau, C. and Benedetti, M.F. (2011) Comparison of dissolved inorganic and organic carbon yields and fluxes in the watersheds of tropical volcanic islands, examples from Guadeloupe (French West Indies). Chem. Geol. 280, 65-78.

Ma, L., Teng, F.-Z., Jin, L., Ke, S., Yang, W., Gu, H.-O. and Brantley, S.L. (2015) Magnesium isotope fractionation during shale weathering in the Shale Hills critical zone observatory: accumulation of light Mg isotopes in soils by clay mineral transformation. Chem. Geol. 397, 37-50.

Maher, K. (2011) The role of fluid residence time and topographic scales in determining chemical fluxes from landscapes. Earth Planet. Sci. Lett. 312, 48-58.

Mavromatis, V., Gautier, Q., Bosc, O. and Schott, J. (2013) Kinetics of Mg partition and Mg stable isotope fractionation during its incorporation in calcite. Geochim. Cosmochim. Acta 114, 188-203.

Mavromatis, V., Rinder, T., Prokushkin, A.S., Pokrovsky, O.S., Korets, M.A., Chmeleff, J. and Oelkers, E.H. (2016) The effect of permafrost, vegetation, and lithology on Mg and Si isotope composition of the Yenisey River and its tributaries at the end of the spring flood. Geochim. Cosmochim. Acta 191, 32-46.

McBean, G., Alekseev, G., Chen, D., Foerland, E., Fyfe, J., Groisman, P.Y., King, R., Melling, H., Vose, R. and Whitfield, P.H. (2005) Chapter 2, Arctic climate: past and present, Arctic climate impact assessment. Cambridge university press, p. 1042.

McGregor, V.R. (1973) The early Precambrian gneisses of Godthab district, West-Greenland. Phil. Trans. R. Soc. Lond. A 273, 343-358.

Meire, L., Sogaard, D.H., Mortensen, J., Meysman, F.J.R., Soetaert, K., Arendt, K.E., Juul-Pedersen, T., Blicher, M.E. and Rysgaard, S. (2015) Glacial meltwater and primary production are drivers of strong CO_2 uptake in fjord and coastal waters adjacent to the Greenland Ice Sheet. Biogeosciences 12, 2347-2363.

Meire, L., Meire, P., Struyf, E., Krawczyk, D.W., Arendt, K.E., Yde, J.C., Juul Pedersen, T., Hopwood, M.J., Rysgaard, S. and Meysman, F.J.R. (2016) High export of dissolved silica from the Greenland Ice Sheet. Geophys. Res. Lett. 43, 9173-9182.

Millero, F.J. (1974) Physical chemistry of seawater. Annu. Rev. Earth Planet. Sci. 2, 101-150.

Millot, R., Gaillardet, J., Dupre, B. and Allegre, C.J. (2002) The global control of silicate weathering rates and the coupling with physical erosion: new insights from rivers of the Canadian Shield. Earth Planet. Sci. Lett. 196, 83-98.

Millot, R., Guerrot, C. and Vigier, N. (2004) Accurate and high-precision measurement of lithium isotopes in two reference materials by MC-ICP-MS. Geostand. Geoanal. Res. 28, 153-159.

Millot, R., Petelet-Giraud, E., Guerrot, C. and Negrel, P. (2010a) Multi-isotopic composition (δ^7Li-δ^{11}B-δD-δ^{18}O) of rainwaters in France: Origin and spatio-temporal characterization. Appl. Geochem. 25, 1510-1524.

Millot, R., Scaillet, B. and Sanjuan, B. (2010b) Lithium isotopes in island arc geothermal systems: Guadeloupe, Martinique (French West Indies) and experimental approach. Geochim. Cosmochim. Acta 74, 1852-1871.

Millot, R., Vigier, N. and Gaillardet, J. (2010c) Behaviour of lithium and its isotopes during weathering in the Mackenzie Basin, Canada. Geochim. Cosmochim. Acta 74, 3897-3912.

Misra, S. and Froelich, P.N. (2012) Lithium isotope history of Cenozoic seawater: changes in silicate weathering and reverse weathering. Science 335, 818-823.

Molnar, P., Anderson, R.S. and Anderson, S.P. (2007) Tectonics, fracturing of rock, and erosion. J Geophys Res-Earth 112.

Moquet, J.-S., Crave, A., Viers, J., Seyler, P., Armijos, E., Bourrel, L., Chavarri, E., Lagane, C., Laraque, A., Casimiro, W.S.L., Pombosa, R., Noriega, L., Vera, A. and Guyot, J.-L. (2011) Chemical weathering and atmospheric/soil CO_2 uptake in the Andean and Foreland Amazon basins. Chem. Geol. 287, 1-26.

Moquet, J.-S., Guyot, J.-L., Crave, A., Viers, J., Filizola, N., Martinez, J.-M., Oliveira, T.C., Sánchez, L.S.H., Lagane, C., Casimiro, W.S.L., Noriega, L. and Pombosa, R. (2016) Amazon River dissolved load: temporal dynamics and annual budget from the Andes to the ocean. Environmental Science and Pollution Research 23, 11405-11429.

Moreira-Turcq, P., Jouanneau, J.M., Turcq, B., Seyler, P., Weber, O. and Guyot, J.L. (2004) Carbon sedimentation at Lago Grande de Curuai, a floodplain lake in the low Amazon region: insights into sedimentation rates. Palaeogeogr. Palaeoclimatol. Palaeoecol. 214, 27-40.

Moriguti, T. and Nakamura, E. (1998) High-yield lithium separation and the precise isotopic analysis for natural rock and aqueous samples. Chem. Geol. 145, 91-104.

Morozov, N. (1968) Geochemistry of rare alkaline elements in the oceans and seas. Oceanology 8, 169-178.

Mortatti, J. and Probst, J.L. (2003) Silicate rock weathering and atmospheric/soil CO_2 uptake in the Amazon basin estimated from river water geochemistry: seasonal and spatial variations. Chem. Geol. 197, 177-196.

Mortensen, J., Lennert, K., Bendtsen, J. and Rysgaard, S. (2011) Heat sources for glacial melt in a sub-Arctic fjord (Godthabsfjord) in contact with the Greenland Ice Sheet. J Geophys Res-Oceans 116.

Mortensen, J., Bendtsen, J., Motyka, R.J., Lennert, K., Truffer, M., Fahnestock, M. and Rysgaard, S. (2013) On the seasonal freshwater stratification in the proximity of fast-flowing tidewater outlet glaciers in a sub-Arctic sill fjord. J Geophys Res-Oceans 118, 1382-1395.

Murphy, M.J., Pogge von Strandmann, P.A.E., Porcelli, D. and Ingri, J. (2014) Li isotope behaviour in the low salinity zone during estuarine mixing. Procedia Earth Planet. Sci. 10, 204-207.

Murray, R.W., Miller, D.J. and Kryc, K.A. (2000) Analysis of major and trace elements in rocks, sediments, and interstitial waters by inductively coupled plasma–atomic emission spectrometry (ICP-AES). ODP tech. Note, 29.

Nesbitt, H.W. and Young, G.M. (1982) Early Proterozoic climates and plate motions inferred from major element chemistry of lutites. Nature 299, 715.

Nesbitt, W.H. and Markovics, G. (1997) Weathering of granodioritic crust, long-term storage of elements in weathering profiles, and petrogenesis of siliciclastic sediments. Geochim. Cosmochim. Acta 61, 1653-1670.

Nishio, Y. and Nakai, S.i. (2002) Accurate and precise lithium isotopic determinations of igneous rock samples using multi-collector inductively coupled plasma mass spectrometry. Analytica Chimica Acta 456, 271-281.

Opfergelt, S., Georg, R.B., Delvaux, B., Cabidoche, Y.M., Burton, K.W. and Halliday, A.N. (2012) Mechanisms of magnesium isotope fractionation in volcanic soil weathering sequences, Guadeloupe. Earth Planet. Sci. Lett. 341, 176-185.

Parkhurst, D.L. and Appelo, C.A.J. (2013) Description of input and examples for PHREEQC version 3-a computer program for speciation, batch-reaction, one-dimensional transport, and inverse geochemical calculations,U.S. Geological Survey Techniques and Methods, book 6, chap. A43, 497p., available only at http://pubs.usgs.gov/tm/06/a43.

Pavlov, M., Siegbahn, P.E.M. and Sandström, M. (1998) Hydration of beryllium, magnesium, calcium, and zinc ions using density functional theory. J. Phys. Chem. A 102, 219-228.

Pawlik, Ł., Phillips, J.D. and Šamonil, P. (2016) Roots, rock, and regolith: Biomechanical and biochemical weathering by trees and its impact on hillslopes—a critical literature review. Earth Sci. Rev. 159, 142-159.

Pearce, C.R., Saldi, G.D., Schott, J. and Oelkers, E.H. (2012) Isotopic fractionation during congruent dissolution, precipitation and at equilibrium: evidence from Mg isotopes. Geochim. Cosmochim. Acta 92, 170-183.

Petit, J.R., Jouzel, J., Raynaud, D., Barkov, N.I., Barnola, J.M., Basile, I., Bender, M., Chappellaz, J., Davis, M., Delaygue, G., Delmotte, M., Kotlyakov, V.M., Legrand, M., Lipenkov, V.Y., Lorius, C., Pepin, L., Ritz, C., Saltzman, E. and Stievenard, M. (1999) Climate and atmospheric history of the past 420,000 years from the Vostok ice core, Antarctica. Nature 399, 429-436.

Petrich, C. and Eicken, H. (2010) Growth, structure and properties of sea ice, Sea Ice. Wiley-Blackwell, pp. 23-77.

Phan, T.T., Capo, R.C., Stewart, B.W., Graney, J.R., Johnson, J.D., Sharma, S. and Toro, J. (2015) Trace metal distribution and mobility in drill cuttings and produced waters from Marcellus Shale gas extraction: Uranium, arsenic, barium. Appl. Geochem. 60, 89-103.

Piper, A. (1953) A graphic procedure in the geochemical interpretation of water analysis, US department of the interior, geological survey. Water Resources Division, Ground Water Branch, Washington.

Pistiner, J.S. and Henderson, G.M. (2003) Lithium-isotope fractionation during continental weathering processes. Earth Planet. Sci. Lett. 214, 327-339.

Pogge von Strandmann, P.A.E., Burton, K.W., James, R.H., van Calsteren, P., Gislason, S.R. and Mokadem, F. (2006) Riverine behaviour of uranium and lithium isotopes in an actively glaciated basaltic terrain. Earth Planet. Sci. Lett. 251, 134-147.

Pogge von Strandmann, P.A.E. (2008) Precise magnesium isotope measurements in core top planktic and benthic foraminifera. Geochem. Geophys. Geosyst. 9.

Pogge von Strandmann, P.A.E., Burton, K.W., James, R.H., van Calsteren, P., Gislason, S.R. and Sigfusson, B. (2008a) The influence of weathering processes on riverine magnesium isotopes in a basaltic terrain. Earth Planet. Sci. Lett. 276, 187-197.

Pogge von Strandmann, P.A.E., James, R.H., van Calsteren, P., Gislason, S.R. and Burton, K.W. (2008b) Lithium, magnesium and uranium isotope behaviour in the estuarine environment of basaltic islands. Earth Planet. Sci. Lett. 274, 462-471.

Pogge von Strandmann, P.A.E., Burton, K.W., James, R.H., van Calsteren, P. and Gislason, S.R. (2010) Assessing the role of climate on uranium and lithium isotope behaviour in rivers draining a basaltic terrain. Chem. Geol. 270, 227-239.

Pogge von Strandmann, P.A.E., Elliott, T., Marschall, H.R., Coath, C., Lai, Y.J., Jeffcoate, A.B. and Ionov, D.A. (2011) Variations of Li and Mg isotope ratios in bulk chondrites and mantle xenoliths. Geochim. Cosmochim. Acta 75, 5247-5268.

Pogge von Strandmann, P.A.E., Opfergelt, S., Lai, Y.J., Sigfusson, B., Gislason, S.R. and Burton, K.W. (2012) Lithium, magnesium and silicon isotope behaviour accompanying weathering in a basaltic soil and pore water profile in Iceland. Earth Planet. Sci. Lett. 339, 11-23.

Pogge von Strandmann, P.A.E., Jenkyns, H.C. and Woodfine, R.G. (2013) Lithium isotope evidence for enhanced weathering during Oceanic Anoxic Event 2. Nat. Geosci. 6, 668-672.

Pogge von Strandmann, P.A.E., Forshaw, J. and Schmidt, D.N. (2014) Modern and Cenozoic records of seawater magnesium from foraminiferal Mg isotopes. Biogeosciences 11, 5155-5168.

Pogge von Strandmann, P.A.E. and Henderson, G.M. (2015) The Li isotope response to mountain uplift. Geology 43, 67-70.

Pogge von Strandmann, P.A.E., Vaks, A., Bar-Matthews, M., Ayalon, A., Jacob, E. and Henderson, G.M. (2017) Lithium isotopes in speleothems: temperature-controlled variation in silicate weathering during glacial cycles. Earth Planet. Sci. Lett. 469, 64-74.

Pozhidaev, A.I., Polynova, T.N., Porai-Koshits, M.A. and Dudakov, V.G. (1974) Crystal structure of disodium magnesium ethylenediaminetetraacetate tetrahydrate. Journal of Structural Chemistry 15, 149-150.

Rad, S., Rivé, K., Vittecoq, B., Cerdan, O. and Allègre, C.J. (2013) Chemical weathering and erosion rates in the Lesser Antilles: an overview in Guadeloupe, Martinique and Dominica. Journal of South American Earth Sciences 45, 331-344.

Richey, J.E., Mertes, L.A.K., Dunne, T., Victoria, R.L., Forsberg, B.R., Tancredi, A.C.N.S. and Oliveira, E. (1989) Sources and routing of the Amazon River flood wave. Global Biogeochem. Cycles 3, 191-204.

Riebe, C.S., Kirchner, J.W., Granger, D.E. and Finkel, R.C. (2001) Strong tectonic and weak climatic control of long-term chemical weathering rates. Geology 29, 511-514.

Riebe, C.S., Kirchner, J.W. and Finkel, R.C. (2003) Long-term rates of chemical weathering and physical erosion from cosmogenic nuclides and geochemical mass balance. Geochim. Cosmochim. Acta 67, 4411-4427.

Riotte, J., Marechal, J.C., Audry, S., Kumar, C., Bedimo, J.P.B., Ruiz, L., Sekhar, M., Cisel, M., Tarak, R.C., Varma, M.R.R., Lagane, C., Reddy, P. and Braun, J.J. (2014) Vegetation impact on stream chemical fluxes: Mule Hole watershed (South India). Geochim. Cosmochim. Acta 145, 116-138.

Rudnick, R.L., Tomascak, P.B., Njo, H.B. and Gardner, L.R. (2004) Extreme lithium isotopic fractionation during continental weathering revealed in saprolites from South Carolina. Chem. Geol. 212, 45-57.

Ryu, J.-S., Vigier, N., Lee, S.-W., Lee, K.-S. and Chadwick, O.A. (2014) Variation of lithium isotope geochemistry during basalt weathering and secondary mineral transformations in Hawaii. Geochim. Cosmochim. Acta 145, 103-115.

Ryu, J.-S., Vigier, N., Decarreau, A., Lee, S.-W., Lee, K.-S., Song, H. and Petit, S. (2016) Experimental investigation of Mg isotope fractionation during mineral dissolution and clay formation. Chem. Geol. 445, 135-145.

Ryu, J.S., Jacobson, A.D., Holmden, C., Lundstrom, C. and Zhang, Z.F. (2011) The major ion, $\delta^{44/40}$Ca, $\delta^{44/42}$Ca, and $\delta^{26/24}$Mg geochemistry of granite weathering at pH=1 and T=25°C: power-law processes and the relative reactivity of minerals. Geochim. Cosmochim. Acta 75, 6004-6026.

Saenger, C. and Wang, Z.R. (2014) Magnesium isotope fractionation in biogenic and abiogenic carbonates: implications for paleoenvironmental proxies. Quat. Sci. Rev. 90, 1-21.

Sauzeat, L., Rudnick, R.L., Chauvel, C., Garcon, M. and Tang, M. (2015) New perspectives on the Li isotopic composition of the upper continental crust and its weathering signature. Earth Planet. Sci. Lett. 428, 181-192.

Sawhney, B. (1972) Selective sorption and fixation of cations by clay minerals: A review. Clays Clay Miner. 20, 93-100.

Schauble, E.A. (2004) Applying stable isotope fractionation theory to new systems. Rev Mineral Geochem 55, 65-111.

Schott, J., Mavromatis, V., Fujii, T., Pearce, C.R. and Oelkers, E.H. (2016) The control of carbonate mineral Mg isotope composition by aqueous speciation: theoretical and experimental modeling. Chem. Geol. 445, 120-134.

Seyler, P.T. and Boaventura, G.R. (2003) Distribution and partition of trace metals in the Amazon basin. Hydrol. Processes 17, 1345-1361.

Sharp, M., Tranter, M., Brown, G.H. and Skidmore, M. (1995) Rates of chemical denudation and CO_2 drawdown in a glacier-covered alpine catchment. Geology 23, 61-64.

Sholkovitz, E.R., Boyle, E.A. and Price, N.B. (1978) Removal of dissolved humic acids and iron during estuarine mixing. Earth Planet. Sci. Lett. 40, 130-136.

Smith, T.M. and Reynolds, R.W. (2005) A global merged land-air-sea surface temperature reconstruction based on historical observations (1880-1997). J. Clim. 18, 2021-2036.

Stallard, R.F. and Edmond, J.M. (1981) Geochemistry of the Amazon. 1. Precipitation chemistry and the marine contribution to the dissolved load at the time of peak discharge. J Geophys Res-Oceans 86, 9844-9858.

Stallard, R.F. and Edmond, J.M. (1983) Geochemistry of the Amazon: 2. The influence of geology and weathering environment on the dissolved load. J. Geophys. Res. Oceans 88, 9671-9688.

Stoffyn-Egli, P. (1982) Conservative behavior of dissolved lithium in estuarine waters. Estuar. Coast. Shelf Sci. 14, 577-587.

Stommel, H. and Arons, A.B. (1959) On the abyssal circulation of the world ocean — II. An idealized model of the circulation pattern and amplitude in oceanic basins. Deep Sea Res. 6, 217-233.

Summerhayes, C.P. and Thorpe, S.A. (1996) Oceanography: an illustrated guide, Chapter 11, 165-181.

Sun, H., Gao, Y., Xiao, Y., Gu, H.-o. and Casey, J.F. (2016) Lithium isotope fractionation during incongruent melting: Constraints from post-collisional leucogranite and residual enclaves from Bengbu Uplift, China. Chem. Geol. 439, 71-82.

Tang, Y.J., Zhang, H.F. and Ying, J.F. (2007) Review of the lithium isotope system as a geochemical tracer. Int. Geol. Rev. 49, 374-388.

Teng, F.-Z., Wadhwa, M. and Helz, R.T. (2007) Investigation of magnesium isotope fractionation during basalt differentiation: Implications for a chondritic composition of the terrestrial mantle. Earth Planet. Sci. Lett. 261, 84-92.

Teng, F.Z., Li, W.Y., Rudnick, R.L. and Gardner, L.R. (2010) Contrasting lithium and magnesium isotope fractionation during continental weathering. Earth Planet. Sci. Lett. 300, 63-71.

Teng, F.Z. (2017) Magnesium Isotope Geochemistry. Non-Traditional Stable Isotopes 82, 219-287.

Tipper, E.T., Galy, A. and Bickle, M.J. (2006a) Riverine evidence for a fractionated reservoir of Ca and Mg on the continents: Implications for the oceanic Ca cycle. Earth Planet. Sci. Lett. 247, 267-279.

Tipper, E.T., Galy, A., Gaillardet, J., Bickle, M.J., Elderfield, H. and Carder, E.A. (2006b) The magnesium isotope budget of the modem ocean: constraints from riverine magnesium isotope ratios. Earth Planet. Sci. Lett. 250, 241-253.

Tipper, E.T., Galy, A. and Bickle, M.J. (2008a) Calcium and magnesium isotope systematics in rivers draining the Himalaya-Tibetan-Plateau region: lithological or fractionation control? Geochim. Cosmochim. Acta 72, 1057-1075.

Tipper, E.T., Louvat, P., Capmas, F., Galy, A. and Gaillardet, J. (2008b) Accuracy of stable Mg and Ca isotope data obtained by MC-ICP-MS using the standard addition method. Chem. Geol. 257, 65-75.

Tipper, E.T., Gaillardet, J., Louvat, P., Capmas, F. and White, A.F. (2010) Mg isotope constraints on soil pore-fluid chemistry: evidence from Santa Cruz, California. Geochim. Cosmochim. Acta 74, 3883-3896.

Tipper, E.T., Calmels, D., Gaillardet, J., Louvat, P., Capmas, F. and Dubacq, B. (2012a) Positive correlation between Li and Mg isotope ratios in the river waters of the Mackenzie Basin challenges the interpretation of apparent isotopic fractionation during weathering. Earth Planet. Sci. Lett. 333, 35-45.

Tipper, E.T., Lemarchand, E., Hindshaw, R.S., Reynolds, B.C. and Bourdon, B. (2012b) Seasonal sensitivity of weathering processes: Hints from magnesium isotopes in a glacial stream. Chem. Geol. 312, 80-92.

Tomascak, P.B., Carlson, R.W. and Shirey, S.B. (1999) Accurate and precise determination of Li isotopic compositions by multi-collector sector ICP-MS. Chem. Geol. 158, 145-154.

Tomascak, P.B. (2004) Developments in the understanding and application of lithium isotopes in the earth and planetary sciences.

Torres, M.A., Baronas, J.J., Clark, K.E., Feakins, S.J. and West, A.J. (2017) Mixing as a driver of temporal variations in river hydrochemistry: 1. Insights from conservative tracers in the Andes-Amazon transition. Water Resources Research 53, 3102-3119.

Tranter, M., Huybrechts, P., Munhoven, G., Sharp, M.J., Brown, G.H., Jones, I.W., Hodson, A.J., Hodgkins, R. and Wadham, J.L. (2002) Direct effect of ice sheets on terrestrial bicarbonate, sulphate and base cation fluxes during the last glacial cycle: minimal impact on atmospheric CO_2 concentrations. Chem. Geol. 190, 33-44.

Tranter, M. (2003) Geochemical weathering in glacial and proglacial environments, in: Turekian, H.D.H.K. (Ed.), Treatise on Geochemistry. Pergamon, Oxford, pp. 189-205.

Trostle, K., Derry, L., Vigier, N. and Chadwick, O. (2014) Magnesium isotope fractionation during arid pedogenesis on the island of Hawaii (USA). Procedia Earth Planet. Sci. 10, 243-248.

Tsai, P.H., You, C.F., Huang, K.F., Chung, C.H. and Sun, Y.B. (2014) Lithium distribution and isotopic fractionation during chemical weathering and soil formation in a loess profile. J. Asian Earth Sci. 87, 1-10.

Udo, E.J. (1978) Thermodynamics of potassium-calcium and magnesium-calcium exchange-reactions on a kaolinitic soil clay. Soil Sci. Soc. Am. J. 42, 556-560.

Uhlig, D., Schuessler, J.A., Bouchez, J., Dixon, J.L. and von Blanckenburg, F. (2017) Quantifying nutrient uptake as driver of rock weathering in forest ecosystems by magnesium stable isotopes. Biogeosciences 14, 3111.

Untersteiner, N. (1968) Natural desalination and equilibrium salinity profile of perennial sea ice. J. Geophys. Res. 73, 1251-1257.

Valley, J.W., Peck, W.H., King, E.M. and Wilde, S.A. (2002) A cool early Earth. Geology 30, 351-354.

Van As, D., Andersen, M.L., Petersen, D., Fettweis, X., van Angelen, J.H., Lenaerts, J.T.M., van den Broeke, M.R., Lea, J.M., Boggild, C.E., Ahlstrom, A.P. and Steffen, K. (2014) Increasing meltwater discharge from the Nuuk region of the Greenland ice sheet and implications for mass balance (1960-2012). J. Glaciol. 60, 314-322.

Vasskog, K., Langebroek, P.M., Andrews, J.T., Nilsen, J.E.Ø. and Nesje, A. (2015) The Greenland Ice Sheet during the last glacial cycle: current ice loss and contribution to sea-level rise from a palaeoclimatic perspective. Earth Sci. Rev. 150, 45-67.

Vauchel, P., Santini, W., Guyot, J.L., Moquet, J.S., Martinez, J.M., Espinoza, J.C., Baby, P., Fuertes, O., Noriega, L., Puita, O., Sondag, F., Fraizy, P., Armijos, E., Cochonneau, G., Timouk, F., de Oliveira, E., Filizola, N., Molina, J. and Ronchail, J. (2017) A reassessment of the suspended sediment load in

the Madeira River basin from the Andes of Peru and Bolivia to the Amazon River in Brazil, based on 10 years of data from the HYBAM monitoring programme. J. Hydrol. 553, 35-48.

Viers, J., Barroux, G., Pinelli, M., Seyler, P., Oliva, P., Dupré, B. and Boaventura, G.R. (2005) The influence of the Amazonian floodplain ecosystems on the trace element dynamics of the Amazon River mainstem (Brazil). Sci. Total Environ. 339, 219-232.

Viers, J., Roddaz, M., Filizola, N., Guyot, J.-L., Sondag, F., Brunet, P., Zouiten, C., Boucayrand, C., Martin, F. and Boaventura, G.R. (2008) Seasonal and provenance controls on Nd–Sr isotopic compositions of Amazon rivers suspended sediments and implications for Nd and Sr fluxes exported to the Atlantic Ocean. Earth Planet. Sci. Lett. 274, 511-523.

Vigier, N., Decarreau, A., Millot, R., Carignan, J., Petit, S. and France-Lanord, C. (2008) Quantifying Li isotope fractionation during smectite formation and implications for the Li cycle. Geochim. Cosmochim. Acta 72, 780-792.

Vigier, N., Gislason, S.R., Burton, K.W., Millot, R. and Mokadem, F. (2009) The relationship between riverine lithium isotope composition and silicate weathering rates in Iceland. Earth Planet. Sci. Lett. 287, 434-441.

Vigier, N. and Godderis, Y. (2015) A new approach for modeling Cenozoic oceanic lithium isotope paleo-variations: the key role of climate. Clim. Past. 11, 635-645.

Walker, J.C.G., Hays, P.B. and Kasting, J.F. (1981) A negative feedback mechanism for the long-term stabilization of Earth's surface temperature. J. Geophys. Res. Oceans 86, 9776-9782.

Wang, Q.-L., Chetelat, B., Zhao, Z.-Q., Ding, H., Li, S.-L., Wang, B.-L., Li, J. and Liu, X.-L. (2015) Behavior of lithium isotopes in the Changjiang River system: sources effects and response to weathering and erosion. Geochim. Cosmochim. Acta 151, 117-132.

West, A.J., Galy, A. and Bickle, M. (2005) Tectonic and climatic controls on silicate weathering. Earth Planet. Sci. Lett. 235, 211-228.

Weynell, M., Wiechert, U. and Schuessler, J.A. (2017) Lithium isotopes and implications on chemical weathering in the catchment of Lake Donggi Cona, northeastern Tibetan Plateau. Geochim. Cosmochim. Acta 213, 155-177.

White, A.F. (2002) Determining mineral weathering rates based on solid and solute weathering gradients and velocities: application to biotite weathering in saprolites. Chem. Geol. 190, 69-89.

White, A.F. and Brantley, S.L. (2003) The effect of time on the weathering of silicate minerals: why do weathering rates differ in the laboratory and field? Chem. Geol. 202, 479-506.

Wilde, S.A., Valley, J.W., Peck, W.H. and Graham, C.M. (2001) Evidence from detrital zircons for the existence of continental crust and oceans on the Earth 4.4 Gyr ago. Nature 409, 175-178.

Williams, L.B. and Hervig, R.L. (2005) Lithium and boron isotopes in illite-smectite: The importance of crystal size. Geochim. Cosmochim. Acta 69, 5705-5716.

Wimpenny, J., Gislason, S.R., James, R.H., Gannoun, A., Pogge Von Strandmann, P.A.E. and Burton, K.W. (2010a) The behaviour of Li and Mg isotopes during primary phase dissolution and secondary mineral formation in basalt. Geochim. Cosmochim. Acta 74, 5259-5279.

Wimpenny, J., James, R.H., Burton, K.W., Gannoun, A., Mokadem, F. and Gislason, S.R. (2010b) Glacial effects on weathering processes: new insights from the elemental and lithium isotopic composition of West Greenland rivers. Earth Planet. Sci. Lett. 290, 427-437.

Wimpenny, J., Burton, K.W., James, R.H., Gannoun, A., Mokadem, F. and Gislason, S.R. (2011) The behaviour of magnesium and its isotopes during glacial weathering in an ancient shield terrain in West Greenland. Earth Planet. Sci. Lett. 304, 260-269.

Wimpenny, J., Yin, Q.Z., Tollstrup, D., Xie, L.W. and Sun, J. (2014) Using Mg isotope ratios to trace Cenozoic weathering changes: a case study from the Chinese Loess Plateau. Chem. Geol. 376, 31-43.

Wimpenny, J., Colla, C.A., Yu, P., Yin, Q.-Z., Rustad, J.R. and Casey, W.H. (2015) Lithium isotope fractionation during uptake by gibbsite. Geochim. Cosmochim. Acta 168, 133-150.

Wohl, E., Barros, A., Brunsell, N., Chappell, N.A., Coe, M., Giambelluca, T., Goldsmith, S., Harmon, R., Hendrickx, J.M.H., Juvik, J., McDonnell, J. and Ogden, F. (2012) The hydrology of the humid tropics. Nat. Clim. Change 2, 655-662.

Wombacher, F., Eisenhauer, A., Heuser, A. and Weyer, S. (2009) Separation of Mg, Ca and Fe from geological reference materials for stable isotope ratio analyses by MC-ICP-MS and double-spike TIMS. J. Anal. At. Spectrom. 24, 627-636.

Wombacher, F., Eisenhauer, A., Böhm, F., Gussone, N., Regenberg, M., Dullo, W.C. and Rüggeberg, A. (2011) Magnesium stable isotope fractionation in marine biogenic calcite and aragonite. Geochim. Cosmochim. Acta 75, 5797-5818.

Wood, T.E., Lawrence, D., Clark, D.A. and Chazdon, R.L. (2009) Rain forest nutrient cycling and productivity in response to large-scale litter manipulation. Ecology 90, 109-121.

Wright, S.L. (2015) Assessing the use of non-traditional stable isotopes as tracers of weathering processes: with evidence from the Southern Alps, South Island, New Zealand. University of Southampton (Doctoral dissertation).

Young, E.D., Galy, A. and Nagahara, H. (2002) Kinetic and equilibrium mass-dependent isotope fractionation laws in nature and their geochemical and cosmochemical significance. Geochim. Cosmochim. Acta 66, 1095-1104.

Young, E.D. and Galy, A. (2004) The isotope geochemistry and cosmochemistry of magnesium. Rev. Mineral. Geochem. 55, 197-230.

Zahibo, N., Pelinovsky, E., Talipova, T., Rabinovich, A., Kurkin, A. and Nikolkina, I. (2007) Statistical analysis of cyclone hazard for Guadeloupe, Lesser Antilles. Atmos. Res. 84, 13-29.